Advanced Structured Materials

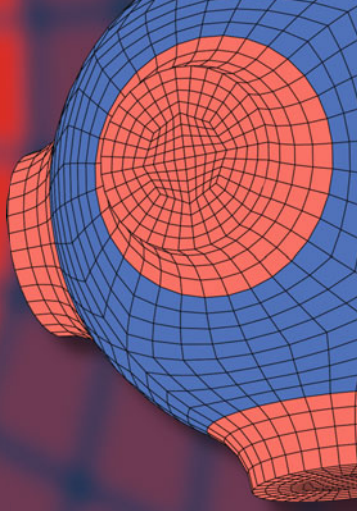

Lucas F. M. da Silva
Chiaki Sato *Editors*

Design of Adhesive Joints Under Humid Conditions

Springer

Advanced Structured Materials

Volume 25

Series Editors

For further volumes:
http://www.springer.com/series/8611

Lucas F. M. da Silva · Chiaki Sato
Editors

Design of Adhesive Joints Under Humid Conditions

Springer

Editors
Lucas F. M. da Silva
Department of Mechanical Engineering
University of Porto
Porto
Portugal

Chiaki Sato
Precision and Intelligence Laboratory
Tokyo Institute of Technology
Yokohama
Japan

ISSN 1869-8433 ISSN 1869-8441 (electronic)
ISBN 978-3-642-37613-9 ISBN 978-3-642-37614-6 (eBook)
DOI 10.1007/978-3-642-37614-6
Springer Heidelberg New York Dordrecht London

Library of Congress Control Number: 2013944519

Printed on acid-free paper

Springer is part of Springer Science+Business Media (www.springer.com)

Preface

Adhesive joints are nowadays a major method of joining in many industries. The pioneers were the aerospace engineers but other more traditional industries such as the automotive engineers are increasingly using adhesives to bond their innovative designs and materials. The joint mechanics are well understood in static conditions, however, concerning other modes of loading such as impact, vibration and fatigue, the information is relatively scarce. However, the major reason concerning the still limited use of adhesives in the automotive industry is the lack of design tools in terms of durability. It is at the moment difficult to predict the failure load after exposure to load, temperature and humidity over a long period of time. With the rapid increase in numerical computing power there have been attempts to formalize the different environmental contributions in order to provide a procedure to predict assembly durability, based on an initial identification of diffusion coefficients and mechanical parameters for both the adhesive and the interface. A coupled numerical model for the joint of interest is then constructed and this allows local water content to be defined and resulting changes in adhesive and interface properties to be predicted. However, there are many challenges associated to this simplified analysis that need to be addresses such as the diffusion of water at the interface, the mechanical behavior of the interface, corrosion of the substrate, etc. The most recent advances and limitations concerning design of adhesive joints under humid conditions are described in this book and future trends are discussed. The book contains eight chapters that cover the effect of water on the adhesive and the interface, surface treatments against water attack, and tools to predict the joint strength under humid conditions.

The editors would like to thank the authors for their patience with the preparation of this book. Finally, we especially thank Dr. Christoph Baumann, Springer editor, who made this book possible.

Porto — Dr. Lucas F. M. da Silva
Yokohama — Prof. Chiaki Sato

Contents

Diffusion of Water in Adhesives

John Comyn

Abstract The diffusion of water into adhesives and adhesive joints is controlled by Fick's laws, and it is solutions to Fick's second law in Cartesian coordinates, which are most used in this context. Such solutions can describe diffusion in both 1 and 2 dimensions. Humidites in air are conveniently controlled using saturated solutions of salts. It is the interactions of water with epoxide adhesives which have been studied most, and diffusion is often fickian, but non-fickian diffusion is not uncommon. When salt is dissolved in water, in effect it dilutes the water, and the amount of water which is absorbed is reduced. Absorption isotherms for water in epoxides are non-linear. Water can change the properties of epoxides by lowering the glass-transition temperature, forming cracks, crazes and voids. Mechanical properties are also affected. Amongst non-structural adhesives, water diffusion has been reported for some silicones and isocyanates.

Abbreviations

The following abbreviations are used to indicate the components of epoxide adhesives.

BF_3MEA	Borontrifluoride monoethylamine
CTBN	Carboxy-terminated butadiene-nitrile polymer
DAB	1,3-diaminobenzene
DAPEE	Di(1-aminopropyl-3-ethoxy)ether
DGEBA	Diglycidyl ether of bisphenol-A
DDM	4,4′-diaminodiphenylmethane
DICY	Dicyandiamide
DMP	Tris(dimethylaminomethyl)phenol
TETA	Triethylenetetramine

J. Comyn (✉)
Department of Materials, Loughborough University, Loughborough LE11 3TU
Leicestershire, UK
e-mail: gloojc@gmail.com

L. F. M. da Silva and C. Sato (eds.), *Design of Adhesive Joints Under Humid Conditions*, Advanced Structured Materials 25, DOI: 10.1007/978-3-642-37614-6_1,

1 Introduction

All polymers are permeable to all gases, vapours and liquids, thus all adhesives, which are based on organic polymers are permeable to water. This means that water will diffuse into the adhesive layer of a joint when exposed to water or water vapour. The basic reason for polymer permeability is the high level of molecular motion in these materials compared with glasses and metals. Molecular motion also means that polymers creep much more than other materials. It has been remarked that if metals creep then polymers gallop.

A basic model for diffusion in polymers is to put a billiard ball into a bucket of spaghetti with sauce. As the ball descends, the strands move out of the way to let it pass, and then reform behind it. Motion of the strands is essential for the ball to pass. The sauce assists motion as does a plasticiser.

Some polymers are partially crystalline, such that small crystals are contained in a continuum of amorphous material. Diffusion only occurs in the amorphous phase as the crystals are too tightly packed to allow a diffusing molecule to enter. Generally adhesive are amorphous and this is the case with structural adhesives. Crystallinity can be present in polychloroprene, polyurethane and hot-melt adhesives.

Although water enters the adhesive in joints and causes some changes in the properties of the adhesive, this is not a significant factor in the weakening of joints. It is water attacking the interface which is the cause of weakening, and this is particularly so when the adherend is a metal which will have a high surface free energy. The principle role of the adhesive is to transmit water to the interface.

2 Fick's 1st Law of Diffusion

Diffusion is controlled by Fick's laws. Fick's 1st law (Eq. 1) states that the flux in the x-direction (Fx) is proportional to the concentration gradient dc/dx.

$$F_x = -D.\ dc/dx \tag{1}$$

F_x is the amount crossing unit area in unit time and D is the diffusion coefficient. The minus sign arises because diffusion is down a slope with a positive gradient. The 1st law is only directly applicable to the *steady state*.

Actually Eq. (1) is not strictly true. The real driving force for diffusion is not concentration gradient, but *gradient of chemical potential* $d\mu/dx$, but this is only something physical chemists would worry about. If concentration gradient were the real driving force then all liquids would be miscible; water would mix with oil as there is an infinite concentration gradient at the interface.

3 Fick's 2nd Law of Diffusion

Fick's 2nd law has several forms. For a box shaped element in cartesian coordinates, there will be six fluxes across the six faces, and the sum of these will control the build up or decay of diffusant in the box. This leads to Eq. (2) where t is time.

$$dc/dt = D(\partial^2 c/\partial x^2 + \partial^2 c/\partial y^2 + \partial^2 c/\partial z^2) \quad (2)$$

Very often experiments are arranged so that diffusion is limited to one direction, the x-direction. Here Eq. (2) simplifies to Eq. (3).

$$dc/dt = D\,\partial^2 c/\partial x^2 \quad (3)$$

For a cylindrical element, the 2nd law has the form

$$dc/dt = (1/r)[\partial(rD.\,\partial c/\partial r)\partial r + \partial(D/r.\,\partial c/\partial\theta)\partial\theta + \partial(rD\,\partial c/\partial z)\partial z] \quad (4)$$

which simplifies to Eq. (5) if diffusion is entirely radial, as in the case for a cylindrical butt joint exposed to water.

$$dc/dt = (1/r)[\partial(rD.\,\partial c/\partial r)\partial r] \quad (5)$$

The problem is generally to find solutions to the 2nd law which are appropriate to the particular conditions. These are generally found in books by Crank [1] and by Carslaw and Jaeger [2]. The latter deals with the conduction of heat, which shares mathematics with the phenomenon of diffusion; the equivalent parameters to permeability coefficient P, diffusion coefficient D and solubility coefficient S are thermal conductivity, thermal diffusivity and heat capacity.

4 Concentration-Distance Profile Across a Long Layer of Adhesive

For a long adhesive joint which is wide and narrow, diffusion at the ends can be neglected. If its width is 2L, the adherends are impermeable to water, and exposure is to a constant bath of water or wet air, concentrations of water (C) at points across the adhesive layer is given by Eq. (6). The centre of the joint is located at $x = 0$. This equation also applies to a film of adhesive exposed at both faces.

$$C/C_1 = 1 - (4/\pi)\sum_{n=0}^{\infty}[(-1)^n/(2n+1)]\exp[-D(2n+1)^2\pi t/4L^2)]\cos[(2n+1)\pi x/2L] \quad (6)$$

C_1 is the concentration of water in the surface layers, and it is an assumption that this concentration is attained instantaneously. Integrating Eq. (6) gives Eq. (16).

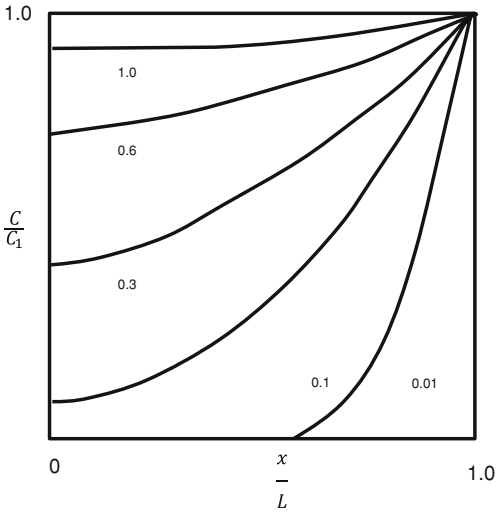

Fig. 1 Plots of Eq. (6). The number against each plot is the value of Dt/L^2

These complex equations can be handled on a personal computer, and generally only a few low values of n are needed, as the summation terms quickly diminish. Plots of Eq. (6) are shown in Fig. 1.

5 Concentrations Within a Rectangular Lap Joint

The rectangular adhesive layer in a lap joint can be represented by the intersection at right angles of two long adhesive layers, each described by Eq. (6). I refer to these as layer A and B, and hence the concentration of water in the layers is C_A/C_1 and C_B/C_1 and their widths are $2L_A$ and $2L_B$. The resulting concentrations of water in the rectangular joint C_J are given by Eq. (7).

$$(1 - C_J/C_1) = (1 - C_A/C_1)(1 - C_B/C_1) \tag{7}$$

If the joint is square Eq. (8) applies.

$$(1 - C_J/C_1) = (1 - C/C_1)^2 \tag{8}$$

This can be extended to diffusion in 3 dimensions, as would be the case for a thick slab of adhesive.

6 Permeation Diffusion and Solubility

If a film of adhesive separates wet air from dry air, then by the process of permeation water will pass through the film. If two evacuated chambers are separated by a polymer membrane of area A and thickness *l*. At zero time, vapour at pressure

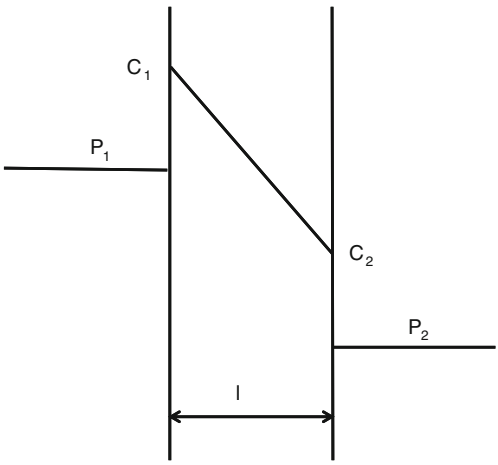

Fig. 2 Permeation through a film of thickness l

p1 is introduced to chamber 1, it permeates the membrane and the pressure p2 builds up in chamber 2.

There are three processes in permeation, Fig. 2. Firstly vapour dissolves in the face of the membrane adjacent to chamber 1. Secondly, it diffuses across the membrane to face 2, and finally evaporates into chamber 2. The concentrations of water in the faces of the membrane are C_1 and C_2, hence the flux is given by Fick's 1st law, i.e.

$$F_x = -D(C_2 - C_1)/l \tag{9}$$

Hence the amount of vapour to have permeated the film Q in time t is

$$Q = -D(C_2 - C_1)At/l \tag{10}$$

Direct measurement of C_1 and C_2 is not possible, but it is assumed that Henry's law (amount dissolved is proportional to vapour pressure) applies at both faces. S is the solubility coefficient so

$$S = C_1/p_1 = C_2/p_2 \tag{11}$$

$$Q = -DSAt\ (p_2 - p_1)/l \tag{12}$$

Experiments are often arranged so that $p_1 \gg p_2$, hence

$$Q = -DSAtp_1/l \tag{13}$$

The product DS is known as the permeability coefficient

$$P = DS \tag{14}$$

$$Q = -PAtp_1/l \tag{15}$$

7 Characteristics of Fickian Sorption

Fickian sorption is typical of diffusion in rubbery polymers, but is widely shown by structural adhesives which are glasses.

Equation (16) is the solution to Eq. (3) for a film of polymer immersed in an infinite bath.

$$M_t/M_e = 1 - \sum_{n=0}^{\infty} 8 \exp\left[-D(2n+1)^2 \pi t/1^2\right]/(2n+1)^2\pi^2 \tag{16}$$

M_t is the mass absorbed at time t and M_e is the mass absorbed at equilibrium. At short times, Eq. (16) takes the simpler form

$$M_t/M_e = (4/l)\,(Dt/\pi)^{1/2} \tag{17}$$

This means that if M_t is plotted against the square root of time, D can be obtained from the initial slope, Fig. 3.

After equilibrium has been attained, drying gives a desorption plot. The plot can be superimposed on a plot of M_t/M_e against $t^{1/2}$, but by plotting fractional desorption instead of fractional uptake. The desorption plot is usually below the sorption plot because D is a function of concentration, and increases with concentration due to plasticization. In desorption, diffusant from within is having to pass through an outer layer were there is less diffusant. Values of D obtained in sorption experiments are an average over a concentration range as given by Eq. (18).

$$\bar{D} = (1/C_1) \int_0^{C_1} D\,dC \tag{18}$$

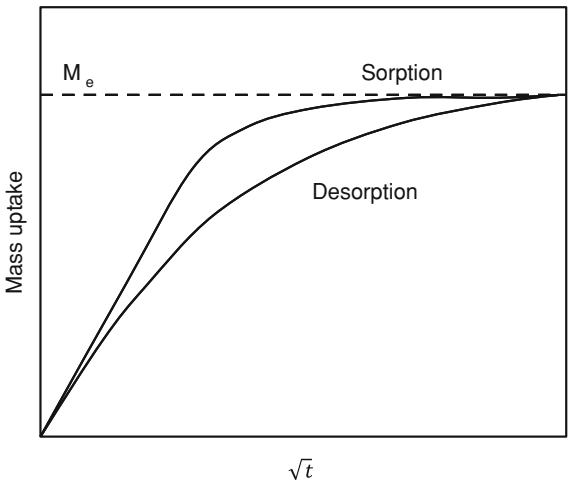

Fig. 3 Fickian sorption plot

The characteristics of Fickian sorption have been summarised by Fujita [3]. They include

(1) Sorption is linear to $M_t/M_e \approx 0.6$, it then curves over to equilibrium.
(2) Sorption with different film thicknesses superimpose on a plot of M_t/M_e against $t^{1/2}/l$
(3) Generally the sorption plot is above the desorption plot, but the two coincide if D is independent of concentration.

8 Measurement of P, D and S

P can be measured by heat sealing water in a small bag of polymer, maintaining at constant temperature and recording weight loss. An alternative is to place a desiccant (silica-gel or molecular sieve) in the bag and then expose to constant humidity and temperature. Another method is to adhesively bond a film of adhesive to the rim of small jar (60 cm^3) which contains a desiccant and expose at constant humidity. If the adhesive absorbs a quantity of water which can be weighed, then by the use of Eq. (14) the diffusion coefficient can be obtained.

If a film of adhesive is exposed to water or wet air, then its weight can be periodically measured and plotted in accordance with Eq. (17). The initial slope gives the diffusion coefficient, and the weight increase at equilibrium is a measure of solubility coefficient.

Chauffaille et al. [4] used electrochemical impedance spectroscopy to measure water sorption of a thin layer of epoxide on a sheet of aluminium. The sample was immersed in water and the measured AC impedance depended on capacitance and permitted the measurement of overall water uptake. Gravimetry was also done on detached films. Temperatures used were 25, 36 and 56 °C and sorption was entirely fickian. Data provided by both methods were “acceptably comparable”.

9 Water and Water Vapour

9.1 Water and Saturated Vapour

If water is placed in a closed vessel and allowed to equilibriate, then at any temperature between 0 and 100 °C the pressure of water vapour in the headspace will be the *saturated vapour pressure of water* at the particular temperature, which has the symbol p_o. For example p_o at 25 °C is 3.1690 kPa but at 25 °C is 12.344 kPa; p_o rises exponentially with temperature. The familiar way in which the wetness of air is quantified is the *relative humidity* (r.h.), which is related to the actual vapour pressure p by Eq. (19).

$$\text{r.h.} = (p/p_o) \times 100 \quad (19)$$

When water vapour and the liquid are in equilibrium, they have the same *chemical potential*. This means that they are equivalent so it does not matter whether a detached film of adhesive or a joint are immersed in the liquid or the saturated vapour; the effect will be the same. Clearly water in the liquid is more concentrated that in the vapour, but as noted above it is *chemical potential* and not concentration which is the controlling factor.

9.2 Variable Humidity

Exposure of adhesives or joints to air at a constant humidity can be done in an expensive environmental chamber, or simply and cheaply using saturated salt solutions. For example if sodium chloride is the salt then at 22.8 °C relative humidity is 75.5 % and at 37.8 °C it is 75.1 %. The procedure is to prepare a saturated salt solution in a small container (such as a polythene sandwich box) and place it in a chamber at constant temperature. It is important that crystals of the salt are present at all times, as the system is self-correcting. What this means is that as some vapour escapes when the container is opened, some salt will be precipitated from solution. On the other hand if some liquid is added some salt will dissolve. Another advantage is that several humidities can be provided in one constant temperature chamber. Salts are available to cover a very wide range of humidities and details are given by Wink and Sears [5] and by Wexler [6].

10 Sorption Data

10.1 Fickian Sorption

The data shown in Table 1 is for a range adhesives which show fickian sorption of water.

Ahmad et al. (2012) measured water sorption by some epoxide adhesives for wood from the liquid at 20 °C and at 95 % r.h at 20, 30 and 50 °C. One adhesive contained silica as a thixotrope, another was rubber modified with CTBN and the 3rd had a mixture of fillers. Except for the case of the rubber-modified adhesive which was "mildly deviant" behaviour was fickian. Values of P, D and S were reported. D fitted the Arrhenius equation with respective activation energies of 73, 47 and 110 kJ mol^{-1}.

Table 1 Water uptake properties of structural adhesives

Adhesive	Temperature (°C)	D (10^{-12} m^2s^{-1})	M_E (%)
Modified phenolic adhesives Brewis et al. [36]			
Nitrile-phenolic	25	3.3	1.50
	50	4.7	4.5
Vinyl-phenolic	25	1.8	3.5
	50	2.3	8.6
Acrylic adhesives Bianchi et al. [37]			
With chlorosulfonated polyethylene	23	0.64	0.73
	37	1.20	0.82
	47	0.94	3.27
With nitrile rubber	23	0.19	1.72
	37	0.28	2.99
	47	0.66	3.89
Epoxides, DGEBA with the following hardeners Brewis et al. [20]			
DAPEE	25	0.13	5.0
	45	0.46	4.7
TETA	25	0.16	3.8
	45	0.32	3.4
DAB	25	0.19	2.3
	45	0.97	3.1
DDM	25	0.0099	4.1
	45	0.006	1.6
Adhesives for wood Brewis et al. [38]			
Urea–formaldehyde	25	25	7.4
	40	49	8.2
Melamine–formaldehyde	25	21	27
	40	39	41
Phenol-resorcinol–formaldehyde	25	110	14
	40	180	14

10.2 Non-Fickian Sorption

Many epoxide adhesives show fickian sorption from water, however there are some exceptions. Brewis et al. (7) showed a second sorption stage and an example is the epoxide based on DGEBA and DDM at 100 °C. Figure 4. At lower temperatures (25, 45 and 70 °C) the same adhesive shows a single fickian stage. A second stage has also been observed by Althof [8] for the modified epoxide adhesive FM73 at 70 °C and 95 % r.h., but at lower temperatures (20, 40 and 50 °C) and the same humidity the second stage was absent.

Other epoxide adhesives show later weight losses. An example is that based on DGEBA with BF_3.MEA hardener which showed weight loss at 50 °C [9]. At 25 °C behaviour was fickian. In liquid water the weight loss was due to the leaching out of some component, which was not lost to moist air. A second sorption in liquid gives fickian sorption. Brewis et al. [7]. The epoxide-polyamide

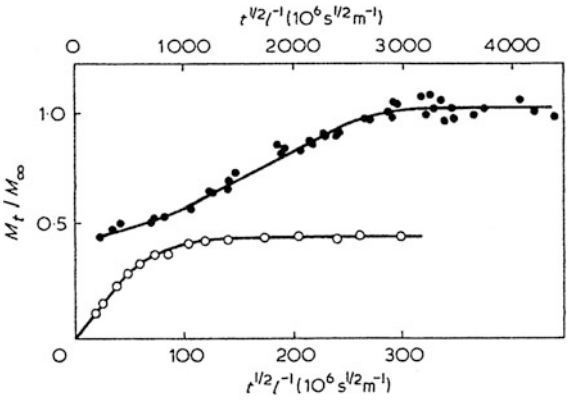

Fig. 4 Sorption plot for water in the DGEBA-DDM adhesive at 100 °C. ❍ lower abscissa at shorter times. ● upper abscissa at longer times. Brewis et al. [20]

adhesive FM1000 shows subsequent weight losses when immersed in water at 1, 25 and 50 °C.

Using a rubber-modified epoxide adhesive, Loh et al. [10] measured mass uptake from wet air at relative humidities of 81.2 and 95.8 % and from water. This was at 50^0 C and the humidities were controlled using saturated salt solutions (potassium chloride and potassium sulfate). The systems demonstrated two uptake stages; D for the first stage was 1.0×10^{-12} m^2s^{-1} but for the second stage D was much reduced and it varied with film thickness. The values for water were 1.5×10^{-14} m^2s^{-1} for a film 0.4 mm thick, 5.0×10^{-14} m^2s^{-1} for a film 0.8 mm thick and 14.0×10^{-14} m^2s^{-1} for a film 2 mm thick. Perhaps the second stage is due to water entering the rubbery particles, but because the level of molecular motion in the rubber will be much higher than in the glassy epoxide: this is not a strong possibility.

However there seems to have been a change of mind, in a later paper Crocombe et al. [11], claim that the data for the 2 mm films is fickian.

Sorption of water in a rubber-toughened DGEBA-DICY adhesive was fickian at 25 and 40 °C but showed a 2nd stage at at 60 and 70 °C [12].

Ameli et al. [13] studied sorption of water in 2 rubber modified epoxide adhesives and their data are shown in Fig. 5. Clearly there is an element of non-fickian sorption particularly at 95 % r.h, but what is striking is that on drying adhesive 1 retains much water, while this is negligible with adhesive 2. Clearly some water molecules are strongly bound to the polymer. In Fig. 5 SDF means sequential dual fickian.

10.3 Salt Solutions

Kahraman and Al-Harthis [14] examined the effect of immersing a 2-part commercial epoxide adhesive, filled with various amount of aluminium powder (10, 25 or 50 %), in distilled water and sodium chloride solutions with concentrations

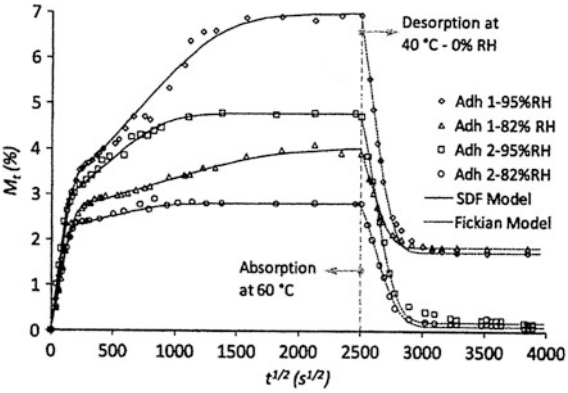

Fig. 5 Sorption plots for epoxide adhesives showing 2nd stages, and for adhesive 1, incomplete removal of water on drying. Ameli et al. [13]

100 ppm, 1000 ppm 0.5 M and 1.0 M. Sorption was essentially fickian, but with some tendency for a second stage. Equilibrium uptake is reduced by the salt, and the authors claim that this is due to reverse osmosis. I disagree and consider it due to the chemical potential of water being reduced by the solute; in effect water is being diluted by salt. Diffusion coefficient was not strongly affected by salt, D having values of about 3×10^{-14} m^2s^{-1} in water and 8×10^{-14} m^2s^{-1} in 1.0 M solution.

Bordes et al. [15] immersed films of an epoxide based on DGEBA and an amine hardener in water and sea water at 20, 40 and 60 °C. Sorption was fickian except in the case of sea water at 60 °C, where there is clear 2nd uptake stage. Diffusion coefficients were slightly higher from sea water.

Datla et al. [16] measured absorption from deionised water and salt water by a rubber-modified epoxide. At room temperature the fickian sorption plots were almost co-incident, but at 40 °C there was a 2nd uptake stage with a higher level of uptake from water.

10.4 Isotherms

The isotherm for the epoxide adhesive DGEBA-DAPEE has been reported by Brewis et al. [7] and is shown in Fig. 6. Figure 7 shows how the diffusion coefficient changes with humidity. The isothrem for the DGEBA-DAB adhesive has been reported by Brewis et al. [17] and is shown in Fig. 8. Both isotherms are non-linear which means that Henry's law does not strictly apply. The increasing curvature is consistent with the formation of water droplets at higher humidities.

The purpose of the latter study was to see if there is a critical humidity for wet durability; that is a humidity below which joints suffer no weakening. Evidence was that it exists at 65 % r.h in the system studied, which corresponds to a water level in the joint of 1.5 %. It is to be noted that there is no change in the isotherm at 65 % r.h.

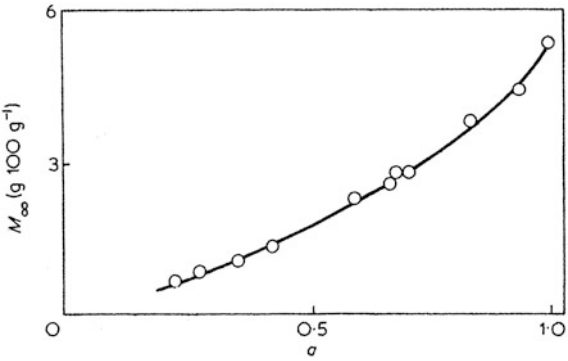

Fig. 6 Dependence of solubility upon humidity for DGEBA-DAPEE adhesive. Brewis et al. [7]. The parameter of the abscissa is a = activity = p/p_o

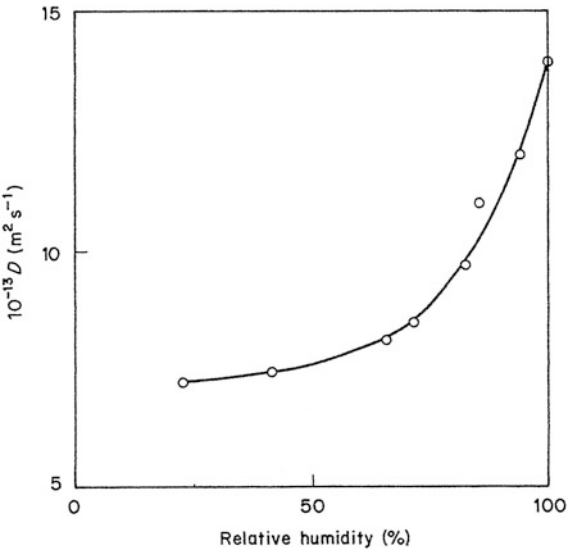

Fig. 7 Dependence of diffusion coefficients upon humidity for water in DGEBA-DAPEE adhesive at 50 °C. Brewis et al. [7]

10.5 Films and Joints

Nuclear reaction analysis was used by Liljedahl et al. [18] to measure water ingress into an epoxide adhesive sandwiched between aluminium adherends. The assemblies were immersed in pure dueterated water at 50 °C and then cooled in liquid nitrogen and cut into pieces. Bombardment with helium 3 ions emitted protons which were detected. Sorption in adhesive films with H_2O was fickian, but it was non-fickian in the sandwiches.

Comparison of water diffusion in joints with that in detached films has been reported by Brewis et al. [19]. Ingress into joints employed radioactively labelled water. It was found that transport into joints was no faster than can be accounted

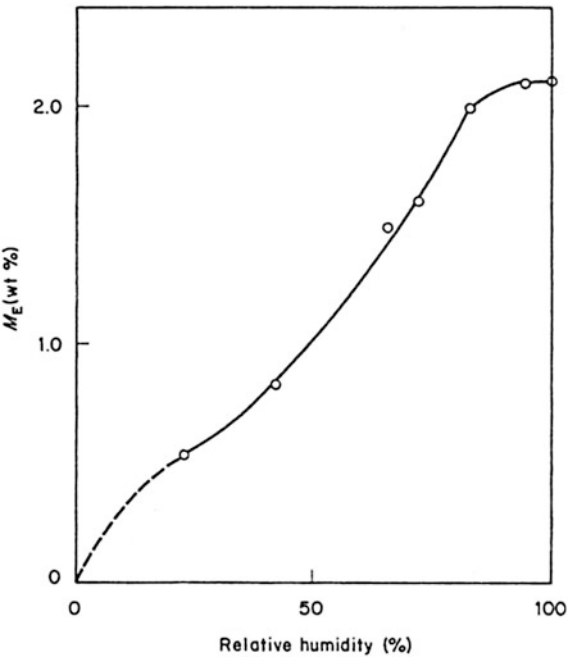

Fig. 8 Absorption isotherm at 50 °C for DGEBA-DAB adhesive. Brewis et al. [17]

for by diffusion and there was no evidence for water entering along the adhesive-metal or adhesive-carrier interfaces. The adherends were of chromic acid-etched aluminium and the adhesive contained a carrier made of knitted nylon.

11 Effect of Temperature

Diffusion is an activated process that obeys the Arrhenius Eq. (20), where E_D is the activation energy for diffusion, R is the universal gas constant and T is the absolute temperature. Some values appear in Table 2.

$$D = D_o \exp(-E_D/RT) \tag{20}$$

Table 2 Activation energies for diffusion and heats of solution for water in some epoxides. Brewis et al. [20]

Hardener	E_D/kJ mol^{-1}	ΔH_s/kJ mol^{-1}
BF_3MEA	−15	4.1
DAPEE	68	−2.8
DAB	38	[a]
DDM	63	[a]
DMP	63	−1.1
TETA	74	−2.6

[a] The plot of log M_e against 1/T was not linear

M_e will vary with temperature and the heat of solution ΔH_s is given by Eq. (21).

$$d \ln M_e / d\,(1/T) = -\Delta H_s / R \tag{21}$$

12 How Water Changes the Properties of Adhesives

12.1 Glass Transition Temperature

Brewis et al. [20] measured heat-distortion temperatures Td of a range of epoxide adhesives, both dry, after reaching equilibrium when immersed in water, and after a total of 10 months immersion. Their data which appear in Table 3 show that distortion temperatures are all initially lowered in water, but all increase on immersion for 10 months. The latter may be due to further crosslinking between unreacted groups in the water-plasticised adhesive. The actual changes after initial immersion were compared with that predicted by the Fox equation for glass transition temperatures, [21]. In some cases the two values are in reasonable accord. Except with DAPEE hardener, the actual depression of Td is less than that predicted by the Fox equation; this can readily be explained by some of the water not being molecularly dispersed in the resin and so not plasticising it, but instead being isolated in clusters.

In such cases the Fox Eq. (22) [21] is moderately successful in accounting for the Tg.

$$1/Tg = w_A/Tg_A + w_w/Tg_w \tag{22}$$

Here w_A and w_w are the weight fractions of the adhesive and water, and Tg_A and Tg_w are the respective glass transition temperatures. The equation assumes that Tg is subject to the free volume theory and that contributions of the components are additive.

Use of the Fox equation requires a value for the glass transition temperature of water. This has been reported in the range –134 to –138 °C using differential thermal analysis and other methods [22–24].

Table 3 Heat distortion temperatures of some dry and wet epoxides. Brewis et al. [20]

Hardener	Equilibrium water absorption at 25 °C		Td/°C			Td depression/°C	
	(%)		Dry	Wet	10 months	Actual	Fox eqn
DAPEE	5.0	67	37		49	30	23
TETA	3.8	99	86		111	13	23
DAB	2.3	161	143		157	18	22
DDM	4.1	119	110		130	9	27
DMP	4.4	68	51		54	17	21
BF_3MEA	2.3	173	155			18	21

12.2 Cracks, Crazes and Voids

Apicella et al. [25–27] demonstrated fickian uptake with an equilibrium plateau for water absorption for an epoxide adhesive hardened with TETA, at 23, 45 and 75 °C. However on altering the temperature for an equilibriated sample, weight always increased and did not move necessarily towards the equilibrium first associated with the new temperature. For example if samples are first equilibriated at 45 and 75 °C, and then the temperature then lowered to 23 °C, a weight loss would be expected. What was seen was a weight increase, and this was attributed to the formation of microcavities. On the basis of there being no microcavities at 23 °C, the water contained in the cavities at 45 and 75 °C were respectively 0.23 and 0.94 %. The water which seemed to be isolated in microcavities did cause cause the Tg to be lowered.

Brewis et al. [20] exposed films of the epoxide adhesive with DGEBA-DAPEE hardener to successive sorption–desorption cycles from saturated air at 48 °C. Their results showed that D decreased with cycling and equilibrium mass uptake increased slightly; these were both ascribed to the formation of microcracks. For both parameters the greatest changes were seen in the first cycle. This information is shown in Fig. 9.

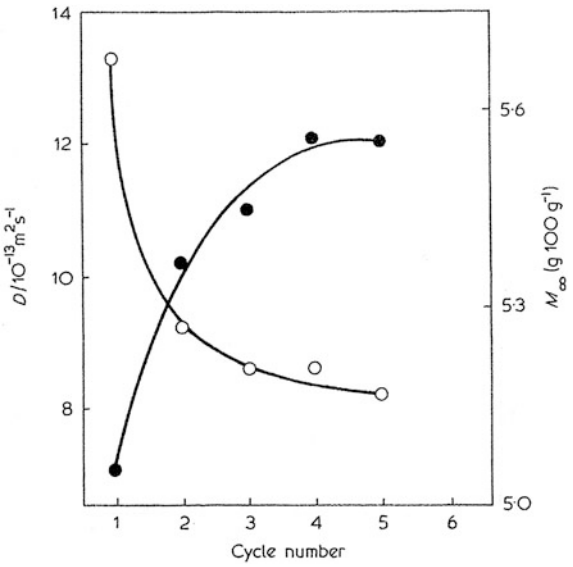

Fig. 9 Changes in diffusion coefficient and solubility during sorption–desorption cycles for DGEBA-DAPEE adhesive at 100 % r.h. Brewis et al. [20]. ○ = diffusion coefficient ● = solubility

Table 4 Mechanical properties of dry and wet adhesives Brewis et al. [30]

Details of exposure	Yield strength (MPa)	Tensile strength (MPa)	Elongation at break (%)
(a) Dry	48.4	41.1	7.1
(b) 24 h in water at 100 °C	23.9	24.4	37.0
(c) as (b) followed by drying for 48 h at 65 °C in vacuum	57.8	52.0	6.8

12.3 Mechanical Properties

Su et al. [28] exposed some commercial epoxide adhesives and found that both young's modulus and shear strength were reduced in all cases. Bowditch et al. [29] studied the effect of wet air on the moduli of an epoxide adhesive with a number of inorganic fillers (aluminium oxide, barium sulfate, lead oxide, stannic oxide and ferric oxide, and titanium dioxide). In all cases modulus fell with increasing humidity, and it was suggested that this was due to the hydrophilicity of the filler surfaces. The effect was greatest with aluminium oxide, which appears to have the highest surface free energy.

The effect of water on the mechanical properties of films of DGEBA-DAPEE adhesive has bee investigated by Brewis et al. [30]. Data are shown in Table 4; all failures were ductile. Clearly water changes mechanical properties, but recovery on drying leads to higher than dry strengths, which might be due to extended cure in the wet adhesive.

13 Non-Structural Adhesives

13.1 Silicones

Some one-part isocyanates and silicones cure by water diffusing from the atmosphere. The chemical reactions which crosslink these adhesives/sealants are fast, and cure proceeds by the layer of cured material thickening with time. Beneath this layer the material is not cured. There is no partial cure because as soon as a molecule of water reaches it, it will react. It has been shown by Comyn et al. [31, 32] that the thickness of the cured layer (z) is given by Eq. (23) where P is the permeability coefficient of water in the cured layer, p is the vapour pressure of water in the air, V is the volume of material which reacts with a mole of water and t is time. Measurements of P have been made on a number of materials. Comyn et al. [31, 32] used a silicone and a fluorosilicone, and Comyn et al. [33] used an alkoxy-terminated silicone.

$$z = (2PpVt)^{1/2} \tag{23}$$

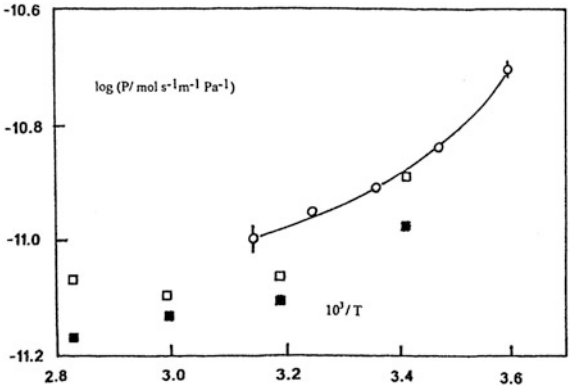

Fig. 10 Dependence of water permeability coefficient upon temperture for some silicones. Comyn et al. [33]

Figure 10 shows an Arrhenius plot for P in a number of cured silicones. Such plots normally show a straight line with a negative gradient, which is not the case here. It is considered that this is due to most water being confined in clusters or droplets. The latter is a common phenomenon in polymers and has been reviewed by Comyn [34]. The actual amounts of water absorbed by silicones is too low to be measured by weighing.

13.2 Isocyanates

Two commercial one-part isocyanates have been studied by Comyn et al. [31, 32]. Using salt solutions to control humidity at 69 and 100 % over water, the value of P was fairly constant for adhesive 69 at about 6×10^{-12} m^2s^{-1} at 25 °C. For adhesive 254 P at 32.7 % r.h. was 1.93×10^{-12} m^2s^{-1} rising to 2.94×10^{-12} m^2s^{-1} at 100 %.

Water sorption in an isocyanate used for 3 automotive windscreen replacement has been examined by Ashcroft et al. [35]. The dependence of P upon temperature is very similar to that seen for silicones, and due to the same cause.

14 Concluding Remarks

The body of information on water diffusion in adhesives is about epoxides based on DGEBA. Sorption is often fickian, but 2nd uptake stages are not uncommon and are favoured by higher temperatures and possibly by the inclusion of toughening rubber particles. The reason for the latter is not obvious. Weight losses are due to leaching of unreacted substances or hydrolysis.

Water uptake levels and diffusion coefficients change when adhesives are subjected to cycles of exposure and drying, and a likely cause is the formation of voids or crazes.

Mechanical properties of adhesives and glass transition temperatures are affected by water but these are not significant causes of joint weakening. The important factor is the affect of water on the interface. A few studies have compared water diffusion in films with that in actual joints, and indicate similar rates of diffusion.

There is much evidence that some of the water in adhesives exists in droplets, in which case only the free water diffuses and causes plasticisation. However water molecules are expected to freely enter and leave the droplets. The limited information on absorption isotherms is that they do not comply with Henry's law.

Absorption from salt solutions is less than from water because the solute lowers the chemical potential of water. Absorption from liquid water and from the saturated vapour in equilibrium will be the same because of equal chemical potentials.

Rates of diffusion of water in epoxides increases exponentiallly with temperature and obeys the Arrhenius equation. Permeability coefficients of water in silicone and polyurethane adhesives are only weakly dependent on temperature and do not obey the Arrhenius equation; droplet formation is the underlying cause.

References

1. Crank, J.: Mathematics of diffusion, 2nd edn. Oxford University Press, Oxford (1975)
2. Carslaw, H.C., Jaeger, J.C.: Conduction of heat in solids, 2nd edn. Oxford University Press, London (1959)
3. Fujita, H.: Adv. Polymer Sci **3**, 1 (1961)
4. Chauffaille, S., Devos, O., Jumel, J., Shanahan, M.E.R.: Int. J. Adhes. Adhes. **30**, 602 (2010)
5. Wink, W.A., Sears, G.R.: TAPPI **33**, 96A (1950)
6. Wexler, A.: Handbook of chemistry and physics (76th Edn). In: Ed Lide, D.R. (ed.) CRC press, Boca Raton, FL (2003)
7. Brewis, D.M., Comyn, J., Shalash, R.J.A., Tegg, J.L.: Int. J. Adhes. Adhes. **21**, 357 (1980b)
8. Althof W.: In: Proceedings of 11th National SAMPE Technical Conference, vol. 309 (1979)
9. Brewis, D.M., Comyn, J., Cope, B.C., Moloney, A.C.: Int. J. Adhes. Adhes. **21**, 344 (1980c)
10. Loh, W.K., Crocombe, A.D., Abdel Wahab, M.M., Ashcroft, I.A.: Int. J. Adhes. Adhes. **25**, 1 (2005)
11. Crocombe, A.D., Hua, Y.X., Loh, W.K., Wahab, M.A., Ashcroft, I.A.: Int. J. Adhes. Adhes. **26**, 325 (2006)
12. Leger, R., Roy, A., Grandidier, J.C.: Int. J. Adhes. Adhes. **30**, 744 (2011)
13. Ameli, A., Papini, M., Spelt, J.K.: Int. J. Adhes. Adhes. **31**, 9 (2011)
14. Kahraman, R., Al-Harthis, M.: Int. J. Adhes. Adhes. **25**, 337 (2005)
15. Bordes, M., Davies, P., Cognard, J.-Y., Sohier, L., Sauvant-Moynot, V., Galy, J.: Int. J. Adhes. Adhes. **29**, 595 (2009)
16. Datla, N.V., Ulicny, J., Carlson, B., Papini, M., Spelt, J.K.: Int. J. Adhes. Adhes. **31**, 88 (2011)
17. Brewis, D.M., Comyn, J., Raval, A.K., Kinloch, A.J.: Int. J. Adhes. Adhes. **10**, 247 (1990)

18. Liljedahl, C.D.M., Crocombe, A.D., Gauntlett, F.E., Rihawy, M.S., Clough, A.S.: Int. J. Adhes. Adhes. **29**, 356 (2009)
19. Brewis, D.M., Comyn, J., Moloney, A.C., Tegg, J.L.: Europ. Polymer J. **17**, 127 (1981)
20. Brewis, D.M., Comyn, J., Tegg, J.L.: Int. J. Adhes. Adhes. **21**, 134 (1980a)
21. Fox, T.G.: Bull. Amer. Phys. Soc. **1**, 123 (1956)
22. McMillan, J.A., Los, S.C.: Nature **206**, 806 (1965)
23. Rasmussen, D.H., MacKenzie, A.P.: J. Phys. Chem. **75**, 967 (1971)
24. Sugisake, M., Suga, H., Seki, S.: Bull. Chem. Soc. Japan **41**, 2591 (1968)
25. Apicella, A., Nicolais, I., Astarita, G., Driola, E.: Polymer **20**, 143 (1979)
26. Apicella, A., Nicolais, I.: Ind. Eng. Chem. Prod. Res. Dev. **20**, 1143 (1981)
27. Apicella, A., Nicolais, I., Astarita, G., Driola, E.: Polymer Eng. Sci. **21**, 17 (1981)
28. Su, N., Mackie, R.I., Harvey, W.J.: Int. J. Adhes. Adhes. **12**, 85 (1992)
29. Bowditch, M.R., Hiscock, D., Moth, D.A.: Int. J. Adhes. Adhes. **12**, 164 (1992)
30. Brewis, D.M., Comyn, J., Shalash, R.J.A.: Int. J. Adhes. Adhes. **24**, 67 (1983)
31. Comyn, J., Brady, F., Dust, R.A., Graham, A., Haward, A.: Int. J. Adhes. Adhes. **18**, 51 (1998)
32. Comyn, J., Day, J., Shaw, S.J.: J. Adhes. **66**, 289 (1998)
33. Comyn, J., de Buyl, F., Shepard, N.E., Subramanian, C.: Int. J. Adhes. Adhes. **22**, 385 (2002)
34. Comyn, J.: Prog. Rubber. Plas. Technol. **1**, 1 (1985)
35. Ashcroft, I.A., Comyn, J., Tellwright, S.: Int. J. Adhes. Adhes. **29**, 155 (2009)
36. Brewis, D.M., Comyn, J., Tredwell, S.T.: Int. J. Adhes. Adhes. **7**, 30 (1987)
37. Bianchi, N., Garbassi, F., Pucciariello, R., Romano, G.: Int. J. Adhes. Adhes. **10**, 19 (1990)
38. Brewis, D.M., Comyn, J., Phanopoulos, C.: Int. J. Adhes. Adhes. **7**, 43 (1987)

Water and Ions at Polymer/Metal Interfaces

Ralf Posner, Ozlem Ozcan and Guido Grundmeier

Abstract The adsorption and transport of water and ions at polymer/metal interfaces has a strong impact on the adhesion of the polymer as well as on the kinetics of corrosive degradation. Although not directly correlated both wet-de-adhesion and corrosive de-adhesion are accelerated by water enrichment at the interface which promotes the ingress of ions. The discussion of these phenomena starts with the consideration of the adsorption of water on oxide surfaces, as all engineering metals are covered with an ultra-thin atmospheric oxide film, and ends with the cathodic and anodic corrosive de-adhesion mechanisms of polymers from oxide covered metals. The bridge between the water adsorption and corrosive de-adhesion reactions is built based on the separation of water and ion transport in polymeric interphases and the discussion of diffusion and migration as the principal processes.

Keywords Adsorption · De-adhesion · Water · Ions · Interface · Delamination · Spectroscopy · Interface electrochemistry · Migration · Diffusion · Corrosion

R. Posner
Henkel Adhesive Technologies, Henkel AG & Co. KGaA, Henkelstrasse 67, 40589 Düsseldorf, Germany

R. Posner
Department of Interface Chemistry and Surface Engineering, Max-Planck-Institut für Eisenforschung GmbH, Max-Planck-Str. 1, 40237 Düsseldorf, Germany

O. Ozcan · G. Grundmeier (✉)
Department of Technical and Macromolecular Chemistry, University of Paderborn, Warburger Str. 100, 33098 Paderborn, Germany
e-mail: g.grundmeier@tc.uni-paderborn.de

L. F. M. da Silva and C. Sato (eds.), *Design of Adhesive Joints Under Humid Conditions*, Advanced Structured Materials 25, DOI: 10.1007/978-3-642-37614-6_2,

1 Introduction

Corrosive de-adhesion processes at polymer coated metal compounds are commonly connected with the interfacial incorporation of water and hydrated ions. H_2O can indeed diffuse directly through the organic matrix, but most coatings nevertheless provide an effective barrier for ion transport based on low dielectric constants and small free volumes of the macromolecular network. In contrast, defects in organic films which penetrate to the metal result in a three phase boundary between aqueous phase, polymer and substrate surface and consequently allow an incorporation of H_2O and hydrated ions along the polymer/oxide/metal interface. Corrosion is initiated at interface sections adjacent to the electrolyte covered defect in the presence of atmospheric oxygen. The present chapter consequently focuses on the aspects of water incorporation at polymer/metal interfaces, on the transport of hydrated ions along the interface, and on thereby induced cathodic as well as anodic de-adhesion processes.

2 Water at Polymer/Oxide Interfaces

2.1 Water Adsorption on Oxide Surfaces

The interaction of water with metal and metal oxide surfaces plays an important role in many interface-governed processes such as adsorption/desorption, heterogeneous catalysis, de-adhesion of polymers and corrosion. From catalytic nanoparticles to the surfaces of engineering alloys all metallic surfaces except that of noble materials are covered with mono- and multiphase, crystalline or amorphous oxide films. Once water molecules reach the polymer/oxide interface, they do not only deteriorate the oxide structure via the formation of metal hydroxides and oxyhydroxides, but also significantly change the properties of the bulk polymer and alter the attractive interactions at the interface.

In general, the surfaces of complex alloys are covered with the native oxides of the alloying elements, for example with those of iron, zinc, aluminium, titanium, copper and magnesium. Due to thermodynamic and kinetic effects such as formation energies, diffusion rates and oxidation affinity, the surface chemistry of alloys usually differs from that of the bulk material.

A profound understanding of the interaction mechanisms with water requires fundamental investigations on single crystalline oxide surfaces of the respective metals. Depending on parameters like temperature or H_2O/O_2 partial pressure during preparation, water will be present on oxide surfaces as molecular H_2O or it may dissociate and form surface hydroxyls. As an adsorbate, water can interact with clean and hydroxylated metal oxide via electrostatic forces or charge transfer reactions and may form hydrogen bonding networks [1].

On Al-terminated α-Al_2O_3 (0001) surfaces, for example, the dissociative adsorption of water has been experimentally and theoretically demonstrated [2–10], but the termination itself is still under discussion. Experiments performed in ultra-high vacuum indicated that α-Al_2O_3 (0001) is either covered with Al [11] or with a combination of Al and O [12]. Crystal truncation rod diffraction studies proved an oxygen terminated, hydrated α-Al_2O_3 (0001) surface with a 53 % contracted double aluminium layer directly below [10]. A molecularly adsorbed water layer was detected about 2.4 Å above the terminal oxygen. Moreover, it was reported that dissociative adsorption of H_2O with low surface mobility is predominant for low degrees of coverage, whereas complex structures of mixed dissociatively as well as molecularly adsorbed water layers should be expected for high coverage levels.

Various studies also focused on the interaction of H_2O with low index surfaces of MgO. Due to the observed reversibility of adsorption isotherms, water has long been considered to adsorb on MgO (001) in a non-dissociative manner [13]. It was also suggested that dissociative adsorption can be only facilitated in the presence of surface defect sites [14]. Recent theoretical work, however, indicated that defects are not required to induce water dissociation [15, 16]. Moreover, it was shown that a certain threshold of water activity is necessary to convert MgO from a state of low, defect-mediated hydroxylation to a fully OH-covered surface [17]. A combined experimental-theoretical investigation proved that initial hydroxylation results in the formation of isolated OH groups and that surface roughening occurs if the water pressure is increased. It points at a mechanism that includes the hydrolysis of Mg–O bonds [18]. This means that extensive hydroxylation should not result in an unstable state of the (001) surface for both MgO bulk and thin films [18].

For some oxides, however, even intense investigations were not sufficient yet to adequately verify possible adsorption mechanisms, for example for the interaction of water with the ideal rutile TiO_2 (110) surface [1, 19, 20]. Experimental results indicate that molecular chemisorption dominates at low temperatures in ultra high vacuum for all degrees of coverage [18, 21, 22], but according to computational studies, dissociative adsorption of water should be the most favorable mechanism for sub-monolayer coverage [23, 24].

2.2 *Molecule and Polymer Adsorption on Water Covered Metal Oxides for the Investigation of Adhesion Forces*

For aluminium, joining by means of welding is rather challenging and bolting/riveting is connected with the disadvantage of increased weight and non-homogeneous stress distribution. Hence, adhesive joining is a very important technological process for the design of light-weight and durable composite structures based on aluminium and aluminium alloys.

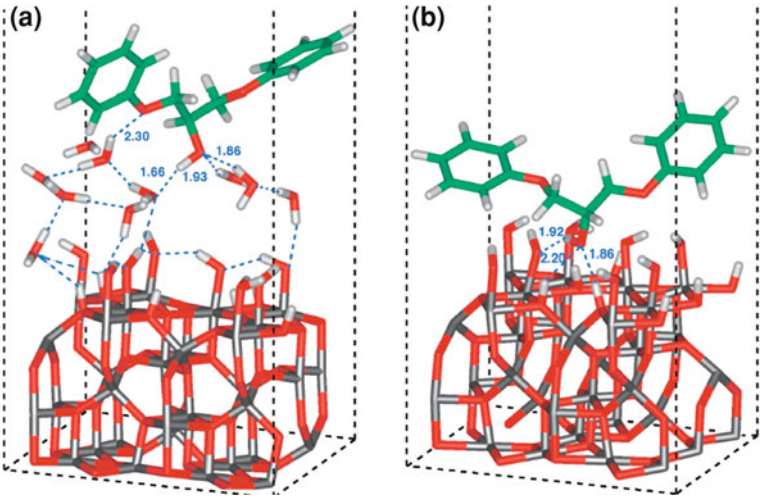

Fig. 1 Optimized structures of adhesive-adherent complexes of (**a**) hydroxylated γ-alumina (001) surface with adsorbed water molecules and (**b**) hydroxylated γ-alumina (001) surface without adsorbed water molecules (Reprinted with permission from Ref. [25]. Copyright 2012, The Chemical Society of Japan)

In this context, theoretical calculations are state-of-the-art to evaluate the resulting adhesion forces. As an example, Fig. 1 illustrates the results of a density functional theory based study that focused on the interaction of diglycidylester-bisphenol (DGEBA) molecules with hydroxylated γ-Al_2O_3 surfaces in the presence and in the absence of a molecular water layer at the interface [25, 26]. For both systems, hydrogen bond formation dominated the interaction mechanism. It results in adhesive energies of 117.5 kJ/mol with and of 66.0 kJ/mol without a molecular water layer. The increased adhesion interaction energies are assigned to a higher number of hydrogen bonds that formed in the presence of water molecules at the interface [25].

The calculated force-distance curves presented in Fig. 2 indicate similar maxima at 0.53 nN and 0.52 nN for water-containing and water-free systems. The shift of the maximum to larger distances refers to a "buffering effect" of molecular water against the shear force of adhesion due to an increased mobility of the H_2O layer. Stress required to peel the adhesive from the surface was evaluated by dividing the maximum force to the projected unit area of the DGEBA molecule. The analysis yielded a maximum adhesion stress of 5.1×10^2 MPa when water was present and of 5.0×10^2 MPa when water was absent. In summary, it was interpreted that H_2O indeed causes higher adhesive interaction energies, but does not induce increased adhesion strengths due to its high mobility at the interface [25].

Taking the next step in the simulation of polymer coatings on metal oxides, the adsorption of epoxy adhesive components on γ-Al_2O_3 surfaces was investigated with a density functional theory based tight binding method [27]. It was focused on diglycidylesterbisphenol (DGEBA), on diethyltriamine (DETA) as well as on the

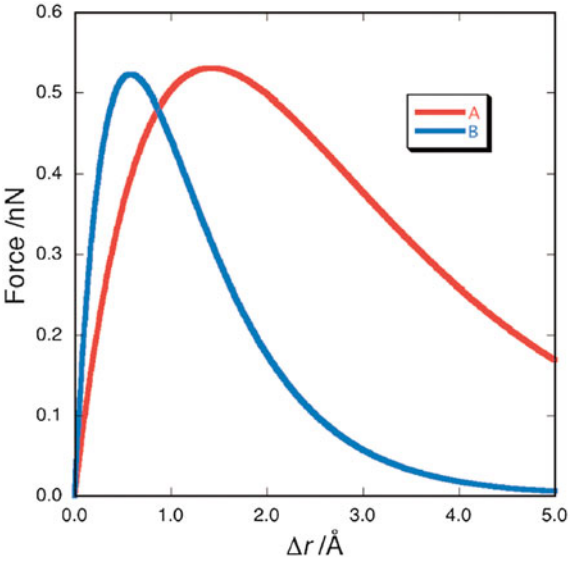

Fig. 2 Calculated force-distance curves for models of adhesive-adherent complexes on the γ-alumina (001) surface (**a**) with and (**b**) without adsorbed water. (Reprinted with permission from Ref. [25] Copyright 2012, The Chemical Society of Japan)

adhesion promoter 3-aminopropylmethoxysilane (AMEO) and shown that the condensation reaction of AMEO via its silane group is favorable compared to those of DGEBA and DETA. Moreover, the process proceeds highly exothermic and with negligible barriers, whereas the reaction of DGEBA depends on the opening of one epoxy ring in the molecule prior to condensation. The curing agent DETA interacts via its amine group with surface hydroxyls and its condensation reaction is highly endothermic. These theoretical results correlate well with the experimental findings which indicate an enrichment of the AMEO molecules at the interface, even when only minor AMEO amounts were added to the polymer formulation [28]. A detailed theoretical analysis of the reaction mechanisms of DGEBA, DETA and AMEO molecules on γ-Al_2O_3 surfaces was based on two possible adsorption sites and focused on the effect of neighboring adsorbates on the adsorption thermodynamics. The structure of the hydroxylated γ-Al_2O_3 surface, the definition of the two adsorption sites and the investigated reaction paths are shown in Figs. 3 and 4 [29].

As seen in Table 1, the presence of neighboring adsorbates results in a significant decrease of most of the condensation barriers. This observation is explained by the creation of movable dipole moments and excess protons which can stabilize the transition states. It also indicates that the presence of proton donors such as physisorbed water molecules effectively support the activation of new reaction routes, for instance by a stabilization of the dangling bonds of opened epoxy rings of DGEBA [29]. Interestingly, silanol type adhesion promoters like AMEO are not affected by this mechanism. Thus, their effect on the interfacial adhesion force cannot be solely explained by the creation of a higher density of interfacial bonds, but in addition by a formation of bonds that are independent of the presence of neighboring adsorbates [29].

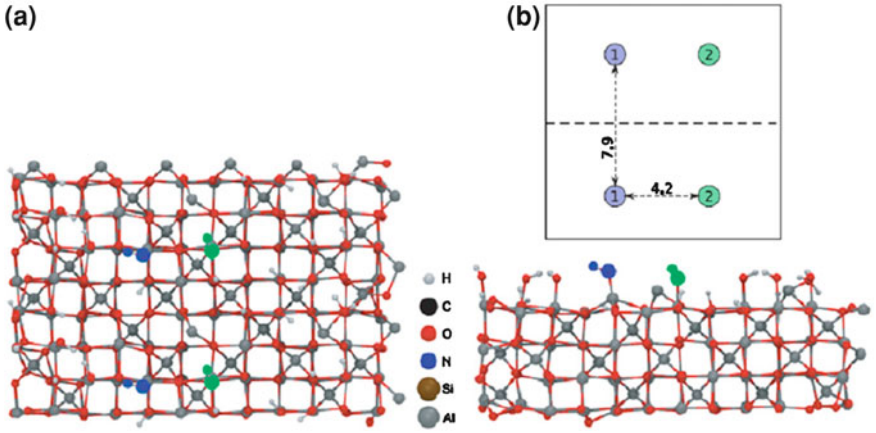

Fig. 3 **a** Views along the (00-1) (*left*) and (010) (*right*) directions of the hydroxylated γ-Al_2O_3 surface model. The adsorption site 1 is marked blue, site 2 is marked green (Reprinted with permission from Ref. [29], Copyright 2012, Springer). **b** Schematic of investigated adsorption sites in the γ-Al_2O_3 supercell and corresponding distances (in Å) (Reprinted with permission from Ref. [29], Copyright 2009, Springer)

For the fundamental analysis of polymer adsorption on metal oxides, combined theoretical and experimental approaches were shown to be promising. As an example, the adhesion of acrylonitrile-butadiene (ABS) on copper and copper oxide surfaces was studied by force field calculations and scanning force microscopy to reveal the applicability of poly(styrene-co-acrylonitrile) (SAN) and poly(styrene-alt-maleic anhydride) (SMAh) as model copolymers for adhesion promotion (see Fig. 5a) [30, 31].

Equivalent adhesion forces on metallic copper of around $\sim$0.5 J/m^2 were detected for SMAh, oxidized SAN as well as for the model polymers ABS and polybutadiene (pBd). However, except for SAN, a strong increase in the work of adhesion was observed when the molecules specifically interacted with oxygen atoms on the substrate surface (see Fig. 5b). SMAh adsorption exhibited the highest work of adhesion and consequently turned out to be the most promising candidate for adhesion promotion [30].

2.3 *Molecular Understanding of Macromolecule/Oxide Interactions in Water Rich Environments*

It is generally accepted that polymer chains are able to form covalent bonds with the oxide surface if the hydrocarbon backbone does not contain polar or charged functional groups. As long as no adhesion promoting molecules are present in the polymer matrix or included in a pre-treatment layer on the substrate, the adsorption

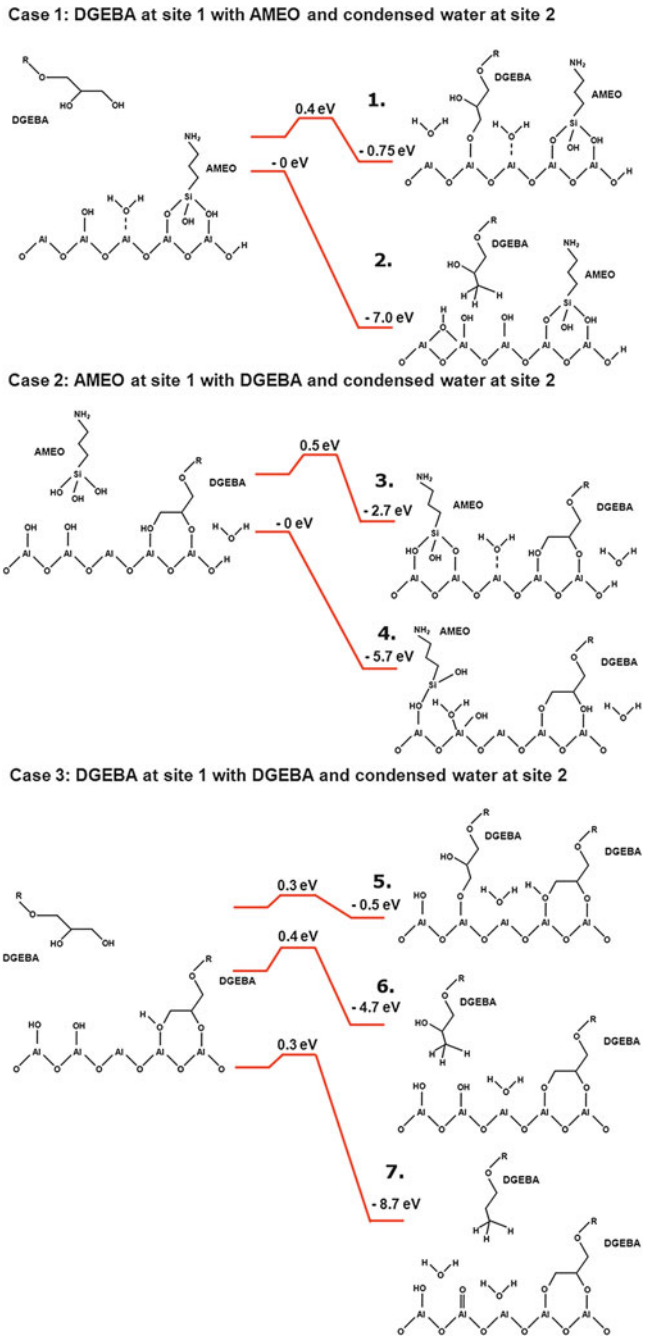

Fig. 4 Possible reactions of DGEBA and AMEO in the presence of pre-adsorbed molecules, illustrating that the presence of proton donors such as physisorbed water molecules can be advantageous in enabling new reaction routes (Reprinted with permission from Ref. [29], Copyright 2009, Springer)

Table 1 Reaction pathways and respective barriers for the co-adsorption of DGEBA and AMEO

Comp. 1	Comp. 2	Mechanism	Mech.	E_r^{sngl}	E_{barr}^{sngl}	E_r^{co}	E_{barr}^{co}
AMEO + H_2O	AMEO	Condensation	–	−4.1	∼0	−3.2	∼0
	DGEBA	Condensation	1	−0.4	2.1	−0.8	0.2
		OH abstraction	2	–	–	−7.0	∼0
AMEO + OH	DGEBA	Condensation	–	−0.4	2.1	−0.4	0.2
DGEBA	AMEO	Condensation	3	−4.1	∼0	−2.7	0.5
		OH abstraction	4	–	–	−5.3	∼0
	DGEBA	Condensation	5	−0.4	2.1	−0.3	0.3
		Single OH abstraction	6	–	–	−4.7	0.4
		Double OH abstraction	7	–	–	−8.7	0.3

Comp. 1 are the components already present at site 2 from the first adsorption reaction, comp. 2 are the newly adsorbed components. E_r^{sngl}, E_{barr}^{sngl} list the isolated adsorption reaction energies and barriers for comp. 2 E^{co} reflect the respective reaction energies and barriers for the co-adsorption scenario. All energies are reported in eV. (Reprinted with permission from Ref. [29], Copyright 2009, Springer)

of macromolecules on oxide surfaces occurs via non-specific van-der Waals interactions [32]. From the perspective of the adhesion of macromolecules, enrichment of water at the polymer/oxide/metal interface on the one hand is problematic, because water molecules can replace polymer-metal/metal-oxide bonds. This can result in wet and/or corrosive de-adhesion [33–36]. On the other hand, for the design of biocompatible materials long-time stability under physiological conditions is a very relevant performance requirement. The prevention of proteins and other macromolecules from adhesion is consequently of crucial importance. Therefore, a profound understanding of the elementary processes of adhesion and de-adhesion at polymer/oxide/metal interfaces is a prerequisite for the design of novel polymer/nanoparticle composites, biocompatible materials, protective polymer coatings as well as high-strength adhesive joints.

The investigation of de-adhesion processes at polymer/metal interfaces and the development of interface-sensitive experimental approaches has been an active area of research during many decades [37–42]. For polymer films on metal electrodes, electrochemical impedance spectroscopy (EIS) was demonstrated to be a versatile tool for the monitoring of water uptake kinetics and the diffusion coefficient of water [41, 43–49]. Alternatively, attenuated total reflection infrared spectroscopy (ATR-IR) [50] can be used to determine water penetration of polymer films with high interfacial sensitivity [50]. It allows for an identification of different interaction modes of water at the interface, such as the formation of clusters or molecular water layers, hydrogen bonding between the polymer and water as well as surface hydroxylation of the metal oxide [37, 40, 41, 51–53]. Additionally, it is sensitive to the local environment of the adorbates and shows deviations in peak locations, shapes and intensities. This offers insights into lateral interactions, vibrational coupling effects, binding modes as well as into molecular conformation and orientation [54]. Additional information about (in situ) adsorption/desorption and adhesion/de-adhesion processes at buried interface may

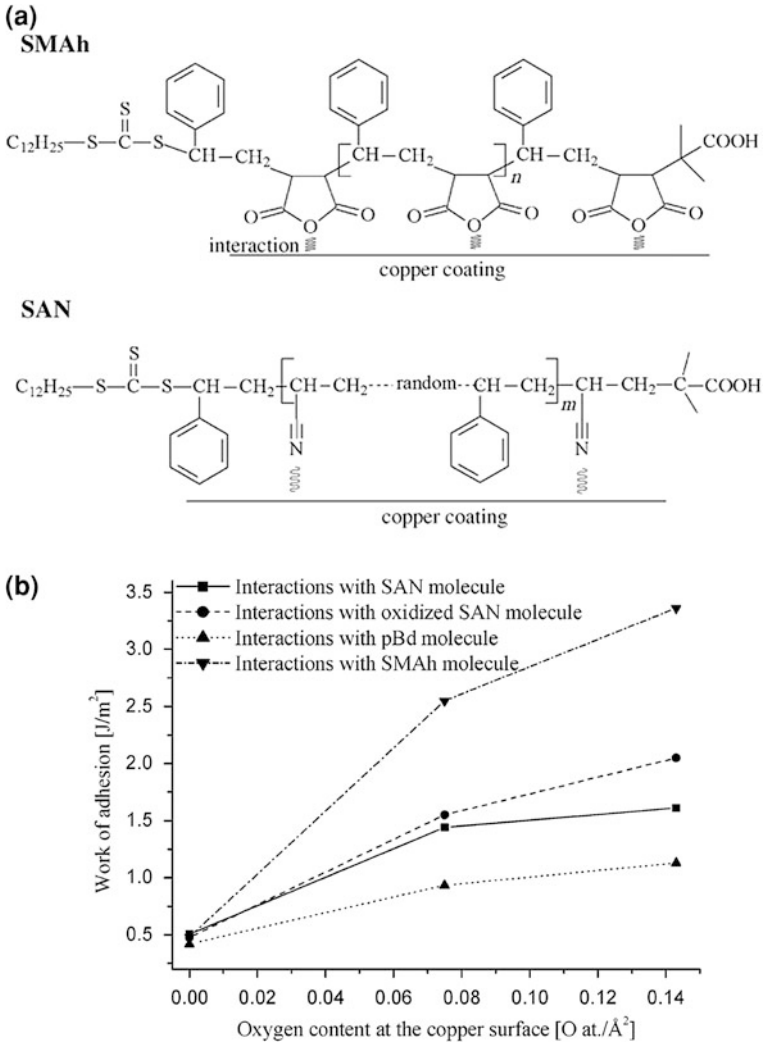

Fig. 5 **a** Schematic illustration of the chemical structure of the SMAh and SAN copolymers and their potential interaction with copper coatings (Reprinted with permission from Ref. [31], Copyright 2006, Wiley–VCH). **b** Values for the work of adhesion between single SAN, oxidized SAN, polybutadiene, and SMAh molecules with pure copper surface and oxygen-modified copper surfaces (Reprinted with permission from Ref. [30], Copyright 2007, American Chemical Society)

be obtained employing surface enhanced infrared absorption spectroscopy as well as surface enhanced Raman spectroscopy [42, 54]. Moreover, the water uptake of polymer films can be investigated by combined setups for simultaneous ATR-IR and EIS measurements [41].

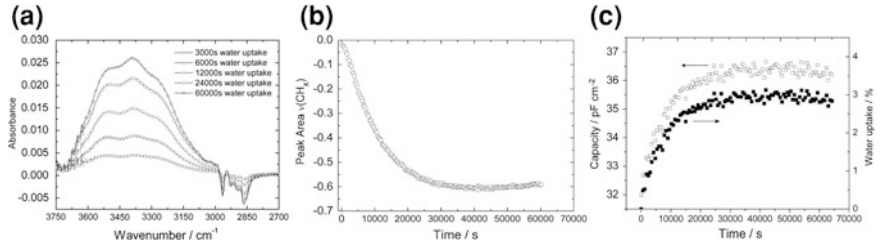

Fig. 6 **a** Increase of the H_2O-peak area in the interphasial adhesive layer during water uptake ($D = (2.0 \pm 0.2) \times 10^{-9}$ cm^2/s). **b** Decrease of the CH_x-stretching peak in the interphasial adhesive layer during water uptake. **c** Capacitance change (measured at 10 kHz) and calculated water uptake for a defect-free adhesive film (Reprinted from Ref. [41], Copyright 2007, with permission from Elsevier)

Figure 6 illustrates experimental data generated with such an approach. Shown are area changes of H_2O (a) and CH_2 (b) stretching vibration peaks of a defect-free epoxy film adsorbed on a silicon substrate during the exposure to borate buffer solution. Capacitance and water uptake profiles obtained by EIS were recorded simultaneously (see Fig. 6c). The CH_2 peak intensity decreased by 4–5 % at maximum, which indicates that wet de-adhesion of the macromolecular film did not take place during water uptake. Moreover, equivalent coefficients for H_2O diffusion through the polymer layer were determined by ATR-IR and EIS: 2.0×10^{-9} cm^2/s.

For a more realistic simulation of technical interfaces, thin metal or oxide films can be deposited on surfaces of the internal reflection elements used for ATR-IR spectroscopy prior to coating with a polymer [40]. The diffusion of water through a two component model adhesive (nitrile rubber and vinylchloride-vinylacetate copolymer) film, for example, was recently investigated using aluminium deposited on ZnSe ATR crystals [40]. Peak area changes indicating an increased water activity at the polymer/aluminium interface (O–H stretching vibrations at 3,450 cm^{-1}, O–H bending vibrations at 1,650 cm^{-1}, and Al–O-/Al–OH-vibrations detected at 960 cm^{-1}, see Fig. 7b) reflected saturation curves (see Fig. 7a) [51]. While exposed to one molar NaSCN solution, the transport of thiocyanate ions through the macromolecular layer was tracked by monitoring of the C = N vibration signal at 2,075 cm^{-1}. In contrast to the development of the peak areas for water as shown in Fig. 7a, the C = N signal intensity increased linearly and thereby confirmed that different mechanisms determine the transport of thiocyanate and H_2O [51].

These results were complemented by a combined ATR-IR/EIS study of structural adjustments occurring at aluminium/polymer sample systems during the exposure to one molar NaSCN solution [53]. It shows that simultaneously recorded infrared and electrochemical impedance spectra provide important additional information. Figure 8a–d illustrates time-resolved intensity changes of the peaks detected at 3,450, 1,650, 2,075 and 950 cm^{-1} for an aluminium surface coated

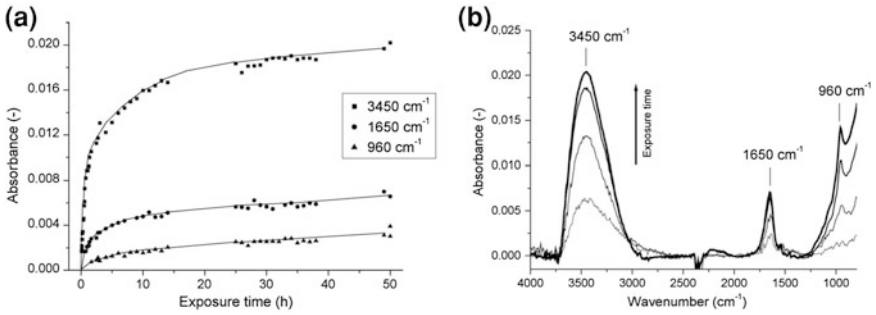

Fig. 7 **a** IR absorption intensities at 3,450, 1,650 and 960 cm^{-1} versus the exposure time for the ZnSe element coated with a thin aluminium film and a polymer film in contact with ultra pure deionized water. **b** ATR-FTIR spectra of a ZnSe element coated with a thin aluminium film in contact with ultra pure deionized water. The exposure times were 40, 163 min, 26 and 50 h, respectively. The ATR-IR absorption peak at 1,650 cm^{-1} stays constant during exposure to water (see Fig. 8b) and thus allows a substrate independent analysis of water uptake on the aluminium oxide film (Reprinted from Ref. [51], Copyright 2006, with permission from Elsevier)

with a transparent alkyd based polymer layer [53]. The corresponding impedance data are presented in Fig. 8e. It is observed that the ingress of H_2O into the polymer film caused a rapid change of the infrared absorbance intensities of the water and hydroxyl stretching bands centered at 3,450 cm^{-1}. The plateau in the impedance curves recorded at low frequency values indicates the presence of pores and small defects in the macromolecular coating. The Al–O and Al–OH vibration peak at 950 cm^{-1} appeared delayed, because a minimum threshold water activity level at the polymer/aluminium interface has to be achieved before oxidation and hydroxylation reactions can initiate. Changes in the absorption signals at 1,650, 3,450 and 950 cm^{-1} show a clear deviation from what has to be expected for Fickean diffusion driven processes, because after approximately 34 h of exposure, a quick and linear increase of the peak intensities is observed. The impedance data in turn reflect an abrupt decline of the film resistance after 34 h of exposure. This confirms distinctly changed water uptake kinetics and indicates the onset of delamination/wet de-adhesion of the polymer layer [53].

3 Ion Transport at Polymer/Metal Interfaces

Once water and hydrated ions are present at polymer/metal interfaces, additional electrochemical processes such as interfacial transport of charged species can initiate and result in corrosive degradation. For polymer coated iron or zinc substrates, for example, de-adhesion of organic films occurred to be often dependent on the cathodic delamination mechanism. It depends on the formation of galvanic cells at the interface with locally separated electrodes, local reduction of O_2 and

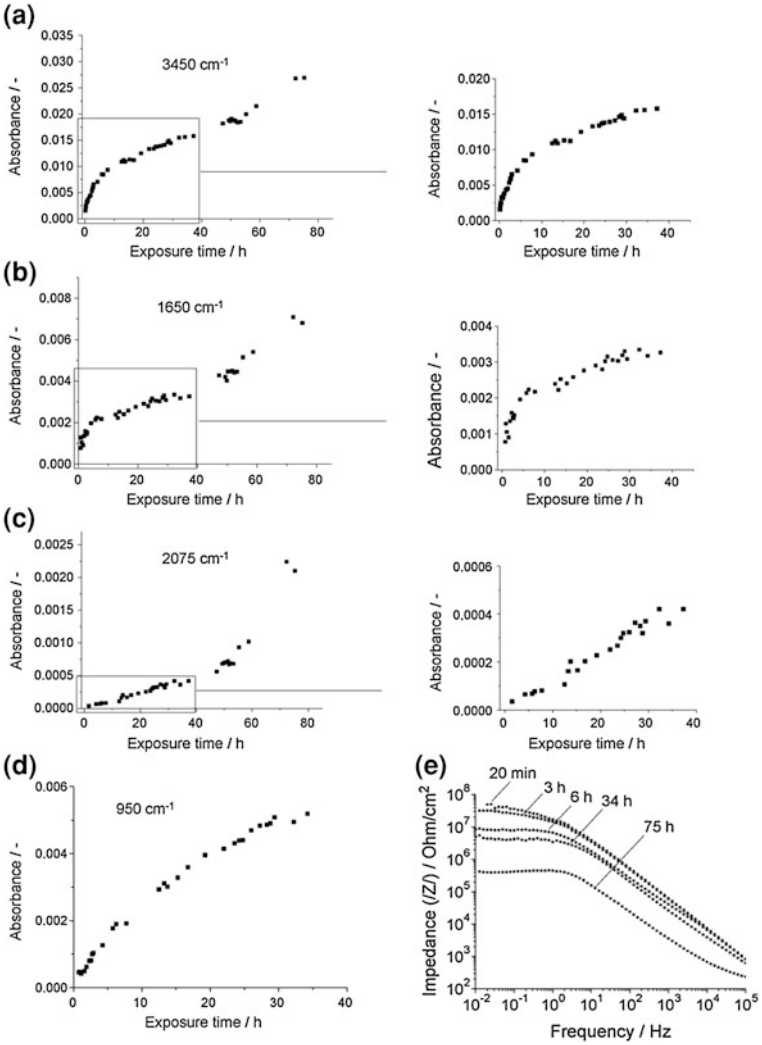

Fig. 8 The absorption intensity versus the exposure time for the ZnSe element coated with a thin aluminium film and a transparent alkyd varnish in contact with a 1 M NaSCN solution for the peaks (**a**) 3,450 cm^{-1} (**b**) 1,650 cm^{-1} (**c**) 2,075 cm^{-1} (**d**) 960 cm^{-1} and (**e**) the corresponding electrochemical impedance spectra at different exposure times. The ATR-IR absorption intensities at 1,650 and 3,450 and 950 cm^{-1} shows a deviation from Fickian behavior, which is in good agreement with the sudden drop in impedance values indicating wet de-adhesion/delamination of the polymer film (Reprinted from Ref. [53], Copyright 2007, with permission from Elsevier)

requires ion transport for charge compensation. Theoretical concepts that sufficiently describe and predict these processes are hardly available due to the complexity of polymer/substrate interface structures. Basic aspects were adopted

from mechanistic considerations developed for bulk electrolyte solutions or idealized model geometries, but still require comparison with experimental observations made at technically relevant interface systems. Therefore, the following paragraphs briefly introduce some background concepts prior to the presentation of the fundamentals of corrosive delamination.

3.1 The Fundamentals of Hydrated Ion Transport: Ion Diffusion, Ion Migration in an Electric Field & Electro Kinetics

Corrosion processes are usually dependent on the formation of a galvanic cell with separated local anode and cathode in contact with a conductive electrolyte. Electrons are exchanged via a metallic connection and the circuit is completed by a transport of ions in bulk electrolyte to compensate the generated charge surplus near the electrodes. Such transport is enforced by an electric field E that exerts a force $\left|\vec{F}_E\right|$ on ions of species i with a charge z·e (e: elementary charge):

$$\left|\vec{F}_E\right| = z_i \cdot e \cdot \left|\vec{E}\right| \tag{1}$$

Anions are accelerated towards the anode and cations move towards the cathode. However, ion transport through an aqueous solution will be decelerated by a rising friction force $\left|\vec{F}_R\right|$ with increasing transport velocity:

$$\left|\vec{F}_R\right| = 6\pi \cdot r_i \cdot \eta \cdot |\vec{v}_i|$$

(r_i: radius of ion species i, η: solvent viscosity, $|\vec{v}_i|$: velocity of ion species i) [55]. A constant transport rate will be achieved for

$$|\vec{v}_i| = \frac{\left|\vec{F}_E\right|}{6\Pi . r_i . \eta}$$

and directly affects the electrolytic conductivity of a salt solution. The mobility of ion species i in bulk water is strongly determined by parameters such as ion concentrations and interionic interactions [55]. For aqueous electrolytes especially the dipole properties of H_2O molecules play an important role. Dependent on the electrostatic field that results from ion charge and ion radius, H_2O species form solvation shells of different structure and spatial dimensions. Na^+ for example exhibits an ion radius of around 0.097 nm and thereby generates a stronger electric field than K^+ with a radius of around 0.133 nm. The number of water molecules that form the hydration shell of Na^+ is 7–8 and consequently larger than for K^+, which is 4–5 [55]. This leads to increasing hydrodynamic radii for alkali cations in the order $Cs < Rb < K < Na < Li$ and is correlated with a decreasing ion mobility at polymer/oxide/metal interfaces.

Exceptional effective charge transfer between the electrodes of a galvanic cell can be achieved with acid and alkaline solutions due to a fast diffusion of protons between H_2O molecules. For high ion concentrations in delaminated areas of polymer coated metal compounds, ion–ion interactions additionally affect the mobility of charged species. Coulomb attractions promote the generation of short range orders between a central ion and hydrated ions of opposite charge encircling it. Brownian motion indeed counteracts such formation of ordered structures within the bulk electrolyte, but cannot fully compensate the process if cations and anions are accelerated in opposite directions due to the electric field of a galvanic cell. In that case, the short range order gets distorted and will be continuously rearranged, which takes some time. The central ion therefore moves ahead its 'cloud' of counter ions and is retained. As contrary charged species are accelerated in opposite direction by the external electric field, the central ion moves additionally decelerated due to electrophoretic effects [55–58].

Ion transport processes are not only affected by electrostatic forces, because inhomogeneous ion distributions are released by diffusion, as well. The proportionality of particle flow J and concentration gradient $\delta c/\delta x$ is expressed by Fick's first law. Moreover, the particle flow is dependent on the particle (drift) velocity $|\vec{v}|$ as well as on the concentration c:

$$J = |\vec{v}| \cdot c = -\boldsymbol{D}\frac{\delta c}{\delta x} \tag{2}$$

(D: diffusion coefficient) [56]. The thermodynamic force $\left|\vec{F}\right|$ for particle movement arises from an inhomogeneous distribution of species i, which results in a locally different chemical potential μ_i [56]:

$$\left|\vec{F}\right| = -\left(\frac{\delta \mu_i}{\delta x}\right)_{p,T\ const}$$

(x: respective location in the first dimension, T: temperature, p: atmospheric pressure). Taking the chemical potential $\mu_i = \mu_{i0} + RT\ln(a_i)$ for species i into account (μ_{i0}: chemical potential for standard conditions, R: universal gas constant, a_i: activity of species i), the following equation results:

$$\left|\vec{F}\right| = -RT\left(\frac{\delta \ln(a_i)}{\delta x}\right)_{p,T\ const}$$

For ambient conditions, the atmospheric pressure and temperature can be expected to remain constant, and for ideal solutions a_i can be replaced by the concentration c_i of species i. With application of Eq. 2 the resulting drift velocity can be additionally attributed to the contributions of concentration gradients and external forces [56]:

$$|\vec{v}_i| = -\frac{D}{c_i}\frac{\delta c}{\delta x} = \frac{D}{RT} \cdot \left|\vec{F}\right|$$

If species i moves in an external electrostatic field, its force $\left|\vec{F}\right|$ can be specified by the electric force $\left|\vec{F}_E\right|$ of Eq. 1. In that case, the drift velocity is equivalent to the ion velocity introduced for Eq. 2. The resulting effective ion mobility then is (F = Faraday constant) [56]:

$$\frac{\left|\vec{v}_i\right|}{\left|\vec{E}\right|} = \frac{z_i \cdot F \cdot D}{RT}$$

Even if no external electric field supports ion transport, an additional electrostatic effect has to be taken into account when cations and anions move along a concentration gradient. If the diffusion coefficients of the two ion types differ from each other, diffusion potentials become effective. The smaller ion exhibits a larger mobility and moves ahead. This results in a separation of positive and negative ion charge and thereby in a potential drop along an emerging phase boundary. Due to the resulting electrostatic field ions with higher mobility are retained, whereas the counter ion transport proceeds accelerated. At steady state conditions both ion types move at same speed and a diffusion potential $\Delta\varphi_{\mathrm{Diff}}$ results [56]. The thermodynamic driving force to overcome the diffusion potential drop ΔG_{Diff} can be calculated by

$$\Delta G_{Diff} = -z \cdot F \cdot \Delta\phi_{Diff}$$

(z: charge number of the ions), and ΔG_{Diff} can be described as the sum of the chemical potential changes $\delta\mu$ of all involved ion species between inner and outer boundary of the diffusion layer [56]. In most cases such diffusion potentials are distinctly smaller than e.g. the potential difference between the electrodes of a galvanic cell. However, they may not be generally neglected if ion transport kinetics at polymer/oxide/metal interfaces are investigated, because the interfacial mobility of cations and anions may differ more than in bulk solution [59].

If this is due to a preferential interaction of positively or negatively charged ions with the metal oxide (preferential adsorption etc.) or with functional groups of the macromolecular network (complexation etc.), ion transport proceeds along electrified interfaces. An electric double layer will be present on the oxide surface of the metal substrate as well as at any boundary between aqueous and organic phase. Therefore, additional electro kinetic mechanisms can be effective which refer to the movement of a liquid phase *along* a solid phase due to an external electric field [55, 56]. They can be best described if the electrolyte saturated polymer/oxide-interface is regarded as an assembly of electrolyte filled capillaries. Ion transport due to cathodic or anodic delamination between an electrolyte covered coating defect and the respective front of corrosive de-adhesion at the adhesive/substrate interface then resembles two electrodes being located at both ends of the capillaries. If ions migrate in an external electric field between cathode and anode, any preferential adsorption of positively or negatively charged species at the capillary walls results in the formation of a diffuse double layer by

oppositely charged ions and a surplus of these oppositely charged ions in solution. The aqueous phase usually exhibits the higher dielectric constant and therefore gets positively charged. Movement of hydrated cations to the cathode will then effectively result in a water flow via the ion hydration shells, a phenomenon known as electro osmosis. Figure 9 provides a schematic overview. It can be shown that the zeta potential ζ, which describes the potential drop across the double layer at the capillary walls, is proportional to the observed (solvent) flow velocity v [55]:

$$\zeta = \frac{\eta \cdot v}{\varepsilon_r \cdot \varepsilon_0 \cdot E}$$

(ε_0: vacuum permittivity, ε_r: relative dielectric constant of the electrolyte solution). It results in a measurable electro osmotic pressure that destabilizes the adhesive/substrate interface and potentially promotes polymer de-adhesion. Electrolyte flow along the interface can also occur due to a pressure gradient Δp between both ends of the capillaries without externally applied electric polarization. In that case, double layer formation at the capillary walls due to preferential ion adsorption will in turn result in an electric field gradient between both ends of the capillaries, the flow potential U_{flow}:

$$U_{flow} = \frac{\varepsilon_r \cdot \varepsilon_0 \cdot \Delta p \cdot \zeta}{\eta \cdot \kappa}$$

(κ: electric conductivity of the electrolyte solution) [55]. As a summary, it should be expected that ion transport at polymer/oxide/metal interfaces will be determined by the synergistic interaction of various processes. The contribution of

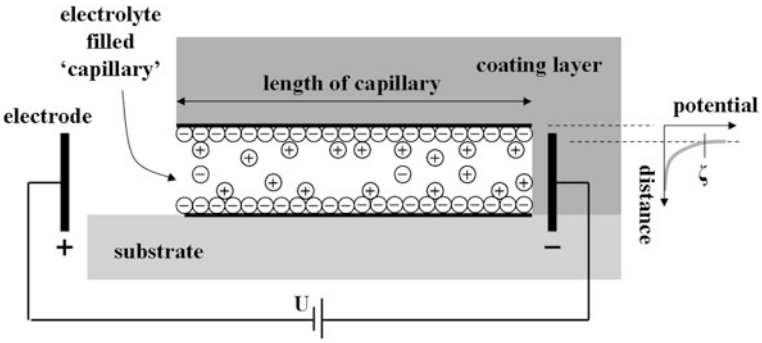

Fig. 9 Schematic illustration of the geometry of a hypothetic capillary at a solid/polymer interface. If this capillary is filled up with aqueous electrolyte, its walls in many cases will get negatively charged due to preferential anion adsorption. This induces a cation surplus in the liquid phase that causes an electro osmotic flow via the hydration shells resulting in an electric field gradient between both ends of the capillary. If an external electric field is generated by polarization with voltage U, electro osmosis in turn will result in a pressure gradient that can destabilize the interface of the sample compound. It was shown that the electro osmotic flow is proportional to the zeta potential ζ, the potential drop across the electric double layer at the capillary walls. (Schematic inspired by [55])

each of these effects to the overall driving force will vary and strongly depend on the structure of the buried interface.

3.2 Corrosive & Cathodic Delamination at Polymer/Oxide/Metal Interfaces

Polymer coatings on metals inhibit electrochemical processes at the substrate surface. Adhesives with adequate barrier properties prevent the access of hydrated ions to the polymer/substrate interface, provide a saturation of adsorption sites at the metal/oxide surface and thereby reduce the maximum interfacial water activity that can be achieved during an exposure to a humid environment. A low interfacial ion concentration will result in a less compact electric double layer at the oxide surface. This is preferred, because a diffuse double layer functions as an additional kinetic barrier for electrochemical processes [42]. As oxidation or reduction process at the oxide surface depend on a discharge or formation of ion species, their passage through a diffuse double layer will consequently occur decelerated and result in reduced interface corrosion under these conditions.

Unfortunately, polymer covered surface areas that surround a coating defect tend to continuously delaminate in humid atmosphere if the defect goes down to the metal substrate and gets into contact with an aerated electrolyte. Already water ingress will weaken the polymer/substrate interface stability, but additional electrochemical processes will even more distinctly accelerate corrosive de-adhesion. They dominate in humid air and on metals such as iron or zinc, which are covered by (semi) conductive oxide structures. Amongst others, the electrochemical properties of the oxide, its solubility at different pH, the oxygen permeability, the adhesion and structure of the organic layer, the type and geometry of an electrolyte filled coating defect as well as the relative humidity of the surrounding atmosphere were highlighted as determinant factors for corrosion mechanisms such as cathodic delamination [60–66].

The resulting electrochemical processes can be interpreted in terms of current–potential-curves (see Fig. 10). On iron substrates oxygen will be reduced in the defect area until the diffusion limiting current density level is achieved or nearly achieved [60, 66, 67]:

$$1/2\ O_2 + H_2O + 2e^- \rightleftarrows 2\ OH^-$$

This diffusion limiting current density level determines the maximum rate of the electrochemical process. The activation energy for oxygen reduction on electrolyte covered iron is usually low and the reaction rate is consequently that fast that all O_2 molecules passing the compact electric double layer at the oxide surface will be almost immediately reduced. This means that the maximum current density level is determined by the rate at which oxygen diffuses to the electrode.

For charge compensation, iron dissolves as anodic counter reaction, a process that can proceed at a higher rate than oxygen reduction:

$$Fe \rightleftarrows Fe^{2+} + 2e^{-}$$

Steady state conditions are achieved if the cathodic current density i_{cath} is equal to the anodic current density i_{anod} (see Fig. 10). Oxygen diffusion to the iron oxide surface consequently does not only limit the cathodic process, but also determines the entire kinetics of the galvanic cell. It should be noted that dissolved iron

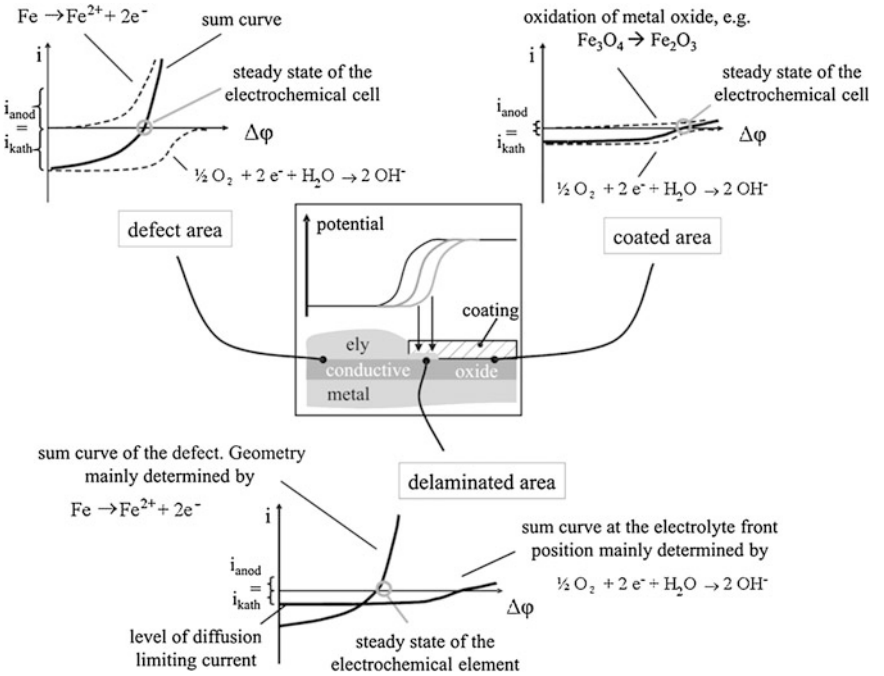

Fig. 10 Illustration of current (i) versus Galvani potential difference ($\Delta\varphi$) curves for the description of electrolyte/substrate, polymer/substrate and polymer/electrolyte/substrate interface potentials at a polymer coated iron compound in humid air. Prior to cathodic delamination, two separated galvanic cells are effective: Metal dissolution and oxygen reduction proceed at high rate in the electrolyte ("ely") covered defect. In contrast, O_2 reduction at the intact polymer/substrate interface is strongly inhibited, because metal dissolution is suppressed and only oxide oxidation occurs. Compared to the defect area, this leads to a more anodic (higher) potential at steady state conditions of the galvanic cell and to a characteristic sigmoid potential profile for the interface (see the illustration in the centre of Fig. 10). As soon as the electrolyte penetrates the polymer/oxide/metal interface, a conductive connection between defect and adjacent polymer coated areas is established, the inhibition of the oxygen reduction process is released and the interface potential is shifted down close to the defect potential. The arrows in the central schematic indicate that this results in a lateral displacement of the inflection point in the sigmoid potential profiles with time, which helps to identify the actual electrolyte front position. [Inspired by [59, 60]]

species precipitate within the defect area as ferric or ferrous (oxidic) hydroxides and form red rust:

$$Fe^{2+} + 2\ OH^- \rightleftarrows Fe(OH)_2\downarrow$$

$$Fe^{2+} + 3\ OH^- \rightleftarrows FeO(OH)\downarrow + 1\ H_2O + e^-$$

Initial oxygen reduction can also occur at the intact polymer/oxide/metal interface, because a small amount of O_2 can diffuse through the polymer depending on the barrier properties of its macromolecular network. But due to the non-compact electric double layer at the buried interface, this process is kinetically strongly inhibited. Iron oxide oxidation (for example from FeO or Fe_3O_4 to Fe_2O_3) as anodic counter reaction quickly results in a depletion of Fe(0) and Fe(II) donor states within the oxide. This further reduces the achievable anodic maximum current density for oxygen reduction and from the electrochemical point of view has to result in a high anodic overpotential of the galvanic cell at steady state conditions. Consequently, a distinct potential difference between defect area and intact interface will be monitored (see Fig. 10).

The electrolyte at the defect can now penetrate adjacent polymer covered interface areas. Thereby, the kinetic barrier for oxygen reduction at the polymer/oxide/metal interface will be bypassed by an increased anodic metal dissolution in the defect. A direct connection of the two formerly isolated electrochemical cells at defect and intact interface results. The two current–potential-sum curves then determine the interface potential in the delaminated area. Steady state conditions will be achieved at or near the oxygen diffusion limited maximum cathodic current density level. As the polymer functions as a certain barrier for oxygen diffusion, i_{cath} will be relatively small compared to the cathodic current density at the defect. This means that the anodic current density for iron dissolution needs to be only slightly increased to compensate the cathodic O_2 reduction process in the area of interfacial electrolyte ingress. The corrosion potential will be hardly anodically shifted, and because no anodic overpotential is effective in the delaminated area any longer, a potential similar to that one of the defect will be detected. This allows tracking of the cathodic delamination progress by continuous monitoring of the polymer/oxide/metal interface potential. The lateral displacement of the inflection point in the sigmoid potential profile is commonly used as an indicator for the front position of corrosive de-adhesion (see Fig. 10) [60, 66, 67].

The separation of local anode (iron dissolution in the defect) and local cathode (oxygen reduction in the delaminated area) requires a transfer of electrons to the electrolyte front position, which is determined by the electric conductivity of the oxide. A transport of (hydrated) ions along the polymer/oxide/metal interface is required to complete the electric circuit (see Fig. 11). Therefore, cations of the defect electrolyte move towards the front of delamination. They are electrostatically attracted by negatively charged hydroxide ions generated while interfacial oxygen reduction proceeds. Increasing OH^- concentration at the polymer/oxide/metal interface results in a pH of around 13 and passivates the iron substrate.

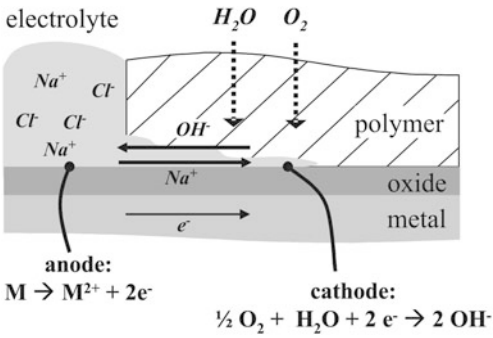

Fig. 11 Schematic illustration of the cathodic delamination mechanism. Electrolyte covering a defect of a polymer coated iron or zinc sheet penetrates the polymer/oxide/metal interface. This is catalysed by a galvanic cell in humid air: Metal ("M") dissolution occurs at the local anode in the defect, whereas oxygen diffusing through the adhesive layer gets reduced at the buried interface. Hydroxide is generated, which results in an increase of the interfacial pH and a transport of cations from the defect electrolyte towards the front of delamination for charge compensation. Expansion of free volumes at the interface due to electrolyte ingress, structural adjustments of the macromolecular polymer structure and the oxide morphology in alkaline environment as well as oxidative degradation by reactive oxygen species then supports de-adhesion of the coating. The electric circuit is completed by a transfer of electrons between anode and cathode [59]

No interfacial Fe-hydroxide precipitation occurs and OH^- ions are transported to the defect to support charge compensation between the local electrodes. It was observed that the interfacial ion transport is often the slowest process step and therefore rate-determining for cathodic delamination [60, 66, 67].

Oxygen reduction at the adhesive/substrate interface promotes an oxidative degradation of the polymer structure. It is expected that this is supported by highly reactive oxygen species, in particular radicals and intermediates evolving during the O_2 reduction process [67]:

$$\begin{gathered}
O_2 + e^- \rightleftarrows O_2^{-\cdot} \\
O_2^{-\cdot} + H^+ \rightleftarrows O_2H^{\cdot} \\
O_2H^{\cdot} + e^- \rightleftarrows O_2H^- \\
O_2H^- + H^+ \rightleftarrows H_2O_2 \\
H_2O_2 + e^- \rightleftarrows OH^{\cdot} + OH^- \\
OH^{\cdot} + e^- \rightleftarrows OH^-
\end{gathered}$$

A destruction of chemical bonds may be thereby induced, for example via a radical chain reaction (R = hydrocarbon chain) [60, 66, 67].

$$\begin{aligned}
&\text{Initiation :} && O_2^- + R - H \rightleftarrows R^{\cdot} + O_2H^- \\
&\text{Propagation :} && R^{\cdot} + O_2 \rightleftarrows ROO^{\cdot} \\
& && ROO^{\cdot} + R - H \rightleftarrows ROOH + R^{\cdot}
\end{aligned}$$

De-adhesion of the adhesive layer results and its corrosion protective properties are distinctly reduced or even completely lost. The basic mechanisms of corrosive delamination are similar on polymer coated iron and zinc substrates, but additional effects arise from the fact that zinc exhibits amphoteric properties at high pH [68–70]. Oxygen reduction at polymer/zincoxide/zinc interfaces passivates Zn and results in the formation of zinc hydroxide. However, $Zn(OH)_2$ tends to dissolve as zincate species, e.g. $Zn(OH)_4^{2-}$ in strongly alkaline solution, which buffers any additional alkalization. This means that a pH value of 13 will not be achieved on polymer coated zinc compounds and that zinc hydroxide can take part in a dissolution/precipitation mechanism in the area of interfacial ion transport [68]:

$$\begin{aligned}
Zn + OH^- &\rightleftarrows ZnOH + e^- \\
ZnOH + 2OH^- &\rightleftarrows Zn(OH)_3^- + 2e^- \\
Zn(OH)_3^- + OH^- &\rightleftarrows Zn(OH)_4^{2-} \\
Zn(OH)_4^{2-} &\rightleftarrows Zn(OH)_2 + 2\ OH^- \\
Zn + 2\ OH^- &\rightleftarrows Zn(OH)_2 + 2e^- \\
Zn + 2\ OH^- &\rightleftarrows ZnO + H_2O + 2e^-
\end{aligned}$$

Distinct thickening of the oxide layer is reported for ongoing delamination at polymer/zinc interfaces. In contrast, additional iron oxide/iron hydroxide growth on polymer coated Fe samples has to occur via solid state diffusion of cations through the already existent oxide structure and is therefore less pronounced. The amphoteric properties of Zn result in another two important consequences for the kinetics of corrosive delamination. First, zinc dissolution at the buried interface is an anodic process and generates additional positive charge which partly 'neutralizes' the negative charge resulting from interfacial oxygen reduction and OH^- formation. Less cations of the electrolyte in the defect thereby have to be transported along the polymer/zincoxide/zinc interface for charge compensation. Moreover, the electrostatic repulsion of anions of the defect electrolyte should be reduced and anion ingress was indeed observed at adhesive/zinc compounds. Second, dissolved zinc species at the interface can react with CO_2 that is present in ambient air and form precipitates of zinc carbonate. This does not only reduce the interfacial pH, but also results in voluminous and white-coloured, gel-like deposits at the interface which promote de-adhesion of the polymer layer. In contrast, iron or low alloyed steel maintains a shiny surface in the delaminated area [59, 60, 66–70].

It has been noted above that the progress of cathodic delamination and interfacial ion transport can be adequately tracked by monitoring of interface potentials. In that context, especially the Scanning Kelvin Probe (SKP) has been established as a method for non-destructive measurements at buried polymer/oxide/metal interface compounds [71–81]. A SKP utilizes a metallic needle that vibrates above a conductive sample surface with the needle tip, the substrate surface directly beneath and the air in between needle and sample forming a parallel-plate capacitor. Thereby, any ad- and desorption, ion ingress, dissolution or structural rearrangement processes at the sample surface will cause an

adjustment of the charging condition of the capacitor. This will induce a current in the external electric circuit of the SKP, which is translated into a change of the Volta potential of the investigated substrate. It was shown that the recorded potentials can be referenced to the standard hydrogen electrode after calibration with a redox couple (e.g. an electrolyte covered metal) of known potential. To investigate the progress of corrosive delamination with time, continuous scanning of the SKP needle along the polymer/oxide/metal interface is required [71–81].

Figure 12 presents an example of potential distributions typically recorded on epoxy covered iron (shown in Fig. 12a, c) and along an epoxy coated iron/zinc transition (shown in Fig. 12b, d). Ion ingress started from a coating defect located at the left, but outside of the scanned area which was filled up with 0.5 molar NaCl solution. During the first stage of the experiment interface potentials were analysed in humid nitrogen atmosphere with an oxygen partial pressure of less than 1 mbar (see Fig. 12a, b). A transport of hydrated ions along the polymer/oxide/metal interface was observed in the coated iron area. It became manifest in a proceeding front that caused a potential shift from −200 to −250 mV_{SHE} (SHE: Standard

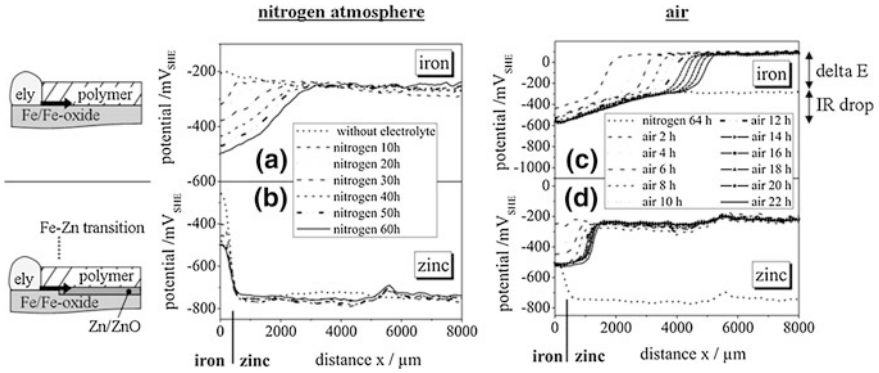

Fig. 12 Study of interfacial ion transport along epoxy/iron and epoxy/zinc interfaces starting in humid nitrogen atmosphere with an oxygen partial pressure below 1 mbar (see Fig. 12a, b). After 64 h, the atmosphere was changed to humid air (see Fig. 12c, d). The schematics at the left provide a cross section view of the sample geometries. In Fig. 12a, c, an epoxy coated iron sample with an artificially prepared, electrolyte ("ely") covered coating defect was investigated. In Fig. 12b, d, ion transport first proceeded along an epoxy/iron interface, then along an epoxy/zinc interface. The Fe-Zn-transition is located at around x = 400 µm. The progress of interfacial ion ingress was tracked by continuous scanning along the sample surfaces with a Kelvin Probe and by monitoring of the polymer/substrate interface potential. The diagrams present the resulting potential profiles for transport processes that proceed from the left to the right. DeltaE indicates the potential difference between intact polymer/metal interface sections and corroded areas. It reflects the electrochemical driving force for cathodic delamination, whereas the IR drop is related to the electrolyte resistance that has to be overcome for ion migration between the local anode in the defect and the electrolyte front position. Figure 12 shows that interfacial ion transport proceeds accelerated in humid air and that a transport cannot be observed on zinc substrates for inhibited interfacial oxygen reduction kinetics (Adapted from Ref. [34], Copyright 2009, with permission from Elsevier)

Hydrogen Electrode scale) to the level of actively corroding iron in the defect with an interface potential of about −500 mV_{SHE}. The polymer coated zinc area did not show any potential changes. No ion transport occurred beyond the iron/zinc transition. After the recipient was flushed with humid air the potential levels between defect and zinc inverted. Figure 12d shows that the potential of the epoxy coated zinc area then is higher than the defect potential and corrosive delamination started, but proceeded more slowly than on iron (see Fig. 12c). After 22 h of exposure to humid air, the electrolyte front is located at approximately x = 4,900 μm on iron and approximately x = 1,200 μm on the iron/zinc sample, which in fact refers to an effective transport distance of not more than 800 μm along the epoxy coated zinc interface [34]. Several conclusions about interfacial ion transport mechanisms can be drawn based on the data presented in Fig. 12 and on additional measurements reported in literature:

- Ion transport at polymer coated iron, steel, zinc or copper samples proceeds at a relevant rate if the potential of the intact polymer/oxide/metal interface is higher than the defect potential [60, 66, 67]. The potential difference deltaE between both areas reflects the electrochemical driving force for interfacial ion ingress. Fig. 12c, d confirm that accelerated ion transport is commonly observed if deltaE is increased. No corrosive delamination is detected if the potential levels are inverted, which means that the potential of the intact interface is lower than the defect potential. This also shows that interfacial ion transport cannot be initiated without electrochemical driving force, because macroscopically relevant ion diffusion along polymer coated zinc surfaces is *not* observed in an atmosphere of distinctly reduced oxygen partial pressure [35].
- The interface potential increases linearly between defect and the electrolyte front position. This IR drop is illustrated in Fig. 12c and reflects the ohmic electrolyte resistance between the local electrodes of the galvanic cell that has to be overcome for Na^+ transport along the epoxy/ironoxide/iron interface [60, 66, 67].
- Reduced oxygen partial pressure in the atmosphere lowers the polymer/substrate interface potential, decelerates interfacial oxygen reduction kinetics and reduces the transport rate of hydrated Na^+ ions along the interface (see Fig. 12a and compare with Fig. 12c) [34, 35].

It should be noted that the progress of cathodic delamination was found to decrease with increasing hydrodynamic radii of the cations of the defect electrolyte, whereas the size of the hydrated anions did not have any influence on the process kinetics. Additionally, the kinetics of interfacial ion transport were subject to a square-root-of-time dependency. This allowed for the calculation of at least 'formal' coefficients for cation transport based on the concept of Fickean diffusion [59, 60, 66, 67].

Moreover, some analogies were drawn between corrosive delamination at polymer coated iron or zinc substrates and droplet spreading observed on uncoated Fe and Zn surfaces. The concept is based on the effects of interface tension and electro kinetics. It may explain why no ion transport is observed on polymer coated

zinc in humid atmospheres of reduced oxygen partial pressure and why even porous adhesive layers do not enforce ion ingress under these conditions [34, 35].

If a droplet of NaCl solution is placed on a zinc sheet in humid air, it will spread with time (see Fig. 13a, b). Figure 13c, d present maps illustrating the elemental distribution on the metal surface resulting from that process. It reveals that chloride is solely observed in the area of the original droplet, whereas sodium can only be detected in the electrolyte spreading zone. This finding is similar to what has to be expected from corrosive delamination at buried polymer/oxide/metal interfaces which starts from an electrolyte covered defect in the coating. Figure 14a schematically describes the basic mechanism on zinc for an atmosphere free of carbon dioxide. A strong alkalisation of the liquid phase in the spreading zone was observed due to oxygen reduction processes in the periphery of the droplet/at the electrolyte front and it was detected that spreading accelerates if the pH is increased [82–84].

The wettability of the zinc oxide surface by electrolyte films is equivalent to the energy that has to be invested to generate an area normalised surface during an isothermal and isobaric process. The surface energy of a solid can be calculated based on measurements of the contact angle θ, which is defined as angle between the vectors of liquid/gas interface tension σ_{lg} and solid/liquid interface tension σ_{sl}

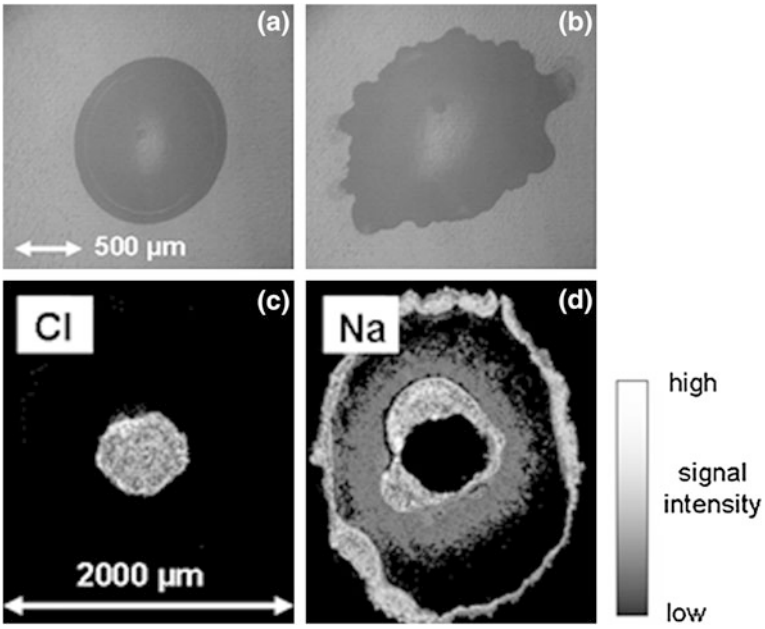

Fig. 13 Electrolyte droplet spreading on zinc in humid air. **a** Photo taken after one hour of droplet spreading, **b** photo taken after two hours. **c** and d): Elemental distribution resulting from spreading of a droplet of NaCl solution. Chloride is only detectable in the area of the droplet, whereas sodium in contrast is only observed in the spreading zone. (Modified from Ref. [82], Copyright 2008 and modified from Ref. [83], Copyright 2002, with permission from Elsevier)

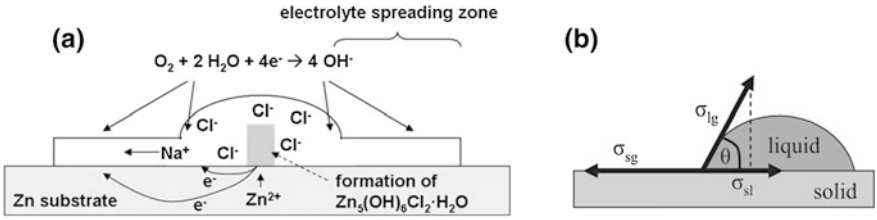

Fig. 14 **a** Schematic illustration of fundamental processes resulting in electro kinetic droplet spreading on zinc in humid, CO_2-free air (Adapted from Ref. [82], Copyright 2008, with permission from Elsevier). **b** Illustration of contact angle θ for the solid/liquid (sl), solid/gas (sg) and liquid/gas (lg) interface tensions σ [55, 59]

(Young's equation; σ_{sg}: solid/gas interface tension; see also Fig. 15b) [55, 56, 85, 86]:

$$\sigma_{sg} = \sigma_{sl} + \sigma_{lg} \cdot \cos\theta$$

Gibb's Free Energy quantifies the thermodynamic driving force for liquid spreading on an oxide-covered zinc surface:

$$-\Delta G \sim (\sigma_{sg} - \sigma_{sl} - \sigma_{lg}) \tag{3}$$

The process will occur spontaneously if the spreading coefficient, which is reflected by the expression in the parenthesis of equation 3, is positive. σ_{sg} and σ_{lg} will hardly be affected or change during droplet spreading, but a reduction of σ_{sl} will effectively promote the process. The oxide/electrolyte interface tension is maximised at the isoelectric point of ZnO, which ranges around pH 9. It decreases if the pH increases above this value. This is achieved by oxygen reduction in the periphery of the electrolyte droplet, which results in the generation of OH^- and a negatively charged substrate surface. Liquid flow towards the outer parts of the droplet will consequently destabilize its edges. If the oxygen partial pressure in the atmosphere is too low to induce relevant O_2 reduction kinetics, stable droplets and no spreading has to be expected and no interfacial ion transport is observed even at polymer/zinc oxide/zinc interfaces [82, 84].

3.3 Anodic Delamination at Polymer/Oxide/Metal Interfaces

Anodic undermining of polymer layers on non-conducting oxide surfaces and insulating inorganic films usually dominates during the exposure of painted metal compounds to an atmosphere with a relative humidity of typically at or above 80 %. It is also observed when the metal is covered by a barrier layer that strongly inhibits the access of water and oxygen to the substrate material. Anodic delamination consequently often occurs as filiform corrosion on Al-alloys and as bondline corrosion of adhesively bonded metals or composites [87–90].

Anodic disbondment is characterised by net anodic current densities ($i_c < i_a$) at the front of delamination adjacent to interface sections for which net cathodic current densities ($i_c > i_a$) are detected. This causes a transport of excess electrons from the anodic to the cathodic region, specific pH values at the delamination front, defect and delaminated area as well as a pH- and electrolyte-dependent formation of corrosion products (see Fig. 15). Anodic disbondment of adhesives on zinc alloy coated steel and filiform corrosion on Al-alloys are technically most important and will be consequently discussed more in detail.

In contrast to the characteristics of cathodic delamination described above, SKP-profiles that are recorded on polymer coated and low-conductive Zn-Al layers on steel exhibit more negative potentials at the front of undermining than close to the defect (see Fig. 16) [92]. Simonkolleite can be detected in the delaminated zone while zinc oxides and zincates form in the cathodic region close to the defect. This anodic undermining was attributed to the specific properties of the polymer film that functions as an effective barrier for oxygen diffusion. It ensures constantly low O_2 concentrations at the buried interface underneath the coating. Similar to the mechanisms of crevice corrosion, anodic dissolution of the base material at the front of delamination occurs as long as de-adhesion or blistering of the polymer does not significantly reduce the barrier properties at the interface against electrolyte, water and oxygen ingress [93].

Growing threadlike filaments on polymer coated, insulating oxide surfaces such as MgO on Mg or Al_2O_3 on Al are characteristic for filiform corrosion. They are observed in not too humid atmosphere and their growth is promoted by the

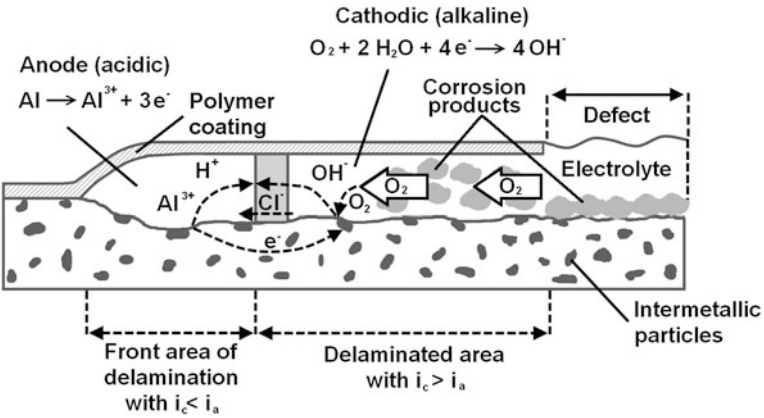

Fig. 15 Schematic illustration of the anodic delamination mechanism at a polymer coated Al-alloy. Anodic undermining is characterised by the formation of a differential aeration cell and by oxidative dissolution of the metal at the head of the filament. In the tail region, O_2 reduction is induced and results in the formation of voluminous corrosion products. For charge compensation, anions of the defect electrolyte are transported to the front of delamination. The entire process is strongly supported by the presence of local conducting sites such as intermetallic particles in the aluminium matrix. In general, acidic pH will be detected at the filament head, whereas an alkaline environment has to be expected in the filament tail (figure adapted from Ref. [63, 91])

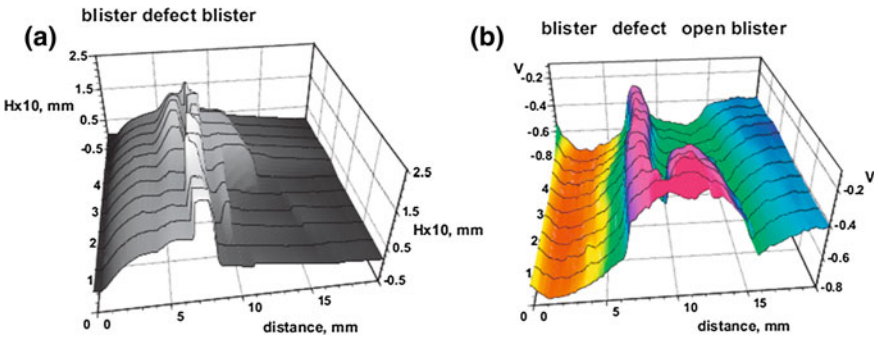

Fig. 16 **a** Topography map and **b** potential distribution for a blister beneath a polymer coating (*on the left*), of a defect zone (*in the centre*) and of an open blister (*on the right*). The measurements were performed on a polymer covered Zn-Al substrate in humid air. As the macromolecular film functions as an effective barrier for oxygen diffusion, no cathodic delamination, but anodic undermining processes are observed at the buried interface. As a result, the potentials at the front of delamination are more negative than those detected close to the defect (Adapted from Ref. [92], Copyright 2012, with permission from Elsevier)

presence of soluble anionic species in coating defects, for example by chloride [67, 94–96]. Relevant conditions for the initiation of filiform corrosion on various metals including aluminium, iron, magnesium and even zinc-coated steel, silver and gold have been studied in detail [61, 77, 97–106]. The filaments propagate by an anodic undermining process, which arises from a differential aeration cell within the filament head. As a consequence, the metal substrate is oxidized at the head front (anode) and oxygen is reduced in the vicinity of the head–tail junction (cathode) [107]. Between anode and cathode, a potential gradient is established that enforces a migration of anions to the front of delamination and of cations to the coating defect. On aluminium substrates, an exceptionally low pH and the oxygen deficiency at the front edge of the filament thread can additionally result in a secondary cathodic hydrogen evolution.

During the initiation period, aluminium oxide dissolves in a coating defect, supported by the presence of chloride [108]. This weakens the oxide layer and delamination of the adjacent polymer coating is promoted due to combined mechanical and electrochemical de-adhesion [109]. In a second step, metal dissolution at the polymer/metal interface results in the formation of a small crevice so that the electrolyte solution can penetrate the coated region. This, in turn, promotes chloride induced weakening of the polymer covered oxide layer and finally results in anodic dissolution of the base material underneath the coating. The corresponding cathode will be primarily located close to the defect, but corrosion products formed by released metal ions and artifacts evolving from oxygen reduction then cause the formation of an occluded cell [110]. The exact anolyte and catholyte compositions are not clear yet, but very low pH values of 1–2 [111–113], hydrogen evolution and high chloride concentrations [112] at the outermost filament tips were reported.

Figure 17 presents a Scanning Kelvin Probe potential- and topography-map. They were simultaneously recorded on a filiform filament that evolved on an epoxy coated aluminium specimen [61, 102, 107]. The graphs show that the potential at the filament tail is about 150 mV higher than that of the surrounding polymer coated aluminium matrix. This indicates the formation of aluminium-oxide/-hydroxide corrosion products and points at processes such as oxygen reduction in the filament tail. The active part of the filament head, where the anodic reaction of active metal dissolution takes place, exhibits a potential of about 500 mV lower than that of the intact sample surface. Direct comparison of potential and topographic maps reveals that a larger surface area is affected by filiform corrosion induced potential shifts than by topographic changes due to deformation and lifting of the epoxy film. This confirms that the polymer/metal interface has to be electrochemically degraded before blistering of the macromolecular coating layer is observed. Moreover, Fig. 17 shows that the anodically

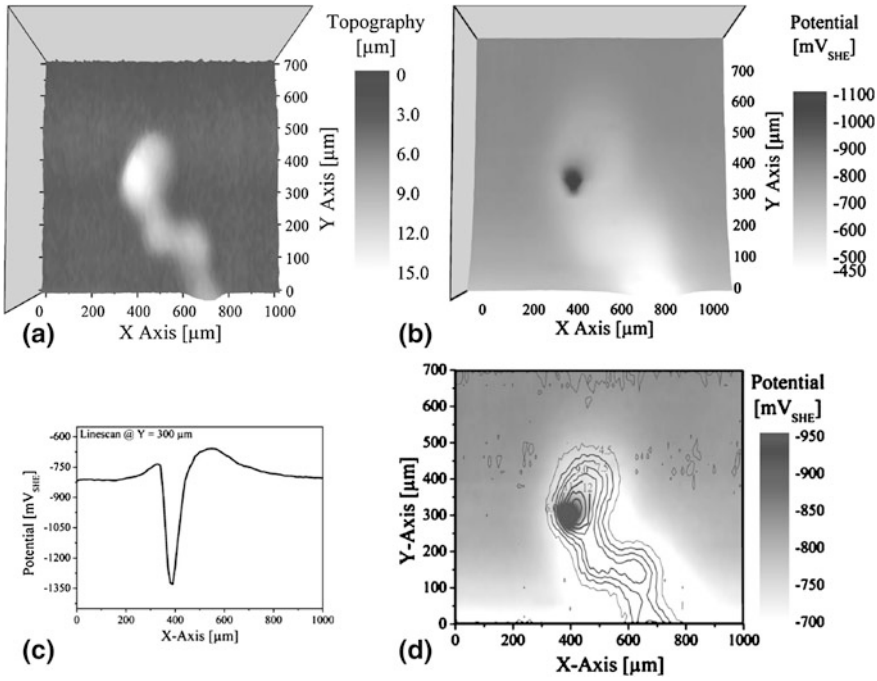

Fig. 17 Height-regulated SKP (HR-SKP) measurement of a single filiform thread on an organically coated aluminium substrate under active filiform corrosion conditions: **a** HR-SKP topography map. **b** HR-SKP potential map. Higher potentials are detected in the filament tail compared to surrounding intact areas. This indicates the formation of aluminium-oxide/-hydroxide corrosion products via oxygen reduction processes. Distinctly lower potentials are observed in the filament head due to anodic metal dissolution (Reprinted with permission from Ref. [81], Copyright 2005, The Electrochemical Society)

active area is confined to a rather small region at the left border of the filament head and not located in the center or across the whole area of the head.

It should be noted that the kinetics of filiform corrosion are strongly dependent on the presence of intermetallic particles in commercially relevant aluminium alloys. These intermetallics function as hot spots for the propagation of the filament thread, a process that can be specifically investigated for example by scanning Kelvin Probe force microscopy [87, 114–117].

4 Conclusions

The design of water- and electrolyte-resistant adhesive joints for humid environments remains a challenge due to the complexity of polymer/metal interface structures. The morphology and chemical properties of metal oxides, barrier properties of macromolecular networks as well as type and nature of chemical interactions between the polymer film and the oxide surface have to be specifically tailored to achieve flexible systems that can dynamically adjust to varying environmental conditions. Some basic facts have to be taken into account based on recent progress in the field of corrosion and adhesion research:

- Water molecules form a highly mobile hydrogen bonding network which lowers the adhesion forces at polymer/oxide interfaces.
- Hydrated ions can be transported along polymer/oxide interfaces in water rich environments.
- The conductivity of the oxide and the interfacial water activity determine corrosive de-adhesion processes at the polymer/metal interface. Conductive oxides and high H_2O concentrations result in cathodic delamination whereas insulating oxides and embedded local conducting sites (‘hot spots of electrochemical reactivity’) promote anodic de-adhesion.

If externally applied mechanical forces are not sufficient to break interfacial bonds, de-adhesion of polymers from metal substrates results from the interaction of water accumuluation at the adhesive/metal interface, from the ingress of hydrated ions as well as from electron and ion transfer reactions across the interface. Therefore, state-of-the-art surface technology approaches generally aim at the development of adhesives with improved covalent and coordinative bonding between the macromolecular phase and the metal to also suppress electrochemically determined corrosion processes.

References

1. Henderson, M.A.: Surf. Sci. Rep. **46**, 5–308 (2002)
2. Coustet, V., Jupille, J.: Surf. Interface Anal. **22**, 280–283 (1994)
3. Coustet, V., Jupille, J.: Surf. Sci. **307**, 1161–1165 (1994)

4. Coustet, V., Jupille, J.: Nuovo Cimento Della Societa Italiana Di Fisica D-Condensed Matter Atomic Molecular and Chemical Physics Fluids Plasmas Biophysics **19**, 1657–1664 (1997)
5. Shapovalov, V., Truong, T.N.: J. Phys. Chem. B **104**, 9859–9863 (2000)
6. Di Felice, R., Northrup, J.E.: Phys. Rev. B **60**, R16287–R16290 (1999)
7. Hass, K.C., Schneider, W.F., Curioni, A., Andreoni, W.: Science **282**, 882 (1998)
8. Hass, K.C., Schneider, W.F., Curioni, A., Andreoni, W.: J. Phys. Chem. B **104**, 5527–5540 (2000)
9. Thissen, P., Grundmeier, G., Wippermann, S., Schmidt, W.G.: Phys. Rev. B **80**, 245403 (2009)
10. Eng, P.J., Trainor, T.P., Brown, G.E., Waychunas, G.A., Newville, M., Sutton, S.R., Rivers, M.L.: Science **288**, 1029–1033 (2000)
11. Ahn, J., Rabalais, J.W.: Surf. Sci. **388**, 121–131 (1997)
12. Toofan, J., Watson, P.R.: Surf. Sci. **401**, 162–172 (1998)
13. Ferry, D., Picaud, S., Hoang, P.N.M., Girardet, C., Giordano, L., Demirdjian, B., Suzanne, J.: Surf. Sci. **409**, 101–116 (1998)
14. Langel, W., Parrinello, M.: Phys. Rev. Lett. **73**, 504–507 (1994)
15. Delle Site, L., Alavi, A., Lynden-Bell, R.M.: J. Chem. Phys. **113**, 3344–3350 (2000)
16. Kim, Y.D., Lynden-Bell, R.M., Alavi, A., Stulz, J., Goodman, D.W.: Chem. Phys. Lett. **352**, 318–322 (2002)
17. Hacquart, R., Jupille, J.: Chem. Phys. Lett. **439**, 91–94 (2007)
18. Carrasco, E., Brown, M.A., Sterrer, M., Freund, H.J., Kwapien, K., Sierka, M., Sauer, J.: J. Phys. Chem. C **114**, 18207–18214 (2010)
19. Jones, F.H.: Surf. Sci. Rep. **42**, 79–205 (2001)
20. Diebold, U.: Surf. Sci. Rep. **48**, 53–229 (2003)
21. Krischok, S., Hofft, O., Gunster, J., Stultz, J., Goodman, D.W., Kempter, V.: Surf. Sci. **495**, 8–18 (2001)
22. Schaub, R., Thostrup, P., Lopez, N., Laegsgaard, E., Stensgaard, I., Norskov, J.K., Besenbacher, F.: Phys. Rev. Lett. **87**, 266104-1–266104-4 (2001)
23. Zhang, C., Lindan, P.J.D.: J. Chem. Phys. **119**, 9183–9190 (2003)
24. Menetrey, M., Markovits, A., Minot, C.: Surf. Sci. **524**, 49–62 (2003)
25. Semoto, T., Tsuji, Y., Yoshizawa, K.: Bull. Chem. Soc. Jpn. **85**, 672–678 (2012)
26. Semoto, T., Tsuji, Y., Yoshizawa, K.: J. Phys. Chem. C **115**, 11701–11708 (2011)
27. Knaup, J.M., Kohler, C., Frauenheim, T., Blumenau, A.T., Amkreutz, M., Schiffels, P., Schneider, B., Hennemann, O.D.: J. Phys. Chem. B **110**, 20460–20468 (2006)
28. Abel, M.L., Watts, J.F.: Surf. Interface Anal. **41**, 508–516 (2009)
29. Knaup, J.M., Tolle, P., Kohler, C., Frauenheim, T.: Eur. Phys. J. Special Topics **177**, 59–81 (2009)
30. Kisin, S., Vukic, J.B., van der Varst, P.G.T., de With, G., Koning, C.E.: Chem. Mater. **19**, 903–907 (2007)
31. Vukic, J.B., Hoeppener, S., Kozodaev, D.A., Kisin, S., Klumperman, B., Schubert, U.S., de With, G., Koning, C.E.: ChemPhysChem **7**, 1912–1916 (2006)
32. Jensen, W.B.: The Lewis Acid-Base Concepts. Wiley, New York (1979)
33. Posner, R., Giza, G., Vlasak, R., Grundmeier, G.: Electrochim. Acta **54**, 4837–4843 (2009)
34. Posner, R., Wapner, K., Stratmann, M., Grundmeier, G.: Electrochim. Acta **54**, 891–899 (2009)
35. Posner, R., Titz, T., Wapner, K., Stratmann, M., Grundmeier, G.: Electrochim. Acta **54**, 900–908 (2009)
36. Posner, R., Giza, G., Marazita, M., Grundmeier, G.: Corros. Sci. **52**, 1838–1846 (2010)
37. Linossier, I., Gaillard, F., Romand, M., Nguyen, T.: J. Adhes. **70**, 221–239 (1999)
38. Curley, A.J., Hadavinia, H., Kinloch, A.J., Taylor, A.C.: Int. J. Fract. **103**, 41–69 (2000)
39. Kinloch, A.J., Little, M.S.G., Watts, J.F.: Acta Mater. **48**, 4543–4553 (2000)
40. Wapner, K., Stratmann, M., Grundmeier, G.: Electrochim. Acta **51**, 3303–3315 (2006)
41. Vlasak, R., Klueppel, I., Grundmeier, G.: Electrochim. Acta **52**, 8075–8080 (2007)
42. Grundmeier, G., Stratmann, M.: Annu. Rev. Mater. Res. **35**, 571–615 (2005)

43. Castela, A.S., Simoes, A.M.: Corros. Sci. **45**, 1631–1646 (2003)
44. Castela, A.S., Simoes, A.M.: Corros. Sci. **45**, 1647–1660 (2003)
45. Barranco, V., Thiemann, P., Yasuda, H.K., Stratmann, M., Grundmeier, G.: Appl. Surf. Sci. **229**, 87–96 (2004)
46. van Westing, E.P.M, van der Weijde, D.H., Bonincontro, S., Vreijling, M.P.W., Ferrari, G.M., de Wit, J.H.W., Bonora, P.L., Deflorian, F.: Electrochemical Methods in Corrosion Research Vi, Pts 1 and 2 289–2 (1998) 293–304
47. Bierwagen, G., Tallman, D., Li, J.P., He, L.Y., Jeffcoate, C.: Prog. Org. Coat. **46**, 148–157 (2003)
48. Hu, J.M., Zhang, J.Q., Cao, C.N.: Prog. Org. Coat. **46**, 273–279 (2003)
49. Hu, J.M., Zhang, J.T., Zhang, J.Q., Cao, C.N.: J. Mater. Sci. **39**, 4475–4479 (2004)
50. Fieldson, G.T., Barbari, T.A.: Polymer **34**, 1146–1153 (1993)
51. Ohman, M., Persson, D., Leygraf, C.: Prog. Org. Coat. **57**, 78–88 (2006)
52. Ohman, M., Persson, D., Leygraf, C.: Electrochem. Solid State Lett. **10**, C27–C30 (2007)
53. Ohman, M., Persson, D.: Electrochim. Acta **52**, 5159–5171 (2007)
54. Bohn, P.W.: Annu. Rev. Mater. Sci. **27**, 469–498 (1997)
55. Wedler, G.: Lehrbuch der physikalischen Chemie. Wiley VCH, Weinheim (2004)
56. Atkins, P.W.: Physikalische Chemie. Wiley VCH, Weinheim (2001)
57. Hamann, C.H., Vielstich, W.: Elektrochemie. Wiley VCH, Weinheim (1998)
58. Schmickler, W.: Grundlagen der Elektrochemie. Vieweg, Braunschweig (1996)
59. Posner, R.: Combined spectroscopic and electrochemical studies of ion transport and corrosive de-adhesion processes at polymer/oxide/metal interfaces. Universität Paderborn, Paderborn (2009)
60. Leng, A., Streckel, H., Stratmann, M.: Corros. Sci. **41**, 547–578 (1999)
61. Leidheiser, H., Wang, W., Igetoft, L.: Prog. Org. Coat. **11**, 19–40 (1983)
62. Leidheiser, H.: Corrosion control by organic coatings. Science Press, Princton (1979)
63. Wapner, K.: Grenzflächenchemische und elektrochemische Untersuchungen zur Haftung und Enthaftung an modifizierten Klebstoff/Metall-Grenzflächen Ruhr-Universität Bochum, Bochum, 248 (2006)
64. Stratmann, M., Leng, A., Fürbeth, W., Streckel, H., Gehmecker, H., Groβe-Brinkhaus, K.H.: Prog. Org. Coat. **27**, 261–267 (1996)
65. Fürbeth, W., Stratmann, M.: Prog. Org. Coat. **39**, 23–29 (2000)
66. Leng, A., Streckel, H., Stratmann, M.: Corros. Sci. **41**, 579–597 (1999)
67. Leng, A., Streckel, H., Hofmann, K., Stratmann, M.: Corros. Sci. **41**, 599–620 (1999)
68. Furbeth, W., Stratmann, M.: Corros. Sci. **43**, 207–227 (2001)
69. Furbeth, W., Stratmann, M.: Corros. Sci. **43**, 229–241 (2001)
70. Furbeth, W., Stratmann, M.: Corros. Sci. **43**, 243–254 (2001)
71. Posner, R., Jubb, A.M., Frankel, G.S., Stratmann, M., Allen, H.C.: Electrochim. Acta **83**, 327–334 (2012)
72. Kelvin, L.: Electrochim. Acta **83**, 327 (1898)
73. Williams, G., McMurray, H.N.: Electrochim. Acta **54**, 4245–4252 (2009)
74. Nazarov, A., Prosek, T., Thierry, D.: Electrochim. Acta **53**, 7531–7538 (2008)
75. Johnson, K.B., Hansen, W.N.: Rev. Sci. Instrum. **66**, 2967–2976 (1995)
76. Zisman, W.: Rev. Sci. Instrum. **3**, 367 (1932)
77. Stratmann, M., Streckel, H.: Corros. Sci. **30**, 681–696 (1990)
78. Rohwerder, M., Leblanc, H., Frankel, G.S., Stratmann, M.: Analytical Methods for Corrosion Science and Engineering, CRC Press, New York, (2005)
79. Trasatti, S.: Electrochim. Acta **36**, 1659–1667 (1991)
80. Rohwerder, M., Turcu, F.: Electrochim. Acta **53**, 290–299 (2007)
81. Wapner, K., Schoenberger, B., Stratmann, A., Grundmeier, G.: J. Electrochem. Soc. **152**, E114–E122 (2005)
82. Chen, Z.Y., Persson, D., Leygraf, C.: Corros. Sci. **50**, 111–123 (2008)
83. Neufeld, A.K., Cole, I.S., Bond, A.M., Furman, S.A.: Corros. Sci. **44**, 555–572 (2002)

84. Chen, Z.Y., Persson, D., Nazarov, A., Zakipour, S., Thierry, D., Leygraf, C.: J. Electrochem. Soc. **152**, B342–B351 (2005)
85. Berg, J.: Adhesion science and engineering-2: surfaces, chemistry and applications. Elsevier, Amsterdam (2002)
86. Allen, K.W.: Handbook of adhesion, pp. 535–538. Wiley, Chichester (2005)
87. de Wit, J.H.W.: Electrochim. Acta **46**, 3641–3650 (2001)
88. Grundmeier, G., Simões, A.: In: Stratmann, M., Frankel, G.S. (eds.) Encyclopedia of Electrochemistry, pp. 500–566. Wiley-VCH Verlag GmbH & Co. KGaA, Weinheim (2003)
89. Grundmeier, G., Schmidt, W., Stratmann, M.: Electrochim. Acta **45**, 2515–2533 (2000)
90. Davis, G.D., Thayer, K., Rich, M.J., Drzal, L.T.: J. Adhes. Sci. Technol. **16**, 1307–1326 (2002)
91. Williams, G., McMurray, H.N., Hayman, D., Morgan, P.C.: Phys Chem Comm. **6**, 1–6 (2001)
92. Nazarov, A., Olivier, M.G., Thierry, D.: Prog. Org. Coat. **74**, 356–364 (2012)
93. Fernando, M., Harjoprayitno, W.W., Kinloch, A.J.: Int. J. Adhes. Adhes. **16**, 113–119 (1996)
94. Cappadonia, M., Doblhofer, K., Jauch, M.: Berichte Der Bunsen-Gesellschaft-Physical Chemistry. Chem. Phys. **92**, 903–908 (1988)
95. Grundmeier, G., Jüttner, K., Stratmann, M.: In: Schütze, M. (ed.) Corrosion and environmental degradation, pp. 285–381. Wiley-VCH, Weinheim (2000)
96. Grundmeier, G., Stratmann, M.: Appl. Surf. Sci. **141**, 43–56 (1999)
97. Doblhofer, K., Armstrong, R.D.: Electrochim. Acta **33**, 453–460 (1988)
98. Doblhofer, K.: Bull. Electrochem. **8**, 96 (1992)
99. Stimming, U., Schultze, J.W.: Berichte Der Bunsen-Gesellschaft-Physical Chemistry. Chem. Phys. **80**, 1297–1302 (1976)
100. Stimming, U., Schultze, J.W.: Electrochim. Acta **24**, 859–869 (1979)
101. Wroblowa, H.S.: J. Electroanal. Chem. **339**, 31–40 (1992)
102. Grundmeier, G., Reinartz, C., Rohwerder, M., Stratmann, M.: Electrochim. Acta **43**, 165–174 (1998)
103. Leidheiser, H.: Corrosion **39**, 189–201 (1983)
104. Ritter, J.J., Kruger, J.: Corrosion Control by Organic Coatings. NACE International, Houston (1981)
105. Kendig, M.W., Lumsden, J.B.: s. P.P., Surface and Interface Characterization in Corrosion, NACE International, NACE International (1994). Houston
106. Sharman, C.F.: Nature **153**, 621 (1944)
107. Van Loo, M., Laiderman, D.D., Bruhn, R.R.: Corrosion **9**, 277 (1953)
108. Foley, R.T.: Corrosion **42**, 277–288 (1986)
109. Li, R., Ferreira, M.G.S.: Mater. Sci. Forum **192–194**, 237 (1995)
110. Rudolf, A., Kaiser, W.-D.: Aluminium **72**, 726 (1996)
111. Huisert, M.H.M., Van Der Weijde, D.H., De Wit, J.H.W., Katgerman, L.: Proceedings of the Eurocorr'98 conference working party 14 coatings. Utrecht, September 28-October 1 (1998)
112. Slabaugh, W.H., Hutchins, L.L., Dejager, W., Hoover, S.E.: J. Paint Technol. **44**, 76 (1972)
113. Hoch, G.M.: NACE **3**, 134 (1974)
114. Senoez, C., Rohwerder, M.: Electrochim. Acta **56**, 9588–9595 (2011)
115. Guillaumin, V., Schmutz, P., Frankel, G.S.: J. Electrochem. Soc. **148**, B163–B173 (2001)
116. Senoez, C., Borodin, S., Stratmann, M., Rohwerder, M.: Corros. Sci. **58**, 307–314 (2012)
117. Buchheit, R.G., Martinez, M.A., Montes, L.P.: J. Electrochem. Soc. **147**, 119–124 (2000)

Surface Treatments for Moisture Resistance

Gary Critchlow

Abstract With metallic adherends it is recognised that some form of surface treatment is required to provide a combination of high performance and long-lasting, or durable, adhesion. This is most evident when bonded structures are exposed to environmental and/or mechanical loads for a significant part of their service life. A range of treatments exists which provide enhanced durability, to one extent or another; usually qualitative intercomparisons are made between treatments with the same alloy and adhesive combination under well-defined environmental and mechanical loading conditions. For a specific adherend, the efficacy of a particular treatment is dependent upon a large number of factors. In this section, specific examples of surface treatments are discussed for aluminium and titanium alloys and carbon steels in terms of how they modify the metal surfaces and how they perform in comparative adhesion studies. Importantly, the most high performance and optimised surface treatments when applied to an appropriate alloy, and using an appropriate adhesive-primer combination, are capable of providing the levels of structural adhesion and durability required in the highly-demanding aerospace, defence and automotive sectors.

1 General Introduction

Many studies have demonstrated the requirement for an optimised surface treatment to attain long-lasting, or durable, adhesion [1–4]. Such a surface treatment is particularly important when adhesive joints utilising metallic adherends are exposed to adverse environments or mechanical loading or a combination of such conditions [1, 5]. There is clearly a broad range of environmental and mechanical

G. Critchlow (✉)
Department of Materials, Loughborough University, Ashby Road,
LE11 3TU Loughborough, UK
e-mail: G.W.Critchlow@lboro.ac.uk

L. F. M. da Silva and C. Sato (eds.), *Design of Adhesive Joints Under Humid Conditions*, Advanced Structured Materials 25, DOI: 10.1007/978-3-642-37614-6_3,

loading conditions likely to be encountered by bonded structures in-service and the exposure periods can be many tens of years; this is particularly the case when considering the use of bonded assemblies in, for example, the defence, aerospace and automotive sectors. The environmental conditions to which such real-life joints are exposed might include various fluids and both high and low temperature variations. This chapter will focus upon the resultant adverse effect of water-only upon adhesive joints, although it should be noted that other fluids can have a similarly damaging, or even more adverse, effect upon adhesion and adhesives.

Details of the modes of transport of water and its influence within adhesive joints are considered in detail elsewhere within this book and within the available literature [1, 5–7]. In brief, however, when present, water has been demonstrated to reduce measured levels of adhesion by the following four mechanisms, as summarised by Bowditch [7].

1. Plasticisation of the adhesive;
2. Introduction of hygroscopic stresses;
3. Chemical degradation of interfacial or interphasial bonds, and;
4. Hydration of metallic substrates.

Of these, only the treatment methods to mitigate against the latter two mechanisms will be dealt with within this chapter. Note that this chapter will not focus upon the specific mechanisms of surface corrosion, or indeed, the testing for corrosion resistance or determination of corrosion rates. These topics are the subject of many studies and both non-standard and standardised test procedures [8, 9]. What this chapter will give, however, is a summary of the available surface treatments to enhance overall bond durability and not simply those which resist surface corrosion. It is important to note that, although bond durability and corrosion resistance are intimately linked, some processes, such as silanes, which potentially increase surface interactions might not necessarily improve bare metal corrosion resistance. However, since increased durability results from the use of processes such as silanes, these treatments will be discussed in Sect. 2.

Due to the large number of conditions to which adhesive joints might be exposed in-service, as mentioned above, for any given metallic substrate there exists a similarly broad range of treatment options; specific examples will be considered in more detail later in this chapter. It is important, first of all, to consider the role of the surface treatment in terms of how a particular process might improve bond durability. Given a wrought, cast, or otherwise processed metal it is possible that there will be adventitious organic contamination present in addition to deliberately introduced processing aids such as rolling or press lubricants, waxes or oils. In addition, beneath this might be a layer of friable oxide or hydrated oxide and possibly there may be present a mechanically or chemically modified layer which could evolve from, for example, thermomechanical processing of the material. In simple terms, an ideal treatment might be expected to: clean the surface; remove any friable material present; homogenise the surface to accommodate the modified layer, and; provide a well-adhered, passive coating which is both receptive to the subsequently-applied adhesive and which will

strongly interact with the adhesive. The latter point may be regarded as facilitating interphase formation. Note that in some very specific industrial scenarios it is acceptable not to treat a surface prior to adhesive bonding [10], however, some form of treatment is required in the vast majority of situations.

To achieve at least some of the required surface physicochemical properties mentioned, above the following processing steps would normally be carried out:

1. Firstly, the surface must be cleaned in order to remove the adventitious organic material from the surface. Conventionally, this is carried out using immersion or vapour degreasing, solvent washing or alkaline degreasing [1, 11]. Alternative "dry" processes such as corona, plasma, laser or cryoblasting exist which can potentially achieve equivalent or better results [12–15]. The "dry" processes are becoming favoured due to the lack of volatile organics or effluent generated.
2. Secondly, any friable or hydrated oxide or otherwise partially soluble surface detritus must be removed as these might be regarded as a likely weak boundary layer. To achieve this, an appropriate treatment might include desmut or deoxidising steps, which can be achieved either mechanically or by chemical etching. Mechanical treatment, for example by grit-blasting using alumina, silica or chilled iron media, will effectively remove such detritus to leave a macro-rough surface. Chemical etching by proprietary solutions ranging from weak alkaline to strong mixed acid solutions can also be used to provide highly etched surfaces on both the macro- and nanometre-scale.

The aforementioned processing would ordinarily be considered as the minimum treatment that a metal will require prior to bonding. Following the degrease, desmut and possibly deoxidise steps most metal surfaces will comprise a relatively thin, compact, well adhered oxide which will have a high surface energy and will therefore be wettable by any subsequently-applied adhesive. Note that all atomically-clean metals will have a surface free energy which will permit wetting by any subsequently-applied adhesive [16] but the presence of any organic material, even at the sub-monolayer level, will reduce surface wettability. Importantly, if the above-mentioned degrease, desmut and deoxidise steps are carried out, the surface will also be receptive to further treatment by the multi-stage processes detailed in the following sections.

In summary, in most situations, some degree of surface treatment is required to optimise adhesive bond durability. The role of the treatment is to impart desirable surface physicochemical properties. The minimum surface treatment which will normally be required will involve degrease, desmut and possibly deoxidise steps. For specific metals, a number of additional or more advanced treatments have been developed to give much increased levels of bond durability to counteract some of the damaging effects of environmental loading, and in particular water, on the bonded joints; examples of these will be discussed for selected metals in the next section. The selected metals are aluminium and titanium alloys and carbon steels; these have been selected due to their usefulness in industry and to illustrate a number of relevant points. It should be noted that many of the same processes which are utilised to treat these materials can also be applied, in some form, to other metals.

2 Specific Surface Treatments

2.1 Aluminium Alloys

The widespread industrial use of aluminium in key industrial sectors, including aerospace and automotive is well known [1, 3, 10, 17, 18]. This widespread utilisation combined with the problems encountered in trying to join aluminium alloys, particularly in thin gauge form, means that adhesive bonding of these materials is similarly widespread. As a result, there have been many studies into the optimisation of surface treatments for aluminium alloys; Minford alone cites over 4,500 references on this general topic [1]. The majority of studies into treatments for optimised bonding of aluminium alloys have, notably, been produced by representatives of the aerospace industry. The most advanced processes, including anodising, being required to meet the high demands, in terms of absolute performance and longevity under adverse conditions, of this sector. Although probably the best-performing prebond treatments for aluminium alloys, all standard forms of anodising such as those used in the aerospace sector, require significant investment in plant and facilities and are relatively complex, time-consuming, energy intensive and expensive to carry out. A number of alternative processes will firstly be considered below.

The usefulness of organosilanes in combination with mechanical roughening, such as the aforementioned grit-blasting procedure, for the improvement of bond durability has been known for some time [19]. A preliminary study by Shaw et al. [20] provided promising results although using steel adherends and a range of five different functionalised organosilanes. Further to this, a major international collaboration was undertaken by Shaw et al. in this field with a focus on aluminium alloys [21]. This major study focussed upon the use of γ-glycidoxypropyltrimethoxy (γ-GPS) silane and its influence on bonded aluminium 2024-T3 alloy using Cytec's FM73 (Wrexham, UK) single-part epoxide adhesive [21]. Within this collaboration, significant studies were carried out to investigate the influence of critical treatment parameters such as: solution pH; silane concentration; solvent type; hydrolysis time, and; drying temperature on durability, as measured by the quasistatic Boeing wedge test method [22]. Importantly, optimisation of all of the aforementioned parameters was shown to be important with the best-performing treatment utilising 1 % γ-GPS at pH 5, hydrolysed for 1 h prior to adhesive application. This process was reported to provide comparable durability to the aerospace standard chromic acid anodise (CAA) treatment in wedge test joints exposed to 96 % relative humidity at 50 °C with both treatments demonstrating a fracture energy of approximately 0.7 $kJ \cdot m^{-2}$ after 168 h exposure [22]. Similarly, the optimised γ-GPS treated 2024-T3 was tested alongside grit-blasted only and chromic acid etched alloy in cyclic fatigue tests using the tapered double cantilever beam (TDCB) geometry carried out in both wet and dry environments. In this fracture mechanics test, comparing grit-blasted joints with and without γ-GPS, a significant improvement was clearly demonstrated when the silane was present.

Specifically, when immersed in water at 28 ± 2 °C the grit-blasted only joints gave a threshold fracture energy (G_{th}) of only 15 J·m^{-2} compared with 100 J·m^{-2} with the optimised silane applied. This latter value was comparable to the chromic acid etch control also used in this study [23]. The improvement in measured G_{th} value afforded by the use of γ-GPS was accompanied by a change in failure mode such that when the silane was absent interfacial failure occurred whereas cohesive failure within the adhesive was apparent with silane treated joints exposed to both "wet" and "dry" conditions. The observed improvement in performance was attributed to the strengthening of the interface by the presence of the silane coupling agent [23]. A number of studies have either proposed or demonstrated a covalent Al–O–Si bond between aluminium and organofunctional silanes which is clearly hydrolytically stable. Other studies have proposed the presence of a Lewis acid–base interaction [24]. The formation of such bonds assumes monolayer deposition of the γ-GPS with the required hydrolysis and condensation reactions occurring [19]. Such a thin monolayer deposit, if present, will, however, not provide significant barrier protection which might be required to provide enhanced durability via corrosion inhibition. A comparison of the corrosion resistance afforded by a number of silanes, as measured by impedance spectroscopy, has been made by Underhill and Duquesnay [25] who indicated that mercapto silanes did, however, perform well in this respect. The reason for this is that bis-functional silanes are capable of being deposited as much thicker layers and have been demonstrated to provide both surface functionality and enhanced corrosion protection. For example, van Ooij and Zhu [26] demonstrated that mixtures of bis[trimethoxysilylpropyl]amine and vinyltriacetoxysilane produce deposits up to 500 nm thick which gave excellent barrier corrosion protection as evinced from both anodic and cathodic polarisation curves. The aforementioned bis-functional silane mixture also demonstrated much improved paint adhesion after thermal cycling compared with conventional processes including zinc phosphating and comparable paint adhesion to chromating in salt spray test conditions.

Utilising similar alkoxysilane sourced chemistry, sol–gel derived coatings have been shown to provide a range of metals with excellent corrosion protection by providing barrier coatings which can extend to over 20 μm in thickness. Wang and Bierwagen, for example, reviewed this topic specifically identifying the corrosion resistant sol–gel coatings for aluminium substrates with approximately 30 precursor types identified [27]. Due to the ability of sol–gel coatings to inhibit corrosion they have been considered for use as a prebond treatment for metals. For example, Akid et al. [28] produced a sol–gel coating based upon: tetraethoxysilane (TEOS), methyltrimethoxysilane (MTMS), modified polysiloxane, ethanol and water in ratios of 2:1.5:1:2:4 plus acetic acid which was doped with polyaniline and titania or alumina nanoparticles. This solution was spray-coated onto aluminium substrates then left to air dry at room temperature prior to adhesive application and bonding in the single lap shear (SLS) geometry. The optimised process, which included the incorporation of alumina nanoparticles, gave a modest SLS strength of 4.48 ± 0.03 MPa under dry conditions. In addition, Blohowiak et al. [29] considered the durability of sol–gel treated aluminium 2024-T3 alloy

when exposed to 100 % relative humidity for 1 h at 60 °C in the wedge test configuration. In this study, a range of sol–gels were considered alongside phosphoric acid anodised (PAA) and acid etched controls. The best performing sol–gel system in this, albeit short-term, durability test was a zirconium isopropoxide catalysed, acetic acid/glycidoxypropyltrimethoxy system which gave a crack extension of 5 mm compared to 3.5 and 10.5 mm for the PAA and etched controls respectively. In the undemanding dry test condition, the aforementioned sol–gel performed better than both controls with only 3.2 mm of crack extension after 18 h under ambient conditions. In summary, sol–gel coatings are easy to apply using, for example, spray or dip coating methods [27] and, when optimised, they have been shown to provide excellent corrosion resistance which aids bond durability [30, 31]. There are, however, very few reported long-term tests under wet cyclic fatigue conditions which would indicate how sol–gel coatings would perform under such circumstances. The fact that such coatings are simply deposits, hopefully, bonded onto a substrate, as opposed to conversion coatings grown from the substrate might mean that the interface could be weakened under the more demanding conditions. In addition, a number of studies have highlighted the requirement for careful control of the sol–gel process and the requirement for a clean, functional surface onto which the sol-gel film will deposit.

Acid etching is another fairly straightforward method of treating aluminium to provide a high energy, highly wettable surface with a compact oxide layer. A large number of durability studies have shown that these surface physicochemical properties are capable of providing a degree of interphase formation and enhanced bond durability. For example, the review by Critchlow and Brewis [32] identified a number of commercially-used etch solutions, the most widely reported were based upon chromic acid (CAE). The CAE is regarded as giving improved durability compared with simple mechanical treatments. However, the relatively thin resultant oxide, the compact part of which extends to only around 5 nm [32], gives little corrosion protection therefore the durability performance of CAE treated aluminium is not comparable with the best-performing anodic oxides in the most demanding tests [32]. This was clearly demonstrated in an early study by Minford [33] who compared a chromic-sulphuric acid etch, a form of CAE, with both sulphuric and phosphoric acid anodising (SAA and PAA) on aluminium 6061-T6 alloy. In this study CAE joints exposed to 100 % relative humidity at 50 °C for 12 months retained 16.6 % of their original bond strength compared with 72.7 and 54.8 % for SAA and PAA respectively. Similarly, for treated joints exposed to a freeze–thaw cycle the CAE treated joints retained less than 25 % of their original strength after 12 months compared with over 50 % for both SAA and PAA. In terms of stress-durability, CAE also performed worse than the other treatments; when stressed to approximately 14 MPa, CAE treated joints failed after 7 days of exposure compared with 20 days for PAA. Another problem, particularly associated with the CAE is that there are both legislative and health and safety drivers which are making the use of hexavalent chromium-containing compounds highly undesirable so other etchants have also been studied [1, 32].

Chemical conversion coatings have also been widely studied for the prebond treatment of aluminium alloys. Conversion coating solutions come in many forms including; chromates, phosphates, chromate-phosphates, zirconates, cerates and vanadates [1, 32, 34, 35]. Converted films are ideally insoluble, so hydrolytically stable, and form by both reaction with the aluminium surface and precipitation from solution. The thickness of such films can be variable from a few nanometres to greater than a micrometre; the thicker films give enhanced corrosion protection. Organic additives may also be included to further aid adhesion. The most widely-reported conversion coating processes for prebond applications are based upon chromate, chromate-phosphate or phosphate chemistry. However, an organically-modified titanate zirconate hexafluoride ($TiZrF_6$) based process has been shown to out-perform a standard chromate-phosphate process and to give results better than CAE and close to PAA in stress durability testing with SLS joints immersed in water at 60 °C and measuring times-to-failure. In this study, the $TiZrF_6$ -based process was shown to provide desirable chemical functionality from the organic phase with a highly nano-rough, nodular surface which was capable of interphase formation. The complex oxide was shown to be approximately 50 nm thick so was thought capable of affording some degree corrosion protection, thereby improving durability [34]. In general terms, chemical conversion coatings can provide excellent levels of adhesion and durability and they are consequently widely-used within industry. Conversion coatings can also offer the advantage of high speed deposition for applications such as coil-to-coil processing. The main limitation of conversion coating is that the deposition process is self-limiting in terms of film thickness. For this reason the barrier corrosion protection afforded by these films is also limited; this may only be a factor, however, in bonded structures exposed to the most extreme environments.

The most successful prebond treatments for aluminium alloys are the anodic oxides [1, 3, 32]. Anodising is essentially an electrolytically-driven conversion coating process where the metal forms the anode in an electrolytic cell and the applied voltage effectively drives the process to increase the thickness of the converted layer on the surface of metal parts. The precise structure and chemistry of the resultant anodic oxide film is dependent upon many factors, including: the specific alloy being treated; any pre-processing including etching; the electrolyte used; the anodising temperature; voltage conditions, whether direct or alternating or pulsed or a combination of these including and ramping; anodising time, and; the use of post-treatments such as sealing or etching.

Importantly, when optimised, anodising is capable of providing all of the physicochemical properties of the ideal bonding surface.

Figure 1 shows the features of an idealised structure of an anodic oxide on aluminium. The barrier layer next to the metal is reported to comprise a compact layer extending to about 1.1–1.2 nm per applied volt. The porous oxide can extend from a few tens of nanometres to tens of micrometres with a value of 1–4 μm being typical. The pore diameter can vary from sub-nanometre to many tens of nanometres across. Note that the above idealised case is observed on pure aluminium or 1xxx series alloys, when higher alloys are anodised a more nodular film

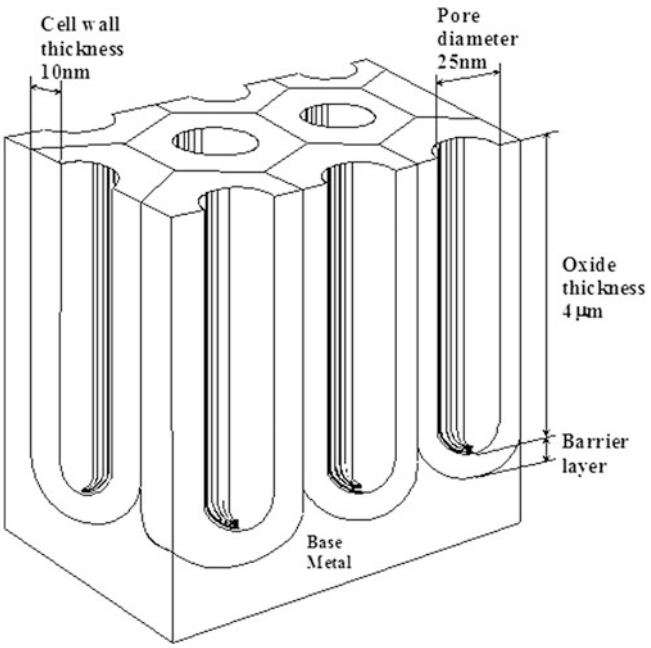

Fig. 1 An isometric drawing to show the idealised structure of an anodic oxide on aluminium after a standard chromic acid anodise (CAA) [36]

is observed. The barrier layer is reported to comprise alumina-only whilst the porous layer may be an oxide or hydrated oxide and may contain salts derived from the anodising electrolyte, such as phosphates. Critically, the anodic oxide will have a high surface free energy and so will be wetted by an adhesive or primer to facilitate interphase formation, providing that the porosity is available to the subsequently-applied organic phase. For successful penetration by an epoxide adhesive, studies have shown that a minimum pore diameter of around 20 nm is required. Given this situation, however, it is clear that upon crosslinking the epoxide will undergo mechanical interlocking and there is also a much increased area over which surface interactions can occur compared with the planar case. Also importantly, the oxide is extremely well-adhered to the underlying metal and being pseudo ceramic in nature can be much stiffer and harder than the underlying metal reinforcing the interphase to provide a strong, durable bond. However, there is the disadvantage associated with the use of anodisation as a pre-treatment of metals in that although these processes improve the lifetime of the metal by reducing the likelihood of corrosion they can reduce the fatigue life of the bare metal [37]. Defects in the anodic film can act as regions of stress concentration if the metal is exposed to high loading or fatigue situations. The relatively stiff anodic films can therefore accelerate crack growth into the underlying metal substrate. This situation can be mitigated against by the use of compliant anodic oxides [37].

A full description of the anodising process and how such films are realised is outside of the scope of this chapter, Refs. [1, 3] and [38], in particular provide additional information. A consideration of the most common types of anodising plus some recent studies in this area is, however, given below.

The most commonly-reported anodising processes for the treatment of aluminium for prebond purposes use phosphoric, chromic and sulphuric acid electrolytes; additional processes of note use boric, tartaric or mixed solutions containing these acids [1, 3, 32, 36]. Note that many of these processes have been successfully used for many years and are known to give excellent bond durability and that many are the subject of standards documents [1, 3]. These standards give precise details of the processing routes including control limits on all of the factors mentioned above from the pre-to post-anodising steps.

At the time of writing, the phosphoric acid anodising (PAA) process [1, 3] is currently preferred for use in America for the treatment of aluminium alloys used in adhesively bonded structures. With the replacement of the Forest Products Laboratory (FPL) etch, which is a form of CAE, in the anodising line with a hexavalent chromium free alternative [39], this has made the PAA process relatively benign. Although many studies have demonstrated that the PAA process provides excellent bond durability this route has not been favoured within the European aircraft industry due to the improved bare metal corrosion resistance [39] and, possibly, superior bond durability offered by chromic acid anodising (CAA). This is most evident only when joints are exposed to the most severe corrosive environments.

Of all the commercially-available prebond treatments for aluminium alloys, the Bengough-Stuart CAA process, as favoured by the European aerospace industry, is generally regarded as giving the best combination of adhesion and corrosion resistance and therefore optimised durability. Although the CAA process demonstrates exceptional performance in adhesively bonded structures, this standard process, however, utilises $\sim 40\ gl^{-1}$ of highly toxic and carcinogenic hexavalent chromium compounds in its final anodising stage. Within Europe, recent legislation, including; End of Life Vehicle (ELV), Registration of Hazardous Substances (RoHS), Waste Electrical and Electronic Equipment (WEEE) and Registration, Evaluation, Authorisation and restriction of Chemicals (REACH) directives has resulted in either a reduction in, or a ban of, hexavalent chromium containing compounds in a variety of sectors. In addition, targeted Health and Safety legislation is making disposal and handling of hexavalent chromium containing compounds difficult. For example, the maximum exposure limit of hexavalent chromium to workers in the UK is currently 50 $\mu g \cdot m^{-3}$. In the USA the Occupational Safety and Health Administration (OSHA) has reduced the equivalent permissible exposure limits of workers to just 5 $\mu g \cdot m^{-3}$. For these and other reasons replacements for the CAA process are urgently being sought. Currently, the favoured replacement for CAA, within the European aerospace sector, is tartaric-sulphuric acid anodising (TSAA).

Significantly, the reason for the difference in performance between PAA and CAA is due to the aforementioned microstructure and chemistry of the respective

anodic. The idealised oxide structure that can be created using CAA provides a pore diameter of approximately 30 nm which is smaller than that created using PAA; however, it is large enough to allow the primer or adhesive to penetrate. The CAA oxide thickness is typically in the range 2.5–4 μm which facilitates excellent corrosion resistance [36]. In comparison, the PAA process creates a very porous oxide that encourages excellent initial adhesion, however, the oxide coating is generally reported to be much less than 1 μm thick, which means it provides less barrier corrosion protection. As discussed by Davies, however, the PAA oxide does contain phosphate salts which are thought capable of enhancing corrosion resistance [40].

Sulphuric acid electrolytes are capable of providing much thicker films with improved corrosion resistance but these provide a less porous oxide. Typically, sulphuric acid anodised (SAA) films might be in the range 5–50 μm thick [38] but with pore diameters less than 10 nm across therefore preventing pore penetration and interphase formation. Historically, SAA anodising has been used for decorative, corrosion protection or wear resistant applications or on non-structurally, bonded aluminium parts in aerospace manufacturing [38]. However, due to the relatively thick oxides, and in turn high coating weights, this limits the fatigue performance of any SAA processed aluminium. Furthermore, despite the ability to achieve good initial bond strengths, adhesion to such SAA treated surfaces has been restricted due to the relatively poor durability that these bonds exhibit under hot humid environmental conditions, possibly due to the lack of interphase formation. This makes SAA films less effective as prebond treatments compared with PAA or SAA; a number of studies have reinforced this view.

Conventional boric-sulphuric acid anodising (BSAA) produces an oxide that is similar to the chromic acid process except that the pore diameter is smaller, typically less than 15 nm across. This process is considered to be a chromate-free alternative to CAA for corrosion protection and paint adhesion [41, 42] but less effective as a prebond treatment. Studies by Critchlow et al. [36] have demonstrated that modified BSAA-based processes, such as high temperature processing (HTBSAA), can produce equivalent microstructure to the CAA surface by a competitive dissolution of the oxide during film growth. The resultant films provide equivalent levels of initial adhesion and durability in a variety of environments and test conditions from the HTBSAA compared with CAA. There is an ongoing need for further developments in surface treatments which offer the performance of the standard Bengough-Stuart CAA but without the shortcomings of PAA, in some respects HTBSAA meets this need. The use of boric acid in such processing, however, is also coming under scrutiny.

All of the aforementioned anodic oxides are been monolithic in nature, such that the outer surface has very similar structure to the oxide adjacent to the barrier. In principle, this means that all monolithic oxides are a compromise with the most porous structures, for example PAA, giving excellent adhesion but poor corrosion resistance and the more compact films, for example SAA, giving excellent corrosion resistance but poor corrosion resistance. Table 1 provides a very brief summary of the advantages and disadvantages of the main anodising processes.

Table 1 A comparison of industrially-used DC anodising processes

Anodising process	Advantages	Disadvantages
Phosphoric acid anodising (PAA)	Produces a very porous oxide coating Produces a highly adherent surface	Little corrosion resistance
Sulphuric acid anodising (SAA)	Good corrosion resistance	Oxide is poor for adhesive bonding
Chromic acid anodising (CAA)	Produces a porous oxide that allows penetration from the adhesive and primer Provides corrosion protection	Dangerous to work with for humans due to the use of hexavalent chromium.
Boric acid sulphuric acid anodising (BSAA)	Good corrosion protection Chromate free Produces good painting surface	Small pores make it unsuitable for adhesive bonding

It is apparent that the ideal prebond treatment will provide a highly open, porous outer layer, providing optimum adhesion, with a compact non-porous layer beneath, adjacent to the metal, to give optimum corrosion protection. To achieve this, Yendall and Critchlow [43] carried out work using SAA to provide a hard anodised surface but with the addition of a further surface modification stage using either an electrolytic phosphoric acid deoxidise (EPAD) or a phosphoric acid dip (PAD) technique in order to generate a duplex oxide structure. The role of the EPAD is to provide the open surface below which the compact SAA oxide will be grown and the role of the PAD is to dissolve away the thinner pore walls of the SAA to effectively open out the microstructure. The substrates chosen for this investigation were 2024-T3 aluminium alloy in both bare and clad forms. The adhesive/primer combination studied was Cytec's (Wrexham, UK) FM 73 M/BR 127 epoxide system. Prior to anodising all samples were given a minimum surface pre-treatment: degreasing in acetone under ultrasonic agitation; alkaline cleaning by submersion for 10 min in a proprietary solution of Isoprep 44, and deoxidising. Subsequently, samples were either treated using the standard 40/50 V Bengough-Stuart chromic acid anodise (CAA) or by EPAD plus SAA with or without PAD. EPAD was carried out in a 20 % phosphoric acid solution, operated at 30 °C with an applied anodic potential of 7.0 ± 2 V for 10 min. SAA was carried out in either a low concentration, 40 g/l solution or a standard concentration of 140 g/l, operated at 26 or 35 °C at potential of 15 V. PAD was carried out in 20 % phosphoric acid at 30 °C for various treatment times. Scanning electron microscopy (SEM) was used to observe the resultant surface structures; see Fig. 2. As expected, the CAA treatment provided oxides with relatively uniform, compact films formed, with few voids present in the coating. The scalloped texture produced from the deoxidising process is evident on all final anodised surfaces at the higher magnification shown; see Fig. 2a and c. A noticeable difference in oxide structure between clad and bare alloys can also be seen from Fig. 2b and d. Significantly, the oxide produced on the 2024-T3 clad material is columnar in structure, perpendicular to the metal surface with some branching and termination of columns,

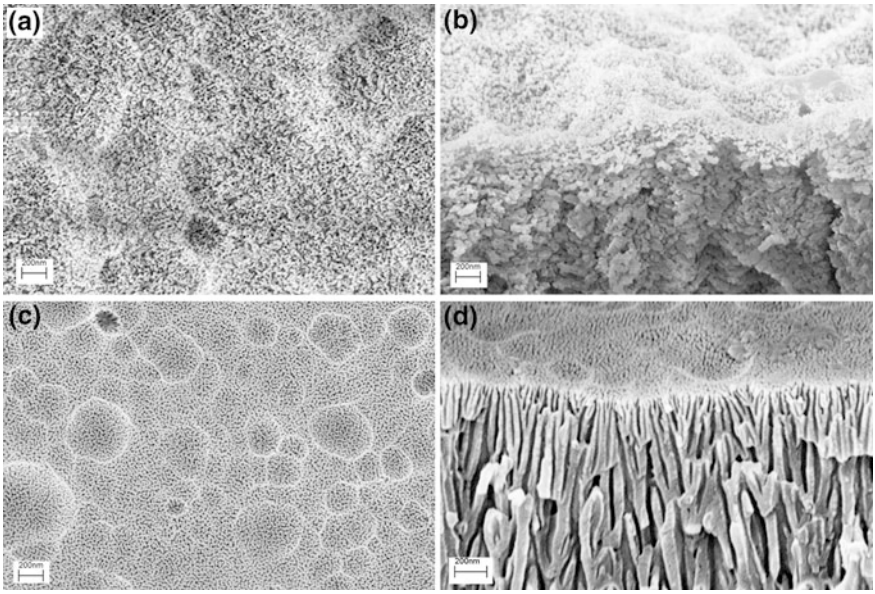

Fig. 2 CAA 40/50 V processed, 2024-T3 bare alloy: **a** in plan view and **b** in cross-section; 2024-T3 clad alloy: **c** in plan view and **d** in cross-section **d** [43]

as seen in cross-section, Fig. 2d. Also, well defined pores are present on the clad alloy, these are in the range of 20–35 nm in diameter. A feature of interest with the clad material, shown in cross-section, see Fig. 2d is the way the pores are smaller in diameter and more closely packed at the surface of the film than they are at depth. This many explain why some studies have shown PAA, with its more open pore structure, to have superior bond strength and durability to that of CAA in the specific case when a primer application is omitted. This would clearly suggest that good penetration of the primer/adhesive system into the oxide is paramount in achieving an optimised adhesive bonding system. In the case of the CAA oxide, the lower viscosity primer can penetrate these pores at the surface whereas a less viscous adhesive is unable to overcome the capillary forces.

In contrast, the hexagonal pore arrangement is not present on the bare alloy substrate. In this case, a more random array exists with a relatively compact nodular surface oxide present. This can be seen both in plan view, Fig. 2a, and in cross-section, Fig. 2b. If fully wetted this nodular oxide would be expected to facilitate interphase formation as previously described.

SEM shows that following EPAD and SAA processing of the 2024-T3 clad alloy there is a clear duplex oxide evident; see Fig. 3a and b. In Fig. 3a, the upper or outer oxide film being the result of the EPAD stage which is analogous to the desirable PAA outer oxide. The purpose of this electro-deoxidising stage is to remove contamination and weakly-bound oxide scale, through an oxide formation and dissolution mechanism in order to leave a clean, uniformly thin but nodular

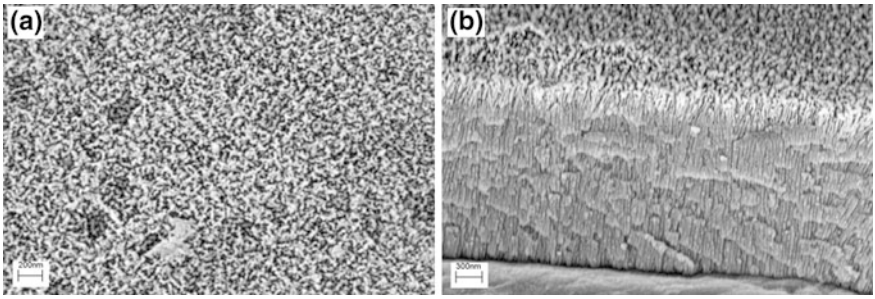

Fig. 3 Plan view (**a**) and cross-section (**b**) of 2024-T3 clad alloy EPAD and SAA [43]

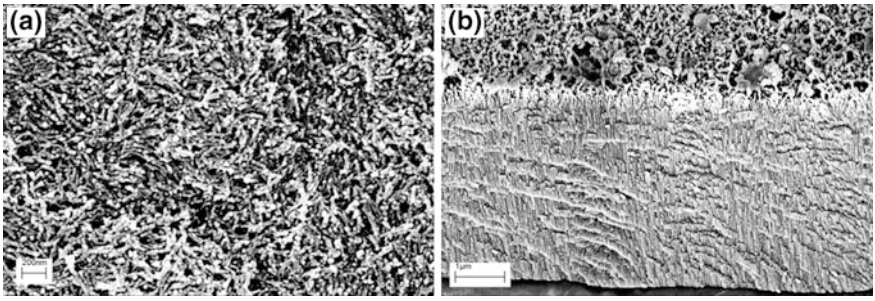

Fig. 4 Plan view (**a**) and cross-section (**b**) of 2024-T3 clad alloy EPAD, SAA and PAD [43]

oxide, ready for subsequent SAA anodising. The thickness of the EPAD layer is approximately 200 nm in thickness which is open and nodular in appearance, as required. The subsequently-deposited SAA oxide is then "grown" underneath the EPAD film. The underlying film of the duplex oxide is shown in, Fig. 3b. This SAA oxide has a columnar structure, similar to that seen for CAA 2024-T3 clad alloy, however, the SAA oxide structure is more compact than that of the CAA oxide. This reduced porosity would be expected to provide increased barrier corrosion properties compared with CAA.

Figure 4a, b show the resultant microstructures following the addition of a PAD stage at the end of the EPAD and SAA process. In Fig. 4a, it can be seen that the PAD has etched the top surface of the EPAD, further increasing the available, open microstructure. In cross-section, Fig. 4b shows that the underlying oxide is left unaffected so corrosion integrity should remain unaffected.

For clarity, Fig. 5 shows the surface region only following an optimised EPAD plus SAA process. A number of process variables, for example, immersion times and temperatures plus acid electrolyte types and concentrations were considered to achieve this optimised structure.

As an additional point of interest, PAA oxides are known to resist sealing or hydration unlike CAA or SAA oxides This is due to the inhibiting properties of the phosphate component in the outer layers of the EPAD oxide. It is anticipated that

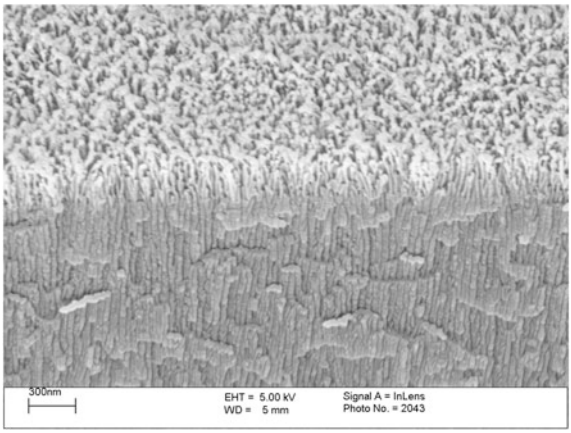

Fig. 5 X20,000 magnification SEM image to show the through thickness duplex structure of the EPAD plus SAA oxide on clad 2024-T3 aluminium

the oxide produced during the electro-deoxidising stage will remain "open" and receptive to the adhesive/primer and the underlying SAA oxide will seal to provide optimised corrosion resistance. In terms of initial SLS joint strength using 2024-T3 alloy adherends, the results were similar, within experimental errors, for all the various anodised joints; see Table 2. In contrast, the degreased-only surface treatment gave relatively poor initial joint strengths and the single FPL acid-etch treatment showed a marginal reduction in joint strength, of 7,250 N, maximum load to failure, compared to all other anodised surface treatments, which were close to 8,000 N.

In addition, durability was established using a modified Boeing wedge test geometry with stressed joints immersed in water at 60 °C. The results of this testing are presented in Fig. 6. Taking the CAA 40/50 V process as a benchmark it can be seen that the initial crack extension, $I_{0,}$ for all the surface treatments are broadly similar. However, when exposed to hot humid conditions, and monitored over 100 h, differences do emerge. For the 2024-T3 clad alloys deoxidised using sodium hydroxide the results vary depending on the subsequent SAA anodising parameters. In terms of durability, both the lower temperature, 26 °C and also the higher concentration, 180 g/l parameters are detrimental to the efficacy of the

Table 2 Summary of single lap shear joint strengths: Note that typical standard deviations are ±200 N

Surface treatment	Force (N)
Degreased-only	3,350
FPL etched	7,250
Degreased + NaOH + SAA (40 g/l: 26 °C)	8,000
Degreased + NaOH + SAA (40 g/l: 26 °C) + PAD	7,750
Degreased + EPAD + SAA (40 g/l: 26 °C)	8,050
Degreased + EPAD + SAA (40 g/l: 26 °C) + PAD	7,800
Degreased + 'optimised' FPL etched + CAA 40/50 V	7,900

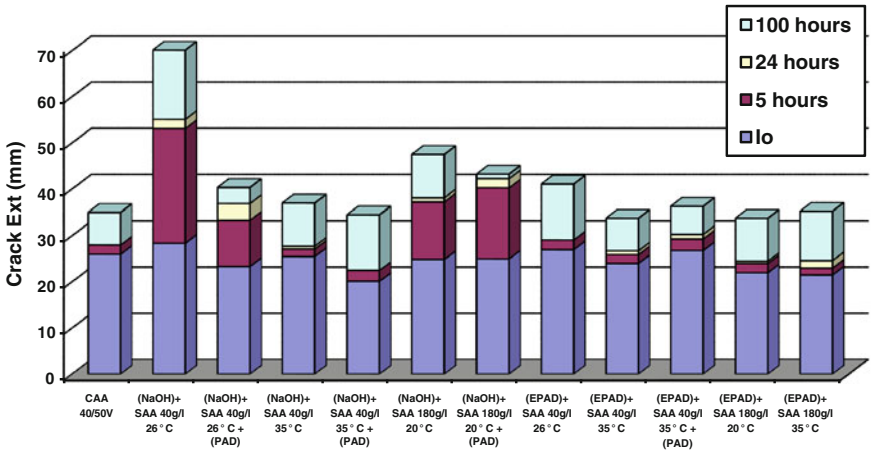

Fig. 6 Summary of wedge test crack extensions using 2024-T3 clad alloy [43]

formed oxide. The two systems using the sodium hydroxide deoxidise that did show comparable crack extension to that of the CAA 40/50 V process where the SAA 40 g/l concentration at 35 °C and the same parameters with a final PAD treatment.

In the case of the anodising systems using the EPAD electro-deoxidiser, all but the 40 g/l concentration, 26 °C temperature SAA, showed equivalent bond durability to the CAA process. Failure analysis using X-ray photoelectron spectroscopy (XPS) showed all anodised specimens to exhibit crack propagation in the region from insertion of the wedge to I_0 to be cohesive within the adhesive. Furthermore, a trend emerged where, for those processes exhibiting crack extensions over 35 mm, the failure mode moved from the adhesive towards the primer/adhesive interface. In the case of both the sodium hydroxide deoxidise and SAA 40 g/l, 26 °C with or without PAD and also the sodium hydroxide deoxidise and SAA 180 g/l, 20 °C with or without PAD, failure was predominately cohesive within the oxide layer. In all other cases cohesive failure of the adhesive was observed. The above study indicates that to provide good initial adhesion and bond durability the outer or upper 200–300 nm of the oxide film needs to be sufficiently open and receptive to any primer or adhesive application, as in the case of all the pre-treatment's using the EPAD. However, the underlying oxide still plays a significant role. From the inferior bond durability of the electro-deoxidised specimens which are then combined with the SAA using 40 g/l and 26 °C, here, a less dense porous oxide is expected to be formed, in comparison to either a higher temperature or increased concentration anodising bath, where both parameters would be expected to increase the dissolution of the pore walls and produce larger pore diameters. This would indicate that primer penetration needs to be achieved further into the oxide than just the first 200 nm so that the adhesive effectively reinforces the oxide. This would be the case of full interphase formation and might be expected given the likely brittle nature of the pseudo-ceramic anodic oxide films.

This also holds true for the sodium hydroxide deoxidised and anodised specimens, where in this case the outermost oxide film will be formed during the anodising. Only the increased solution temperature of 35 °C is sufficient to provide the open pore structure required for good primer penetration, where an additional treatment of PAD only serves to increase this desired surface feature even further. In this study it has been demonstrated that by nano-engineering such desirable two-stage or duplex architecture equivalent performance to that of the CAA 40/50 V process, currently used as an industry standard, has been achieved but using much more benign chemistry.

The aforementioned direct current based processes are, however, all extremely complex, time and energy consuming. A more recently-developed process uses a rapid alternating current (AC) anodise to produce the porous layer followed by a conventional direct current (DC) to provide the compact oxide [44]. The combined ACDC process uses a benign, low concentration phosphoric-sulphuric acid electrolyte and processing times are extremely rapid. Processing times are reduced by a factor of 5–10 compared with the standard CAA. Figure 7 shows the optimised ACDC structure in cross-section at various magnifications. A range of tests have been conducted using a range of aluminium alloys including clad 2024-T3. These tests include measurement of both adhesion and corrosion performance. In all cases, the ACDC process performed favourably compared with either SAA or CAA controls. Boeing wedge test data, with the joints immersed in water at 60 °C, are presented in Table 3; these data indicate that variations in the AC process followed by a 10 V DC anodise in the phosphoric-sulphuric acid electrolyte gave comparable performance to CAA. The highly optimised microstructure indicated in Fig. 7 is responsible for the excellent levels of adhesion observed. Figure 8 presents linear polarisation data for degreased-only, CAA and ACDC processed clad 2024-T3 alloy. The low limiting currents in both anodic and cathodic directions for the ACDC processed material indicate comparable electrochemical activity to the CAA control. Such corrosion protection is thought responsible for the enhanced durability offered by the ACDC process.

2.2 Titanium Alloys

In simple terms, many of the processes that have found success as prebond treatments for aluminium alloys have been applied to titanium and its alloys [45, 46]. As with aluminium alloys, mechanical treatments, for example, by simply abrading or grit-blasting have been found to give modest improvements in durability and the more successful processes have been based upon chemical or electrochemical processes [45].

Amongst the acid or alkaline etchants: phosphate-fluoride based processes; Pasa Jell; Turco 5578; hydrochloric and hydrofluoric acids; sodium hydroxide, and; and chromic acid based processes have been widely reported [45]. In the review of such processes by Critchlow the proprietary Pasa Jell and Turco 5578 processes

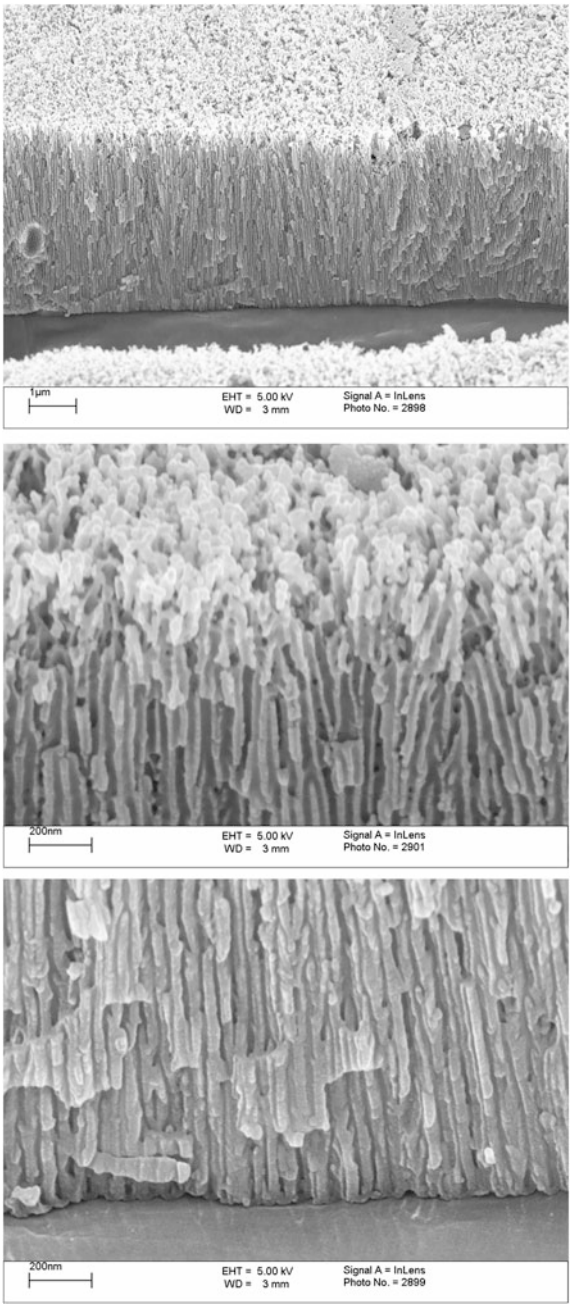

Fig. 7 SEM images to show the structure of optimised ACDC oxides on clad 2024-T3 clad aluminium. *Top* image shows the through thickness (×6,500), middle image the outer oxide (×40,000), *bottom* image the inner oxide (×40,000) [44]

Table 3 Wedge crack length data to show the influence of varying the AC anodising parameters and electrolyte temperature for the ACDC process; Note a 10 m, 20 V DC process has been deposited beneath each AC film [44]

AC anodising parameters	Exposure time (h)							
		1	4	8	24	48	72	96
10 V 120 s 35 °C	Mean crack length (mm)	33.25	33.25	33.25	35.00	35.38	35.50	35.50
	Σ	0.82	0.82	0.82	0.74	0.75	0.54	0.54
10 V 120 s 50 °C	Mean crack length (mm)	31.33	31.50	31.58	32.83	33.33	33.33	33.33
	Σ	0.37	0.41	0.45	1.07	1.18	1.18	1.18
10 V 240 s 35 °C	Mean crack length (mm)	31.33	31.42	31.42	33.00	33.33	33.42	33.42
	Σ	0.56	0.69	0.69	0.79	0.95	0.99	0.99
10 V 240 s 50 °C	Mean crack length (mm)	33.50	33.67	33.67	34.50	34.83	35.25	35.42
	Σ	0.19	0.25	0.25	0.84	0.45	0.69	0.91
15 V 120 s 35 °C	Mean crack length (mm)	31.33	31.67	32.25	33.08	33.25	33.25	33.25
	Σ	0.82	1.25	2.07	1.65	1.57	1.57	1.57
15 V 240 s 35 °C	Mean crack length (mm)	31.92	32.17	32.58	33.58	34.08	34.25	34.92
	Σ	0.29	0.56	0.75	1.11	0.90	1.11	1.41
40/50 V CAA	Mean crack length (mm)	31.50	33.10	33.35	33.90	34.45	34.45	34.45
	Σ	0.95	1.09	0.84	1.37	1.90	1.90	1.90

were identified as providing, possibly, the best levels of durability amongst these options [45]. Acid etching of titanium alloys is reported to initiate brittle failure due to hydrogen embrittlement of the metal during processing. It is thought that this failure mode does not occur post Pasa Jell and Turco 5578 processing. The Pasa Jell process is reported to produce a very smooth surface with a thin oxide extending up to 5–7 nm. In contrast the Turco 5578 provides a macro-rough texture with a much thicker oxide, estimated to extend to nearly 20 nm. These surface characteristics enable the Turco 5578 process to perform well in durability tests. In bond durability tests, the Turco 5578 is generally only out-performed by the anodising processes in comparative studies. For example, Wegman and Levi [47] measured the time-to-failure of SLS joints stressed to 13.7 MPa in condensing humidity at 60 °C. In this test, the phosphate-fluoride etch survived for 754 h, whilst Turco 5578 and chromic acid anodisation lasted for 1,622 and over 7,000 h respectively. Such relative performance was observed with a number of different adhesive/primer combinations.

Also, as with aluminium, silane primers or coupling agents and sol–gel processing has been applied to titanium alloy bonding. Notably, Blohowiak et al. [48] compared an acetic acid catalysed GTMS/tetra-n-propoxyzirconium (TPOZ) derived sol–gel on titanium Ti-6Al-4 V alloy versus CAA. In this test SLS joints

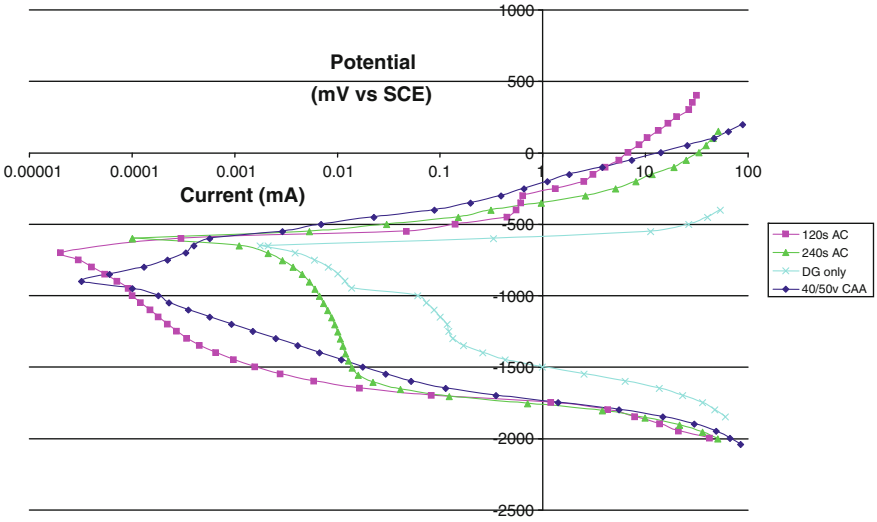

Fig. 8 Cathodic and anodic electrochemical polarisation curves in 3.5 % NaCl solution for ACDC with varying AC anodising voltage parameters plus control samples of CAA and degreased-only clad 2024-T3 aluminium [44]

were assembled with a polyimide adhesive with joint strengths measured before and after 72 h immersion in boiling water. A number of sol–gel based processes were investigated. In all cases the sol–gel gave higher initial SLS values, close to 55 MPa, compared with approximately 41 MPa for the CAA. After immersion, the sol–gel derived processes gave values close to 34 MPa whilst the CAA treated joints were reduced to approximately 19.4 MPa. The same workers also tested a number of sol–gel processes against a number of treatments, including CAA, in the wedge test configuration with joints exposed to condensing humidity at 60 °C. In these tests the sol–gel processes out-performed both the mechanical, abrasion and hydrofluoric-nitric acid etch treatments and performed comparably well to the CAA. This, and other relevant studies [49, 50], highlights the potential usefulness of sol–gel coatings even compared to the well-regarded CAA surface treatment.

As with aluminium alloys, the anodic oxides are regarded as providing amongst the most durable adhesion with titanium alloys. Although the aforementioned chromic acid electrolyte has been used to process titanium alloys the sodium hydroxide electrolyte is often preferred. Sodium hydroxide anodisation (SHA) produces a highly rough oxide, capable of interphase formation. Kennedy et al. [51] demonstrated that the bond performance of SHA was dependent upon parameters such as anodising temperature, anodising voltage and temperature. The optimised process involves degreasing followed by anodising at 10 V for 30 min in 5 M sodium hydroxide at 20 °C followed by rinsing and drying. In the study by Kennedy et al. [51], a comparison was made between the optimised SHA treatment and a number of alternatives, including CAA, using the wedge test configuration

with joints immersed in 96 % relative humidity for up to 144 h. The Redux 312/5 (Duxford, UK) epoxide adhesive was used throughout these tests. After 144 h of exposure the joints incorporating the alkaline hydrogen peroxide (AHP) etch gave crack growth of 7.3–22.2 mm. In contrast, the CAA treated joints gave crack growths in the range 6.2–9.0 mm. Both treatments were out-performed by the SHA treated joints which gave much reduced crack growths in the range 2.8–3.6 mm. A number of other studies have also demonstrated that the SHA can out-perform the CAA anodise on titanium alloy substrates [45].

Also of note is the use of plasma-spray coatings to provide durable adhesion to the Ti-6Al-4 V alloy. In an early study, Zatorski et al. [52] used plasma-sprayed alumina powder to provide a coating with a roughness, R_a, of close to 20 μm and with around 9 % film porosity. Such a plasma-sprayed film provided over 40 MPa in SLS joints bonding titanium alloy against a glass reinforced composite (GRP) using an epoxide adhesive. In terms of durability, the wedge test geometry was used to demonstrate that the alumina plasma-spray technique gives comparable performance to Pasa Jel 107 when exposed to 96 % relative humidity at 49 °C for periods up to 200 h.

2.3 Steels

Steels come in many forms, including; plain carbon; high alloy, such as stainless steels, and; inorganic coated, for example, zinc galvanised or galvanealed. Bonding to these different surfaces presents unique and different challenges. For example, in order to introduce desirable texture to stainless steels it might be required to mechanically treat or etch the material, thereby removing the passivating chromium-rich oxide, making the alloy more prone to subsequent corrosion. In the case of zinc coated surfaces, processes such as trication conversion coatings might be used which will form insoluble salts with the highly reactive zinc [53]. In the interests of brevity, this section will, therefore, be limited to a consideration of available treatments for plain carbon steels only.

Adhesion to such steels is critically important if paint or lacquer adhesion is considered and there exists a number of dedicated processes which increase the durability of such for diverse interests including the canning and automotive industries [54]. In both these instances, rapid processing and long-lasting adhesion or product lifetimes are important. In the case of structural bonding there are, however, relatively few reported treatments for uncoated, plain carbon steels (hereafter simply referred to as "steels") for enhanced durability.

A large number of studies have focussed upon the use of grit-blasting plus silane application, for example [20] and [55]. Tod et al. [56] have discussed the advantages of this treatment specifically for military applications. In this chapter they also discuss some of the process parameters which need to be optimised for

the successful application of the aforementioned γ-GPS. The efficacy of the optimised γ-GPS process has been proven by Shaw et al. [20] using axial butt joints made using mild steel adherends and bonded using an epoxide adhesive. These were either simply grit-blasted or grit-blasted plus γ-GPS silane treated then immersed in water at 60 °C with joints removed and tested by measuring the residual joint strengths at various time intervals up to 144 h. After 144 h of exposure the grit-blasted only joints demonstrated a residual joint strength close to 5 MPa, in contrast, the joints treated with a γ-GPS solution from an aqueous solution gave a comparable joint strength of 22.4 MPa and from an ethanol–water mixture 12.4 MPa. These and many other studies have demonstrated the efficacy of silane treatment, when optimised, on steels. As with aluminium alloys, the presence of the primer or coupling agent is thought to increase the hydrolytic stability of the metal-adhesive interphase. Although the deposition of sol-gels onto steels has been conducted for corrosion resistant and tribological coatings [27, 31] there are, however, few reported studies on their ability to improve bond durability.

The most widely-used corrosion inhibiting treatments for steels are the conversion coatings [54, 57–60]. Of particular note are the chromate- and phosphate-based processes. However, given the current status of chromate-containing processes, as previously discussed, this section will focus upon the chromate-free conversion coating treatments. That stated, mention should be made of the chromate-containing Accomet C treatment which Fay and Maddison have shown provides better durability to the γ-GPS process on uncoated steels in SLS joints exposed to salt-spray conditions [57]. In the same study [57], it was also shown that Accomet C provided higher residual strengths in SLS joints tested after a combination of environmental ageing and statically applied stress were applied. Freeman [54] provides a consideration of the conversion coating film formation mechanisms on both ferrous and non-ferrous metals; from this it is apparent that conversion coatings are capable of providing optimised bonding surfaces. Critchlow et al. [60] have investigated the use of non-chromated conversion coatings. In their study, a number of iron, manganese and zinc phosphate coatings were compared with grit-blasting plus γ-GPS and Accomet C treatment in terms of initial adhesion and measuring residual strengths of single lap shear joints after immersion in deionised water at 60 °C for up to 8 weeks. In terms of both initial adhesion and durability the iron phosphate process performed best, giving 57.9 MPa prior to exposure and retaining 46.2 ± 2.5 MPa after 8 weeks immersion. These values compare with 55.0 MPa and 33.4 ± 1.9 MPa for grit-blast plus γ-GPS silane application. The iron phosphate was shown to provide a highly complex organic–inorganic oxide coating extending to approximately 150 nm and which was highly wettable and nodular on the sub-micrometre level. This study also highlighted the need to optimise conversion coating chemistry to avoid the possibility of the deposit acting as an internal weak boundary layer.

3 Summary

In summary, For all metals there exist a range of surface treatment options which can mitigate the influence of moisture within the adhesive bondline by one or more of the following mechanisms: increasing interfacial adhesion; providing interphase formation, and; by providing barrier or chemical corrosion protection. The selection of a specific treatment for a particular application will depend upon a number of factors, including: the environmental and mechanical loading conditions, i.e. the process must be fit-for-purpose; process speed and availability, and; cost. Other factors such as repairability might also be important. It is important to note that there are currently-available processes which satisfy the requirements of the most demanding applications, including those in the aerospace, defence and automotive sectors. There is, however, an ongoing requirement to develop further prebond treatments. This requirement may be driven by, for example; legislative, performance or financial reasons. It is also important to note that bond durability is not simply a function of the metal and generic treatment carried out. For optimised durability it is necessary to consider the bonding system, that is: the specific alloy or grade of metal; the adhesive and or primer to be used, and; the optimised treatment.

References

1. Minford, J.D.: Handbook of Aluminum Bonding Technology and Data. Marcel Dekker, New York USA (1993)
2. Mahoon, A.: Durability of Structural Adhesives. In: Kinloch, A.J (ed.) Applied Science Publishers, London, UK, p. 255 (1983)
3. Thrall, E.W., Shannon, R.W. (eds.): Adhesive Bonding of Aluminum Alloys. Marcel Dekker, New York USA (1985)
4. Sykes, J.M.: Surface Analysis and Pretreatment of Plastics and Metals. In: Brewism, D.M. (ed.) Applied Science Publishers, London, UK, p. 153 (1982)
5. Ashcroft, I.A., Comyn, J.: Handbook of Adhesion Technology vol. 2, p. 789. In: da Silva, L.F.M., Ochsner, A., Adams, R.D. (eds.) Springer, Berlin, Germany (2011)
6. Bowditch, M.R., Hiscock, D., Moth, D.A.: The role of the substrate in the hydrolytic stability of adhesive joints. Trans. Inst. Metal Finish. **76**(6), 209–212 (1998)
7. Bowditch, M.R.: The durability of adhesive joints in the presence of water. Int. J. Adhes. Adhes. **16**, 73–79 (1996)
8. Schweitzer, P.A. (ed.): Corrosion Engineering Handbook. Marcel Dekker, New York USA (1996)
9. Baboian, R. (ed.): Corrosion Tests and Standards: Applications and Interpretation. ASTM International, Baltimore, USA (2005)
10. Burchardt, B.: Handbook of Adhesion Technology (vol. 2, p. 1185). In: da Silva, L.F.M., Ochsner, A., Adams, R.D. (eds.) Springer, Berlin, Germany
11. Watts, J.F.: Handbook of Adhesion: Second Edition. In: Packham, D.E. (ed.) Wiley, Chichester, UK, p. 101 (2005)
12. Briggs, D.: Handbook of Adhesion 2nd edn. In: Packham, D.E. (ed.) Wiley, Chichester, UK, p. 89, 235 (2005)

13. Critchlow, G.W., Bedwell, K.H., Cottam, C.A.: The effectiveness of TEA CO_2-laser ablation for the treatment of hot dipped galvanized mild steel prior to adhesive bonding. Trans. Inst. Metal Finish. **76**(5), 203–206 (1998)
14. Critchlow, G.W., Litchfield, R., Curtis, C., Owen, M.: Hot and cold cleaning methods: CO_2 and Nd:YAG laser ablation, sodium hydride immersion and CO_2 cryoblasting. Trans. Inst. Metal Finish. **87**(6), 284–286 (2009)
15. Critchlow, G.W., Brewis, D.M., Emmony, D.C., Cottam, C.A.: Initial investigation into the effectiveness of CO_2-laser treatment of aluminium for adhesive bonding. Int. J. Adhes. Adhes. **15**(4), 233–237 (1995)
16. Rance, D.G.: Surface Analysis and Pretreatment of Plastics and Metals. In: Brewis, D.M. (ed.) Applied Science Publishers, London, UK, p. 121 (1982)
17. Hart-Smith, L.J.: Handbook of Adhesion Technology (vol. 2, p. 1104). In: da Silva, L.F.M., Ochsner, A., Adams, R.D. (eds.) Springer, Berlin, Germany (2011)
18. Desagulier, C.: Handbook of Adhesion Technology (vol. 2, P. 1150). In: da Silva, L.F.M., Ochsner, A., Adams, R.D. (eds.) Springer, Berlin, Germany (2011)
19. Pleuddemann, E.P.: Silane Coupling Agents. Plenum Press, New York, USA (1982)
20. Gledhill, R.A., Shaw, S.J., Tod, D.A.: Durability of adhesively-bonded joints employing organosilane coupling agents. Int. J. Adhes. Adhes. **10**(3), 192–198 (1990)
21. Digby, R.P., Shaw, S.J.: The international collaborative programme on organosilane coupling agents: an introduction. Int. J. Adhes. Adhes. **18**, 261–264 (1998)
22. Abel, M.-L., Allington, R.D., Digby, R.P., Porritt, N., Shaw, S.J., Watts, J.F.: Understanding the relationship between silane application conditions, bond durability and locus of failure. Int. J. Adhes. Adhes. **26**, 2–15 (2006)
23. Abel, M.-L., Adams, A.N.N., Kinloch, A.J., Shaw, S.J., Watts, J.F.: The effects of surface treatment on the cyclic-fatigue characteristics of bonded aluminium-alloy joints. Int. J. Adhes. Adhes. **26**, 50–61 (2006)
24. Rattana, A., Abel, M.-L., Watts, J.F.: ToF-SIMS studies of the adsorption of epoxy resin molecules on organosilane treated aluminium: adsorption kinetics and adsorption isotherms. Int. J. Adhes. Adhes. **26**, 28–39 (2006)
25. Underhill, P.R., Duquesnay, D.L.: Silanes and Other Coupling Agents (vol. 2, p. 149). In: Mittal, K.L. (ed.) VSP, Utrecht, The Netherlands (2000)
26. Zhu, D., van Ooij, W.J.: Corrosion protection of metals by water-based silane mixtures of bis[trimethoxysilylpropyl]amine and vinyltriacetoxysilane. Prog. Org. Coat. **49**, 42–53 (2004)
27. Wang, D., Bierwagen, G.P.: Sol-gel coatings on metals for corrosion protection. Prog. Org. Coat. **64**, 327–338 (2009)
28. May, M., Wang, H., Akid, R.: Bond strength of hybrid sol-gel coatings with different additives. J. Coat. Technol. Res. (published online 26 Oct 2012)
29. Osborne, J.H., Blohowiak, K.Y., Sekits, D.F.: Environmentally benign sol-gel surface treatments for aluminum bonding applications. Wright Laboratory report WL-TR-95-4060, issued April 1996
30. Voevodin, N.N., Balbyshev, V.N., Donley, M.S.: Investigation of corrosion protection performance of sol-gel coatings on AA2024-T3. Prog. Org. Coat. **52**, 28–33 (2005)
31. Metroke, T.L., Parkhill, R.L., Knobbe, E.T.: Passivation of metal alloys using sol-gel-derived materials—a review. Prog. Org. Coat. **41**, 233–238 (2001)
32. Critchlow, G.W., Brewis, D.M.: Review of surface pretreatments for aluminium alloys. Int. J. Adhes. Adhes. **16**, 255–275 (1996)
33. Minford, J.D.: Comparison of aluminium adhesive joint durability as influenced by etching and anodizing pretreatments of bonded surfaces. J. Appl. Polym. Sci.: Appl. Polym. Symp. **32**, 91–103 (1997)
34. Critchlow, G.W., Brewis, D.M.: A comparison of chromate-phosphate and chromate-free conversion coatings for adhesive bonding. J. Adhes. **61**, 213–230 (1997)
35. Bockmair, G.: Non-chromate surface protection for aircraft maintenance. Adv. Mater. Res. **38**, 7–13 (2008)

36. Cree, A.M., Devlin, M., Critchlow, G., Hirst, T.: Fatigue and fracture assessment of toxic metal replacement coatings for aerospace applications. Trans. Inst. Metal Finish. **88**(6), 303–310 (2010)
37. Sheasby, P.G., Pinner, R.: The Surface Treatment and Finishing of Aluminum and its Alloys, 6th edn. Finishing Publications Ltd, Stevenage UK (2001)
38. Critchlow, G.W., Yendall, K.A., Bahrani, D., Quinn, A., Andrews, F.: Strategies for the replacement of chromic acid anodising for the structural bonding of aluminium alloys. Int. J. Adhes. Adhes **26**, 419–453 (2006)
39. Tarr, L.E., Holmquist, H.H.: In: Proceedings of the 35th International SAMPE Symposium, pp. 2102–2111 (1990)
40. Davis, G.D., Sun, T.S., Ahearn, J.S., Venables, J.D.: Application of surface behaviour diagrams to the study of hydration of phosphoric acid-anodized aluminium. J. Mater. Sci. **17**, 1807–1818 (1982)
41. Wong, C., Moji, Y.: US Patent No. 4,894,127 (1990)
42. MIL-A-8626.: Anodic Coatings for Aluminium and Aluminium Alloys
43. Yendall, K.A., Critchlow, G.W.: Novel methods, incorporating pre- and post-anodising steps, for the replacement of the Bengough-Stuart chromic acid anodising process in structural bonding applications. Int. J. Ades. Adhes. **29**, 503–508 (2009)
44. Cartwright, T.: PhD Thesis, Loughborough University (2005)
45. Critchlow, G.W., Brewis, D.M.: Review of surface treatment for titanium alloys. Int. J. Adhes. Adhes. **15**, 161–172 (1995)
46. Molitor, P., Barron, V., Young, T.: Surface treatment of titanium for adhesive bonding to polymer composites: a review. Int. J. Adhes. Adhes. **21**, 129–136 (2001)
47. Wegman, R.F., Levi, D.W.: Evaluation of titanium prebond treatments by stress durability testing. In: Proceedings of the 27th National SAMPE Symposium (1982)
48. Blohowiak, K.Y., Osborne, J.H., Krienke, K.A.: US Patent No. 5,939,197 (1999)
49. Patsi, M.E., Hautaniemi, J.A., Rahiala, H.M., Peltola, T.O., Kangasniemi, I.M.O.: Bonding strengths of titania sol-gel derived coatings on titanium. J. Sol-gel Sci. Technol. **11**, 55–66 (1998)
50. Osborne, J.H., Blohowiak, K.Y., Taylor, S.R., Hunter, C., Bierwagon, G., Carlson, B., Bernard, D., Donley, M.S.: Testing and evaluation of nonchromated coating systems for aerospace applications. Prog. Org. Coat. **41**, 217–225 (2001)
51. Kennedy, A.C., Kohler, R., Poole, P.: A sodium hydroxide anodize surface pretreatment for the adhesive bonding of titanium alloys. Int. J. Adhes. Adhes. **3**(2), 133–139 (1983)
52. Pike, R.A., Patarini, V.M., Zatorski, R., Lamm, F.P.: Plasma-sprayed coatings as adherend surface pretreatments. Int. J. Adhes. Adhes. **12**(4), 227–231 (1992)
53. Critchlow, G.W., Bedwell, K.H., Chamberlain, M.E.: Pretreaments to improve the bondability of hot dipped galvanised mild steel. Transactions of the Institute of Metal Finishing. **76**(6), 209–213 (1998)
54. Freeman, D.B.: Phosphating and Metal Pre-treatment. Woodhead-Faulkner, Cambridge, UK (1986)
55. Tod, D.A., Atkins, R.W., Shaw, S.J.: Use of primers to enhance adhesive bonds. Int. J. Adhes. Adhes. **12**(3), 159–163 (1992)
56. Cunliffe, A.V., Evans, S., Tod, D.A., Torry, S.A., Wylie, P.: Optimum preparation of silanes for steel pre-treatment. Int. J. Adhes. Adhes. **21**, 287–296 (2001)
57. Fay, P.A., Maddison, A.: Durability of adhesively bonded steel under salt spray and hydrothermal stress conditions. Int. J. Adhes. Adhes. **10**(3), 179–186 (1990)
58. Davis, R.E., Fay, P.A.: The durability of bonded coated steel joints. Int. J. Adhes. Adhes. **13**(2), 97–104 (1993)
59. Bistac, S., Vallat, M.F., Schultz, J.: Durability of steel-polymeradhesion in an aqueous environment. Int. J. Adhes. Adhes. **18**, 365–369 (1998)
60. Critchlow, G.W., Webb, P.W., Tremlett, C.J., Brown, K.: Chemical conversion coatings for structural adhesive bonding of plain carbon steels. Int. J. Adhes. Adhes. **20**, 113–122 (2000)

Influences of Water on the Adhesive Properties

Chiaki Sato

Abstract The property change of cured bulk adhesive by water immersion is described in this chapter. Preparation of bulk adhesive specimens is firstly explained because dense bulk adhesives without porosity are not easy to make. Experimental methods to determine the water diffusion coefficient and saturated water absorption are also discussed. Based on the parameters obtained from these tests, water distribution in bulk adhesives can be calculated using the finite element method. Influence of water immersion on the stress–strain relations of bulk adhesives is also discussed.

Keywords Water immersion · Water ingress · Plasticizing · Diffusion · The Fick's law · Young's modulus · Bulk adhesive

1 Introduction

Since the components of adhesives are mainly polymers, adhesives can be degraded by water absorption, which leads to hydrolysis, softening and decrease of the glass transition temperature (Tg) [1]. The water absorption also leads to strength decrease of joints bonded with adhesives [2]. The water absorbed by an adhesive layer may move to the interfaces between the adhesive and adherends, and may cause interfacial fracture along the interfaces. Therefore, the absorption, diffusion and accumulation of water by adhesive and interfaces are very important to predict the strength of adhesively bonded joints.

Water diffusion in polymers basically yields to the simplest model called the Fick's law. Therefore, water distribution in the adhesive layer in a joint can be

C. Sato (✉)
Precision and Intelligence Laboratory, Tokyo Institute of Technology,
4259 Nagatsuta, Midori-ku, Yokohama 226-8503, Japan
e-mail: csato@pi.titech.ac.jp

L. F. M. da Silva and C. Sato (eds.), *Design of Adhesive Joints Under Humid Conditions*, Advanced Structured Materials 25, DOI: 10.1007/978-3-642-37614-6_4,

predicted solving a partial differential equation derived from the Fick's theory. For this solution, we need two parameters: saturated water absorption and diffusion coefficient, which can be determined experimentally.

Water absorption tends to change the mechanical properties of adhesive layer, i.e. volume, modulus, strength, maximum strain, Tg, damping, etc. In these properties, change of strength is crucial in terms of predicting joint strength bonded with the adhesive, and it should be measured experimentally, although water immersion of specimens needs long period and testing the specimens after the immersion is not easy.

In this chapter, the phenomenon of water diffusion and accumulation will be shown. Methods and specimens for testing water absorption will be discussed. A model to predict water diffusion in the adhesive layer will also be shown. Finally, the change of mechanical properties of the adhesive in bulk will be discussed.

2 Experimental

2.1 Specimens

2.1.1 Specimens for Measuring Water Absorption

The amount of water absorption can be measured using fully cured adhesive bulk specimens. A specimen configuration of a bulk adhesive for measuring water absorption, which is designated by ISO294-3, is shown in Fig. 1. The specimens are immersed in water or exposed to humidity, and the weight change of the specimens is measured during the tests. Since large specimens have bigger weight change than smaller specimens, fine resolution of weight measurement is not necessary, but exposure time becomes longer. Therefore, the configuration of the specimens should be selected so as the surface area is large. In addition, when the diffusion coefficient of water needs to be obtained, thin and plane specimens are convenient because one dimensional diffusion can be assumed, which leads to an easier solution of the diffusion equation. The author uses a disk-shaped specimen configuration shown in Fig. 1 because this shape has the shortest side per frontal projected area, which can minimize the influence of water ingress from the side. The residue of oil or release agent can be barriers for water penetration, and it should be perfectly removed before the immersion of the specimens in water.

2.1.2 Specimen for Strength Measurement

The strength of cured adhesive bulk specimens is usually measured by tensile tests using dumbbell specimens. Bending tests of bulk adhesive can be applicable especially for the cases where fixing the specimen is difficult, although the elastic

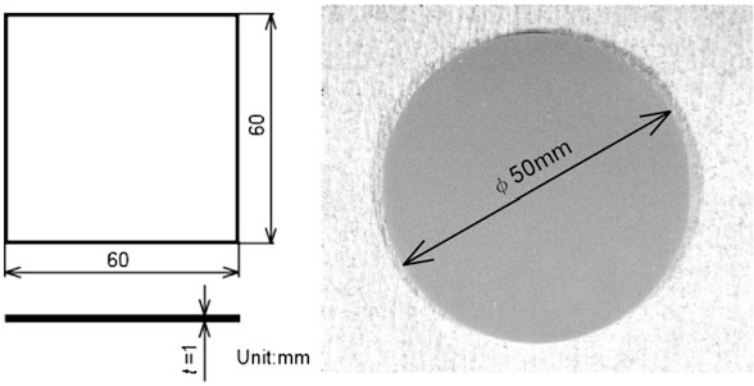

Fig. 1 Specimen configurations for immersion tests to examine water absorption (*Left*: ISO294-3, *Right*: disc shape specimen that the author often uses)

constants and the failure strength should be calculated by the beam theory. Compression tests, which are easier to conduct than tensile or bending tests, are not popular for measuring the strength of adhesive bulk specimens because the compressive strength of the adhesive in bulk is much higher than the tensile strength which is the main parameter to obtain.

2.1.3 Specimen Preparation

Almost all adhesives include main components and hardeners. Adhesives provided as two parts as the main component and hardener are called two part types, and adhesives provided as one part including both a liquid main component and a liquid or solid hardener are called one part type. Two part type adhesives are cured by mixing the two parts due to a chemical reaction. One part type adhesives start the chemical reaction by various modes such as heating, ultraviolet irradiation, humidity, absence of oxygen and evaporation of solvents.

Hardening mechanisms are very influential on the specimen preparation methods. For instance, two part type adhesives need to be mixed, and may introduce porosity in the mixing process. In addition, two part type adhesives need to be mixed keeping a precise mixture ratio of the main component and the hardener. In contrast, one part type adhesives are easier to manufacture than two part type adhesives because no mixture of components is necessary. However, for one part type adhesives that cure by humidity such as urethanes and cyanoacrylates, a long time is needed to perfectly cure the adhesive because of the small diffusion coefficient of humidity in liquid resins. Room temperature vulcanized (RTV) silicone adhesives are another one part type adhesive difficult to make in bulk because the evaporation of chemicals, which is necessary for the curing, is suppressed from the center parts of the bulk.

Control of defects is very important and necessary to make bulk adhesive specimens because even small defects influence the tensile strength of the specimens. The most common defects are bubbles which are trapped in the adhesive during the mixture process of the two parts. The bubbles are spherical in the initial stage, and become crack-like flaws by applying shear stress, which decrease the tensile strength of the cured bulk adhesive. Even spherical bubbles can affect the strength, and they may become the reservoir of water or humidity during exposure tests. Thus, such defects should be eliminated as much as possible.

Specimen of Two Part Type Adhesives

For making bulk specimens of two part adhesives, it is necessary to mix the parts. The ratio of parts should be strictly controlled because the strength of the adhesive in bulk highly depends on the ratio. Perfect mixing of the parts is also important in order to cause the total chemical reaction and reduce the residue that is not reacted. Recent two part adhesives can be provided stored in the MixPac© package (Sulzer Ltd, Switzerland), which has two cylinders and a static mixer, as shown in Fig. 2. By using the MixPac package, the portion of parts can be precisely controlled and mixed enough to cause perfect chemical reaction. In addition, the parts of adhesive in the cylinders are stored with very few air bubbles, and no additional bubble can be formed during the mixture process in a static mixer. Therefore, it is possible to make very good bulk specimens because the number of air bubbles in bulk can be reduced and are negligible.

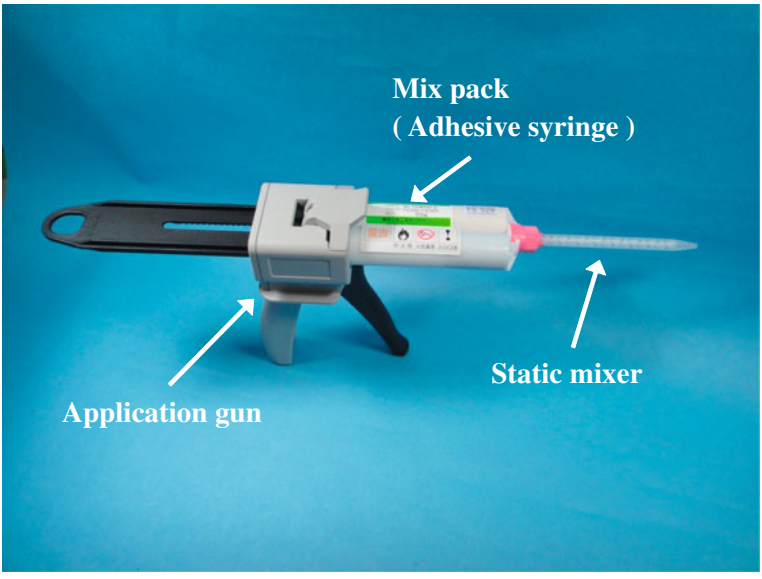

Fig. 2 MixPac© package for two part type adhesives, applicator and static mixer

If adhesives cannot be provided with MixPac, mixing of two parts should be done with another method. Mixing in ambient condition with a spatula leads to porous bulk specimens with many air bubbles. For this case, de-bubbling after the mixing process is indispensable. Low viscous adhesives can be de-bubbled in a vacuum chamber. It should be noted that the mixture of an adhesive begins the gelation during the vacuum de-bubbling process if the pot life is very short. For adhesives that have long pot lives, the use of de-bubbling agents is effective to reduce the bubbles. The de-bubbling agents sprayed on the surface of the mixed adhesive liquid cause easily the burst of air bubbles in the liquid at the surface. However, too viscous adhesives cannot be de-bubbling perfectly only by the vacuum process. In this case, vacuum mixer, centrifugal mixers, or vacuum centrifugal mixers should be used.

The vacuum mixer is a device for mixing liquids under vacuum. Simple vacuum mixers are commercially available for laboratory works. For example, the type of vacuum mixer having a vacuum chamber and a magnetic stirrer shown in Fig. 3 has a reasonable price, and it is convenient to mix small amounts of low viscous adhesives.

For highly viscous adhesives, centrifugal mixers are suitable for mixing because mixing and de-bubbling of an adhesive can be simultaneously carried out. This machine can apply a very high gravity force by revolution of a container, by which de-bubbling of a liquid in the container is accelerated. In addition, some type of centrifugal mixers can mix the liquids in the container by means of rotation of the container. If more perfect de-bubbling is required, centrifugal mixers with vacuum chambers, shown in Fig. 4, are available. The demerit of the machine is its

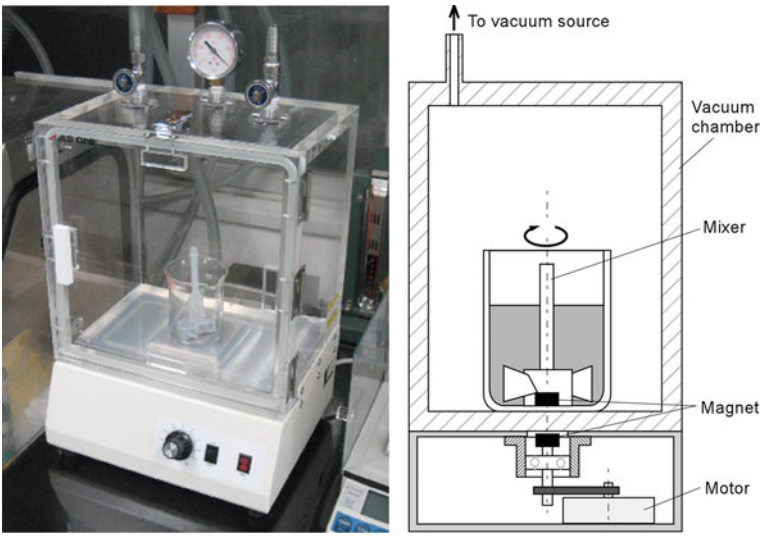

Fig. 3 Vacuum mixer with a magnetic stirrer (*Left*: photograph, *Right*: schematic of inner structure)

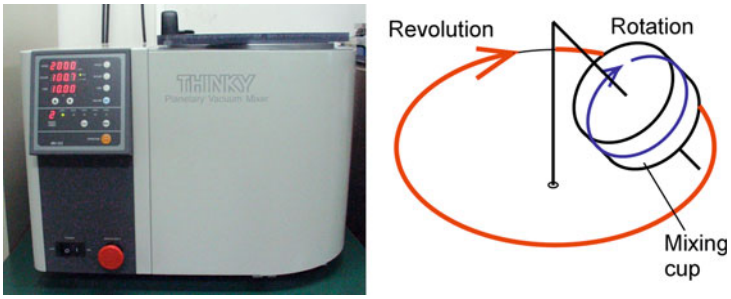

Fig. 4 Centrifugal mixer with a vacuum chamber (*Left*: photograph, *Right*: motion of mixing cup in the mixer)

high price because such machines are very expensive. In addition, it has the problem at increasing the temperature of the liquids during the mixing process, which leads to gelation in the container. For making bulk specimens of adhesives, a method using a hot-press machine is often applied based on the French standard NF T 76-142 [3].

The mixture of adhesive after the de-bubbling is poured in a mould and cured. When the mixture is injected in the mould, bubbles may be trapped in the adhesive. In the case of using MixPac, the tip of the static mixer should be inserted to the filling port of the mould and the mixture of adhesive should be injected. Even if adhesives are not provided with MixPac, it is possible to inject the adhesive into a mould using a syringe, as shown in Fig. 5. A pre-mixed adhesive is filled in the syringe and de-bubbled with a centrifugal mixer with a vacuum chamber. After that, the adhesive is injected into the mould under compressed air. Even using the centrifugal mixer, the perfect mixing of the adhesive in the syringe is quite difficult. Therefore, it is recommended that adhesives are pre-mixed with a cup type container in advance.

Adhesives of low viscosity are easy to make because open moulds can be used. The adhesives are filled into the open moulds after the mixing and de-bubbled by vacuum. If bubbles can be seen in the mould, they can be broken with a needle. Vacuum de-bubbling in this stage is not recommended because the adhesive can over-flow from the open mould. Keeping open-moulds horizontally is another important point because deviation in thickness of specimens may occur if the mould tilts.

After curing the adhesive in the mould, the cured specimen is removed from the mould. For the purpose, release agents should be used to coat the surface of the moulds. Another method is to use moulds made of materials difficult to adhere such as Teflon© or Silicone rubber. If adhesives have to be cured at high temperature, the material of the moulds has to be selected carefully because time delay of temperature rise is not negligible due to the heat conduction. Aluminum alloy is better than steel in terms of heat conductivity, and Teflon and Silicone rubber are very bad conductors. In addition, the total curing time of an adhesive should be

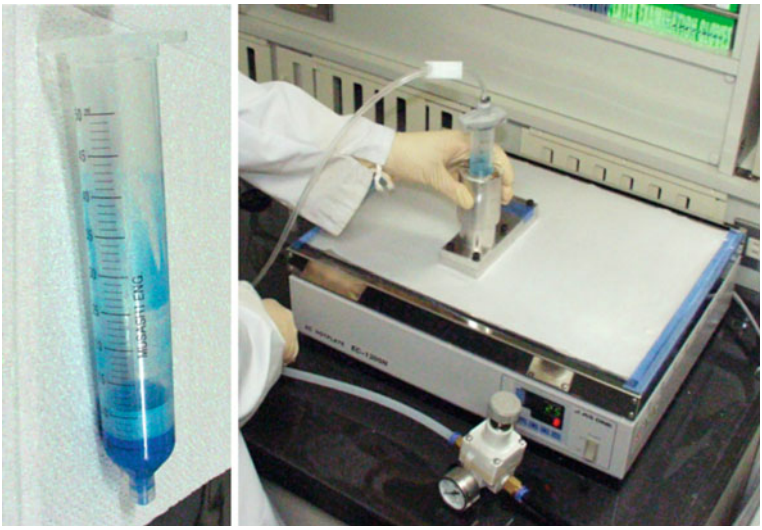

Fig. 5 Method to make specimens of cured adhesive using a syringe for centrifugal mixers (*Left*: syringe, *Right*: injection of adhesive to a mould by compressed air on a hotplate)

longer than the minimum time required by the maker of the adhesive considering the time delay of temperature rise.

When a mould has the specimen shape, the cured bulk can be used as a specimen after the de-moulding. Machining an adhesive bulk to the specimen shape is also possible. Punching with a blade which has the specimen shape is available for soft bulk adhesives. Hard bulk adhesives should be shaped with a milling machine.

As the final process of specimen preparation, the release agent on the surface of specimens should be removed with solvents because release agent can prevent water diffusion into the bulk adhesive, which leads to error of experiments on water absorption.

Methods to Prepare Specimens of One Part Type Adhesives

The specimen making procedure for one part type adhesives is similar to that of two part type adhesives except for the mixing process. If a one part type adhesive is provided with a syringe, the adhesive can be injected directly into a closed mould with a gun-type applicator. Since almost all one part type adhesives need to be cured at high temperature, some of them have a quite high viscosity at room temperature in order to prevent the adhesive from flow from the joints during the curing process at high temperature. Therefore, a quite high force should be applied to the gun-type applicator in this case. One of the recommendable methods for this situation is pre-heating of the adhesive by heating the syringe in a temperature

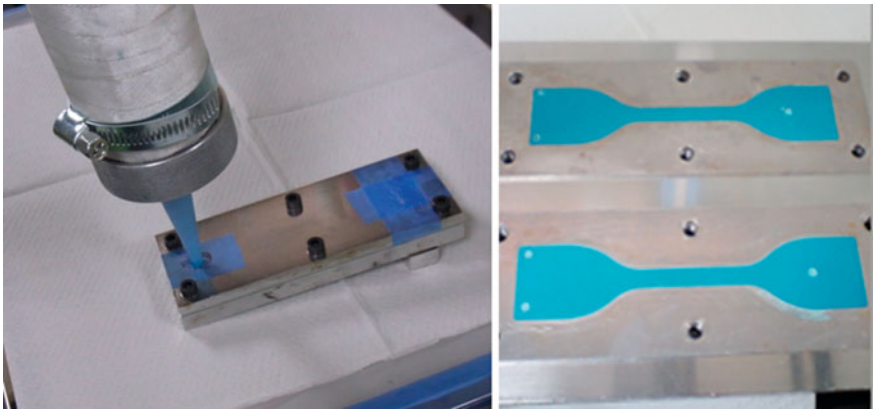

Fig. 6 Injection of adhesive resin into moulds (*Left*: A mould and a pneumatic applicator with an electric heater, *Right*: specimen of cured adhesive in moulds)

chamber in advance of its application. Another method is to use pneumatic applicators. For instance, the author has been using the gun-type pneumatic applicators shown in Fig. 6, which has a electric heater to keep the temperature of the syringe inside high.

Methods to Prepare Specimens of Other Special Adhesives

When bulk specimens that cure with moisture are made, open-moulds are necessary. For instance moisture cured urethane adhesives require moisture to cure, and a very long period should be consumed to obtain the total curing. Another type of moisture cured adhesives, cyanoacrylate adhesives, are difficult to make in bulk. To make the bulk specimen of the adhesive strong enough, special curing agents are often used.

Adhesives, which are cured by evaporation of chemical vapors, such as rubber contact adhesives or RTV silicone adhesives also need open-moulds to make bulk specimens. If vapor of solvents or acetic acid are evaporated, we have to be careful with the ventilation of the room in which the specimen preparation is carried out. For making thick specimens of these adhesives, quite long time should be consumed. A disadvantage to use open moulds is that it is difficult to make a surface flat specimen. To solve the problem, doctor-blades are sometimes used to flatten the open surface of specimens. RTV silicone adhesives have another problem in which release agents are not effective for the material and bulk specimens are difficult to separate from the moulds. The only solution is to use moulds made of Teflon.

Recently, the use of ultraviolet light cured adhesives has become popular, especially in electronics applications. To make bulk specimens of these adhesives, ultraviolet light irradiation to the adhesive in an open-mould (or closed moulds

having a transparent part such as glass on a side) should be carried out. The Ultraviolet light irradiation may cause a temperature rise that is not uniform, and this may lead to residual stresses, which cause bending phenomena in the bulk specimens. In this case, annealing at high temperature may be effective to reduce the residual stresses and deformation.

2.2 Experimental Method

2.2.1 Equipments for Exposure

To investigate the influence of water or vapor absorption in cured adhesive bulk specimens, some equipment is required to exposure the specimens. Immersion of specimens in water is easy to carry out and it can be done only with containers and temperature chambers. The containers have to have enough strength at the temperature at which an experiment is conducted. When a container cannot resist the temperature, the container deforms and vapor leakage may occur from the gap of the container and the cover that leads to the loss of water in the container. The use of hot water baths, as shown in Fig. 7, is another method to conduct the water immersion test of specimens. The type of water is not very influential. For instance, distilled water and tap water have not a big difference in absorption. Though only ultra pure water has quite different characteristics in absorption from other types of water, the characteristics become similar to the ordinary waters soon after specimens are immersed in it due to the diffusion of ions form the specimen into the water. Sea water has a smaller absorption than other types of water. However, since sea water can corrode metals, direct use in hot water baths is not suitable. In this case, containers including sea water and specimens should be immersed in tap water in the hot water bath.

For exposure to vapor, the humidity-temperature chambers shown in Fig. 7 can be used, or containers in which the specimens and a water cup are placed, as

Fig. 7 Temperature humidity chamber (*Left*) and hot water chamber (*Right*)

Fig. 8 Water immersion specimens in containers (*Left*: water immersion, *Right*: vapor exposure)

shown in Fig. 8. The use of humidity-temperature chambers is convenient to keep precisely the humidity and temperature. A problem of the humidity-temperature chambers is its expensive price. A humidity-temperature chamber has a heater, a water evaporator, and a condenser (cooler) inside the machine. The heater controls the temperature in the chamber, and the evaporator makes vapor. The humidity is controlled by the condenser cooling the vapor made with the evaporator. Though this system is complicated, the stable control of both temperature and humidity can be done only with this method.

In contrast, the method to use containers can be used only for saturated humidity at each temperature. This method has another problem that the vapor in the container can be over-saturated if the temperature slightly decreases and this condition causes water drops on the surface of specimens, by which the vapor exposure situation becomes equivalent to a kind of water immersion. It is a good idea to wrap specimens that should be exposed to vapor because humidity cannot reach the specimen surfaces if the specimens are in contact with each other or piled. Gauze or rough fabric is appropriate for warping the specimens.

2.2.2 Experimental Procedure of Water or Vapor Absorption

In order to obtain the water absorption of cured adhesive bulk specimens, the weight change of the specimen immersed in water should be measured. The change is small and just few percents of the total weight, so that precise weight measurement is indispensable. The specimen should be taken from water when the weight of the specimen is measured because precise measurement is difficult in water.

The experimental procedure of weight measurement is as follows:

(1) Keep the temperature and humidity in the room where the measurement is carried out stable, especially in winter season, as the atmosphere can be very

dry, and water may evaporate from the specimens. This phenomenon can lead to the weight decrease of the specimen. Therefore, humidity should be supplied with humidifiers.

(2) Remove the specimen from the water, wipe drops on the surface of the specimen with lint-less fabrics such as Kimwipe© (Kimberly-Clark. U.S.A.) or gauze because the weight of the drops is quite large and almost equivalent to the weight increase of the specimen by water absorption.

(3) Measure the weight of the specimen after removing the drops with an electric balance that has high resolution in weight such as 0.1 mg. The electric balance should have a wind shield, as shown in Fig. 9.

(4) After the weight measurement, immerse again the specimen into water and continue the immersion. Since the duration in which the specimen is out of the water should be short, the weight measurement has to be carried out as soon as possible. Repeat the cycle of the measurement and immersion to obtain the change of the weight with respect to time.

The saturated water absorption and the coefficient of water diffusion of a cured adhesive bulk specimen can be calculated from the weight change as a function of time obtained by the experiment shown above. The water absorption C of a specimen is given as:

$$C = \frac{M - M_0}{M_0} \tag{1}$$

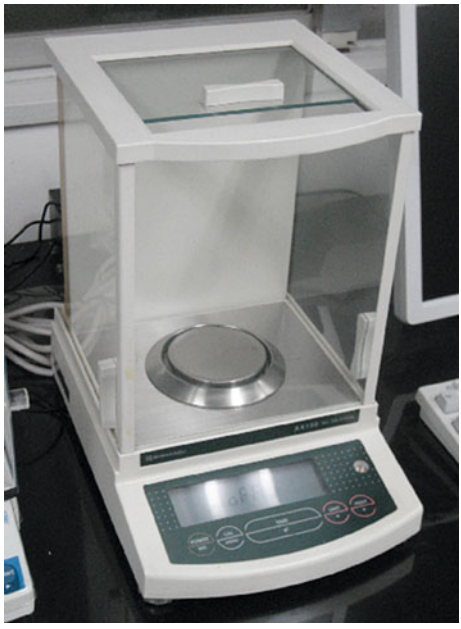

Fig. 9 Precise electric balance with a wind shield

where M_0 and M are the initial weight and the weight at each time respectively. Water distribution in a specimen can be determined based on the Fick's diffusion theory described with the following partial differential equation considering three dimensional diffusion

$$\frac{\partial C}{\partial t} = D\left(\frac{\partial^2 C}{\partial x^2} + \frac{\partial^2 C}{\partial y^2} + \frac{\partial^2 C}{\partial z^2}\right) \tag{2}$$

where x, y, and z denote the Cartesian coordinates, t represents time, and D is the diffusion coefficient of water. Now, we assume the condition that the thickness of the specimen is smaller than the length and width such as the water diffusion can be described as a one-dimensional phenomenon. For this case, Eq. 2 can be simplified to the following equation.

$$\frac{\partial C}{\partial t} = D\frac{\partial^2 C}{\partial x^2} \tag{3}$$

Assuming the surface of the specimen is always in the condition of water saturation, the solution of Eq. 3 can be given as Eq. 4.

$$\frac{C}{C_\infty} = 1 - \frac{4}{\pi}\sum_{n=0}^{\infty}\frac{(-1)^n}{2n+1}\exp\left\{\frac{-D(2n+1)^2\pi^2 t}{4l^2}\right\}\cos\left(\frac{(2n+1)\pi x}{2l}\right) \tag{4}$$

C_∞ and l represent the saturated water absorption and the half thickness of the media respectively. Therefore, the total water absorption of the whole specimen is obtained by integration of Eq. 4, as shown in Eq. 5.

$$\frac{M}{M_\infty} = 1 - \sum_{n=0}^{\infty}\frac{8}{(2n+1)^2\pi^2}\exp\left\{-D(2n+1)^2\pi^2 t/4l^2\right\} \tag{5}$$

where M_∞ is the final weight of the specimen fully saturated with water [4].

2.2.3 Strength Test

The influence of water absorption on the strength of cured bulk adhesives can be measured by strength tests of the specimen after water immersion or vapor exposure. The most ordinary specimen configuration is the dumbbell shape for tensile tests. However, since water diffusion in cured adhesive bulk specimens is low, the total saturation of a specimen needs long time. For acceleration of the water saturation, the use of specimens thinner than the dimension given by the standards is a good method.

The nominal stress applied to a specimen can be easily calculated by dividing the applied load by the cross sectional area of the specimen. In contrast, the strength of the specimen is often difficult to measure because some bulk adhesives become very soft and ductile. In this case, the usual methods to measure the strains

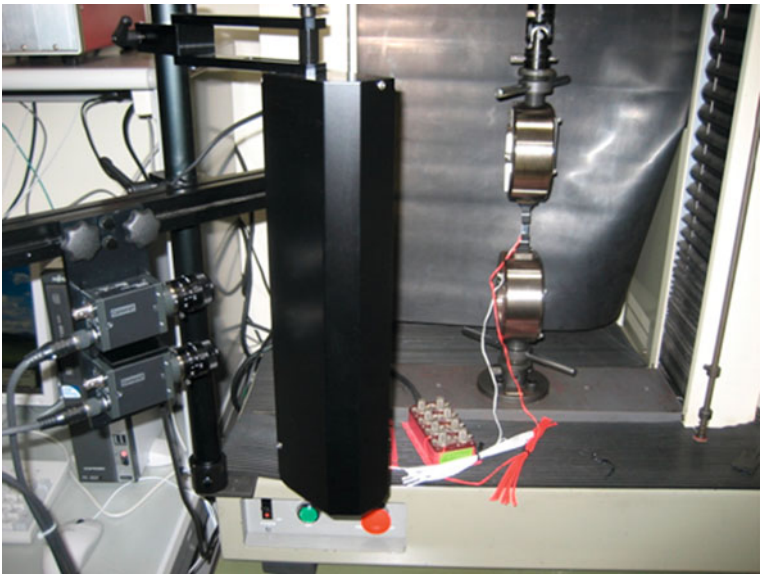

Fig. 10 Optical extensile meter

such as strain gauges cannot be used because the maximum range measured by the method is up to 10 %, although the maximum deformation of bulk adhesives absorbing enough water is often greater than the limit. In addition, just after water immersion, the surfaces of specimens maybe wet, which makes difficult the bonding of strain gauges to the specimens. Therefore, other types of strain measurement should be applied. The optical strain meter shown in Fig. 10 is one of the good methods that can be applied to ductile and wet specimens because non contact strain measurement is possible by this method. In addition, the dimension of a specimen can change very much after water immersion. Therefore, the initial dimension should be measured in advance of the water immersion or vapor exposure in order to calculate the nominal stress and the engineering strain.

3 Water Absorption in Cured Bulk Adhesives and Strength Change

3.1 Water Absorption and Diffusion in Cured Bulk Adhesives

Water absorption and diffusion in cured bulk adhesives have been investigated by many researchers. Rubbery polymers often exhibit water diffusion that can be predicted by the Fick's law [4]. However, glassy polymers may exhibit a slightly

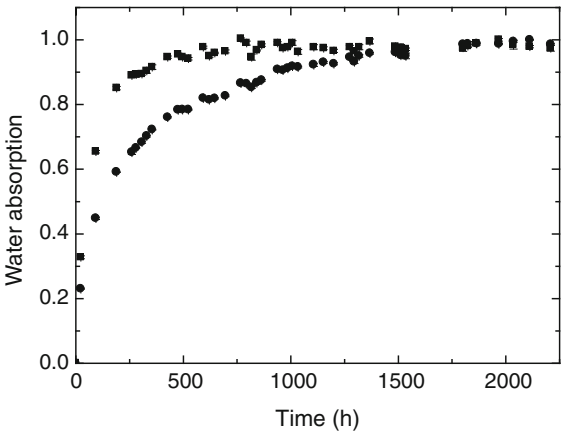

Fig. 11 Representative data of the relative mass uptake of an epoxy resin hardened with DDM (■) and the same epoxy resin hardened with ATU amine (●) during immersion into water at 23° C (water absorption is denoted as normalized value in which 1.0 represents saturation) [12]

different type of diffusion to some extents. This is called 'anomalous' or 'non-Fickian' behaviour [5]. For instance, Zhou and Lucas have done precise experiments on graphite/epoxy composites, and concluded that non-Fickian diffusion occurred [6]. Loh et al. have also re-considered the diffusion law of water in polymers based on the relaxation of molecular crosslink [7]. Bockenheimer et al. have carried out a variety of experiments on hydration of epoxy resin and found that epoxy systems have significant chemical and structural changes by hydrothermal loading even when they are in the glassy state [8]. Frenandez-Garcia and Chiang have examined a particle-filled epoxy adhesive in hygrothermal aging conditions and found a non-Fickian behaviour [9]. On the other hand, it has been reported that epoxy resin including diglycidyl ether of bisphenol-A (DGEBA) cured with triethylene tetramine (TETA) and phenolic resin show fairly good agreements to the curve predicted by the Fick's law [10, 11].

Typical adhesives have quite small water absorption. For example, DGEBA cured with TETA has 3.8 wt% of maximum water absorption at 25 °C, where diffusion coefficient is 1.6×10^{-13} m^2/s [1]. Even DGEBA is used, the values of maximum water absorption and diffusion coefficient change if different hardeners are used. 4,4′-Diaminodiphenylmethane (DDM) cured DGEBA has 4.1 wt% of maximum water absorption and 9.9×10^{-15} m^2/s of diffusion coefficient at 25 °C [1].

Figure 11 shows the water absorption curve of epoxy bulk adhesives cured with two types of hardeners: DDM and 2,4,8,10-Tetraoxaspiro[5.5]undecane-3, 9-dipropanamine (AUT amine) [12]. In this graph, the weight changes of the specimens are plotted with respect to water immersion time. The vertical axis indicates the non-dimensional water absorption calculated by Eq. 1 and the horizontal axis is the water immersion time. Almost all cured adhesives have low diffusion coefficient of water, and the movement of water in the adhesive layers in joints is very slow. For instance, assuming that the water ingress into the adhesive layer of a single lap joint occurs only along the edges of the joint, the water diffusion can be easily calculated using the finite element analysis, as shown in Fig. 12. As seen in the figure, the time to the total saturation at the center of the

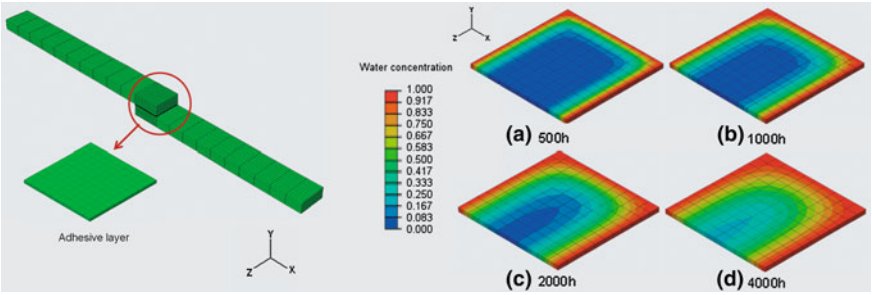

Fig. 12 Half finite element analysis model of a single lap joint bonded with epoxy adhesive (*Left*) and distributions of water absorption with respect to time (*Right*)

adhesive layer is very long. Therefore, very long time is necessary to investigate the strength of adhesively bonded joints that are totally saturated by water. Use of smaller specimens whose dimensions are reduced is a good method to shorten the time.

Unfortunately, the gravimetric analysis is quite difficult because the results highly depend on the performance of electric balance. In addition, the results are very sensitive to disturbance that comes from environmental conditions and human factors. Zanni-Deffarges and Shanahan have presented an alternative method to estimate the diffusion coefficient of an adhesive by considering changes in the elastic modulus to water ingress [13].

3.2 Characteristics Change of Cured Bulk Adhesives by Water Absorption

The strength of adhesively bonded joints subjected to hygrothermal conditions was measured and reported by many researches. However, the mechanical properties of cured bulk adhesives have rarely been reported because the experiments are not easy to conduct quickly after hygrothermal exposure. If the specimens are left in dry condition, absorbed water can be evaporated and the mechanical properties change soon. In addition, the specimen just after hygrothermal exposure may be wet and it is quite different to adhere strain gauges on the surface. Therefore, non-contact strain measurement methods have to be applied. Sugiman et al. have carried out tensile tests of FM 73 M OST adhesive (Cytec Industries Inc., U.S.A.) using cured bulk specimens, and showed that the adhesive became softer and more ductile with respect to exposure time [14].

Other characteristics of adhesive also tend to change by water absorption. For instance, it is reported that the modulus, damping and Tg of a sealant vary after water immersion [15]. Bordes et al. have tested a two-part epoxy after immersion

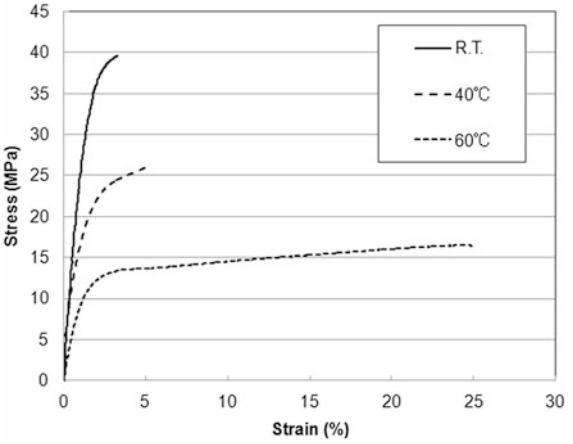

Fig. 13 Stress strain curves of a cured epoxy adhesive immersed in water for 2,000 h at different temperatures

to sea water and measure the modulus and yield stress, which degreased with respect to water content [16].

The stress strain curves of fully cured epoxy adhesive specimens, which is one part type for automotive applications and immersed in water at different temperatures for 2,000 h, is shown in Fig. 13. The Young's modulus and the maximum stress decrease and the maximum stress increases as the water temperature increases. Therefore, the water, especially hot water, absorbed by the specimens seems to play a roll of plasticizer. The dimensions of the specimens increased much by water absorption, and decreased to the original values by drying. The stress strain curves of these specimens with absorbed water can go back to the original curve by drying. Therefore, the phenomenon caused by water absorption is reversible, and no chemical reaction seems to occur. Of course, this reversibility is not general but special for the particular adhesive, another adhesive may exhibit irreversible recovery because chemical reaction and degradation by water, which is called ' hydrolysis', highly depend on the type of adhesive, i.e. the chemical composition of adhesive. In addition, hydrolysis of adhesive in water may occur gradually even at temperature much lower than Tg, and it may lead to the failure of adhesive after long period.

4 Conclusions

The influence of water absorption on the characteristics of cured adhesive has been shown in this chapter. Experimental methods for water immersion tests and the change caused by water absorption were also described. Almost all cured adhesives become softer by water absorption and the characteristics such as Young's modulus, maximum stress decreases, although the maximum strain can increase.

Water diffusion occurs slowly in cured bulk adhesive specimens. To obtain total saturation by water of the specimens needs a long time (a few month for specimens shown in Fig. 11). If experiments are done with shorter immersion times, the specimens are not saturated by water, and they have a distribution of water absorption inside them. It is quite difficult to predict the strength change of adhesively bonded joints by water absorption if data applied to the prediction are obtained by water immersion tests of bulk adhesive specimens that are not completely saturated. Therefore, in this case, the simulation of water diffusion not only in the adhesive layer in a joint, but also in the bulk adhesive specimens is important to understand what happens inside the joints.

Some adhesive has quite high resistance against hydrolysis and the characteristic change of the adhesive by water absorption exhibits reversibility. However it is not general. Another type of adhesive may cause hydrolysis and lead to degradation or decrease of mechanical properties.

References

1. Adams, R.D., Comyn, J., Wake, W.C.: Structural Adhesive Joints in Engineering, 2nd edn, pp. 211–220. Chapman & Hall, New York (1997)
2. Kinloch, A.J.: Adhesion and Adheisves–Science and Technology, pp. 353–362. Chapman and Hall, New York (1987)
3. da Silva, L.F.M., Adams, R.D.: Measurement of the mechanical properties of structural adhesives in tension and shear over a wide range of temperatures. J. Adhesion Sci. Technol **19**, 109–141 (2005)
4. Crank, J.: "The Mathematics of Diffusion", 2nd edn, pp. 47–49. Oxford University Press, Oxford (1975)
5. Crank, J.: "The Mathematics of Diffusion", 2nd edn, pp. 245–265. Oxford University Press, Oxford (1975)
6. Zhou, J., Lucas, J.P.: The effects of a water environment on anomalous absorption behavior in graphite/epoxy composites. Comp. Sci. Technol. **53**, 57–64 (1995)
7. Loh, W.K., Crocombe, A.D., Abel Wahab, M.M., Ashcroft, I.A.: Modelling anomalous moisture uptake, swelling and thermal characteristics of a rubber toughened epoxy adhesive. Int. J. Adhes. Adhes. **25**, 1–12 (2005)
8. Bockenheimer, C., Fata, D., Possart, W.: New aspects of aging in epoxy networks. II. Hydrothermal aging. J. Appl. Polym. Sci. **91**, 369–377 (2004)
9. Fernandez-Garcia, M., Chiang, M.Y.M.: Effect of hygrothermal aging history on sorption process, swelling, and glass transition temperature in a particle-filled epoxy-based adhesive. J. Appl. Polym. Sci. **84**, 1581–1591 (2002)
10. Brettle, J., Brewis, D.M., et al.: The interaction of water with an epoxide adhesive based on the diglycidylether of bisphenol-A and triethylene tetramine. Int. J. Adhes. Adhes. **3**, 189–192 (1983)
11. Brewis, D.M., Comyn, J., Tredwell, S.T.: Diffusion of water in some modified phenolic adhesives. Int. J. Adhes. Adhes. **7**, 30–32 (1987)
12. Iwasaki, R., Sato, C., Yamabe, H.: Characterization of the water diffusion pm the interphase of the epoxy resin adhesive/metal and the visualization of the water accumulation on the interphase using fluorescence. J. Jap. Adhes. Soc. **43**, 81–88 (2007)

13. Zanni-Deffarges, M.P., Shanahan, M.E.R.: Diffusion of water into an epoxy adhesive: comparison between bulk behaviour and adhesive joints. Int. J. Adhes. Adhes. **15**, 137–142 (1995)
14. Sugiman, S., Crocombe, A.D., Ashcroft, I.A.: Experimental and numerical investigation of the static response of environmentally aged adhesively bonded joints. Int. J. Adhes. Adhes. **40**, 224–237 (2013)
15. Giannis, S., Adams, R.D., Clark, L.J., Taylor, M.A.: Investigation of the water and fuel exposure characteristics of aircraft fuel tank sealants and the effect on their glass transition temperature. J. Appl. Polym. Sci. **108**, 3073–3091 (2008)
16. Bordes, M., Davies, P., Cognard, J.-Y., Sohier, L., Sauvant-Moynot, V., Galy, J.: Prediction of long term strength of adhesively bonded steel/epoxy joints in sea water. Int. J. Adhes. Adhes. **29**, 595–608 (2009)

Influence of Water on the Interface Properties

Hidetoshi Yamabe

Abstract It is generally observed that, while the locus of bonding failure of well-prepared metallic adhesive joints is invariably by cohesive fracture in the adhesive layer, after environmental attack it is by apparent interfacial failure between the adhesive and the metallic substrate. The environmental stability of the adhesive-substrate interface and of the oxide, invariably present on metallic substrates, needs therefore to be considered in detail. This chapter considers the service performance of adhesive metallic bonding upon exposure to aqueous environments and reviews the mechanisms of environmental attack and methods for increasing bonding durability.

Keywords Interface · Water · Adhesion durability

1 Introduction

Structural adhesive bonding for metallic materials is now established as an indispensable industrial technology for constructions of airplanes and cars. Nevertheless, several technological problems of strategic importance are left unsolved in this important industrial technology, the most important of which include:

(1) loss of adhesion strength in the presence of humidity;
(2) lack of non-destructive inspection technique for the adhered interface;
(3) Need for high temperature to achieve perfect solidification (curing) of the adhesive.

H. Yamabe (✉)
Sumitomo Metal Mining Co., Ltd, Tokyo, Japan
e-mail: Hidetoshi_Yamabe@ni.smm.co.jp

L. F. M. da Silva and C. Sato (eds.), *Design of Adhesive Joints Under Humid Conditions*, Advanced Structured Materials 25, DOI: 10.1007/978-3-642-37614-6_5,

Problem No. 1 is actually identical to the problem of adhesion of corrosion protective coating layers to substrates in humid environment. Loss of adhesion between layers is believed to be a result of the penetration and accumulation of water to adhered interface between two layers. In the case of a corrosion protective coating, surface modification of the metal substrate is practiced to inhibit undesired loss of adhesion between the coating layer and the metallic substrate in humid environments. In the present chapter, the fundamental aspects of degradation of structural adhesive bonding and its interface in humid environment are summarized. Available research results are also reviewed and are described.

2 Interface Degradation by Water in Metallic Adhesion

As mentioned above, loss of adhesion due to water penetration is a common problem in adhesive bonding for metallic materials and in corrosion protection coating. Based on the results of the work of Funke [1], the penetrated water goes to the metal-polymer interface and causes a decrease in adhesion. It has long been known that the corrosion protection performance of coating layer depends largely on the adhesion of the coating layer to the substrate surface. It is known empirically that a paint coating with superior adhesion would protect the substrate satisfactorily. That is, when the bonding between the coating layer and the steel substrate is tight so the penetration water into the interface is difficult, corrosion would not develop readily. But, when the bonding is weak, water tends to penetrate readily to the interface and, due to resultant water accumulation, under-coat corrosion is induced. Such water accumulation at the interface is known to take place at interface between binder and oxide pigment, dispersed in polymer, as shown in Fig. 1. This water accumulation is detected through comparison of weight gain in humid environment between pigment-dispersed coating layer and pigment-free reference coating layer [2]. Similar comparison in weight gain behavior was made between a free coating layer and a coating layer applied over Fe foil in humid atmosphere using high sensitivity electronic balance as shown in Fig. 2. In the initial stage of the exposure, weight gain of coated layer specimen (S) was smaller than that of the free coating layer specimen (F). But, as exposure period prolonged, two distinguishable types of weight variation patterns were observed as depicted in Fig. 3; in one type of weight variation pattern, weight of both specimen F and specimen S reached steady state levels holding heavier weight of F than that of S at any given time but, in another type, weight of S exceeded that of F after some time of immersion. Funke [2] called the time at which the inversion weight of F and that of S took place the “cross-over time”. The cross-over time might be appreciated as the moment at which the accumulation of the water at the coating layer/Fe foil interface would initiate.

Thus, the longer it takes for the emergence of the cross-over period, the better the corrosion resistance of the system. Significant correlation was found between cross-over time and corrosion protection performance [3]. It is interesting to note

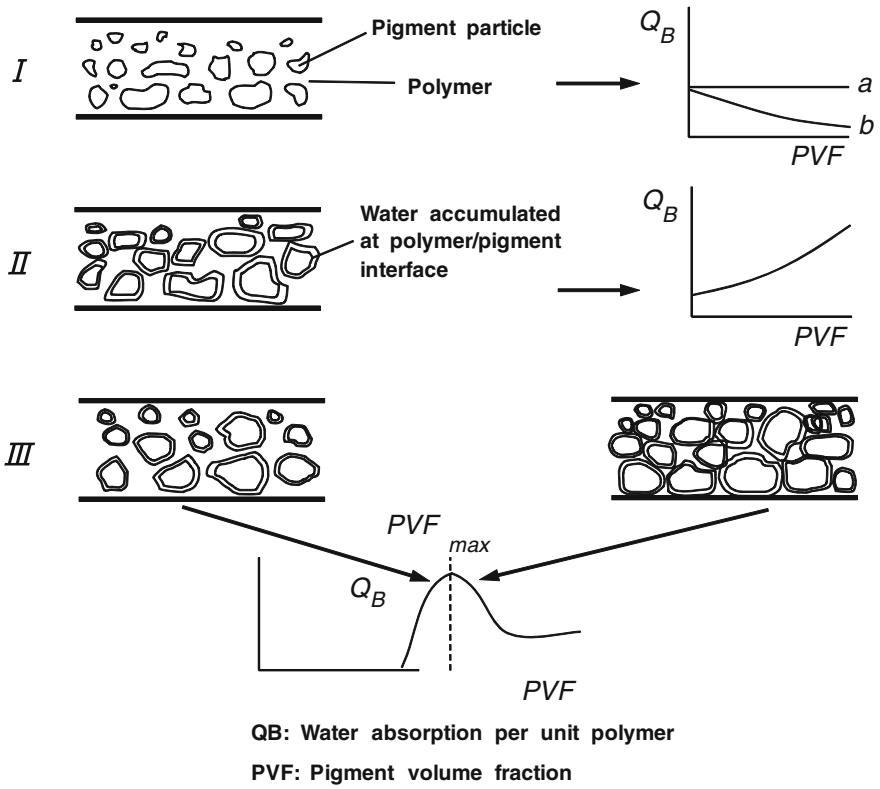

Fig. 1 Schematic accumulation process of water at polymer/pigment interface [1]

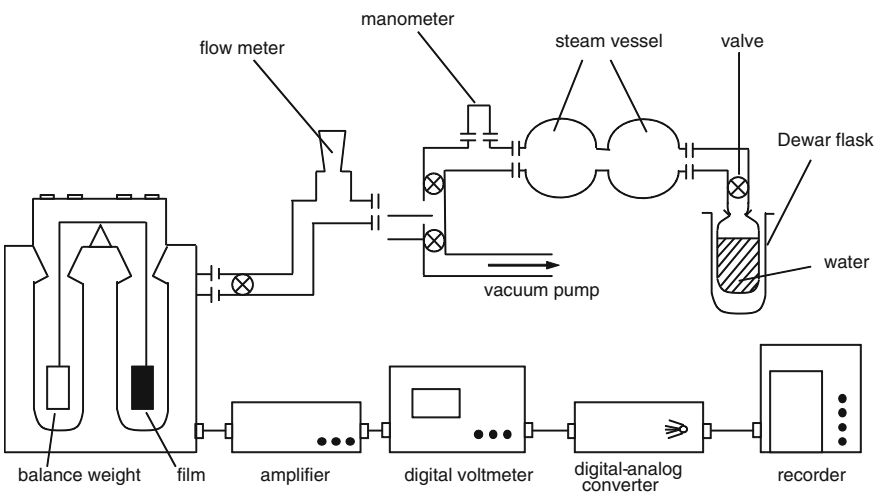

Fig. 2 Electronic microbalance for determination of water absorption [2]

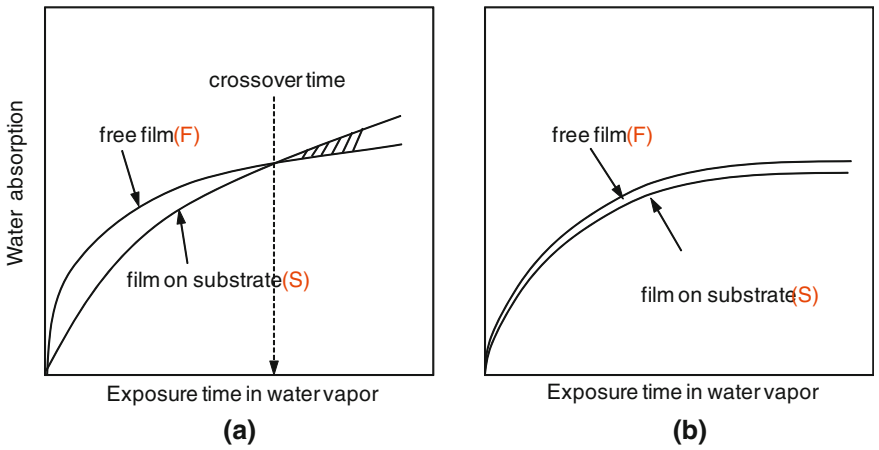

Fig. 3 Relationship between exposure time in water vapor and water absorption [2]

that cross-over time strongly influenced by bonding strength between coating and the substrate but not by the permeability of the coating layer to water. According to Christ and Haagen [4], cross-over time for epoxy-coated Al–Mg alloy specimen was strongly influenced by primary processing of the specimen surface prior to application of the coating layer. Long cross-over time and resultant enhancement of corrosion resistance was obtained by pretreatment formation of stable oxide layer which is not easily hydrated. As such, cross-over time seemed to be considered as significant factor indicative of effectiveness of pretreatment prior to coating layer application. Leidheiser and Funke [5] defined the water penetration to the coating layer/metal substrate interface as the loss of adhesion in humid environment. That is, coating system which would retain adhesion in humid environment for prolonged period might be considered as the system with improved corrosion resistance. In other words, good corrosion protective layer would adhere tightly to the substrate surface to retard accumulation of water at the coating layer/metal substrate surface. Similarly, tight adhesion would be essential condition for superior adhesive bonding for metallic substrates.

Water penetration process to the adhered metal substrate interface is analyzed on the basis of thermodynamics and reviewed by Gledhill and Kinloch [6]. They defined the work of adhesion as the energy required to the separate unit area of two phases forming an interface. In an inert medium the work of adhesion can be expressed by:

$$W_A = \gamma_A + \gamma_S - \gamma_{AS} \tag{1}$$

where γ_A and γ_S are surface free energies of the adhesive and substrate, respectively, and γ_{AS} is the interfacial free energy. In the presence of a liquid the work of adhesion W_{AL} is:

$$W_{AL} = \gamma_{AL} + \gamma_{SL} - \gamma_{AS} \tag{2}$$

where γ_{AL} and γ_{SL} are the interfacial free energies between the adhesive-liquid and substrate-liquid interfaces, respectively. The values of W_A and W_{AL} may be calculated from:

$$W_A = 2(\gamma_A^D \gamma_S^D)^{1/2} + 2(\gamma_A^P \gamma_S^P)^{1/2} \tag{3}$$

And

$$W_{AL} = 2[\gamma_L - (\gamma_A^D \gamma_L^D)^{1/2} - (\gamma_S^D \gamma_L^D)^{1/2} - (\gamma_A^P \gamma_L^P)^{1/2} - (\gamma_S^P \gamma_L^P)^{1/2} + (\gamma_A^D \gamma_S^D)^{1/2} + (\gamma_A^P \gamma_S^P)^{1/2}] \tag{4}$$

where γ^D and γ^P indicate the dispersion and polar force components of the surface free energy. The surface free energy can be obtained from contact angle and adsorption experiments [7], and some of their typical values are listed in Table 1.

For an adhesive-substrate interface in an inert environment, the work of adhesion, W_A, always has a positive value, indicating thermodynamic stability the interface. However, in the presence of liquid, the value of W_{AL} may have a negative value, indicating that the interface is now unstable and will dissociate. For example, in the case of epoxy/steel bonding system in water, the work of adhesion W_{AL} is -255 mJ/m^2, and this interface will dissociate. This thermodynamic approach reveals that high energy substrates, e.g. metal oxides, will be the most difficult materials to be epoxy-bonded with respect to ensuring a long service life in the presence of water.

It is not easy to give a general description of the metal/polymer adhesive interface because the pickled, chemically treated or mechanically processed metal surface reacts readily with oxygen of the atmosphere and is covered with an oxide layer (thickness approx. 1–3 nm). This oxide layer can react with water in the atmosphere and become hydrated. Thus, the metal surface in an atmospheric environment is covered with hydroxyl groups. The surface hydroxyl groups readily form hydrogen bonds with water of the atmosphere and so the metal surface at the air interface is covered eventually with several layers of water molecules.

Thus, for the polymer adhesive to form tight bonding with a metal surface, polar or active centers of the polymer must reach through layers of water molecules to the hydroxyl base connected to the metal surface to form a tight bond like a covalent bond or an ionic bond. Water is known to be a substance with dual

Table 1 Surface free energy of epoxy, steel and water [6]

	Surface free energy (mJ/m^2)		
	γ^D	γ^P	γ^T
Amine-cure epoxy	41.2	5.0	46.2
Fe_2O_3 (steel)	107	1,250	1,357
Water	22	50.2	72.2

γ^T (total surface free energy) = γ^D (dispersion force component) + γ^P (polar force component)

Table 2 Bonding type and bonding energy [8]

Bonding type	Bonding energy (k J • mol^{-1})
Ionic bond	590 ~ 1050
Covalent bond	63 ~ 710
Metallic bond	113 ~ 347
Dipole–dipole interaction	
Hydrogen bond containing F	≦42
Hydrogen bond not containing F	4 ~ 26
Dispersion force	0.08 ~ 42

nature exhibiting either an acidic or a basic property depending on the situation. Thus, when there is very weak acidic group or basic group alone present at the adhered interface, water would easily penetrate into the interface by reacting with the weak polar groups present at the interface and lead to eventual destruction of the adhered interface.

There is no doubt that improvement for adhesive performance is gained with enhanced chemical adhesion where optimized physical adhesion is realized. However, water would not penetrate the interface with primary bonding energy of 63 ~ 710 kJ/mol as shown in Table 2 [8]. And from energetic considerations it would be unlikely that water would not readily displace such a chemisorbed layer. Therefore, with the aim of promoting the formation of primary bonds for structural adhesive bonding for metallic materials, phenol resin and organometallic silane coupling agents are employed where desirable. In the following, features of chemical (primary) bond formation at metal/polymer interface and contribution of the chemical bond for the interface adhesion are reviewed.

3 Ionic Interaction Formation for Improving Adhesion in Humid Environment

Yamabe and Funke [9] reported that a thin layer of poly (acrylic acid) (PAA) improved adhesion in water. They showed that between carboxyl groups of PAA and steel the carboxylate anion (COO−) is formed between a coating layer and steel substrate as a result of the strong ionic interaction. For surface investigation, the reflection–absorption Fourier transform infrared spectroscopy (RA-FTIR) technique was employed, because the C = O stretching vibration of the free carboxyl group (1,710 $cm^{-1}\nu$ (C = O) str.) shifts strongly (1,550 $cm^{-1}\nu$ (C = O) asym.) if the carboxylate anion is formed. Sugama et al. [9] pointed out that two possible types of interaction exist, namely, the ionic interaction of the carboxyl group and surface hydroxyl group of Fe_2O_3 or salt formation as a result of the strong interaction between the carboxyl group and free ions in the steel surface. Only the former interaction will contribute to a good adhesion in humid environment.

3.1 Investigation by Reflection–Absorption Fourier Transform Infrared Spectroscopy

Yamabe [10] investigated the interface between PAA and several metallic substrates (Cu, Al, Fe, Sn). As a first step in the specimen preparation, the substrates were etched by 15 wt% aqueous HCl solution for 3 min at room temperature. After etching, the fresh surface were washed with deionized water and subsequently dried for 10 min at 80 °C. A thin PAA layer was applied by immersing the metal substrates in aqueous PAA solutions (0.1, 1.0 and 2.5 wt%) for 5 min at room temperature. After immersion, the substrates were left in the oven at 140 °C for 3 min, and served for surface and interface investigation. For adhesion measurements, a commercial grade of epoxy adhesive (type EP007, supplied by Cemedine, Japan) was applied on the treated substrates.

RA-FTIR spectra from various substrates showed that only in the case of Fe can apparent shift of the C = O stretching vibration be observed. Allara [11] has reported that the carboxyl group causes a redox reaction with Al and thereby a hydrogen atom and an aluminum carboxylate are formed. The C = O stretching vibration of aluminum carboxylate is assigned to a weak band at 1,620 cm^{-1}, which is also observed for Cu, but not for Sn.

3.2 Investigation by X-ray Photoelectron Spectroscopy

X-ray photoelectron spectroscopy (XPS) is employed as a powerful analytical method in the field of surface characterization. The spectra obtained by XPS contain chemical information. As the chemical environment of atoms changes, the photoelectron spectrum undergoes changes in peak shape, position or intensity. Since the wet adhesion is a fundamental local phenomenon involving only a few atom layers of substrate and polymer, the resulting data from the XPS studies should contribute toward an improved understanding of the chemical interaction at the interface of carboxyl groups and hydrated metal oxides.

High-resolution XPS examinations of O(1 s) region of various metal oxide substrates treated with PAA solution in various concentrations were carried out by Yamabe [10].

The investigation of the O(1 s) peak coming from Fe clearly indicates the presence of the carboxylate anion. In these spectra, attention was paid to the peak shifting of the carboxyl group in the bulk (PAA 2.5 %) to a lower binding energy at the interface regions (PAA 0.1 %). The decrease of binding energy of ~0.7 eV (Table 3) suggests two possible formations, as mentioned above, a salt complex having a $(COO^{-})_2\,Fe^{2+}$ group and a strong interaction. The former can result from carboxylate anions formed by the proton exchange between the carboxyl groups and active electrophilic metallic ions existing in the hydrated iron oxide.

Table 3 Ionic bond of metal substrates with carboxyl group [10]

Metal	Concentration of PAA (%)				Shift at the lowest PAA concentration
	0	0.1	1.0	2.5	
Al	531.3[a]	531.3	532.1	532.3	0.5
Cu	530.6[a]	531.5	532.0	532.7	1.2
Fe	530.3[a]	531.2	531.3	531.9	0.7
Sn	530.5[a]	531.8	531.8	531.8	0.0

[a] O1 s electron of metal oxide

On the other hand, carboxyl species diffused into the hydrated oxide layer can easily undergo strong ionic interactions with the polar hydroxyl groups of a hydrated iron oxide. Therefore, it is possible that another reason for the shift of the O(1 s) peak of the carboxyl group is due to the formation of hydrogen bonds which can be described by the Lewis acid–base interaction model (5):

$$-\mathrm{COOH} + \mathrm{HO} - \mathrm{Fe} \rightarrow -\mathrm{COO}^{-} \cdots + \mathrm{H_2O} - \mathrm{Fe} \tag{5}$$

This reaction can play an essential role in improving the interfacial forces and in converting the hydrophilic nature of the carboxyl and hydroxyl groups into a less hydrophilic one. This kind of interfacial structure could be responsible for the stability of an adhesive/metal interface in humid environment. A similar consideration is possible for other cases, such as Al and Cu, based on the results given in Table 3. On the other hand, the decrease of the binding energy was not observed in the case of Sn.

3.3 Adhesion in Humid Environment

The effect of exposure to water vapor at 70 °C on the strength of Cu, Fe and Sn-plated Fe epoxy adhesive joints was carried out by Yamabe [10], and the results are shown in Figs. 4, 5, and 6. A significant improvement in joint durability in humid environment was achieved by a thin layer of PAA for Cu and Fe (Figs. 4 and 5). However, for Sn this thin layer resulted in a poor environmental resistance in humid environment (Fig. 6).

A PAA aqueous solution as a polymeric adhesion promoter has several advantages: (1) since the reactive groups are connected by a polymer backbone which has a certain strength and entanglement, the polymeric layer needs to be only the thickness of a molecule; (2) a PAA layer with suitable thickness has the ability to relieve stress at the interface which is caused by differences in thermal expansion coefficient or curing shrinkage of epoxy resins; (3) PAA may be designed to dissipate energy and blunt an interfacial crack tip.

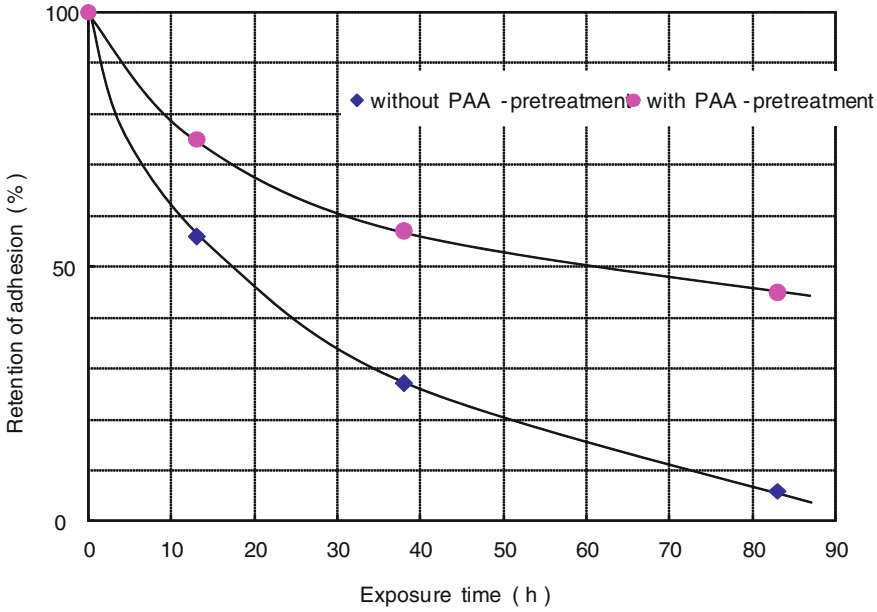

Fig. 4 Effect of vapor exposure on the strength of epoxy adhesive/Cu joints with a thin layer of poly (acrylic acid); 70 °C, 98 % relative humidity [10]

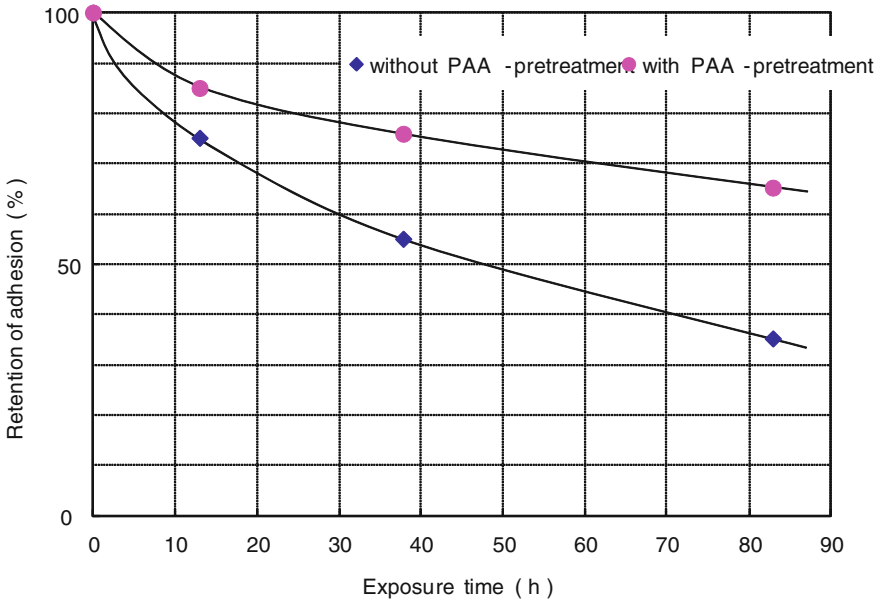

Fig. 5 Effect of vapor exposure on the strength of epoxy adhesive/Fe joints with a thin layer of poly (acrylic acid); 70 °C, 98 % relative humidity [10]

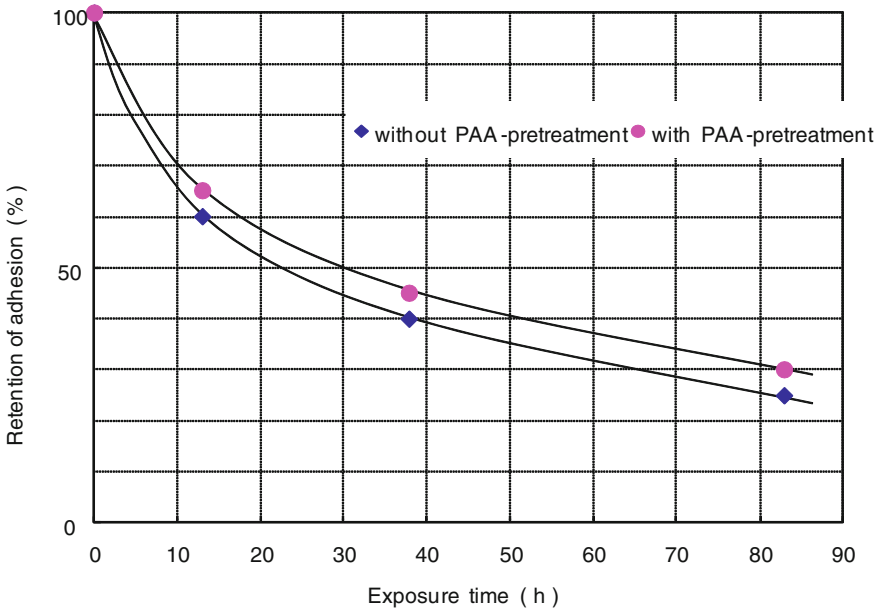

Fig. 6 Effect of vapor exposure on the strength of epoxy adhesive/Sn joints with a thin layer of poly (acrylic acid); 70 °C, 100 % relative humidity [10]

4 Covalent Bond Formation for Improving Adhesion in Humid Environment

It is well known that stainless steel exhibits inferior adhesion property to organic materials as compared with other metals such as cold rolled steels or aluminum [12–14]. From industrial viewpoint, it is important to develop a reliable adhesion promoter in humid environments.

Stratmann [15, 16] deposited a thiol compound layer over a steel iron surface electrochemically treated in advance to remove the oxide layer and he evaluated the bonding stability of the deposited thiol compound layer by means of XPS. He concluded that covalent bond was formed between the thiol and Fe.

Yamabe [17] investigated the effect of a thin layer of an electrolytic polymerized 1,3,5-triazine-2,4,6-trithiol monosodium salt (TTN) on the durability of an epoxy/stainless adhesive system If one of thiol groups is in the form of salt (SNa, SK), the triazine thiol compound is soluble in water. In this study, the stainless steel (SUS304) at the anode was pretreated electrolytically in 5 mM TTN of water at constant current. In this case, the current density was kept constant at 5 mA/cm^2 as indicated in Fig. 7.

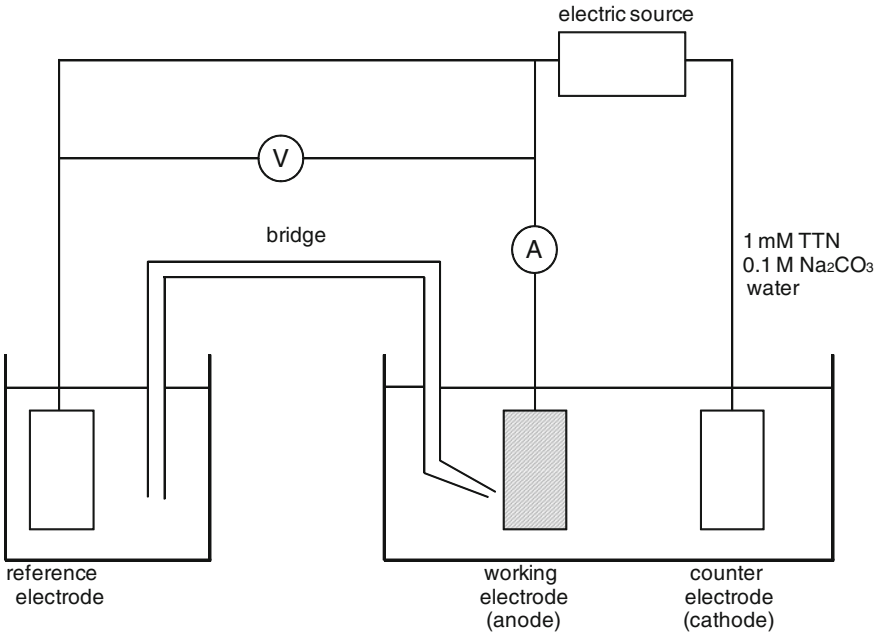

Fig. 7 Schematic diagram of an electrolytic polymerization system [17]

4.1 Investigation by RA-FTIR [17]

RA-FTIR spectra from the stainless steel treated with TTN are shown in Fig. 8. As seen in this figure, in the case of immersion only, the IR spectrum of TTN layer can not be observed. On the other hand, in the case of an electrolytic polymerization treatment, the apparent spectrum of the TTN layer can be observed. Absorbance at 1,510 and 1,460 cm^{-1} can be assigned to stretching vibration of –N = C < in triazine ring. Absorbance at 1,260 and 1,220 cm^{-1} is assigned to the stretching vibration of C–N in the triazine ring.

4.2 Investigation by XPS [17]

Figure 9 shows XPS high resolution examinations of S(2p) region from stainless steel, which was electrolytically treated with TTN. The peak at a binding energy of 162 eV indicates the presence of covalent bonding between thiol of TTN and the stainless steel surface. The kind of covalent bonding was also observed between n-decanthiol and mild steel by Stratmann [15, 16]. He came to the conclusion that thiol group has a relatively high reactivity with metal surface and form a covalent

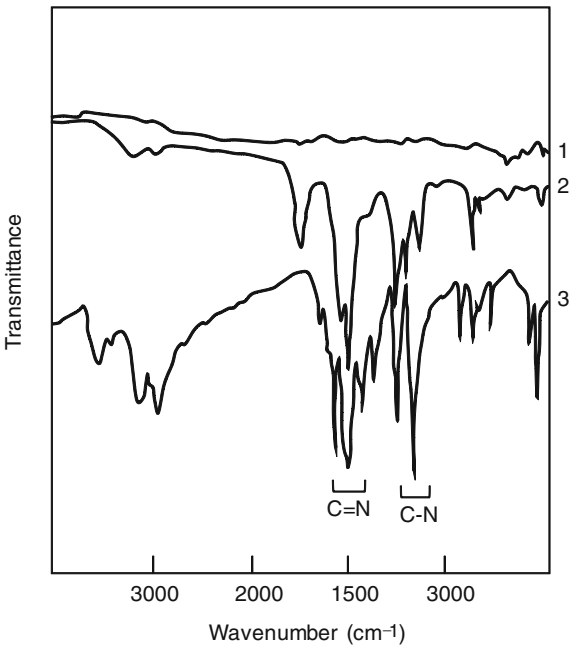

Fig. 8 RA-FTIR spectra from stainless steel (SUS304) treated with TTN [17], 1, immersion; 2, polymerized layer; 3.TTN crystal/KBr

bonding with metal, such as Fe. This kind of interfacial structure is responsible for the stability of TTN/stainless steel interface in wet environments.

4.3 Investigation by Static SIMS(SSIMS) [17]

It is evident from Fig. 10 that the surface of stainless steel contains traces of many elements. At 84 and 88 amu the molecular ion of CrS^+ and FeS^+ can be observed respectively. These two molecular ions may be associated with the covalent bonding between thiol of TTN and metallic elements of stainless steel such as Cr and Fe.

4.4 Adhesion in Humid Environment [17]

TTN pretreated specimens for lap joints were bonded using the epoxy (EPIKOTE828, supplied by Mitsubishi Chemical)/polyamide (Versamid 140, supplied by BASF) adhesive system. The effect of humidity exposure (70 °C, 98 %r.h.) on the adhesion strength is shown in Fig. 11. A significant improvement in adhesion durability can be achieved by the application of an electrolytic polymerization treatment with TTN.

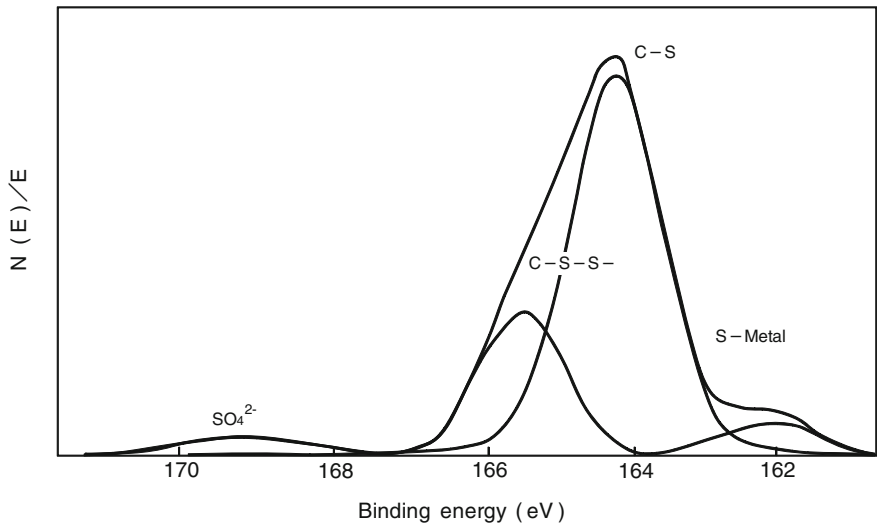

Fig. 9 S_{2P} XPS spectra from stainless steel (SUS304 2B) treated with TTN [12]

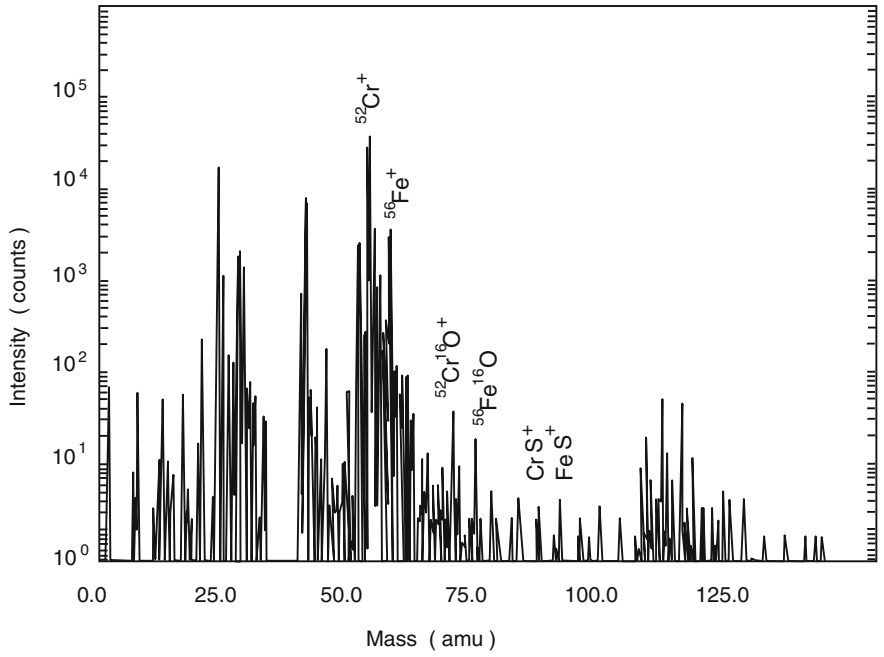

Fig. 10 Static SIMS spectra from stainless steel (SUS304) treated with TTN [17]

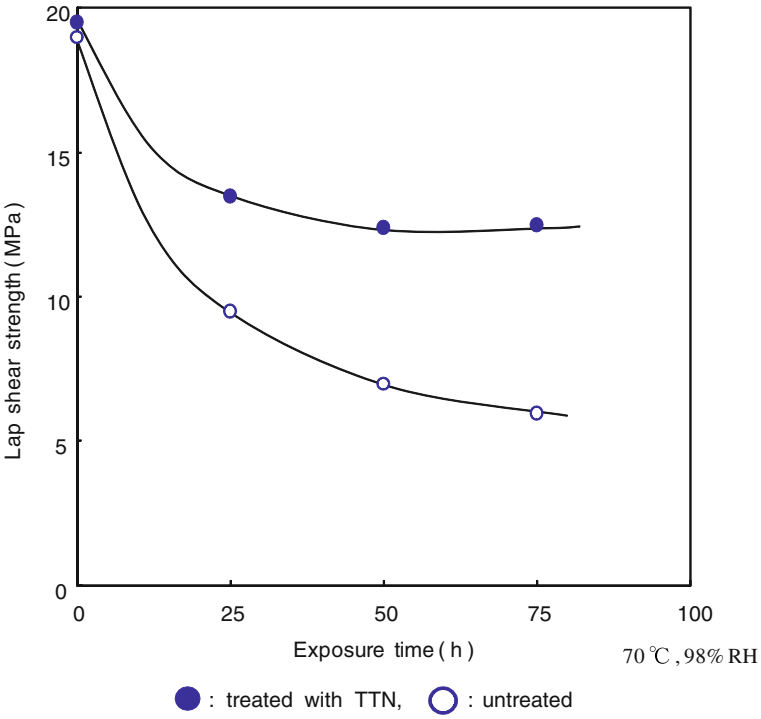

Fig. 11 Effect of TTN polymerized thin layer on the adhesion of stainless steel in high-humidity exposure test [17]

4.5 Polymerization and Adhesion Mechanisms of TTN on Metal Surface

The electrolytic polymerized TTN layer is an excellent pretreatment for stainless steel/epoxy adhesive bonding. The results of RA-FTIR, XPS and SSIMS gave information of the polymerized layer and its interface with stainless steel. Especially, the evidence of covalent bonding with stainless steel was observed from XPS analysis, which is responsible for the stability of TTN/stainless steel interface in humid environment. Figure 12 shows the proposed adhesion stabilizing mechanism in humid environment. For these reasons, an aqueous TTN solution with electrolytic polymerized layer could be employed for the purpose of adhesion promoter for metallic materials.

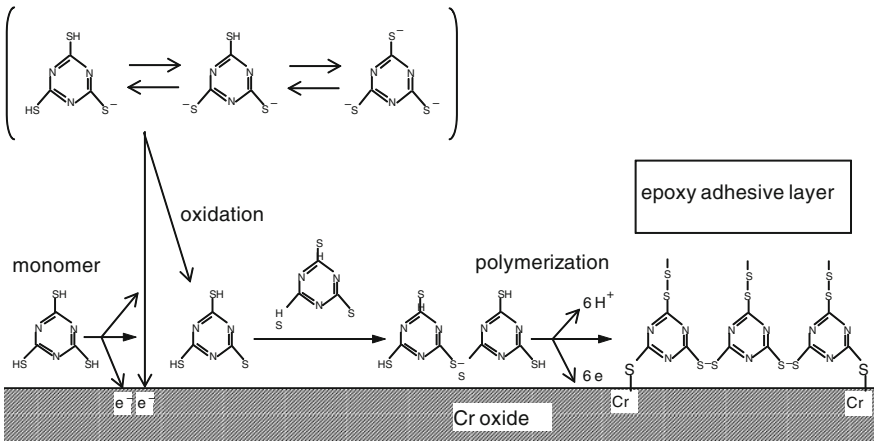

Fig. 12 Polymerization and adhesion mechanism of TTN on stainless steel [17]

5 Interface Destruction Models that Include the Effect of Water

Leidheiser and Funke [5] believe that the adhesion of polymeric materials to metal substrates may be lost due to disruption by water molecules of the covalent, hydrogen or polar bonds across the metal/polymer interface. The hypothesis offered below proposes a mechanical or hydrodynamic mechanism of disbonding. These two mechanisms are schematically illustrated in Fig. 13.

(1) Water disbonding is a consequence of the formation at the metal/adhesive interface of a discontinuous or, in some cases, continuous water film with several molecular layers in thickness. Loss of adhesion is a consequence of splitting of this layer upon the application of a force.
(2) Water moves through the adhesive by diffusion through the compact polymer phase or through capillaries or pores in the polymer.
(3) The driving force for directional water transport through the adhesive is diffusion under a concentration gradient. Osmotic force, temperature differences and chemisorptions or physisorption of water on the metal oxide at the interface are among the mechanisms that may lead to accumulation of water at the interface.
(4) The water accumulation at the interface is made possible by the presence of non-bonded areas of sufficient dimension to permit formation locally of an aqueous phase.
(5) The local water volume grows laterally along the metal/adhesive interface under the driving forces noted in (3) above. The lateral growth occurs because of continuing condensation of water molecules. Lateral growth is permitted because of the stress caused by water condensation and dynamic nature of metal/adhesive bonds at the interface.

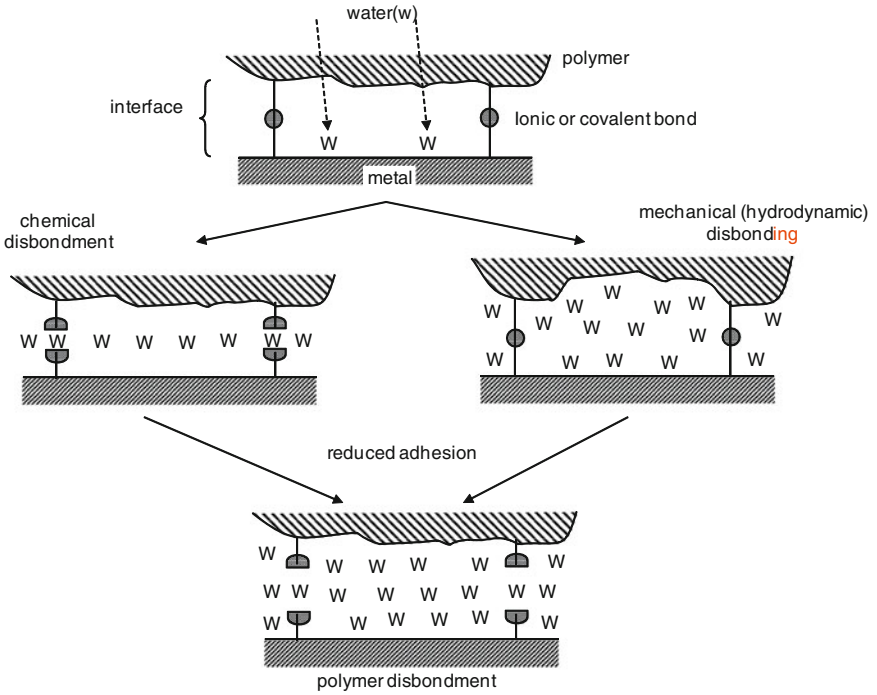

Fig. 13 Schematic representation of the mechanisms of adhesion reduction and water disbonding [5]

The strong affinity of metal oxide for water is also shown at oxide pigment/binder interface. In many cases, exposure of pigmented organic coatings to water results in the accumulation of water at the pigment/binder interface [1].

6 Conclusions

Water is aggressive environment for adhesive joints. The adhesive joints loose seriously their stability by exposure to humid environments. This environmental attack occurs mainly at the interface regions of the joints.

Disbonding of adhesive on the metallic substrate by water is caused by rupture of secondary bonds at the interface of adhesive and substrate, which was predicted from thermodynamic consideration.

The significance of formation of ionic bond and covalent bond for improved adhesion stability of bonded metallic materials in humid environment was discussed. Modeling for adhesive bonding advanced remarkably in recent years thanks to progress in surface analysis technologies.

References

1. Funke, W., Zorll, U., Murthy, B.G.: J. Paint Tech. **41**, 210 (1969)
2. Funke, W., Zatloukal, H.: Farbe + Lack **84**, 584 (1978)
3. Funke, W.: Farbe + Lack **84,** 865 (1978)
4. Christ, U., Haagen, H.: Surtech Berlin'87, 569
5. Leidheiser, H., Funke, W.: J. Oil Colour Chem. Assoc. **5**, 121 (1987)
6. Gledhill, R.A., Kinloch, A.J.: J. Adhesion **6**, 315 (1974)
7. Kinloch, A.J.: J. Mater. Sci. **15**, 2141 (1980)
8. Pauling, L.: Nature of the chemical bond, 3rd edn. Cornell University Press, New York, p. 10 (1960)
9. Yamabe, H., Funke, W.: Farbe + Lack **96**, 497 (1990)
10. Yamabe, H.: Prog. Org. Coat. **28**, 9 (1996)
11. Allara, D.L.: Polym. Sci. Technol. **12B**, 751 (1980)
12. Haak, R.P., Smith, T.: Int. J. Adhesion Adhesives **3**, 15 (1983)
13. Gaillard, F., Romand, M., Hocquaux, H., Solomon, J.S.: Surf. Interf. Anal. **10**, 163 (1987)
14. Bouquet, F., Cuntz, J.M., Coddet, C.: J. Adhesion Sci. Technol. **6**, 233 (1992)
15. Stratmann, M.: Farbe + Lack **99**, 16 (1993)
16. Stratmann, M.: Adv. Mater. **2**, 191 (1996)
17. Yamabe, H.: Improvement of wet-adhesion on stainless steels by electrolytic polymerization treatment with Triazine Thiol compounds. In: Sekine, I. (ed.) Advances in corrosion protection by organic coatings III, p. 134. The Electrochemical Society, Inc., (1997)

Prediction of Adhesion Strength for IC Plastic Package Under Humid Conditions—Fracture Mechanics Approach

Naotaka Tanaka

Abstract We introduce a new adhesion test method for IC molding compounds that can experimentally separate residual stress from adhesion strength. This chapter describes the dependence of the measured true adhesion strength of molding compounds on adherent materials, temperature, and moisture absorption. We also evaluate interface delamination in a moisture-absorbed package by considering the swelling of the molding compound caused by moisture absorption. The predicted interface delamination agrees well with experimental data for moisture-soaked IC packages.

Keywords Adhesion strength · IC plastic package · Interface delamination · Moisture absorption · Molding-compound swelling · Residual stress · Stress intensity factor

1 Introduction

Interfaces between the molding compound and the silicon chip or the lead frame within an Integrate Circuit (IC) plastic package are subjected to high stress due to cure shrinkage of the compound and thermal expansion mismatch between materials. The continuing growth in chip size and expanding use of packages for different applications further increase package stress, which sometimes causes interface delamination during temperature cycling tests and reflow soldering process. Reflow soldering processes have become common methods for mounting IC packages onto printed circuit boards. In these soldering processes, the package is heated to above 250 °C with a Pb-free solder. If the molding compound has

N. Tanaka (✉)
Hitachi Research Laboratory, Hitachi, Ltd., Hitachi, Ibaragi, Japan
e-mail: naotaka.tanaka.vt@hitachi.com

L. F. M. da Silva and C. Sato (eds.), *Design of Adhesive Joints Under Humid Conditions*, Advanced Structured Materials 25, DOI: 10.1007/978-3-642-37614-6_6,

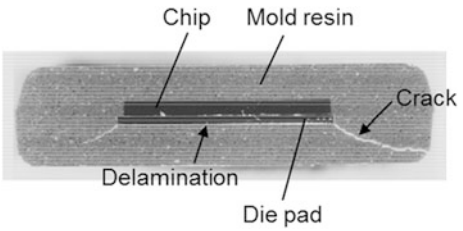

Fig. 1 Package cracking during reflow process [3]

absorbed moisture, package cracking may occur during reflow soldering as shown in Fig. 1. These cracks are caused by vapor pressure generated in the space between the die pad and the molding compound [1–3]. Since the prediction of interface delamination in a moisturized package was difficult, package design for preventing package cracking has been conducted by allowing for interface delamination [4–6]. However, using this design method has become more difficult as the package size has become smaller and thinner. A method for quantitatively evaluating interface delamination in a packaging that has absorbed moisture is therefore a critical issue in both the structural design and material selection for plastic IC packages.

Most conventional methods for measuring the adhesion strength of IC molding compounds apply tensile or shear loads to adhering specimens, and divide the obtained fracture loads by the adhesion area or length [7, 8]. These methods suffer from two problems in evaluating the adhesion strength of molding compounds. One is a stress singularity problem at the adhering edges where delamination occurs. The other is the effect of residual stress at the interface due to cure shrinkage of the molding compound and thermal expansion mismatch between the compound and the adherend. In the case of IC molding compound specimens, the ratio of residual stress to the adhesion strength is high. Since the degree of the these effects depends on the geometry, size, and material composition of the specimen, an adhesion strength that includes the effect of residual stress cannot be used for design. When the residual stress effect is negligible, a universal adhesion strength is obtained by analyzing fracture parameters at the adhering edges [9–11].

Therefore, in this chapter, adhesion test method for obtaining the "true" adhesion strength unaffected by residual stress is introduced [12]). The true adhesion strengths of molding compound were measured by this method under various condition such as adherend material, temperature and moisture-absorption. Predictions are made for both dry and moisture-absorbed packages.

2 Adhesion Test Method

The test method used in this section is shown schematically in Fig. 2 [12–14]. We perform 3-point bending tests using two-layer end-notched flexure (ENF) specimens composed of a molding compound and an adherend. The specimen is

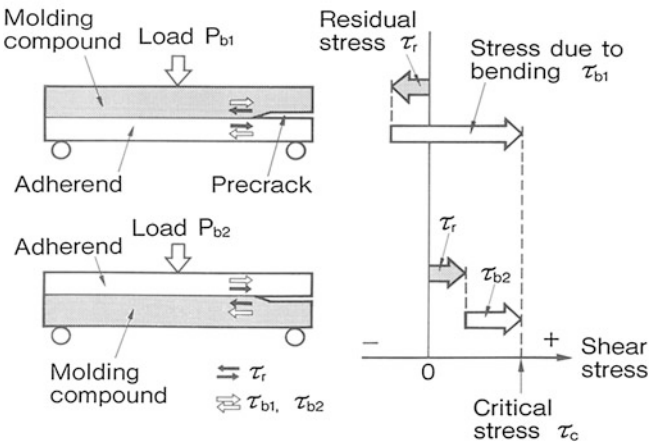

Fig. 2 Principle of the adhesion test method [12]

precracked at one end of the adhering interface, and this crack propagates along the interface. We measure the critical bending loads in both directions when the interface crack begins to propagate.

We assume here that the normal stress component at the interface in the front of the precrack tip is sufficiently small in comparison with the shear stress component. The specimen already contains a residual stress (τ_r), which is primarily a thermal stress caused by cooling from the molding temperature. The shear stress due to bending (τ_{b1}), acts in the direction which cancels residual stress (τ_r) and reverses the sigh of the stress. Delamination is supposed to start propagating when the sum of the stress reaches a critical stress. On the other hand, sum of the stress reaches the critical stress with a smaller load, because the shear stress due to bending (τ_{b2}), acts in the direction which increases the residual stress (τ_r). Therefore, the true adhesion strength (critical shear stress) (τ_c), can be estimated by arithmetically averaging the apparent strength (shear stresses) due to bending alone, τ_{b1} and τ_{b2}. These stress fields near the precracked tip caused by the critical bending loads P_{b1} and P_{b2} are expressed in terms of the stress intensity factor of the interface crack K_i [15, 16] as K_{ib1} and K_{ib2}. These apparent stress intensity factors can be calculated using a finite element method or beam theory [12]. We can obtain the "true" adhesion strength K_{ic}, which is not affected by residual stress, by calculating the average of K_{ib1} and K_{ib2}.

The adhesion strength were measured by using three kinds of epoxy molding compounds and two kinds of lead frame materials (Fe-42Ni and copper). The properties of these materials are listed in Table 1, and the specimen dimensions used for measuring adhesion strength are listed in Table 2.

Table 1 Measured material properties of molding compounds and lead frame materials [13]

Material	Young's modulus (GPa)	Poisson's ratio	Thermal expansion coefficient ($\times 10^{-6}$/ °C)	Glass transition temperature T_g (°C)
Compound A	16/1.3[a]	0.25/0.37[a]	15/65[b]	160
Compound B	24/1.1[a]	0.25/0.37[a]	12/48[b]	120
Compound C	20/1.2[a]	0.25/0.37[a]	8/38[b]	140
Alloy 42	147	0.3	5	–
Copper	115	0.35	17	–

[a] At 20 °C/at 200 °C
[b] Below T_g/above T_g

Table 2 Specimen dimensions [13]

Specimen	Molding compound thickness (mm)	Lead frame thickness (mm)	Span (mm)	Precrack length (mm)	Width (mm)
Type I	1.5	0.25	40	12 or 15	6
Type II	2.5	0.25	40	15	6
Type III	4	0.5	45	15	6

3 Measurements of True Adhesion Strength

3.1 Adherend Material Dependence

Adhesion strengths were compared for three adherend materials: Alloy 42, copper, and Sn/Ni-plated copper [8]. The results are shown in Fig. 3. For the apparent adhesion strength due to bending loads from the molding compound side and from the lead frame side, K_{ib1} and K_{ib2}, measurements results are plotted for individual specimens. The average of the apparent strength for both loading directions, which

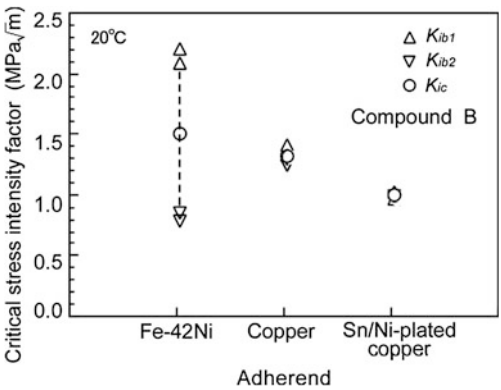

Fig. 3 Dependence of adhesion strength on adherend material [13]

gives the true adhesion strength K_{ic}, was taken after averaging the strength for each directions.

The difference between the true adhesion strength and the apparent strength, which corresponds to the initial residual stress, was large when Alloy 42 was used as the adherend material because of the large thermal mismatch between Alloy 42 and the molding compound (Table 1). Most adhesion strength measurements obtained with conventional methods [7, 8] correspond to the apparent strength K_{ib2}, which is lowered by residual stress. The conventional measurements therefore show much higher adhesion strength when copper is used than for Alloy 42. On the other hand, our new test method gave the opposite results, i.e., that the true adhesion strength when Alloy 42 is used is higher than that when copper is used.

3.2 Temperature Dependence

An example of the temperature dependence of the adhesion strength is shown in Fig. 4 [13]. The tested materials were compound A and Alloy 42. The apparent adhesion strength in relation to bending, K_{ib1} and K_{ib2}, and their arithmetic average, i.e., the true adhesion strength K_{ic}, are plotted in Fig. 4. Measurements were made after the specimens had been held in an isothermal chamber at the test temperatures for 10 min.

Both the true adhesion strength and residual stress decreased as the temperature was increased. However, the conventional test methods not only gave an incorrect value (difference between K_{ic} and K_{ib2}) but also the opposite tendency that the adhesion strength (K_{ib2}) slightly increased with increased temperature. The true adhesion strength at temperatures above the glass transition temperature was about an order of magnitude lower than at room temperature.

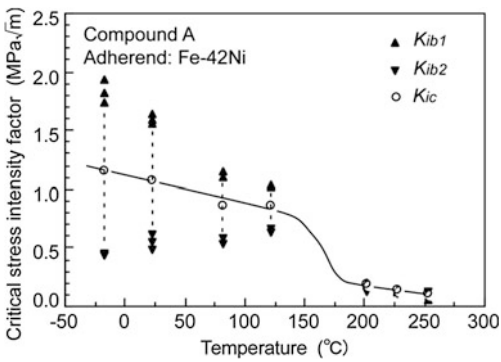

Fig. 4 Temperature dependence of adhesion strength [13]

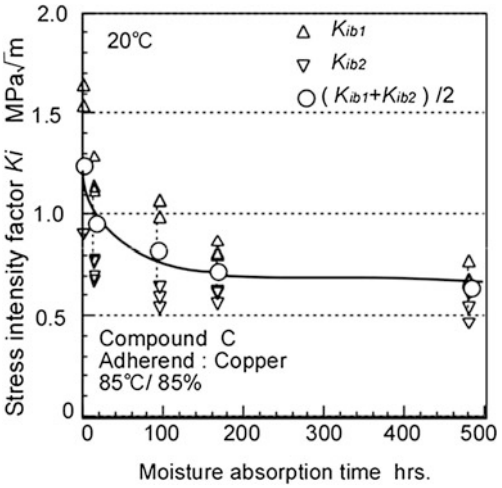

Fig. 5 Change in K_i due to moisture absorption [14]

3.3 Moisture Absorption Dependence

The relationships between the apparent adhesion strength K_{ib1} and K_{ib2}, the true adhesion strength, and the moisture absorption time is shown in Fig. 5 [14]. The tests were conducted after exposing as-mold specimens to the moisture condition, 85 °C and 85 % relative humidity. The tested materials were compound C and copper. Half of the difference between K_{ib1} and K_{ib2} corresponds to the stress intensity factor due to the residual stress. We can see that both the true adhesion strength and residual stress decreases as the moisture absorption time increased. In particular, the difference between K_{ib1} and K_{ib2} became almost zero when the moisture absorption time was 500 h in spite of a constant temperature. Since the hydroxy groups strongly interact with water [17], the molding compound swells due to moisture absorption. In order to confirm the effect of the swelling of molding compounds, the change in warpage of specimen due to moisture absorption were measured. Measurement results are shown in Fig. 6. We can see that the warpage of the specimen decreases as moisture absorption time increases. This result reveals that the molding compound expanded due to moisture absorption. Therefore, the change in residual stress at the interface is caused by the swelling of the molding compound.

4 Prediction of Interface Delamination in IC Packages

To evaluate the interface delamination in a moisturized package, the change in residual stress due to the swelling of the molding compound, in addition to the thermal stress and the stress due to cure shrinkage of the molding compound, must be considered. The effect of the stress caused by cure shrinkage is very small when

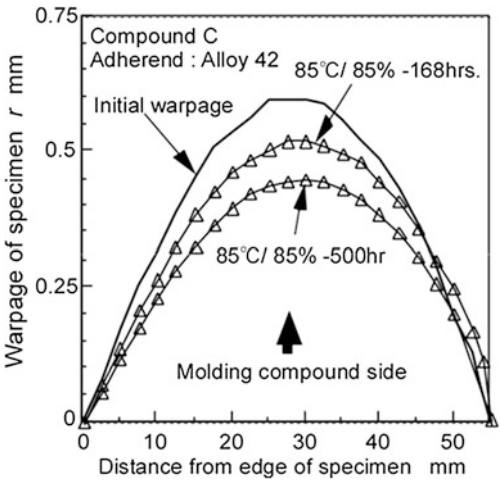

Fig. 6 Change in warpage of specimen due to moisture absorption [14]

the thermal expansion mismatch between materials is large. Therefore, interface delamination in a moisturized package can be predicted by simulating the thermal stress and the mismatch stress due to the swelling of the molding compound. The stress intensity factor K_{ip} of a moisturized package at high temperature is expressed by the sum of the stress intensity factor K_{ith} (due to thermal stress caused by heating from molding temperature) and the change in stress intensity factor ΔK_{irp} due to the swelling of the molding compound [14].

That is,

$$K_{ip} = K_{ith} + \Delta K_{irp}. \tag{1}$$

Interface delamination in a moisturized package occurs when K_{ip} exceeds the true adhesion strength after exposure to moisture, $K_{ic'}$.

Based on the results described above, we predicted the interface delamination in a moisturized package. Measurements of the true adhesion strength at high temperature and analyzed stress intensity factor [13] are plotted in Fig. 7. The K_{ith} curve (solid curve) in this figure indicates the stress intensity factor due to thermal stress in a dry package caused by heating it above the molding temperature. The data points (×) along this curve indicate the results of measuring the temperature at which delamination occurred in a dry package [13]. The interface delamination occurred at the temperature where the K_{ith} curve and the measured true adhesion strength K_{ic} curve intersect.

The K_{ip} curve (dotted curve) indicates the sum of stress intensity factor K_{ith} due to thermal stress and the change in stress intensity factor ΔK_{irp} due to swelling. The data points (×) along this curve indicate the results of measuring the temperature at which delamination occurred in moisturized packages [14]. We can see that interface delamination occurred at the temperature where the K_{ip} curve and the curve of the measured true adhesion strength after exposure to moisture, $K_{ic'}$, intersect. In this figure, the $K_{ic'}$ curve obtained with our test method is a

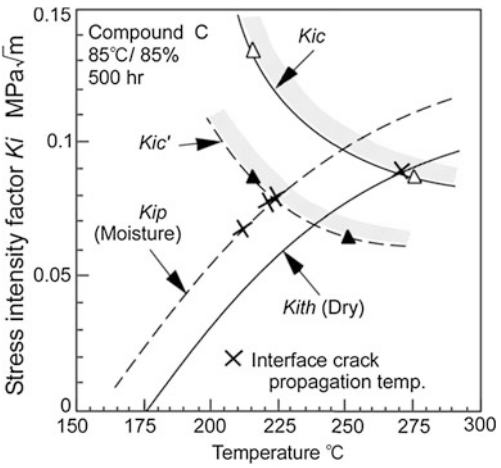

Fig. 7 Prediction of interface delamination in moisture-absorbed IC package due to thermal load [14]

quantitative strength that is not affected by thermal stress at high temperature and the stress due to swelling of the molding compound. This result suggests that the delamination occurrence temperature in a package exposed to moisture is greatly decreased because of both the decrease in true adhesion strength due to moisture absorption and the increase in mismatch stress due to the swelling of the molding compound. These results therefore confirmed that the delamination of the adhering interface in a moisture-absorbed package can be quantitatively predicted by considering the swelling of the molding compound.

5 Conclusions

We quantitatively examined the effect of adherend material, temperature, and moisture absorption of IC molding compounds on adhesion strength by using an adhesion test method for obtaining "true" adhesion strength. We used the true adhesion strength to predict interface delamination in a moisture-absorbed package by considering the swelling of the molding compound due to moisture absorption. The major results can be summarized as follows. First, conventional methods, which suffer from the effect of residual stress, give much higher adhesion strength for copper than for Alloy 42. On the other hand, our test method gives the opposite result, i.e., that the true adhesion strength for Alloy 42 is slightly higher than that for copper. Second, both the true adhesion strength and the residual stress decrease as the temperature is increased, whereas the conventionally measured apparent strength slightly increases with temperature because of the decrease in residual stress. Third, both the true adhesion strength and residual stress decrease as the moisture absorption time increases. The decrease in residual stress due to moisture absorption is caused by the swelling of the molding compound. Lastly, delamination of the adhering interface in an IC package exposed to moisture can be

predicted by comparing the measured true adhesion strength after exposure to moisture with the calculated thermal stress considering the increase in mismatch stress caused by the swelling of the molding compound.

References

1. Furusawa, I., Ishiguro, S., Nanbu, S.: Moisture resistance degradation of plastic LSIs by reflow soldering. In: Proceeding, 23th international reliability physics symposium, pp. 192–197 (1985)
2. Kitano, M., Nishimura, A., Kawai, R., Nishi, K.: Analysis of package cracking during reflow soldering process. In: Proceeding, 26th international reliability physics symposium, pp. 90–95 (1988)
3. Kitano, M., Nishimura, A., Kouno, R.: Development of damage detection system for surface mount package during reflow soldering. In: Proceeding, 41st electronic components and technology conference, pp. 615–620 (1991)
4. Bair, H.E., Boyle, D.J., Ryan, J.T., Taylor, C.R., Tighe, S.C., Crouthamel, D.L.: Thermomechanical properties of IC molding compounds. Polym. Eng. Sci. **30**, 90–95 (1990)
5. Nishimura, A., Tatemichi, A., Miura, H., Sakamoto, T.: Life estimation for IC plastic package under temperature cycling based on fracture mechanics. IEEE Trans. Compon. Hybrids Manuf. Technol. **CPMT-10**, 673–642 (1987)
6. Nishimura, A., Kawai, S., Murakami, G.: Effect of lead frame material on plastic-encapsulated IC Package cracking under temeperature cycling. IEEE Trans. Compon. Hybrids Manuf. Technol. **12**, 639–645 (1989)
7. Kim, S.: The role of plastic package adhesion in performance. IEEE Trans. Compon. Hybrids Manuf. Technol. **14**, 809–817 (1991)
8. Yoshioka, O., Okabe, N., Yamagishi, R., Nagayama, S., Murakami, G.: Improvement of moisture resistance in plastic encapsulation MOS-IC by surface finishing copper leadframe. In: Proceeding, 39th electronic components and technology conference, pp. 464–471 (1989)
9. Malyshev, B., Salganik, R.L.: The strength of adhesive joints using the theory of cracks. Int. J. Fract. Mech. **1**, 114–128 (1965)
10. Kinloch, A.J.: The science of adhesion, part 2 mechanics and mechanism of failure. J. Mater. Sci. **17**, 617–651 (1982)
11. Hattori, T., Sakata, S., Murakami, G.: A stress singularity parameter approach for evaluating the interfacial reliability of plastic encapsulated LSI devices. ASME J. Electron. Packag. **111**, 243–248 (1989)
12. Nishimura, A., Hirose, I., Tanaka, N.: A new method for measuring adhesion strength of IC molding compounds. ASME J. Electron. Packag. **114**, 407–412 (1992)
13. Tanaka, N., Nishimura, A.: Measurement of IC molding compound adhesion strength and prediction of interface delamination within package. ASME Adv. Electron. Packag. **EEP-Vol. 10.2**, 765–773 (1995)
14. Tanaka, N., Kitano, M., Kumazawa, T., Nishimura, A.: Evaluating IC-package interface delamination by considering moisture-induced molding-compound swelling. IEEE Trans. Compon. Packag. Technol. **22**(3):426–432 (1999)
15. Sawyer, S.G., Anderson, R.B.: Collocated interfacial stress intensity factors for finite Bi-material plates. Eng. Fract. Mech. **4**, 605–616 (1972)
16. Yuuki, R., Cho, S.B.: Efficient boundary element analysis of stress intensity factor for interface crack in dissimilar materials. Eng. Fract. Mech. **34**, 179–188 (1989)
17. Ogata, M., Kinjo, N., Kawata, T.: Effects of crosslinking on physical properties of phenol-formaldehyde Novolac cured epoxy resins. J. Appl. Polym. Sci. **48**, 583–601 (1993)

Prediction of Joint Strength Under Humid Conditions: Damage Mechanics Approach

Ian A. Ashcroft and Andrew D. Crocombe

Abstract Damage mechanics is a tool that is used to model the deterioration of a material under load, ultimately leading to failure. This is achieved through an association of the properties representing the mechanical behaviour of the material with the effects of loads acting upon it, often via a defined damage variable. The result is the representation of micro-damage as a reduction in the material properties in a damage or process zone in which the effects of the loads are great enough to initiate damage but less than that to cause complete failure. This will affect the response of the structure to further loading and hence damage mechanics is often applied in a progressive fashion. In this way, the method is able to predict not just the final failure load of a structure, but can also predict the state of damage and response to loading at any point in the load-time history. Two forms of damage modelling have been applied to adhesively bonded joints, those based on cohesive zone laws and those based on continuum damage mechanics, with the former being more common. These methods are now well developed and have been validated for a number of different adhesive joint types. Although there have been few applications of damage mechanics to environmentally aged joints to date, the published work indicates that it can be practically applied to the prediction of the effects of the environment, specifically moisture and temperature, on bonded joints and that the technique can offer certain advantages in the representation of the response of adhesives in these conditions compared with alternative analysis methods. Further development and validation of these techniques are still required and it would also be useful to develop simplified analysis tools based on the

I. A. Ashcroft (✉)
Faculty of Engineering, University of Nottingham, University Park,
Nottingham NG7 2RD, UK
e-mail: ian.ashcroft@nottingham.ac.uk

A. D. Crocombe
Department of Mechanical Engineering Sciences, University of Surrey,
Guildford, Surrey GU2 7XH, UK
e-mail: a.crocombe@surrey.ac.uk

L. F. M. da Silva and C. Sato (eds.), *Design of Adhesive Joints Under Humid Conditions*, Advanced Structured Materials 25, DOI: 10.1007/978-3-642-37614-6_7,

damage mechanics methods for the non-specialist designer. However, the results from the studies to date have clearly shown the potential of these methods.

Keywords Cohesive zone modelling · Continuum damage mechanics · Finite element analysis · Environmental ageing

1 Introduction

This chapter presents a review of the current state-of-the-art in the application of damage mechanics to predict the effects of the environment, specifically absorbed moisture, on the mechanical performance of adhesively bonded joints. Damage mechanics is a tool that is used to model the deterioration of the properties of a material under load, it can therefore be compared with the classic strength of materials and fracture mechanics approaches to predicting failure. The distinctive feature of damage mechanics is the representation of micro-damage, in a damage or process zone, as a reduction in the material properties in that zone. This will affect the response of the structure to further loading and hence damage mechanics is often applied in a progressive damage modelling context. In this context the method is able to predict not just the final failure load, as is commonly the case when using the strength of materials approach, but can also predict the state of damage and response to loading at any point in the load-time history. This is extremely useful for a number of reasons, including the development of in-service health monitoring of structures and understanding the mechanisms of failure and their dependence on environmental, geometric and load factors. Two different forms of progressive damage modelling have generally been used with adhesive joints; cohesive zone modelling (CZM), where the failure is localised along a plane and continuum damage modelling (CDM), where the failure can occur throughout the material. Whilst a full review of these branches of damage mechanics is beyond the scope of this chapter, an overview of the ideas relevant to their application to adhesive joints is presented in Sect. 2 and references are made to more complete works in the area.

In order to apply one of the progressive damage mechanics approaches discussed above to predict the environmental degradation in adhesively bonded joints, it must be integrated into a durability modelling framework. Current state-of-the-art environmental degradation modelling of bonded joints involves multi-physics finite element analysis combined with one of the progressive damage modelling approaches discussed above. Essentially, this involves three main steps. The first step is modelling moisture transport through the joint in order to determine the moisture concentration distribution in the joint as a function of time. The second step involves determination of the transient mechanical-hygro-thermal stress–strain state resulting from the combined effects of hygro-thermal and mechanical loads. The final step involves the incorporation of damage processes in

order to model the progressive failure of the joint and hence enable the residual strength or lifetime to be predicted. These steps may be either sequential or simultaneous and an outline of such a durability predictive framework is presented in Sect. 3.

The potential sites for damage modelling in an adhesively bonded joint include the adhesive, the interface (or interfacial region) and the adherend. The CZM approach is more directly applicable to interfacial failure and certain forms of adherend failure, e.g. delamination in fibre reinforced composite adherends, whilst the CDM approach is more relevant to cohesive failure within the adhesive layer. However, the CZM approach can also be used to model the cohesive failure of the adhesive and this has advantages, particularly in large structural models. CDM approaches can also be applied to typical adherend materials, such as aluminium or CFRP, however, this is beyond the scope of this chapter and will not be discussed.

Although damage mechanics is increasingly being applied to adhesives, to date there has been little application to modelling the effects of moisture on the adhesive. Section 4 will briefly review the application of damage mechanics to adhesive joints in general before focussing on those works specifically addressing the effect of the environment on joint degradation. It should be noted that the application of damage mechanics to predict the effects of cyclic loads on bonded joints is not discussed in the chapter as it is comprehensively covered in the chapter "Prediction of Joint Strength Under Humid Conditions with Cyclic Loading". Section 5 summarises the current state-of-the-art in applying progressive damage mechanics approaches to predicting the effect of the environment on adhesively bonded joints and considers where further advances in this area could be made in future work.

2 Damage Mechanics

In order to predict failure, a suitable failure criterion needs to be applied. The simplest form of failure analysis is to define failure when a suitable failure criterion has exceeded a permissible limit, e.g. when the equivalent von Mises stress has exceeded the yield stress of a material. However, this type of analysis is problematic when one has theoretical stress singularities, such as in adhesive joints, as the definition of failure becomes mesh dependent in a finite element analysis. Also, there is no indication of how the part eventually fails, what the sequence of events leading to failure is or what is the maximum load sustained. In order to predict this, progressive damage modelling is required. In ductile materials a progressive damage approach can be based on plastic yielding, with failure defined when a complete path of yielded material has developed between load points. In a brittle material a fracture mechanics approach may be more applicable where the propagation of a macro-crack through otherwise undamaged material is predicted by analysing the conditions for crack growth. However, in many modern engineering materials, particularly those exhibiting a variety of concurrent,

micro-mechanical failure mechanisms, neither of the methods above can fully capture the sequence of progressive damage under loading in a mechanistically accurate way. For example, a modern polymeric adhesive is a complex multi-phase material, typically comprised of a viscoelastic matrix with rubber particles for toughening, some form of filler particle and a carrier mat. Failure in such a material is complex and can involve the initiation and propagation of a macro-crack accompanied by a region ahead and/or around the crack exhibiting numerous forms of micro-damage such as particle debonding and cavitation, carrier mat debonding and micro-cracking and yielding of the matrix material. In such a system the state of the material after undergoing loading induced damage may be better represented by some form of damage mechanics. Progressive damage models are useful because of their capability to simulate the response of both ductile and brittle materials, including unloading of structures at a degraded stiffness, in contrast to elastic–plastic models, which assume unloading at the initial stiffness. The two main forms of damage mechanics applied to adhesive joints can be characterised as cohesive zone modelling, which is best applied when damage is limited to a zone directly ahead of a macro-crack, and continuum damage mechanics, where a more diffuse zone of damage is seen. These will be discussed in the sub-sections below.

2.1 Cohesive Zone Modelling

The cohesive zone model has been used increasingly in recent years to simulate crack initiation, propagation and failure. The cohesive zone model allows multiple cracks to be modelled and the direction of crack propagation need not be known in advance, however, cohesive zone elements need to be present at all possible crack paths.

The basis for cohesive zone models (CZM) can be traced to the works of Dugdale [1] and Barenblatt [2] who investigated techniques for simulating crack initiation and growth using cohesive laws. Fracture in many materials involves a process zone ahead of the macro-crack tip where initiation, growth and coalescence of micro-cracks or voids occur. This process zone can be modelled by assuming that the material along the crack path obeys the specified traction–separation law of an appropriate cohesive zone model. The implementation of models with traction–separation laws is quite simple and can be found in many commercially available finite element packages. As opposed to fracture mechanics, cohesive zone models consider fracture as a gradual phenomenon where material separation occurs along an extended crack tip or cohesive zone that is opposed by cohesive tractions. Damage ahead of the crack tip is represented by a decrease in these cohesive tractions, reaching zero at the crack tip. Consequently, cohesive zone elements only describe the forces that arise when a material continuum is being pulled apart and not the physical material.

Several forms of traction separation law have been proposed (e.g. [3, 4]) but they all exhibit the same general behaviour. As the cohesive surfaces start to separate, the traction increases until a critical value is reached (t_c) which

corresponds to a critical opening displacement (v_c). After this, the traction progressively decreases to zero, at which point there is a complete loss of (local) load carrying capacity and complete (local) separation occurs. This behaviour is true for both shear and normal tractions. A schematic illustration of bilinear, exponential and trapezoidal cohesive material models is shown in Fig. 1. The area under the traction–separation curve is termed the cohesive energy (G_c) and can be correlated with the critical strain energy release rate in fracture mechanics.

For a 3-dimensional system, the effective opening displacement, which is based on the relative displacements of the shear and normal components, is defined as:

$$v_e = \sqrt{v_n^2 + \beta^2 v_s^2 + \beta^2 v_t^2} \tag{1}$$

where v_n, v_s and v_t are the relative displacement components (one normal and two shear) and β is the shear-normal weighing coefficient, which is the ratio between the critical shear and normal tractions. The effective traction t_e is a function of the effective opening displacement and is reversible until the critical effective opening displacement has been reached. The exponential traction separation law is given by:

$$t_e = G_c \frac{v_e}{v_c^2} e^{-v_e/v_c} \tag{2}$$

And the bilinear traction separation law is given by:

$$\begin{aligned} t_e &= \frac{2G_c v_e}{v_m v_c} \quad if \quad 0 \le v_e \le v_c; \\ t_e &= \frac{2G_c}{v_m} \left(\frac{v_m - v_e}{v_m - v_c} \right) \quad if \quad v_c \le v_e \le v_m; \\ t_e &= 0 \quad if \quad v_e > v_m \end{aligned} \tag{3}$$

where v_m is the maximum opening displacement, seen when $t_e = 0$. The trapezoidal traction–separation law is similar to the bilinear law but with a constant traction section, requiring the definition of critical effective opening displacements, v_{c1} and v_{c2}, to signify the beginning and end of the plateau region

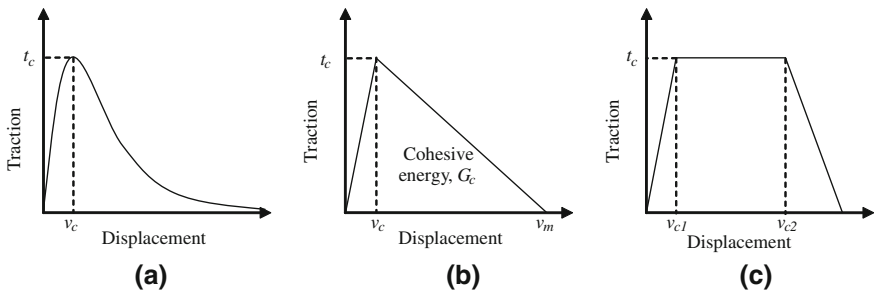

Fig. 1 Schematics of **a** exponential, **b** bilinear and **c** trapezoidal traction–separation laws

respectively. The shape of the traction–separation law is difficult to determine from experimental methods and is often assumed or simplified. The effect of the shape of traction–separation law is dependent on the nature of the problem including specimen geometry and material behaviour. The shape of the traction–separation law also influences the numerical performance of the solution and more convergence difficulties have been observed when using trapezoidal than bilinear traction–separation laws in a finite element analysis. Thus the selection of cohesive zone law should be based on all the above factors. Generally, a trapezoidal traction–separation curve is considered more suitable for ductile materials while a bilinear cohesive zone law is commonly used for brittle and composite materials.

2.2 Continuum Damage Mechanics

Continuum damage mechanics (CDM) has been researched extensively over the last few decades and has become the basis for models developed for phenomena such as fatigue, creep, brittle and ductile damage. Several works and reviews of continuum damage mechanics have been carried out, such as Kachanov [5], Kattan and Voyiadjis [6], Lemaitre and Desmorat [7], and these should be referred to for more complete coverage of the field. Continuum damage models are able to predict damage and failure in a variety of materials. A damage variable is used in continuum damage models to determine the degradation in material properties, such as elastic modulus. The damage variables used are of two types; the first type can predict the value of damage but does not characterise the damage itself, such as damage equivalent stress. The second type of damage variable is linked to some physical definition of damage such as porosity or relative area of micro-cavities. This type of variable is based on macroscopic material properties and its evolution is governed by a state equation. If several damage mechanisms occur in a material, each of them may be represented by an independent damage variable. The choice of damage variable is important as it characterises the type of failure and the practicability for engineering applications. Ideally, the selected damage criterion should be capable of an accurate continuum representation of the micro-damage features seen in the material and still be simple enough to make the model applicable to engineering applications.

Damage in a material can be considered in relation to a representative volume element (RVE) which is large enough compared to the damage induced material defects to enable material properties in the element to be represented by homogenized variables, but small enough to enable the representation of spatial variation in damage in a loaded structure. Kachanov [8] proposed a scalar damage variable, D, in such an element for the case of isotropic damage, given by:

$$D = \frac{\delta S_D}{\delta S} \tag{4}$$

where δS and δS_D are the cross section of a plane cutting the RVE and area of microcracks and microvoids on the plane respectively. $D = 0$ in the undamaged state, and $D = 1$ when failure has occurred. If several mechanisms of damage occur they may be represented by a number of different damage variables and if the damage is non-isotropic the variable D in Eq. (4) will be dependent on the direction of the normal of the plane of intersection, in which case a tensorial damage variable may be defined. Damage within the RVE, as defined above, will decrease the load bearing capacity of the element and this was described by Rabotnov (9) in terms of an effective stress. For the case of isotropic damage and uniaxial loading an effective stress may be defined as

$$\tilde{\sigma} = \frac{\sigma}{1 - D} \tag{5}$$

In practice, the determination of the density of microdefects is often difficult and it is more convenient to represent damage in terms of the effect of the damage on a measurable parameter, such as elastic modulus. Hence for the case of isotropic damage and uniaxial loading, damage may be related to an effective elastic modulus $(\hat{E})$ by

$$D = 1 - \frac{\tilde{E}}{E} \tag{6}$$

A general framework for damage models was provided by Lemaitre and Desmorat [7] based on the thermodynamics of irreversible processes. This involved the definition of state variables to represent damage, a state potential and a dissipation potential, to derive the laws of evolution of the state variables. A unified isotropic damage law was proposed in which the damage evolution rate above a critical value of the plastic strain energy, p_D, was defined by

$$\dot{D} = \left(\frac{Y}{S}\right)^s \dot{p} \tag{7}$$

where Y is the energy density release rate and S and s are temperature dependent material parameters. The energy density release rate for isotropic damage can be derived from the state potential for isotropic damage as:

$$Y = \frac{\tilde{\sigma}_{eq}^2 R_v}{2E} \tag{8}$$

where $\tilde{\sigma}_{eq}$ is the effective von Mises stress and R_v is a triaxiality function, given by:

$$R_v = \frac{2}{3}(1 + \upsilon) + 3(1 - 2\upsilon)\left[\frac{\sigma_H}{\sigma_{eq}}\right]^2 \tag{9}$$

where υ is Poisson's ratio and σ_H is the hydrostatic stress. Substitution of (5) into (8) gives:

$$Y = \frac{\sigma_{eq}^2 R_v}{2E(1-D)^2} \tag{10}$$

A limiting value of damage, D_c, was also suggested to represent the initiation of meso-cracking. The source of the plastic strain, p, in Eq. (7) enables this approach to be applied to the ductile, creep, fatigue and quasi-brittle damage of materials.

The Gurson, Tvergaard, Needleman (GTN) model takes a micromechanical approach to the characterisation of damage and failure. Gurson [10] proposed a model to describe the growth of microscopic voids in materials by plastic deformation and derived a set of modified constitutive equations for elastic–plastic materials with a damage variable, f_v, representing the volume fraction of voids. Needleman and Tvergaard [11] modified this model to include the behaviour of void initiation and coalescence. In the modified model, the damage is represented by an effective void volume fraction, f_v^*, given by:

$$f_v^* = \begin{cases} f_v & if \quad f_v < f_c \\ f_c + \left(\frac{f_u^* - f_c}{f_F - f_c}\right)(f_v - f_v) & if \quad f_v \geq f_c \end{cases} \tag{11}$$

where f_c represents a critical volume fraction for the fast coalescence of voids, f_F is the volume fraction at failure and $f_u^* = 1/q_1$. The parameters q_1 and q_2 were introduced to improve the Gurson model at small values of void volume fraction and can be considered as material constants. Experimental studies have shown that values of $q_1 = 1.5$ and $q_2 = 1$ are accurate for solids with sporadic spaced voids. The yield criterion for the GTN model is given by:

$$F = \frac{\sigma_{eq}^2}{\sigma_s^2} + 2q_1 f_v^* cosh\left(\frac{3q_2\sigma_H}{2\sigma_s}\right) - 1 - \left(q_1 f_v^*\right)^2 \tag{12}$$

where σ_s is the yield stress.

Zaïri et al. [12] used the GTN model coupled with a modified viscoplastic material model to investigate the mechanical response of rubber toughened polymethylmethacrylate (PMMA) at room temperature and compared the results with experimental tests to produce a quantitative agreement with experimental observations. Some of their experimental observations also included stress whitening caused by cavitation of rubber particles. Dean and Mera [13] carried out extensive work on a rubber toughened propylene-ethylene copolymer containing about 17 % by weight of filler and introduced a modification of the GTN model to account for the cavitation of rubber particles. This phenomenon is usually visible as stress whitening in the failure of rubber toughened plastics. They also produced a detailed framework for the determination of the model material parameters through experimental testing. They modified the GTN model by the introduction of a void nucleation function relating the void fraction to the applied volumetric strain. The modified criterion allows for the changing composition of the polymer matrix during void nucleation. The model was shown to predict the stress/strain

response of bulk adhesives in tension and compression, and adhesively bonded tensile-butt joints.

3 A General Framework for Durability Modelling

In the durability modelling of adhesively bonded joints it is usually the case that it is the combined effects of moisture, heat and mechanical loading that are most damaging and, hence, these should be included explicitly in any mechanistically based durability model. Figure 2 shows the framework for a general approach to the durability modelling of adhesive joints based on these effects. The modelling can be considered in three main stages. The first is the determination of moisture and temperature distribution within the joint from diffusion and thermal analyses (although often a uniform temperature distribution can be assumed). The second is an evaluation of the combined effects of moisture, temperature and applied mechanical loads in a hygro-thermo-mechanical analysis. The final step is the application of a failure criterion to the mechanical model, which can be through the application of a progressive damage model. This section will outline the first two steps described above whilst Sect. 4 will discuss the third step. A more

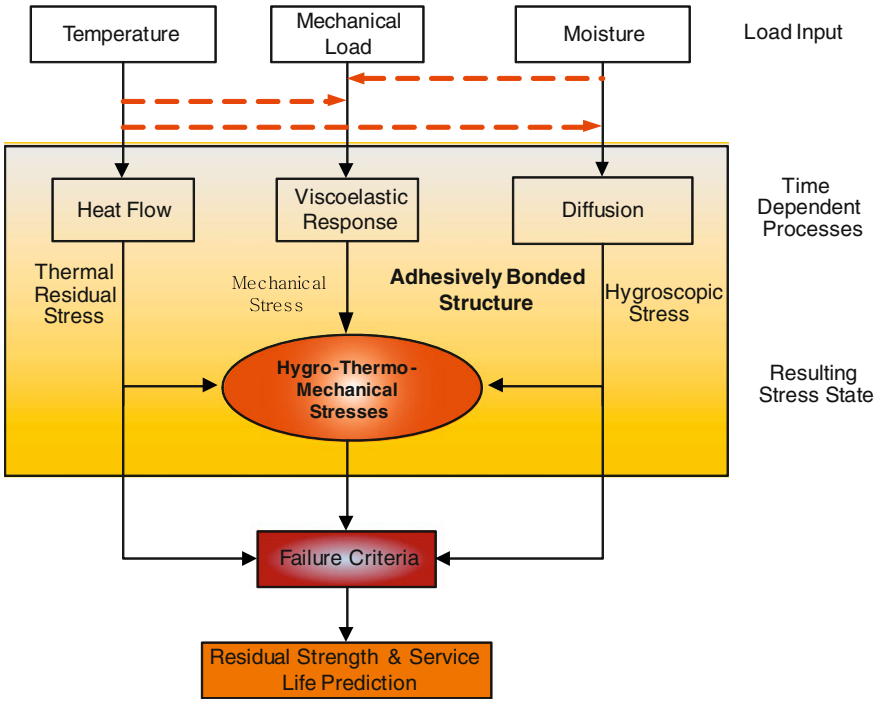

Fig. 2 General framework for the durability modelling of adhesively bonded joints

Table 1 Comparison of heat conduction and moisture diffusion

Field problem	Unknown (T) (potential)	Material constant (K_T)	Load (Q)
Heat conduction	Temperature	Thermal conductivity	Thermal load
Diffusion	Moisture concentration	Diffusion coefficient	Moisture source

detailed discussion of the elements of the various steps involved in this durability model can be found in [14, 15]. Although this model can be realised using analytical techniques for simple cases, a more powerful method of implementation is via finite element (FE) analysis.

The governing equations for Fickian diffusion and heat conduction are both forms of the quasi-harmonic equation, which can be applied to a general class of stochastic transport problems in which the rate of transport is proportional to the concentration gradient. This class of problem can be solved using the general field solvers available with many commercial finite element packages. A comparison of the parameters used in thermal conduction and diffusion problems is given in Table 1. It can be seen that using the analogues in Table 1, similar techniques can be used to analyse both thermal and diffusion problems in adhesively bonded joints. Thermal conduction within a joint is generally much faster than moisture diffusion, hence, it is generally the case that a steady state thermal analysis is sufficient whereas a transient diffusion analysis is required unless the joint has been held under steady state conditions for an extended period of time, which is unlikely in practice. Unfortunately, there are a number of complications that may affect the modelling of moisture uptake in an adhesively bonded joint using the technique described above. Firstly, uptake in adhesively bonded joints is often non-Fickian [16, 17], especially at high activity levels. Secondly, there may be accelerated moisture uptake at the interface (or in an interfacial region) between the adherend and adhesive. Thirdly, the rate of absorption and desorption of moisture in an adhesive can be moisture history dependent [18]. Finally, the substrate may also absorb moisture, introducing an added complexity to the diffusion path. These issues are discussed in more detail in Ashcroft and Comyn [15]. An example of the calculated moisture distribution in an adhesive joint can be seen in Fig. 3. In this case the adherends are aluminium which means that moisture is absorbed only from the edges, giving a minimum diffusion path of approximately 6.5 mm, which is half the overlap length plus fillet. As expected the adhesive at the edges is saturated. However, it is perhaps surprising, given that this is a short overlap joint subjected to immersion in water at a relatively high temperature, that there is a large central portion of the adhesive that is still less than 20 % saturated. This gives an indication of the length of time required to reach moisture equilibrium in adhesive joints. Of course, in most cases adhesive joints in service will be subjected to fluctuating environmental conditions, such that a true equilibrium moisture concentration will never be achieved. An investigation of the effect of fluctuating moisture conditions on diffusion and moisture uptake in adhesive joints can be seen in Mubashar et al. [18].

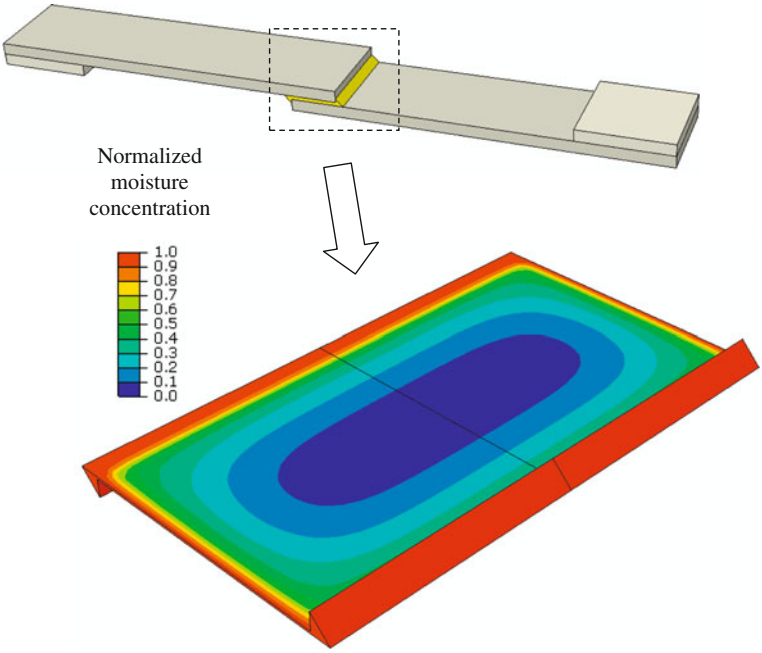

Fig. 3 Calculated moisture distribution in the adhesive layer of an aluminium-epoxy single lap joint conditioned in water at 50 °C for 6 months

Once the moisture and temperature distribution with the joint has been determined, their effects must be analysed. Changes in both temperature and moisture concentration will induce a strain, proportional to the coefficient of thermal expansion and coefficient of hygroscopic expansion respectively. If these strains are constrained, as will generally be the case in an adhesive joint due to the differential straining between adhesive and adherend, hygro-thermal residual stresses will develop. The mechanical properties of an adhesive are generally highly dependent on temperature and moisture concentration and this must also be taken into account in the mechanical model. This can be done through empirical relationships or look-up tables mapping the parameters of the chosen material constitutive model to the environmental conditions. These changes are generally considered to be reversible; however, irreversible effects on material properties may also be seen. The development of stresses in an aluminium-epoxy single lap joint due to the effects discussed above can be seen in Fig. 4. The plots in Fig. 4 show the variation in von Mises equivalent stress over the joint overlap along a line in the middle of the width and thickness of the adhesive layer. The adhesive was cured at 120 °C, then cooled to a room temperature of 20 °C and it can be seen that the differential contraction of the adhesive and adherend has resulted in a relatively uniform stress of approximately 25 MPa along much of the overlap. There is a rise in stress towards the end of the overlap, which then decreases in the

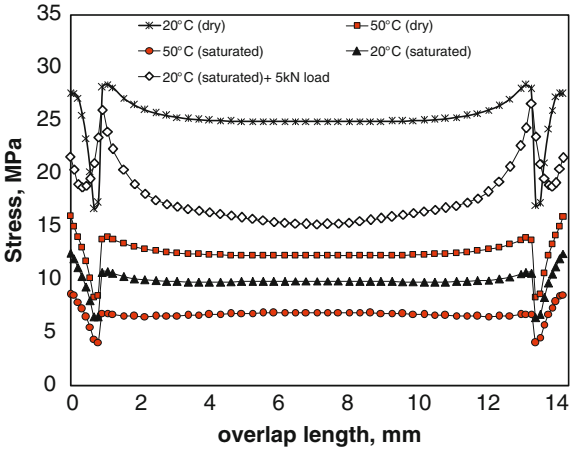

Fig. 4 Equivalent von Mises stress along the middle of the joint overlap in an aluminium-epoxy single lap joint conditioned at 50 °C/95 % r.h. [46]

fillet area before increasing once again as the stress concentration at the end of the fillet is reached. The sample was then conditioned at 50 °C and 98 % relative humidity until saturation. The increase in temperature to 50 °C reduces the stress in the central portion of the joint to approximately 13 MPa and on saturation this has reduced further, to approximately 7 MPa. This is because the moisture induced swelling of the adhesive acts to offset the increased shrinkage of the adhesive compared with the aluminium on cooling from the cure temperature. Reducing the temperature to 20 °C for testing increases the stress to approximately 10 MPa and the application of a tensile mechanical load increases the stress in the centre of the overlap to approximately 16 MPa and also greatly increases the variation of stress along the overlap due to differential straining of the adherend along the overlap and joint rotation. These results give an indication of the significance of the stresses induced by changes in temperature and absorbed moisture and why they need to be included in any realistic analysis of the durability adhesive joints. A final effect of absorbed moisture on adhesive joints may be to affect the strength or stability of the interface between adherend and adhesive. This can be accommodated by having moisture and/or time dependent interfacial strength properties, as discussed further in Sect. 4.1.

4 Application of Damage Mechanics to Adhesive Joints

4.1 Cohesive Zone Modelling Approach

A number of researchers have investigated the application of cohesive zone models to adhesively bonded joints. A variety of traction–separation laws have been used in these investigations, including bilinear [19], trapezoidal [20] and cubic polynomial [21]. Applications have been to a variety of different joint types,

including double cantilever beams (DCBs), thick adherend shear tests, single strap repairs and single lap joints, and materials, including metal and fibre reinforced polymer adherends (e.g. [22–24]). Sugiman et al. [25] modelled the static failure of fibre metal laminates with bonded aluminium doublers and combined the use of cohesive zone models for the aluminium and the GFRP bondlines with an elastic-brittle continuum damage model for the GFRP. In related work, Sugiman and Crocombe [26] extended this to include a ductile continuum damage model for fatigue failure of the aluminium.

In most of the published work the cohesive energy is assumed to be equivalent to the critical strain energy release rate from fracture mechanics, however, there is less agreement on the possible physical meaning and method of determining the critical traction. In some cases an attempt has been made to equate the critical traction with a meaningful material property. For example Campilho et al. [27] used the bulk adhesive strength as the critical traction value in a trapezoidal traction–separation law. Li et al. [22] proposed a three parameter traction–separation model for the case when two failure mechanisms occurred, assigning an initial critical traction to the intrinsic cohesive strength of the interface and a second, lower critical traction to the characteristic strength, which could be attributed to a secondary toughening mechanism after interfacial failure, such as crack bridging. An alternative is to use an inverse approach involving numerical analysis in which the value of the critical traction is calibrated using experimental data. In a recent paper, Katnam et al. [28] proposed a method of characterising the moisture dependent cohesive zone properties for adhesively bonded joints using such a technique. This was based on the peel testing of environmentally conditioned miniature cantilever samples. However, to date there has been comparatively little published work on the application of cohesive zone models to predict the durability of adhesively bonded joints. The use of cohesive zone models in predicting fatigue durability is described in the chapter "Prediction of Joint Strength Under Humid Conditions with Cyclic Loading", the remainder of this section will be used to describe the application of cohesive zone models to the prediction of the effects of absorbed moisture in adhesive joints.

Although a number of authors had previously investigated the effect of moisture on the fracture energy for adhesive joints (e.g. [29, 30]), it was Loh et al. [31] who first used such a relationship to create a moisture dependent cohesive zone model. They proposed a mixed mode, bilinear separation law that was incorporated into a finite element model via modified spring elements they termed interfacial rupture elements. It should be noted that the use of discrete springs to represent the cohesive zone law rather than a continuum element has been termed the discrete cohesive zone method, as discussed by Gustafson and Waas [20]. The moisture dependent fracture energy was determined from mixed mode fracture (MMF) tests after environmental conditioning of the samples and moisture dependent material properties for the adhesive were obtained from testing conditioned bulk samples. The initiation of damage in the interfacial rupture elements was defined by a tripping strain, which was determined from calibration tests. It was seen that between certain limits the failure load was relatively insensitive to the value of the

tripping strain, and this was termed the energy–dominated region. It was seen that the process zone length decreased with increasing tripping strain and the limiting value of the tripping strain for the energy-dominated region was when the process zone length equalled the distance between the interfacial rupture elements. It was, therefore, recommended, that the minimum mesh density at the crack tip should be controlled by this condition, in which case the performance of the interfacial rupture elements is largely independent of tripping strain and mesh. The interfacial rupture elements were incorporated into a semi coupled hygro-mechanical finite element model in which moisture uptake was modelled using a dual Fickian method to account for anomalous uptake (as described in [17]). The resulting model was used to predict the effect of moisture on the load displacement response in the MMF test.

The approach described above was significantly extended by Liljedahl et al. [32]. The interfacial rupture element was replaced by a user defined cohesive zone element which followed a bilinear traction–separation law, with moisture dependent properties determined in a similar way as that used by Loh et al. [17]. In this case the effects of differential thermal and hygroscopic expansion were included in the model and the parameters determined from MMF calibration tests were used to predict the effect of environment on a different sample geometry, the notched coating adhesion (NCA) test. Initial results resulted in poor predictions of the NCA response. This was attributed to an over-prediction of the residual stresses, which were in fact largely relieved by viscoelastic relaxation in the adhesive. This effect was incorporated into the model by the inclusion of moisture dependent creep of the adhesive, resulting in good predictions of the NCA response, as shown in Fig. 5.

Further extensions to this model included stress and corrosion enhanced degradation, application to single lap joints and L-joints [33, 34], application to joints with polymer composite substrates in which moisture absorption into the adherend had to be taken into account [35] and the application to aluminium laminated substrates subjected to both static and fatigue loading [36, 37]. Mubashar et al.

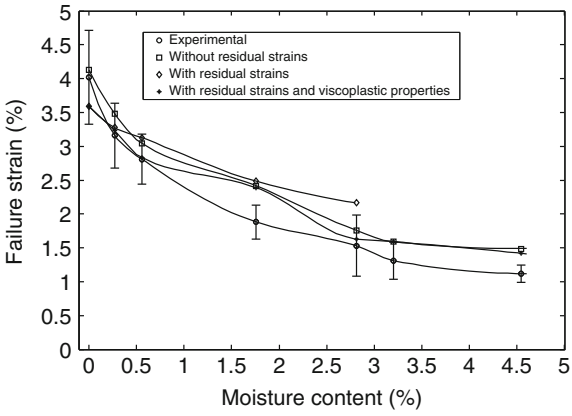

Fig. 5 Experimental and predicted effect of moisture on the failure strain of epoxy-steel NCA samples using a bilinear CZM [32]

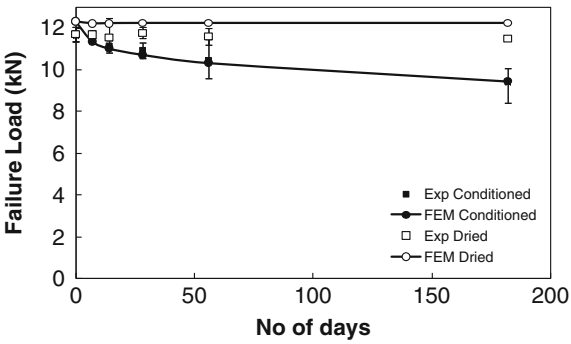

Fig. 6 Predicted and experimental failure loads for aluminium alloy-epoxy single lap joints conditioned in water at 50 °C [38]

[38] accounted for the effect of moisture history by using a moisture history dependent diffusion model and a cohesive zone model in which the cohesive energy was dependent on both the instantaneous moisture concentration and the moisture history. This enabled a partial recovery of joint strength after drying, as observed experimentally. Figure 6 shows good agreement between the predicted and experimentally observed failure loads after conditioning aluminium alloy-epoxy single lap joints in deionised water and then drying them, although the finite element method slightly over-predicts the degree of strength recovery after drying. It should be noted that in these experiments the aluminium alloy adherends were pre-treated prior to bonding using a patented anodization process [39] to create a surface engineered for strong adhesion and durability. Damage and crack development in the unconditioned joints, as predicted by the finite element modelling, are shown in Fig. 7. The contour plots show the damage, represented by a scalar damage variable SDEG, in the adhesive layer and it can be seen that most of the overlap region was damaged before rupture occurred. The crack initiated in the fillet region, labelled as A in Fig. 7a, and the major crack growth direction initially was towards the edges i.e. in the z-direction; as shown in Fig. 7b. Once the crack reached the edges, it propagated towards the middle of the overlap, in the x-direction as may be seen from Fig. 7d. A similar pattern of crack initiation and growth was experimentally observed by Shenoy et al. [40].

Crack initiation in the joints conditioned for 182 days was in the fillet region, labelled as B in Fig. 8a, which was similar to the unconditioned joints. However, at the time of the crack initiation, the damage zone in the conditioned joints was much smaller than in the unconditioned joints. After crack initiation, the major crack growth occurred from region B towards the edges, as shown in Fig. 8b. However, in the conditioned joints, cracks also initiated from the edges of the adherends, as shown in Fig. 8c, the two sets of cracks eventually joining to form a cross width crack as shown in Fig. 8d. The crack then progressed towards the middle of the overlap, in the x-direction, however, in the conditioned joint the crack length is longest at the edges, whereas, it can be seen in Fig. 7d that in the unconditioned joints the crack length is always greater in the middle of the joint width. This is potentially significant if crack length is being measured experimentally by observation of the joint edges.

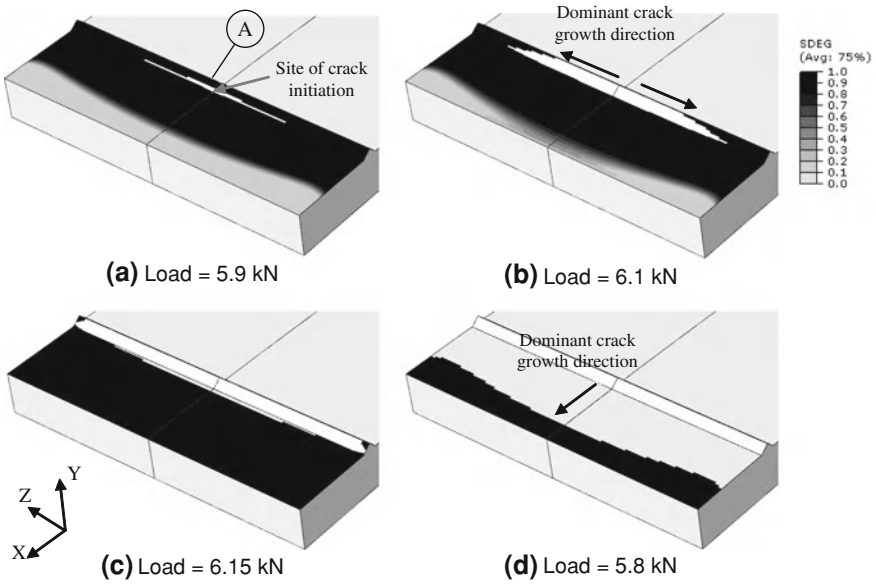

Fig. 7 Damage and crack propagation in aluminium alloy-epoxy single lap joint in dry conditions. Damage is represented by the scalar damage variable SDEG [38]

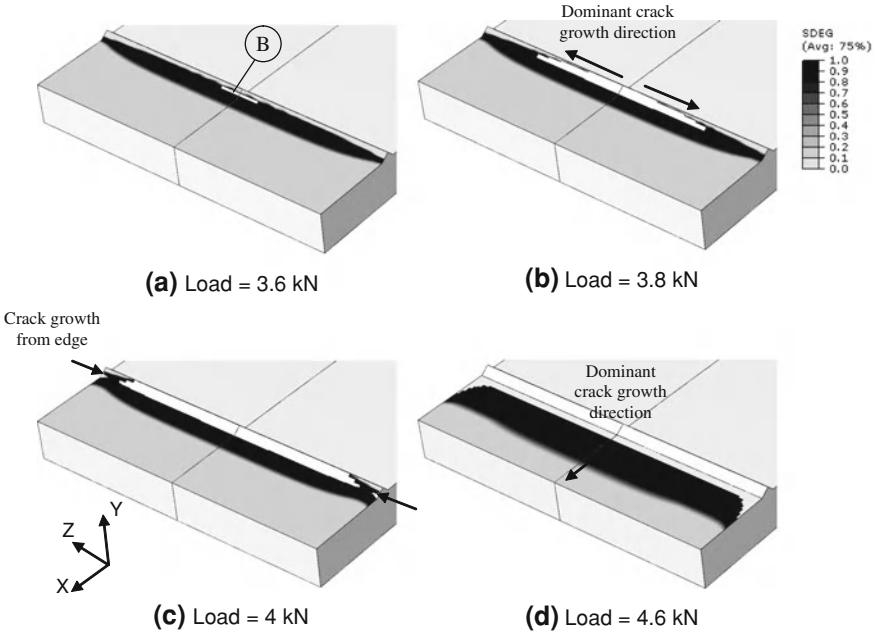

Fig. 8 Damage and crack propagation in aluminium alloy-epoxy joints, conditioned at 50 °C for 182 days. Damage is represented by the scalar damage variable SDEG [38]

The work described above demonstrates that the incorporation of a moisture dependent cohesive zone model into a coupled, finite element based diffusion-stress analysis provides a powerful method of modelling the environmental degradation of adhesively bonded joints. Moreover, the method is flexible enough to enable extension to experimentally observed effects, such as corrosion at the interface, stress enhanced degradation, adhesive creep, residual stresses and moisture history dependent degradation, with relative ease. A potential difficulty in applying this technique is in determining the many material parameters required for the model, particularly the moisture dependent tripping traction. However, the papers cited above suggest practical methods with which this can be achieved.

4.2 Continuum Damage Mechanics Approach

In comparison with cohesive zone modelling, relatively little work has been published on the application of continuum damage mechanics methods to predict failure in adhesively bonded joints, even less so regarding the prediction of environmental ageing. Abdel Wahab et al. [41] applied Lemaitre's thermodynamic based damage approach to the fatigue of double lap and lap-strap joints, showing an effective prediction of fatigue life compared with a fracture mechanics approach. Subsequent work in this field applied the method to other joint types [42] and more explicitly considered the evolution of damage in the joints and the nature of the triaxility function [43, 44]. However, to date there has been no extension of the method to durability modelling. A number of researchers have also applied the GNT damage model to adhesively bonded joints. For example Imanaka et al. [45] used the GNT model to explain the crack growth resistance behaviour observed in single edged notched beam and DCB joints with rubber modified epoxy adhesives. However, the only application of the GTN model to durability seen to date is that in Jumbo [46]. This work will be described in the next section.

Jumbo [46] used the GTN model to predict failure in a variety of single and double lap joints. In the model the value of the void volume fraction changes due to the growth of existing voids and the nucleation of new voids, as characterised by

$$\dot{f}_v = \dot{f}_{growth} + \dot{f}_{nucleation} \tag{13}$$

The rate of growth of voids is given by

$$\dot{f}_{growth} = (1 - \dot{f}_v)\dot{p} \tag{14}$$

and statistically based plastic strain controlled nucleation of voids was used [47], as given by

$$\dot{f}_{nucleation} = \frac{f_N}{S_N\sqrt{2\pi}} exp\left[-\frac{1}{2}\left(\frac{p-\varepsilon_N}{S_N}\right)^2\right]p \tag{15}$$

where f_N is the void volume fraction of voids that can nucleate, ε_N is the mean strain at which nucleation occurs and S_N is the standard deviation of the rupture strain. The direct experimental determination of some of the constants for the GTN model is difficult, hence, in Jumbo [46] some of the models parameters were determined from experimental data, and others by calibrations from FE analysis of a representative joint. The model was applied to both aged and unaged joints, using both 2D and 3D models and accounting for residual stresses from differential hygro-thermal expansions. Figure 9 shows a comparison of the predicted failure load as a function of exposure time for CFRP-aluminium-epoxy double lap joints conditioned at 50 °C, 95 % relative humidity. It can be seen that the 3D model results in a good prediction of the experimental trends, whereas the 2D model tends to over-predict the residual strength after ageing.

An obvious drawback to the application of the GTN model to predict the environmental ageing of adhesive joints is the large number of parameters required, many of which are difficult to obtain directly and must be deduced using inverse methods or through estimation. A less mechanistically based, but more readily applicable approach to continuum damage modelling was suggested by Hua et al. [48]. This was based on a representation of damage based on the stress-plastic displacement response shown in Fig. 10, together with the introduction of a damage parameter, D, which varies from 0 at the onset of damage to 1 when the material has lost its load bearing capacity. From points a–c in Fig. 10 the material response is dictated by an elastic–plastic constitutive law and the moisture degrades this response. Point c represents the onset of damage, as determined by a damage initiation criterion, after which, along curve c–d, the material response is determined by a damage evolution law. The curve c–d' shows the stress-plastic displacement path without damage. The moisture dependent damage parameter was calibrated from aged MMF tests and the model was then shown to be able to

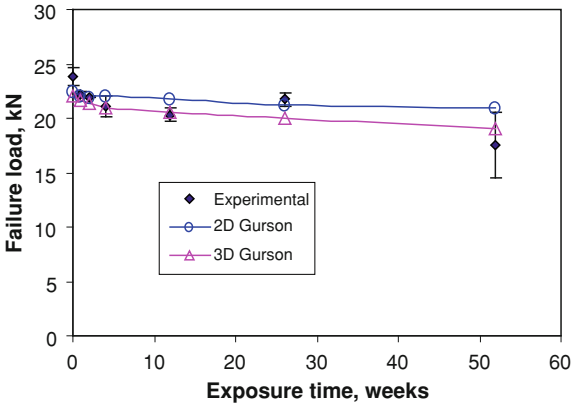

Fig. 9 Effect of ageing at 50C, 95 % r.h. on the failure load of a CFRP/Al/epoxy DLJ predicted using the Gurson CDM [46]

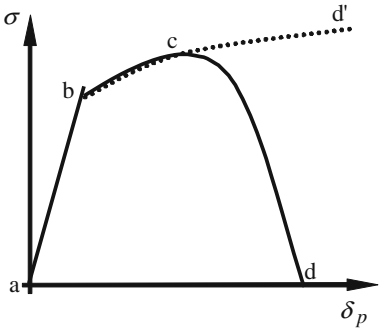

Fig. 10 Schematic of stress-plastic strain based continuum damage model [48]

predict the effect of ageing on single lap joints using the same adhesive. The model was also successfully applied to the prediction of environmental ageing in joints using a more ductile adhesive, in which case a yield model incorporating hydrostatic stress sensitivity was implemented [49]. The spatial damage propagation in the 3D continuum damage model for an aged single lap joint is illustrated using a series of contour plots in Fig. 11. The contours represent the damage parameter *D*. The arrows in Fig. 11 indicate the faces exposed to the environment. It can be seen that the damage initiates at the corner of the joint with the saturated edge (A), rather than the slightly less degraded mid-plane section (B), and then, propagates from the saturated corner to the middle (B) and the central section (C) of the adhesive layer. The predicted failure load of the joint as a function of environmental ageing time is compared with the experimental results in Fig. 12. Good agreement between the predicted and experimental results can be seen and the prediction appears to be largely mesh independent over the range of mesh sizes investigated.

The work described above shows that although there has been little published literature to date on the application of continuum damage mechanics to the environmental ageing of adhesively bonded joints, it is potentially capable of predicting the progressive failure of aged adhesive joints, particularly when failure is within the adhesive layer, rather than at the adherend-adhesive interface. It was seen that the more mechanistically based models, such as the GNT model, can potentially be used to elucidate the mechanisms of failure in the adhesive, however, the drawback in this is the number of material parameters required for the model. As many of these are difficult to obtain directly and must be estimated or derived using an inverse method, this makes the models difficult to implement and of less mechanistic relevance. The simpler method proposed by Hua et al. [48] was seen to provide a method of predicting the progressive damage and failure of adhesively bonded joints after ageing and was also seen to predict the effect of environmental ageing on the failure load of joints to good accuracy.

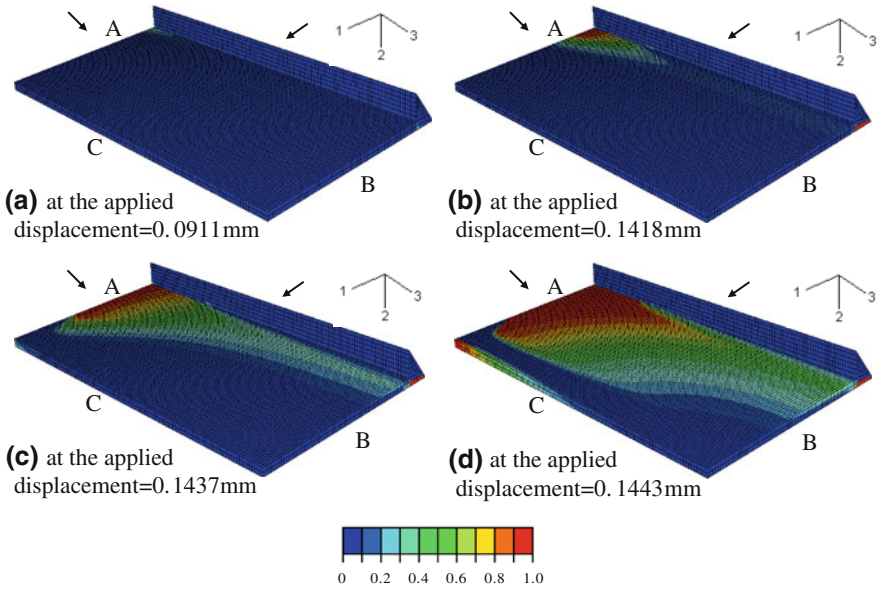

Fig. 11 3D damage propagation in an epoxy-aluminium SLJ aged for 26 weeks using a continuum damage model [50]

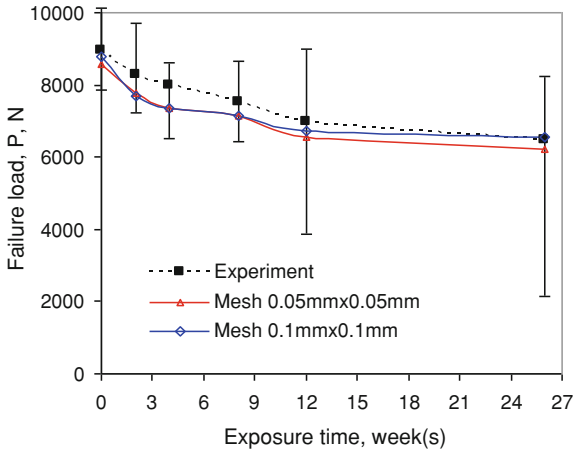

Fig. 12 Predicted ultimate failure load of aged epoxy-aluminum SLJs using a continuum damage model with different mesh schemes [50]

5 Summary and Conclusions

It is often seen that the strength of adhesive joints decreases on ageing in natural environments. This is usually because of the effect of environmental moisture, which is absorbed by polymeric adhesives and affects both the mechanical behaviour of the adhesive and the interface between the adhesive and adherend.

These effects are usually increased by increasing temperature or the application of stress. The effect on the interface with metallic adherends is potentially the most damaging, however, this can often be mitigated by the application of a suitable surface treatment prior to bonding. In this case it is often seen that the effects of absorbed moisture are largely reversible.

The effect of the environment on adhesively bonded joints is commonly investigated experimentally through accelerated ageing tests in which joints are exposed to high temperature and humidity. This can provide a useful comparison of different systems but cannot be used to predict the performance of joints under actual service conditions. Currently, the best method of predicting the effect of environmental ageing on the strength of bonded joints is through coupled hygro-thermal–mechanical finite element analyses. The first stage in this method is to determine the moisture distribution in the joint as a function of time from a diffusion analysis. This is used to determine the spatial distribution of mechanical properties and the applied hygroscopic strain. A mechanical analysis is then used to determine the stresses in the joint as a function of ageing time and an appropriate failure criterion can be used to predict the residual strength of the joint as a function of ageing time. One of the most powerful and flexible methods of predicting failure is by the application of a progressive damage model to the mechanical model of the joint. Two forms of progressive damage models have been identified as being suitable for adhesively bonded joints, those based on cohesive zone laws, that are particularly suited to interfacial failure, and those based on continuum damage mechanics, that are particularly suited to cohesive failure within the adhesive layer. These methods are now well developed and have been validated for a number of different adhesive joint types. To date there has been little published work on the application of damage mechanics methods to the environmental ageing of bonded joints, however, the results from the limited studies to date have clearly shown the potential of these methods. Further development and validation of these techniques is still required and it would also be desirable if a more direct correlation was made with the observable mechanisms of failure in bonded joints. However, as seen in the application of the GNT model to adhesive joints, a more mechanistically representative model can proliferate the number of material parameters required, many of which may be difficult to obtain. Hence, dependant on the purpose of a particular analysis, a compromise should be made between the ability of the model to represent the desired phenomenon and the practicality of its application.

In terms of the practical application of damage mechanics to the prediction of the in-service performance of bonded joints, probably the main technical challenge is to extend the capabilities of these techniques to more typical environmental conditions involving fluctuating loads and fluctuating environments. The next chapter outlines some techniques that may form the basis for fluctuating loads and this chapter has highlighted an approach that begins to address the effects of a fluctuating environment. However, currently the effect of load on the transport and degradation of both the adhesive and the interface still need to be characterised. This requires a fully coupled multi-physics approach but such techniques are

becoming increasingly feasible. It would also be useful to develop analysis tools based on the principles described above that were available to the non-specialist designer or engineer to encourage wider investigation and help enable industrial implementation.

Acknowledgements The authors would like to acknowledge the contributions of fellow researchers and PhD students including, Dr Keat Loh, Dr. David Liljedahl, Dr. Yongxia Hua, Dr. Furo Jumbo and Dr. Aamir Mubashar. We also gratefully acknowledge the financial support of DSTL and the technical input from Industrial collaborators BAe Systems, Airbus and MBDA.

References

1. Dugdale, D.: Yielding of steel sheets containing slits. J. Mech. Phys. Solids. **8**, 100–104 (1960)
2. Barenblatt, G.I.: The mathematical theory of equilibrium cracks in brittle fracture. Adv. Appl. Mech. **7**, 55–129 (1962)
3. Yan, G., Mai, Y.-W., Yuan, Q., Ye, L., Sun, J.: Effects of substrate materials on fracture toughness measurement in adhesive joints. Int. J. Mech. Sci. **43**, 2091–2102 (2001)
4. Chandra, N., Li, H., Shet, C., Ghonem, H.: Some issues in the application of cohesive zone models for metal-ceramic interfaces. Int. J. Solids. Structs. **39**, 2827–2855 (2002)
5. Kachanov, L.M.: Introduction to Continuum Damage Mechanics. Martinus Nijhoff Dortrecht, Netherlands (1986)
6. Kattan, P.I., Voyiadjis, G.X.: Damage Mechanics with Finite Elements. Springer, Berlin (2002)
7. Lemaitre, J., Desmorat, R.: Engineering Damage Mechanics. Springer, Berlin (2005)
8. Kachanov, L.M.: On rupture time under conditions of creep. Ivestia Akademi Nauk USSR **8**, 26–31 (1958)
9. Rabotnov, Y.N.: (1968) Creep Rupture. In: Proceedings of the 12th International Congress on Applied Mechanics, pp. 342–349
10. Gurson, A.L.: Continuum theory of ductile rupture by void nucleation and growth: part 1. Yield criterion and floe rules for porous materials. J. Eng. Mater. Technol. **99**, 2–15 (1977)
11. Needleman, A., Tvergaard, V.: An analysis of ductile rupture in notched bars. J. Mech. Phys. Solids. **32**, 461–490 (1984)
12. Zairi, F., Nait-Abdelaziz, M., Woznica, K., Gloaguen, J.M.: Constitutive equations for the viscoplastic-damage behaviour of a rubber-modified polymer. Europ. J. Mech.—A/Solids **24**, 169–182 (2005)
13. Dean, G.D., Mera, R.: Determination of Material Properties and Parameters Required for Simulation of Impact Performance of Plastics Using Finite Element Analysis NPL Materials Centre. National Physical Laboratory, Middlesex (2004)
14. Crocombe, A.D., Ashcroft, I.A., Abdel Wahab, M.M.: Chapter 6: environmental degradation. In: da Silva, L.F.M., Öechsner, A. (eds.) Advances in Modelling Adhesively Bonded Joints. Springer Publishing, New York (2008)
15. Ashcroft, I.A., Comyn, J.: Chapter 33: effect of water and mechanical stress on durability. In: Da Silva, L.F.M., Öechsner, A., Adams, R.D. (eds.) Handbook of Adhesion Technology, Springer, New York (2011)
16. Abdel Wahab, M.M., Ashcroft, I.A., Crocombe, A.D., Shaw, S.J.: Diffusion of moisture in adhesively bonded joints. J. Adhes. **77**, 43–80 (2001)
17. Loh, W.K., Crocombe, A.D., Abdel Wahab, M.M., Ashcroft, I.A.: Modelling anomalous moisture uptake, swelling and thermal characteristics of a rubber toughened epoxy. Int. J. Adhes. Adhes. **25**, 1–12 (2005)

18. Mubashar, A., Ashcroft, I.A., Critchlow, G.W., Crocombe, A.D.: Modelling cyclic moisture uptake in an epoxy adhesive. J. Adhes. **85**, 711–735 (2009)
19. Liljedahl, C.D.M., Crocombe, A.D., Wahab, M.A., Ashcroft, I.A.: Damage modelling of adhesively bonded joints. Int. J. Fract. **141**, 147–161 (2006)
20. Gustafson, P.A., Waas, A.M.: The influence of adhesive constitutive parameters in cohesive zone finite element models of adhesively bonded joints. Int. J. Solid. Struct. **46**, 2201–2215 (2009)
21. Blackman, B.R.K., Hadavinia, H., Kinloch, A.J., Williams, J.G.: The use of a cohesive zone model to study the fracture of fibre composites and adhesively bonded joints. Int. J. Fract. **119**, 25–46 (2003)
22. Li, S., Thouless, M.D., Waas, A.M., Schroeder, J.A., Zavattieri, P.D.: Use of mode I cohesive zone models to describe the fracture of an adhesively-bonded polymer-matrix composite. Comput. Sci. Technol. **65**, 281–293 (2005)
23. Fan, C., Ben Jar, P.-Y., Roger Cheng, J.J.: Cohesive zone with continuum damage properties for simulation of delamination development in fibre composites and failure of adhesive joints. Eng. Fract. Mech. **75**, 3866–3880 (2008)
24. De Moura, M.F.S.F., Goncalves, J.P.M., Chousal, J.A.G., Campilho, R.D.S.G.: Cohesive and continuum mixed-mode damage models applied to the simulation of the mechanical behaviour of bonded joints. Int. J. Adhes. Adhes. **28**, 419–426 (2008)
25. Sugiman, S., Crocombe, A.D., Katnam, K.B.: Investigating the static response of hybrid fibre-metal laminate doublers loaded in tension. Compos. B Eng. **42**, 1867–1884 (2011)
26. Sugiman, S., Crocombe, A.D.: The static and fatigue response of metal laminate and hybrid fibre-metal laminate doublers joints under tension loading. Compos. Struct. **94**(2937–2951), 2012 (2012)
27. Campilho R.D.S.G., de Moura M.F.S.F., Domingues J.J.M.A.: Using a cohesive damage model to predict the tensile behaviour of CFRP single-strap repairs. Int. J. Solids. Struts. **45**, 1497–1512 (2008)
28. Katnam, K.B., Sargent, J., Crocombe, A.D., Khoramishad, H., Ashcroft, I.A.: Characterisation of moisture-dependent cohesive zone properties for adhesively bonded joints. Eng. Fract. Mech. **77**, 3105–3119 (2010)
29. Chang, T., Lai, Y.H., Shephard, N.E., Sproat, E.A., Dillard, D.A.: A test method for accelerated humidity conditioning and estimation of adhesive bond durability. J. Adhes. **60**, 153–162 (1997)
30. Wylde, J.W., Spelt, J.K.: Measurement of adhesive joint fracture properties as a function of environmental degradation. Int. J. Adhes. Adhes. **18**, 237–246 (1998)
31. Loh, W.K., Crocombe, A.D., Abdel Wahab, M.M., Ashcroft, I.A.: Modelling interfacial degradation using interfacial rupture elements. J. Adhes. **79**, 1135–1160 (2003)
32. Liljedahl, C.D.M., Crocombe, A.D., Wahab, M.A., Ashcroft, I.A.: The effect of residual strains on the progressive damage modeling of environmentally degraded joints. J. Adhes. Sci. Technol. **19**, 525–548 (2005)
33. Crocombe, A.D., Hua, Y.X., Loh, W.K., Wahab, M.A., Ashcroft, I.A.: Predicting the residual strength for environmentally degraded adhesive lap joints. Int. J. Adhes. Adhes. **26**, 325–336 (2006)
34. Liljedahl, C.D.M., Crocombe, A.D., Wahab, M.A., Ashcroft, I.A.: Modelling the environmental degradation of the interface in adhesively bonded joints using a cohesive zone approach. J. Adhes. **82**, 1061 (2006)
35. Liljedahl, C.D.M., Crocombe, A.D., Wahab, M.A., Ashcroft, I.A.: Modelling the environmental degradation of adhesively bonded aluminium and composite joints using a CZM approach. Int. J. Adhes. Adhes. **27**, 505–518 (2007)
36. Sugiman, S., Crocombe, A.D., Ashcroft, I.A.: Experimental and numerical investigation of the static response of environmentally aged adhesively bonded joints. Int. J. Adhes. Adhes. **40**, 224–237 (2013)
37. Sugiman, S., Crocombe, A.D., Ashcroft, I.A.: The fatigue response of environmentally degraded adhesively bonded aluminium structures. Int. J. Adhes. Adhes. **41**, 80–91 (2013)

38. Mubashar, A., Ashcroft, I.A., Critchlow, G.W., Crocombe, A.D.: Strength prediction of adhesive joints after cyclic conditioning using a cohesive zone model. Eng. Fract. Mech. **78**, 2746–2760 (2011)
39. Critchlow, G.W., Ashcroft, I.A., Cartwright, T., Bahrani, D.: Anodising Aluminium Alloy, UK Patent no. GB2421959(A) (2006)
40. Shenoy, V., Ashcroft, I.A., Critchlow, G.W., Crocombe, A.D., Abdel Wahab, M.M.: An investigation into the crack initiation and propagation behaviour of bonded single-lap joints using backface strain. Int. J. Adhes. Adhes. **29**, 361–371 (2009)
41. Abdel Wahab, M.M., Ashcroft, I.A., Crocombe, A.D., Hughes, D.J., Shaw, S.J.: Prediction of fatigue threshold in adhesively bonded joints using damage mechanics and fracture mechanics. J. Adhes. Sci. Technol. **15**, 763–782 (2001)
42. Abdel Wahab, M.M., Hilmy, I., Ashcroft, I.A., Crocombe, A.D.: Evaluation of fatigue damage in adhesive bonding: part 2: single lap joint. J. Adhes. Sci. Technol. **24**, 325–345 (2010)
43. Abdel Wahab, M.M., Hilmy, I., Ashcroft, I.A., Crocombe, A.D.: Damage parameters of adhesive joints with general triaxiality. Part 1: finite element analysis. J. Adhes. Sci. Technol. **25**, 903–923 (2011)
44. Abdel Wahab, M.M., Hilmy, I., Ashcroft, I.A., Crocombe, A.D.: Damage parameters of adhesive joints with general triaxiality. Part 2: scarf joint analysis. J. Adhes. Sci. Technol. **25**, 925–947 (2011)
45. Imanaka, M., Motohashi, S., Nishi, K., Nakamura, Y., Kimoto, M.: Crack growth behaviour of epoxy adhesives with rubber and cross-linked rubber particles under mode I loading. Int. J. Adhes. Adhes. **29**, 45–55 (2009)
46. Jumbo, F.S.: Modelling Residual Stress and Environmental Degradation in Adhesively Bonded Joints, PhD thesis, Loughborough University, Loughborough, UK (2007)
47. Chu, C.C., Needleman, A.: Void nucleation effects in biaxially stretched sheets. J. Eng. Mater. Technol., Trans. ASME **102**, 249–256 (1980)
48. Hua, Y., Crocombe, A.D., Wahab, M.A., Ashcroft, I.A.: Continuum damage modelling of environmental degradation in joints bonded with EA9321 epoxy adhesive. Int. J. Adhes. Adhes. **28**, 302–313 (2008)
49. Hua, Y., Crocombe, A.D., Wahab, M.A., Ashcroft, I.A.: Continuum damage modelling of environmental degradation in joints bonded with E32 epoxy adhesive. J. Adhes. Sci. Tech. **21**, 179–195 (2007)
50. Hua, Y.: Modelling Environmental Degradation on Adhesively Bonded Joints, PhD thesis, University of Surrey (2006)

Prediction of Joint Strength Under Humid Conditions with Cyclic Loading

Andrew D. Crocombe and Ian A. Ashcroft

Abstract This chapter outlines research that has been undertaken in seeking to model the combined effect of fatigue and environment on the durability of adhesively bonded structures. The main modelling approach outlined is based on progressive damage where both fatigue cycles and the environment degrade the response of the joint. In this work the progressive damage has been incorporated using a cohesive zone model with damage models for the material parameters being defined in terms of fatigue loading on the joint and the moisture distribution in the joint. The fatigue damage model is based on the maximum fatigue load but has been generalised for varying mean loads thus enabling generalised fluctuating loads to be modelled. Two configurations of joint have been extensively tested both statically and in fatigue under a range of environmental conditions and the degraded fatigue life recorded. Progressive damage finite element (FE) modelling has been undertaken on these joints and the static and fatigue response predicted. In order to assess how the damage progresses in these joints backface strain measurements have been recorded. These have been used to validate the damage predicted by the FE modelling and the good correlation serves to further validate this approach. The chapter concludes with an outline of possible developments extending the range of application of this work.

Keywords Progressive damage FE modelling · Cohesive zone model · Durability · Environmental and fatigue degradation · Fatigue cyclic damage model · Backface strain · Predicting fatigue life

A. D. Crocombe (✉)
University of Surrey, Guildford GU2 7XH, UK
e-mail: a.crocombe@surrey.ac.uk

I. A. Ashcroft
University of Nottingham, Nottingham NG7 2RD, UK
e-mail: i.a.ashcroft@lboro.ac.uk

L. F. M. da Silva and C. Sato (eds.), *Design of Adhesive Joints Under Humid Conditions*, Advanced Structured Materials 25, DOI: 10.1007/978-3-642-37614-6_8,

1 Introduction

This chapter presents a "state of the art" summary of a topic that combines two areas of major complexity; environmental degradation and fatigue damage. The reader will note that both aspects cause damage of the joint which will affect its residual strength. However considering "strength" alone (as the title suggests) is only part of the story. Joint life is also a main concern. Perhaps a better term to use is "joint integrity" rather than "joint strength". Most structural failure comes from cyclic fatigue and the use of the word "fatigue" is quite apt, implying that the material tires. The primary cause of concern with cyclic fatigue is that structures can potentially fail at loads that are significantly lower than the static failure load. The repeated application of these "non-critical" loads leads to an accumulation of damage within a material resulting in its final failure as the residual strength reduces to the maximum load in the fatigue cycle.

Exposure of an adhesive joint to a wet environment has a similar effect in that the moisture penetrates the joint and damages the material (and the interface) leading to a residual strength that reduces with increasing time or aggressiveness of the exposure. Given that bonded structures can experience fluctuating loads in a hostile environment during service and that both aspects can have a detrimental effect on the integrity of the structure it is important to be able to characterise their response. There are a number of ways in which the joint performance can be characterised including (a) long term testing under natural loading and environment (b) shorter term testing in accelerated environmental and loading conditions and (c) predictive modelling of the long term response from measurable material and joint parameters. These approaches all have advantages and disadvantages and are better used in a complementary way rather than in isolation.

This chapter focuses on the last of these three approaches and begins with Sect. 2 that outlines experimental and modelling work that has been undertaken in this area that does not come under the heading of progressive damage modelling. The following section describes what progressive damage modelling is and outlines various approaches that have been used to model fatigue damage in adhesive joints. Section 4 then gives details of the specific fatigue damage model developed by the authors and the framework for introducing environmental degradation and combining it with fatigue damage. The following two sections then provide details of experimental and modelling work that implement the combined damage modelling approach outlined in Sect. 4. The chapter then ends with some concluding comments and suggestions for areas of future research. It should be understood that this area of combined environmental and fatigue damage is very much an area of on-going research and that there are still plenty of problems to solve and improvements to be made.

2 Historical Approach

This section summarises the work that has been carried out prior to the (coupled) progressive damage modelling approaches that form the main focus of this chapter. Relatively little work has been carried out experimentally assessing the effect of moisture on the fatigue response of bonded structures (Sect. 2.1) and even less has been undertaken in developing predictive methods for use in bonded joint design (Sect. 2.2). A final short section (Sect. 2.3) has been included summarising a few other (non progressive damage) approaches that have been used in conjunction with adhesively bonded joints.

2.1 Experimental Characterisation of Moisture Degraded Fatigue Joint Response

2.1.1 Load-Life Data

Zhang et al. [35] tested glass fibre reinforced polymer double lap joints (GFRP DLJs) following immersion in water at 40 °C for 70 days. Although this is a relatively short period of exposure, the authors provide evidence that this was sufficient for the joints to reach equilibrium moisture saturation. Fatigue testing was undertaken at 10 Hz and 4 load levels with a load ratio (minimum load/maximum load) of 0.1. Load-life plots were obtained and immersion was seen to cause a reduction in life of up to 1 decade, as shown in Fig. 1.

Much earlier, Mackie and Su [18] and Su et al. [29] tested five possible adhesive systems for civil engineering applications following exposure at 90 %RH and natural weathering for a period of 10 years. The configurations tested were

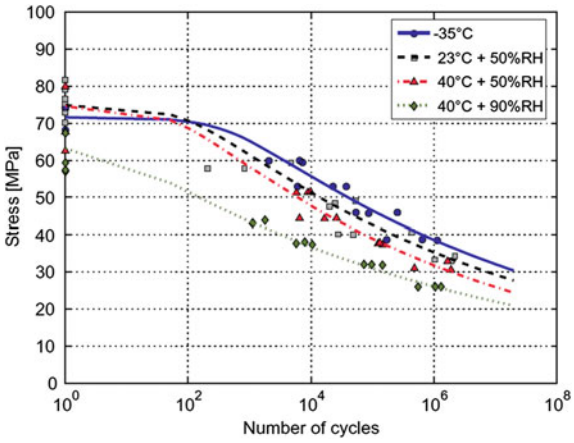

Fig. 1 Moisture degraded load-life fatigue data for adhesively bonded GFRP DLJs [35]

shot blast bright mild steel DLJs. Only a single load level was considered for each configuration, giving an unaged fatigue life of around 300000 cycles. About half the adhesives actually showed an increase in fatigue life.

Rushforth et al. [24] undertook fatigue tests on aluminium SLJs with and without a silicon pre-treatment. Testing was undertaken in two environments, ambient laboratory and 96 %RH and no preconditioning was undertaken. A load ratio of 0.1 and a frequency of 20 Hz were used and complete load-life curves were produced. It was found that the joints with untreated substrates degraded more significantly, with decreases in fatigue life of around a decade. The treated joints also degraded but less significantly.

2.1.2 Crack Growth Data

Another approach that has been used to experimentally characterise the degradation of the fatigue strength of adhesive joints is based on fracture mechanics. The cyclic crack growth rate (da/dN) is measured and subsequently defined in terms of fracture mechanics parameters such as strain energy release rate (G). Such crack growth characterisation is commonly known as the Paris law and is represented as

$$da/dN = A\Delta G^n \tag{1}$$

which produces a straight line in a log–log plot or a sigmoidal version of this which more realistically represents the fast fracture and threshold crack growth rate at either extreme.

Jethwa and Kinloch [11] and Fernando et al. [9] adopted this method to quantify moisture induced fatigue degradation. They considered two different substrate (aluminium and steel)—adhesive pairs and two surface treatments (chromic acid etch, CAE, and phosphoric acid anodise, PAA) for the aluminium joints. Testing was undertaken in fatigue at 5 Hz with a load ratio of 0.1. Displacement control rather than load control was used as it was easier to identify the threshold energy release rate value, G_{th}. This is the value for G below which no crack growth occurred. Although the complete Paris law was found G_{th} forms a natural design parameter and was the parameter of primary interest. As with Rushford et al. [24] joints were not pre-conditioned. In this case they were either tested in ambient laboratory conditions or immersed in water. It was found that G_{th} for the joints tested in water were considerably decreased (by between 2 to 3 times) from the values tested in ambient conditions, Fig. 2

Leitchi et al. [16] pre-saturated their GFRP-urethane cracked lap shear (CLS) joints for 2 years prior to fatigue testing. They obtained Paris law plots for 6 test configurations (dry and wet at 10, 26 and 90 °C). The decreases in G_{th} at the lower 2 temperatures was really quite modest (only around 30 % reduction).

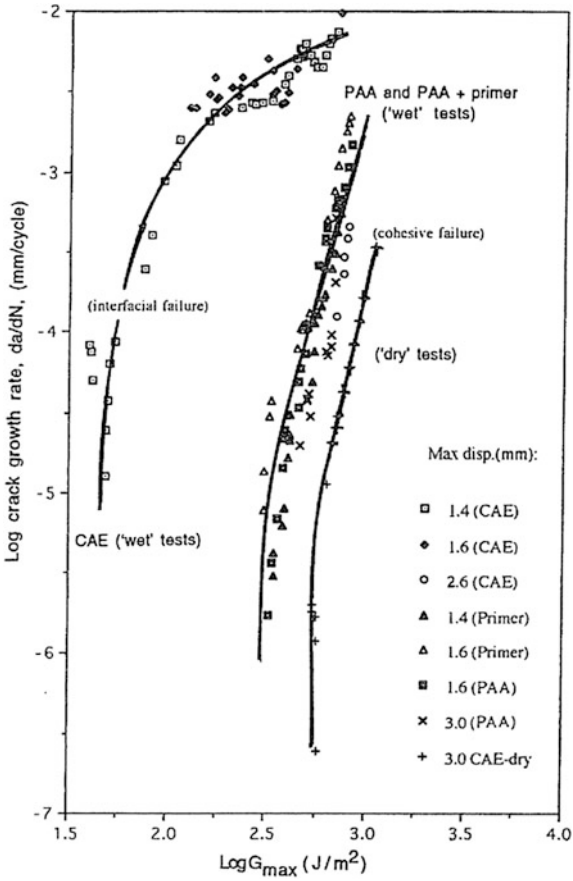

Fig. 2 Moisture degraded Paris Law data for bonded aluminium tapered double cantilever beam (*TDCB*) specimens [9]

2.2 *Predictive Modelling Approaches for Moisture Degraded Fatigue Joint Responses*

2.2.1 Load-Life Based Approach

One approach is based on an observation made from the wide range of "dry" joint load life (S–N) data that is available in the literature, that a reasonable lower bound fatigue endurance limit can be taken as 20 % of the static failure load. This is clearly an oversimplification but is reasonable for many joints. If we assume that the same is valid for "wet" joints (and the data of Zhang et al. [35] and Rushford et al. [24] support this) then one needs to design a joint that has a "wet" static strength of 5 times the fatigue load that will be applied. Where "wet" failure is cohesive in the adhesive (and this can often be the case for a well made joint) then the design approach outlined by Crocombe [5] can be applied. In this approach the residual static strength (P_{max}) of a joint exposed to moisture for time t can be found

from Eq. 2, where L is the overlap length, τ_{dry} is the dry adhesive limiting shear stress, D the diffusion coefficient and F_τ is the factor that defines the wet adhesive limiting stress (going from 0 for no loss of shear strength to 1 for complete loss of shear strength).

$$\frac{P_{\max}}{\tau_{dry}L} = \left[1 - F_\tau\left(1 - \frac{8}{\pi^2}\sum_{0}^{\infty}\frac{1}{(2j+1)^2}e^{-(2j+1)^2\left(\frac{D\pi^2 t}{L^2}\right)}\right)\right] \tag{2}$$

2.2.2 Fracture Mechanics Based Approach

In this approach the Paris law data obtained from a fracture mechanics test (such as those outlined in Sect. 2.1.2) can be used in conjunction with finite element (FE) analysis to predict crack growth in a different joint of the same materials. An initial crack length is assumed, the FE model run to give G which can then be used in conjunction with Eq. 1 (or the more complex sigmoidal variant) to calculate the crack growth rate and hence the crack growth for a block of cycles. The FE model is then updated with the new crack length and the process iterated until the entire joint is cracked or static fracture occurs. A flow chart illustrating this technique is found in Wahab et al. [34], Fig. 3, where this technique has been used to determine the load-life curve of "dry" carbon fibre reinforced polymer (CFRP) single and double lap joints (SLJ and DLJ's). Curley et al. [7] have applied this technique to both "wet" and "dry" joints and predicted the service life of the joints they tested, which were discussed in Sect. 2.1.2.

As the slope of the Paris law curve is steep for adhesive joints, a more conservative approach is to design for no crack growth and this can be done by using

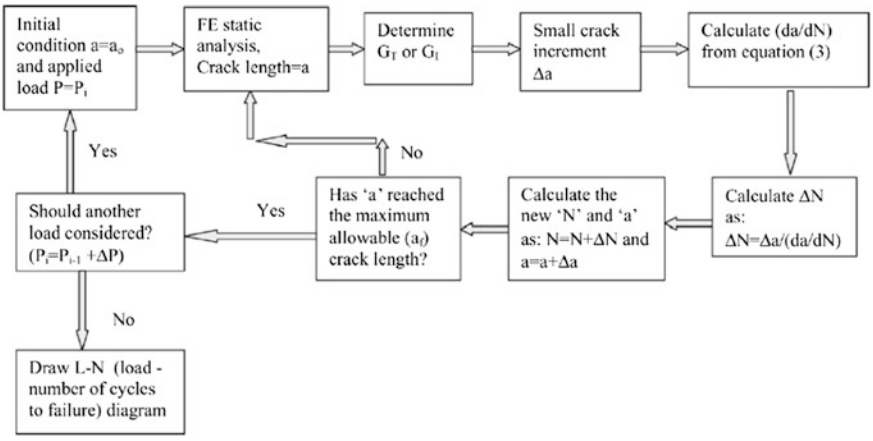

Fig. 3 Flow chart illustrating fatigue life prediction using an iterative application of the Paris law [34]

G_{th} on the Paris Law. Ashcroft et al. [1] analysed CFRP lap strap joints (both uni-directional (UD) and multi-directional (MD) fibre orientation) that had been aged at 45 °C and 85 % RH. As the joints were only partially saturated they undertook a diffusion analysis, to obtain the moisture distribution in the joint, followed by a fracture mechanics analysis that provided the value of G for a given applied load. The value of G_{th} was calibrated using the UD joints and used to predict the threshold load for the MD joints. Predictions of the threshold loads obtained in this way correlated well with measured data.

2.3 Other Predictive Modelling Design Approaches

A number of other design approaches have been applied to unaged, fatigued, adhesively bonded structures. Here only a brief mention of some of these will be given as they have not been used in conjunction with moisture degradation. A more comprehensive review of these techniques can be found elsewhere [2].

Cumulative damage:
This is based on derivatives of Miner's Law and allows the effect of blocks of cycles at different fatigue loads to be combined. It is expressed as

$$\sum \frac{n_i}{N_{fi}} = C \tag{3}$$

where C is conventionally 1 and n_i and N_{fi} the number of cycles and the fatigue life at a given level of loading.. However, Erpolat et al. [8] applied this to CFRP DLJs subject to variable amplitude (VA) fatigue loading and found that C varied between 0.04 and 0.3, decreasing with increasing load.

Strength wearout:
This is based on the fact that as fatigue cycles accumulate the joint damage increases and this reduces the residual strength. Failure will occur when the residual strength reaches the maximum applied fatigue load ($P_{max,i}$). The load degradation/cycle (P_{Di}) in a constant amplitude (CA) set of cycles (i) can be defined as

$$P_{Di} = (P_u - P_{max,i})/N_{fi} \tag{4}$$

Additionally, to account for increases in damage that occur at transitions between sets of CA cycles where the mean load increases, a cycle mix parameter (CM) can be included. This cycle mix parameter can be calibrated by comparing constant amplitude and variable amplitude results. Thus the reduction in residual strength from a single block of various sets of constant amplitude cycles $\left(\Delta P_{res,block}\right)$ can be expressed as

$$\Delta P_{res,block} = \sum (P_{Di} + CM) \tag{5}$$

Erpolat et al. [8] applied this approach to the same CFRP DLJs considered in the cumulative damage section above and found a better prediction of fatigue life. This method was further extended and validated by Shenoy et al. [25, 26].

3 Overview of Progressive Fatigue Damage Modelling

Progressive damage modelling is the term used when damage is incorporated into a finite element material model causing the materials under consideration to degrade, ultimately to a complete loss of integrity. In this way the loading and the failure process can be simulated within a single FE analysis. This is particularly useful for:

(a) Modelling adhesively bonded structures that have been exposed to a wet environment, as in this case the adhesive around the periphery is weaker (wetter) than in the interior and so failure may occur at the outside well before the joint reaches its peak load. Thus it is essential to model the growth of damage as the peak load is not identified with the initial failure event.
(b) Modelling fatigue where considerable damage and crack growth (initiation and propagation) generally occur before final fatigue failure. Thus, again it is necessary to model the growth of damage as the fatigue life is not associated with the initial failure event.

So in the context of this chapter, progressive damage modelling is doubly useful, as we consider the combination of both the factors mentioned above. The use of progressive damage to model the fatigue process is a fairly recent development, over say the last 5 years or so. Currently there are two common ways of modelling the progressive damage. The first is known as the *cohesive zone* approach where the damage is localised on a line or a plane in 2D and 3D modelling respectively. As nodes on this line or plane separate they follow the traction separation response (TSR) such as the one illustrated in Fig. 4, which illustrates a simple triangular TSR. Initially (OA) the nodes are connected with a

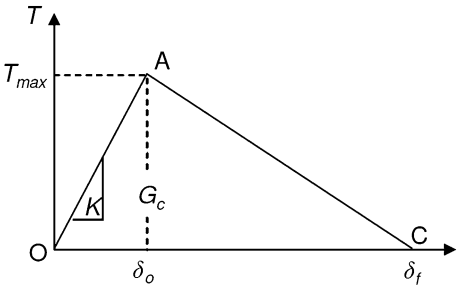

Fig. 4 Illustrating triangular TSR for the cohesive zone approach

high spring stiffness (K) until they reach a critical stress (traction, T_{max}) at point A. They then unload (AC) with increasing displacement (from δ_o to δ_f) absorbing energy (G_c) in the process. The second way is known as the *continuum damage* approach. Here the damage is spread through the material, i.e. on a plane or in a volume in 2D and 3D modelling respectively. Undamaged elasto-plastic material behaviour is defined along with a cyclic fatigue damage model. The fatigue damage parameter is used to degrade the underlying material parameters such as tensile modulus (E), yield stress (σ_{yl}), etc.

A brief summary of the application of both these approaches to modelling the unaged fatigue response of adhesively bonded structures will be presented in the next two subsections. This should provide a useful background to the main focus of this chapter, the progressive damage modelling of the fatigue response of moisture degraded adhesive joints.

3.1 Cohesive Zone Fatigue Damage Modelling

There are three main approaches used when applying cohesive zone modelling (CZM) to predict the fatigue response, as illustrated in Fig. 5. These differ in how the damage is determined: (a) cycle by cycle, (b) selected cycle extrapolation and (c) based on the maximum fatigue load. The first has the potential to more directly incorporate varying cycle profiles whilst the latter two are more suited for high cycle fatigue (as they are less computationally intensive).

Nguyen et al. [20], Maiti and Guebelle [19] and Roe and Siegmund [23] are among the researchers that have adopted the cycle by cycle approach. The first two degrade the traction and stiffness with increasing fatigue cycles whilst the last provides a specific formulation for a fatigue damage parameter in terms of cyclic tractions and separations. Figure 6 shows the predicted response obtained by Roe and Siegmund [23] for a double cantilever beam (DCB) with aluminium substrates bonded with an high density polyethylene (HDPE) thermoplastic adhesive.

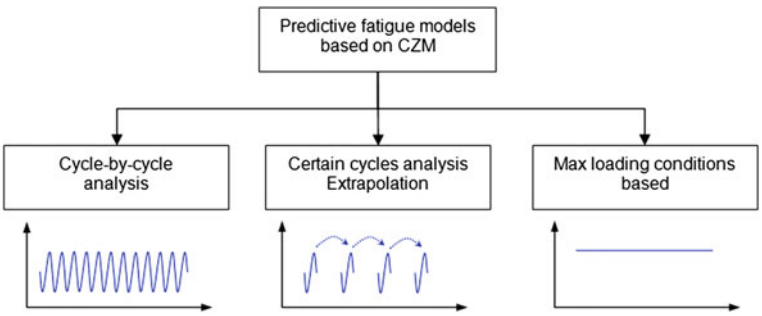

Fig. 5 Illustrating the *three* approaches adopted for CZM for fatigue

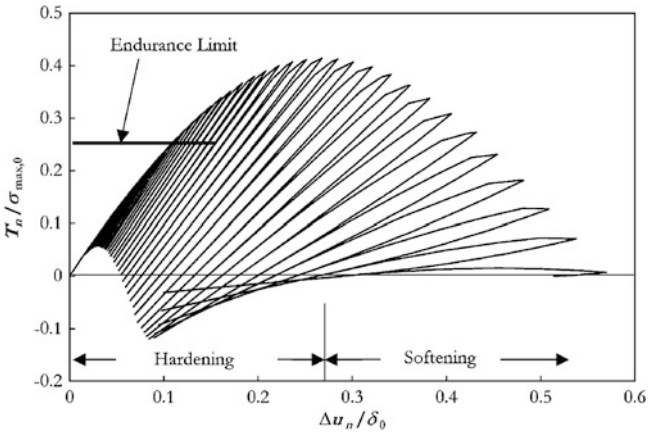

Fig. 6 Illustrating the *traction* separation response of an element of adhesive in a DCB subject to fatigue loading [23]

Turon et al. [33] use a cycle extrapolation approach. They defined this as a "jump strategy" and used the Paris law coefficients to define the cyclic damage (which they added to any static "overload" damage that might also accumulate). Essentially this technique is just an adaptation of the cycle by cycle approach discussed above.

However the final approach, based on the maximum fatigue load is significantly different. Robinson et al. [22], Tumino and Cappello [32] and Khoramishad et al. [13] are amongst those who have followed this scheme. Robinson et al. [22] expressed the cyclic fatigue damage rate in terms of the cyclic displacements and 3 independent parameters. However they found that the parameters were mode dependent and required different sets for each configuration considered, even though the same materials were used in every case. Tumino and Cappello [32] resolved this problem by defining the parameters in terms of the mode mixity. The resulting predictions of specimens with very different mode mixes were good, as can be seen in Fig. 7. However, to do this they increased the number of parameters to be determined significantly. The work of Khoramishad et al. [13] forms the basis of the moisture dependent fatigue damage model that forms the main focus of this chapter and is discussed in more detail in Sect. 4.

3.2 Continuum Fatigue Damage Modelling

This approach appears to have been used less frequently for predicting fatigue response than the CZM. Solana et al. [28] considered only the maximum fatigue load and used the fatigue damage model of Eq. 6, where ε_{max} and ε_{th} were the principal strain associated with the maximum fatigue load and the threshold strain respectively. They tuned their model parameters (b and z) by using measured

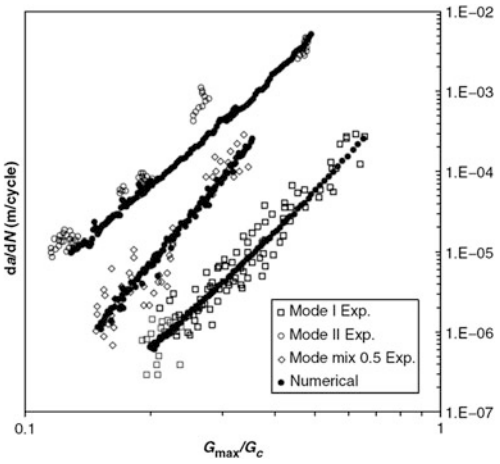

Fig. 7 Comparison between FE and experimental results for *three fracture specimens* of the same material having different mode mixes (from Tumino and Cappello [32]

backface strain data as well as the load-life response of bonded aluminium SLJs tested in CA fatigue at a range of different load levels

$$\mathrm{d}D_f/\mathrm{d}N = b * (\varepsilon_{max} - \varepsilon_{th})^z \tag{6}$$

Shenoy et al. [27] have applied a similar approach to predicting the response of CA fatigue and VA fatigue. They however used the plastic strain ε_{pl} in place of ε_{max}-ε_{th} in Eq. 6. A threshold still exists, when the adhesive experiences no plastic strain (i.e. elastic strain produces no damage). A further advance on the work of Solana et al. [28] is that the adhesive plasticity model included a pressure sensitive yield criterion rather than standard von Mises yielding.

4 Progressive Damage Modelling Approach

4.1 Fatigue Damage Modelling

4.1.1 Fatigue Model Details

This section contains a brief summary of the key points of the progressive fatigue damage modelling that forms the focus of this work. For further detail the reader is referred to Khoramishad et al. [13, 14]. A typical mixed mode version of the mono-mode traction separation law illustrated in Fig. 6 in the previous section is shown in Fig. 8. It shows that damage initiation occurs when a combination of normal and shear tractions (T_n, T_s, T_t) reach a critical value and that the critical mixed mode fracture energy G^c is a function of the component fracture energies. The parameters T_i^{max} and G_i^C, where i stands for each of the normal and shear components (n, s and t respectively), are degraded by the fatigue damage parameter D_f that is defined using the cyclic fatigue damage rate give in Eq. 7.

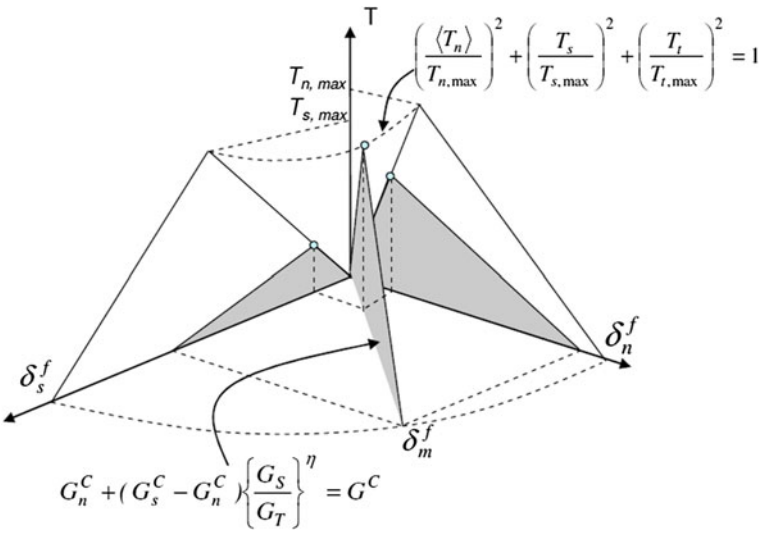

Fig. 8 Illustrating the mixed mode traction separation law used in this modelling

$$\frac{\Delta D_f}{\Delta N} = \begin{cases} \alpha[(\varepsilon_{\max} - \varepsilon_{th})\gamma^n]^\beta, & \varepsilon_{\max} > \varepsilon_{th} \\ 0, & \varepsilon_{\max} \leq \varepsilon_{th} \end{cases} \tag{7}$$

Here, ΔD_f is the increment of damage, ΔN is the cycle increment, $\varepsilon_{\max}$ is the maximum principal strain in the cohesive element, ε_{th} is the threshold strain, α, β, m and n are fatigue damage model parameters that, together with ε_{th}, need to be calibrated against the experimental data and γ is a correction factor to account for the load ratio. This latter parameter is necessary as the approach being adopted uses only the maximum load in the fatigue cycle to determine the damage. This is only acceptable if the load ratio ($R = P_{min}/P_{max}$) remains constant. Figure 9a shows different cyclic loads, both having the same maximum fatigue load. Clearly the fatigue lives resulting from these loads will not be the same, the life will increase as the load ratio, and thus the mean load, increases.

The conventional way of dealing with varying mean loads is through Goodman and Gerber curves which provide the fully reversed ($R = -1$) fatigue load that has the same life as the cyclic loading profile under consideration. Such curves are shown schematically in Fig. 9b and are given explicitly in Eq. 8, where m = 1 and 2 for Goodman and Gerber curves respectively.

$$\frac{P_a}{P_a} + \left(\frac{P_m}{P_s}\right)^m = 1, \tag{8}$$

Substituting for P_a (load amplitude) and P_m (mean load) in terms of P_{max} and R and rearranging yields an expression for the equivalent fully reversed load given in Eq. 9. By considering Eq. 7 it can be seen that the parameter γ has been used as a modifier of the maximum strain rather than the applied load.

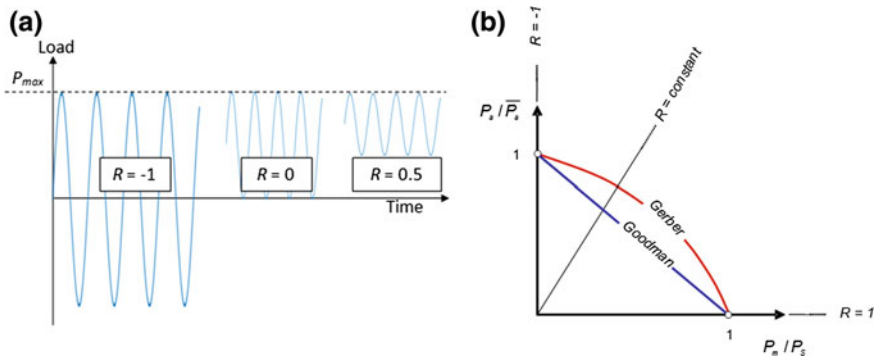

Fig. 9 **a** Cyclic loads having the same maximum loads (P_{max}). **b** Constant life diagram with Gerber and Goodman *curves*

$$\overline{P_a} = P_{\max}\gamma$$

$$\gamma = \frac{(1-R)/2}{1-\left[\frac{P_{\max}}{2P_S}(1+R)\right]^m}, \tag{9}$$

4.1.2 Fatigue Solution Procedure

The solution procedure is outlined in Fig. 10, which shows how the TSL parameters, the critical traction and the fracture energy, are degraded cyclically (Fig. 10b). Two steps have been applied in the FE modelling, Fig. 10a. The first simply applies the maximum fatigue load to the joint, with no degradation of the TSL parameters. Step 2 is broken into a number of increments, each increment representing a block of cycles, ΔN. In each increment the fatigue damage is updated at every integration point using the cyclic damage equation (Eq. 7) and the TSL parameters degraded appropriately. This process continues, with successive integration points damaging and failing, until the remaining adhesive is no longer able to withstand the maximum fatigue load and static rupture occurs with all CZM elements failing. The number of increments to failure provides the fatigue life. Alternatively, a fixed number of fatigue cycles (increments) can be applied and the joint then loaded statically to rupture to determine the residual strength (strength wearout) of the joint.

4.1.3 Validation of the Fatigue Damage Modelling Procedure

To illustrate the effectiveness of this approach two separate studies are reported here. The first concerns predicting the dependence of the load-life response on the applied mean fatigue load. Fatigue tests were carried out on i) aluminium SLJs

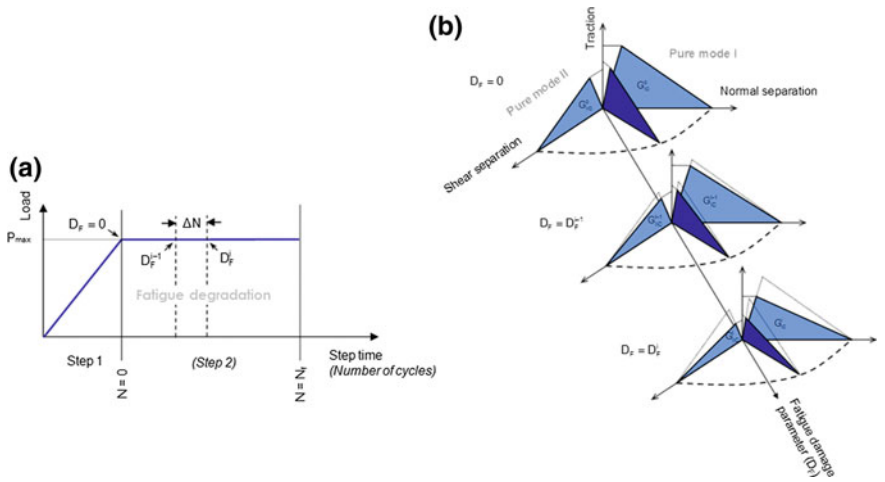

Fig. 10 A Schematic representation of the fatigue damage solution procedure. **a** Load stepping scheme, **b** Environmental and fatigue degradation

bonded with FM73M adhesive at load ratios of 0.1 and 0.5 (Khoramishad et al. [14] and ii) steel tapered SLJs bonded with AV119 adhesive [21] at load ratios of 0.1 and 0.5. The respective four load life curves are shown in Fig. 11. It can be seen that, as anticipated, for a given maximum fatigue load (P_{max}), joints with a lower mean load (lower value of R) have a shorter fatigue life. By extracting the data for a constant fatigue life (10^5 cycles in this case), it can be shown, Fig. 12, that the Gerber curve is a better fit for FM73M (CYTEC) aerospace film adhesive and the Goodman a better fit for AV119 (Huntsman) 1 part epoxy paste adhesive (refer to Fig. 9b).The CZM and the fatigue damage model parameters were

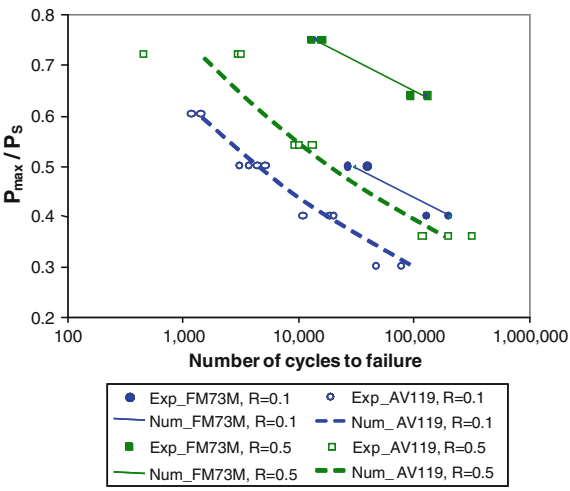

Fig. 11 Details of the effect of mean load on the load-fife *curves* of two different adhesive joint configurations

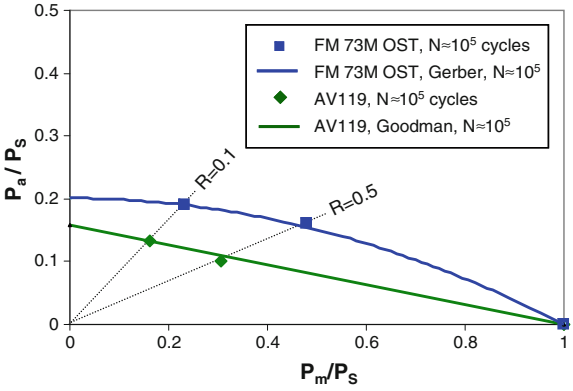

Fig. 12 Constant life *curves* for two adhesive systems

calibrated from static tests and the R = 0.1 fatigue tests and used to predict the R = 0.5 results. The good fit is apparent in Fig. 11. Although not detailed here, the backface strain was measured and used as part of the static and fatigue calibration and validation process. Without this additional data, which provides information on the damage zone size, it is not possible to define a unique set of CZM parameters. A more detailed discussion on determining the CZM parameters and the use of backface strain can be found in Katnam et al. [12] and Khoramishad et al. [14].

The same fatigue damage model has been used to predict the life of various variable amplitude sequences of fatigue load applied to aluminium SLJs bonded with FM73M adhesive. The experimental work is detailed elsewhere (Shenoy et al. [27] but the 4 fatigue cycle spectra being considered are shown in Fig. 13a and a schematic of the incremental way the load is applied (specifying the load ratio, maximum load and number of cycles for each set of fatigue cycles) is shown in Fig. 13b. Other than grouping the cycles into sets having the same loading profile no other changes to the modelling procedure to that outlined above were required.

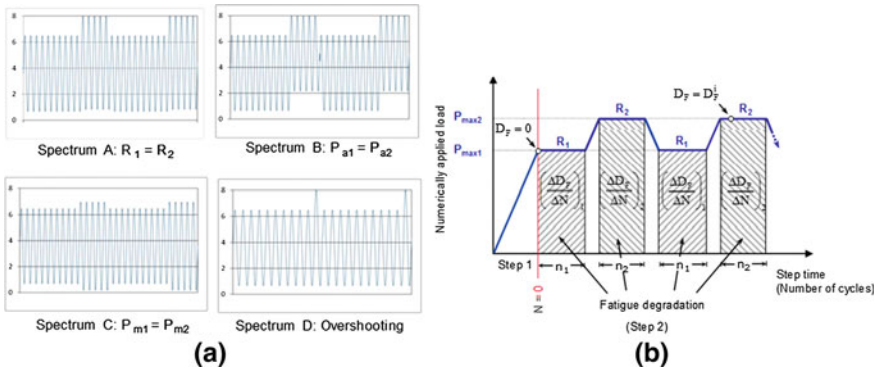

Fig. 13 Showing **a** The different load-time cyclic spectra and **b** The incrementation used in the FE modelling

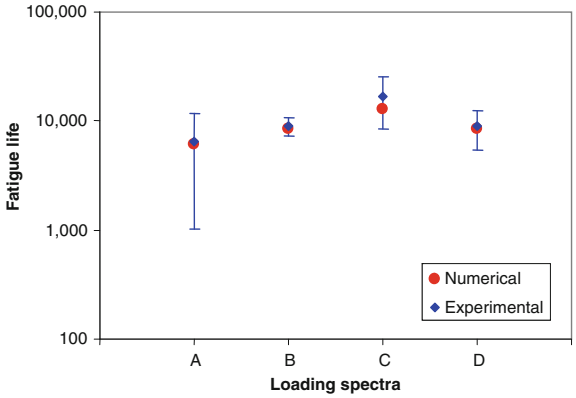

Fig. 14 Experimental and predicted lifetime from the 4 VA fatigue spectra shown in Fig. 13a

Table 1 A summary of the errors in predicted VA fatigue lifetime for the spectra shown in Fig. 13a

VA fatigue Loading spectra	% Error			
	Palmgren-Miner (%)	Fracture mechanics (Shenoy et al. [27]) (%)	Damage mechanics (Shenoy et al. [27]) (%)	Proposed model CZM (%)
A	25	−70	72	−4
B	63*	−76	17	−5
C	2*	−79	31	−24
D	103*	−70	94	−7

The measured and predicted fatigue lives are shown in Fig. 14 and the errors obtained using various predictive approaches, including the current one, are summarised in Table 1. The "*" indicates that the required CA for load ratios other than 0.1 were predicted as the experimental data was not available. It can be seen that the correlation to the experimental data is good and that this technique provides enhanced predictions compared with the other techniques. Full details of the work can be found in Khoramishad et al. [15].

4.2 Durability Framework

The approach used is a coupled diffusion-stress FE analysis, as illustrated in Fig. 15. This is similar to the approach presented in the chapter "Prediction of Joint Strength Under Humid Conditions: Damage Mechanics Approach" of this book and the work outlined in Chap. 8 of an earlier book, Crocombe et al. [6]. The initial FE phase determines the moisture distribution in the joint and this is passed into the second phase which uses progressive damage modelling techniques in

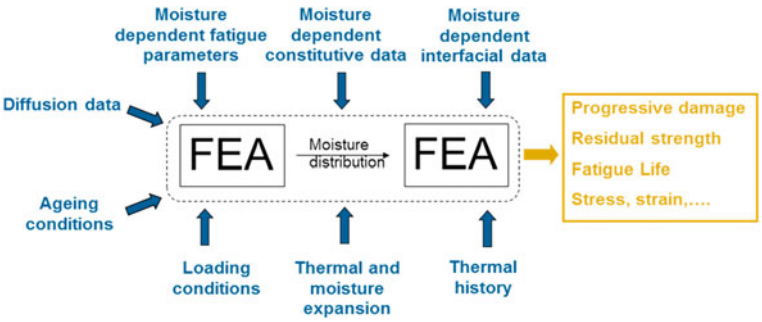

Fig. 15 A schematic representation of the modelling framework adopted

conjunction with moisture dependent material parameters to determine the response to an imposed load history. Figure 15 shows the modelling process as being sequentially coupled but, using finite elements with moisture and displacement nodal unknowns, the process can be fully coupled. Sequential coupling is reasonable when ageing precedes loading but with combined loading and ageing, typical of many service conditions, then a fully coupled approach is preferable. The techniques outlined here for sequentially coupled models are equally valid for fully coupled analyses. Note also that the process of elevated temperature cure and of ageing in moisture will produce swelling strains due to thermal and hygroscopic expansion and these need to be incorporated.

4.3 Incorporating Moisture Degradation into Fatigue Damage Modelling

Since a framework for predictive modelling was first outlined by Crocombe [3] much work has been undertaken considering the effect of moisture on the static response of a bonded structure. This includes continuum damage modelling of the degraded adhesive Hua et al. [10], cohesive zone modelling of the degraded interface Liljehahl et al. [17] and cohesive zone modelling of the degraded adhesive Katnam et al. [12]. A common theme in all these approaches was to define the material properties to be a function of moisture content. This provides a degrading stress strain curve for continuum damage or TSR for the cohesive zone modelling. This is similar in nature to the degrading of the TSR parameters for fatigue damage, as discussed and illustrated in Sect. 4.1.2.

This then provides a natural way forward for combining environmental damage and fatigue damage. In the experimental and modelling work presented later, the adhesive joint has been exposed to the environment prior to fatigue testing and so the modelling degrades the material parameters for exposure to moisture initially and then further degrades these parameters for fatigue. This approach is illustrated in Fig. 16. The following two sections in this chapter provide some detail of the

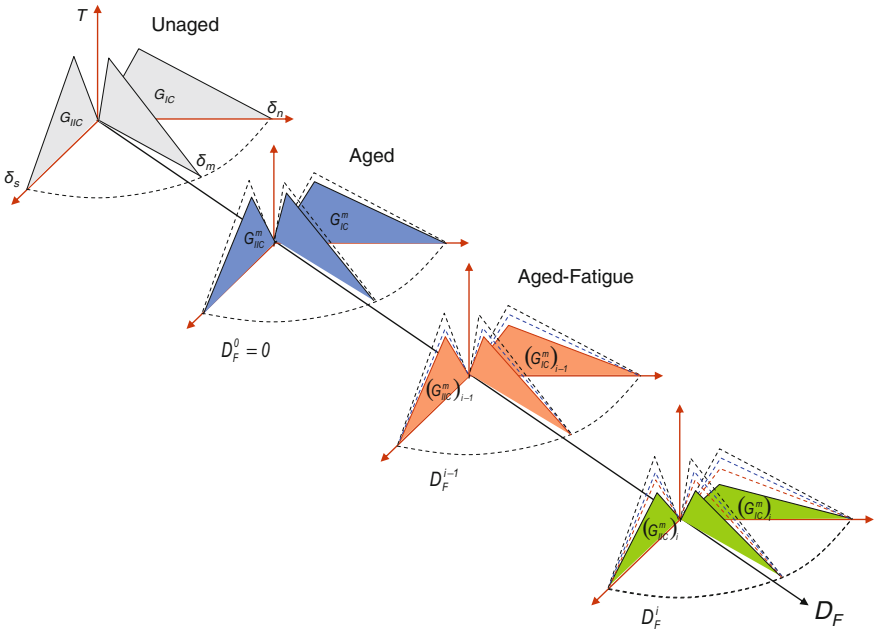

Fig. 16 Illustrating the combined moisture ageing and fatigue degradation of the adhesive CZM parameters

application of this combined moisture and fatigue damage modelling to actual adhesively bonded joints.

5 Experimental Data

The sections below provide an overview of the aged fatigue experimental work that has been undertaken. Further details can be found in Sugiman et al. [30, 31].

5.1 Joint Configurations

Two different configurations using the same materials (aluminium 2024T3 and FM73M adhesive) and surface treatment (chromic acid etch, phosphoric acid anodise and BR127 primer) were aged and tested. These were a monolithic single lap joint (MSLJ) and a laminated doubler in bending (LDB), both illustrated in Fig. 17. The laminate in the LDB specimen consisted of sheets of aluminium alloy bonded with FM73M. The same pre-treatment was used for the aluminium alloy sheets and the aluminium doubler. Due to the load transfer that takes place at

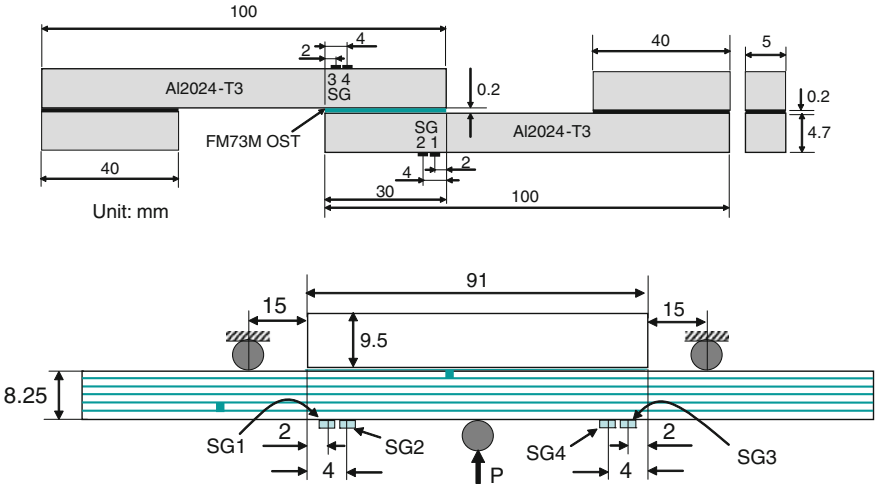

Fig. 17 Showing the monolithic single lap joint (*top*) and the laminated doubler in bending (*lower*) specimens

either end of the doubler, it was anticipated that the doubler bondline, rather than the laminate bondlines would be the site of failure and this was found to be the case, as will be seen in the next section. Note that (backface) strain gauges were used on both specimens. These, together with in situ video microscopy, have quantified the spread of damage during both static and fatigue loading, providing critical information both for calibration and validation.

5.2 Test Procedure

Specimens were aged at 50 °C immersed in deionised water for 1 year and 2 years. As the MSLJ was only 5 mm wide, diffusion calculations indicated that this would be fully saturated by 1 year and so the 2 year exposure enabled the effect of time at saturation on joint integrity to be assessed. The LDB was 15 mm wide and diffusion calculations showed that this was only partially saturated, even after 2 years.

Joints (unaged and after 1 and 2 years ageing) were tested quasi-statically to failure to determine the residual strength. Specimens were also tested in fatigue at 5 Hz, with a load ratio of 0.1 and with the maximum fatigue load set to 50 and 60 % (MSLJ) and 40 and 50 % (LDB) of the corresponding static strengths.

In addition to the joints, additional testing was undertaken on the FM73M adhesive to determine (a) the moisture dependency of the bulk stress–strain response, (b) the diffusion characteristics, (c) the coefficient of hygroscopic expansion (swelling coefficient) and d) the coefficient of thermal expansion.

5.3 Experimental Results

The measured static strengths for the MSLJ and the LDB are summarised in Table 2. Failure of both joints at all ageing conditions was cohesive within the adhesive. Clearly the interface was degraded less than the bulk adhesive and this is primarily due to the high durability surface pre-treatment used on the aluminium. It can be seen that the strength of the MSLJ degrades by 22 and 24 % and the strength of the LDB degrades by 14 and 20 % after 1 and 2 years ageing respectively. The wider LDB experiences a larger decrease between years 1 and 2 and this, presumably, is because, unlike the narrower MSLJ, the joint has not reached saturation after 1 year.

Backface strain data and video-microscopy suggest slightly higher levels of damage in the aged than the unaged MSLJ specimens. At 2.5 kN, damage extends to around 1 mm in the aged joints but is not discernible in the unaged joints. Figure 18 shows the damage observed in the 2 year aged specimen at around 65 and 90 % of the failure load. By comparing the two images it is possible to get an idea of the growth of the static damage zone. The same trend is noted in the LDB with damage zones of between 1 and 2 mm at around 90 % of the failure load.

The load life curves from fatigue tests on the MSLJ are shown in Fig. 19a. It can be seen that, at a given load, there is a reduction in fatigue life of about a decade for the aged joints. Further it can be seen that the reduction in life following a 2nd year of ageing is not significant. This is consistent with the reduction in static strength observed above and was attributed to the joint already being saturated after 1 year. As with the static testing, the failure remains cohesive within the adhesive for all specimens. Figure 19b shows the backface strain plots from gauges mounted 2 mm inside each end of the overlap for a joint aged for 1 year and tested at 50 % of its static failure load. Also shown in this figure are measures of the evolving damage zones determined from video microscopy at either end of the joint. The similar nature of the two backface strain plots indicates that damage evolved essentially symmetrically and this is also observed in the damage evolution plots. However, such symmetric damage growth was not always observed and the backface strain plots are a good way to pick this up. In very broad terms a peak in the backface strains implies the damage/crack passing under the location of the gauge (in fact the crack is generally a little further advanced, see Crocombe et al. [4] for a more detailed discussion of this). Corresponding backface strains plots for the unaged specimens tend to exhibit a period of no change in backface strain during the initial part of the fatigue testing. This suggests that damage initiation is much quicker in the aged specimens. This is further verified in

Table 2 Summary of the unaged and aged static monolithic single lap (MSLJ) and Laminated doubler in bending (LDB joint strengths

	Unaged (kN)	1 year (kN)	2 year (kN)
MSLJ	3.93	3.06	2.97
LDB	5.06	4.32	4.02

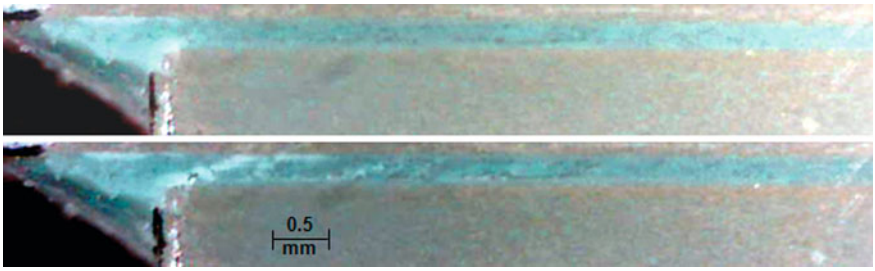

Fig. 18 Showing static adhesive damage at around 65 % (*top*) and 90 % (*bottom*) of the static failure load in MSLJ aged for 2 years

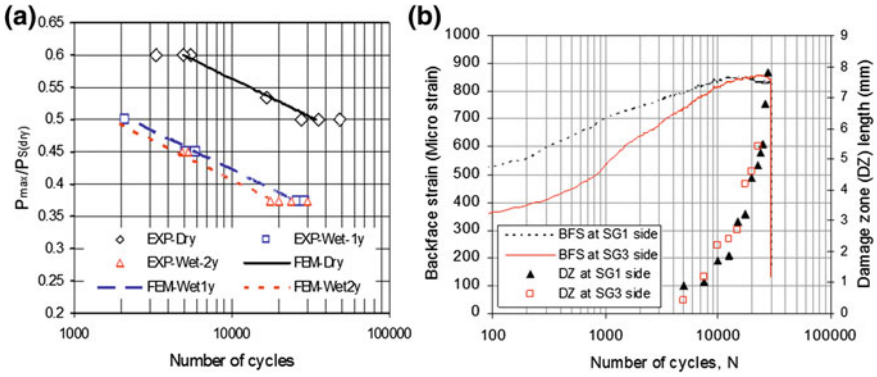

Fig. 19 Illustrating **a** Load life plot of the MSLJ specimens and **b** backface strain (*BFS*) and damage zone (*DZ*) for a specimen exposed for 1 year

the fatigue of the LDB where the damage initiation (indicated by the transition from a flat to a rising backface strain) occurred at around 21, 12 and 6 % of the fatigue life for unaged and 1 and 2 year aged specimens respectively, i.e. initiation occupied a decreasing amount of the life as the ageing increased.

The load life curves for the unaged and aged LDB specimens are shown in Fig. 20. It can be seen that, at a given load, the reduction in fatigue life is a factor of around 2 or 3. The specimen conditioned for 1 year under wet conditions (EXP Wet-1y) at the lowest load failed prematurely due to a poor bond between the fillet and the substrate end. In all other specimens failure ran directly through the fillet. The role of the fillet can be seen in Fig. 21, which shows the backface strain plot and associated video microscopy images. It can be seen that the sudden increase in backface strain is associated with the crack running through the adhesive fillet. The arrows on the video microscopy images indicate the extent of the damage zone.

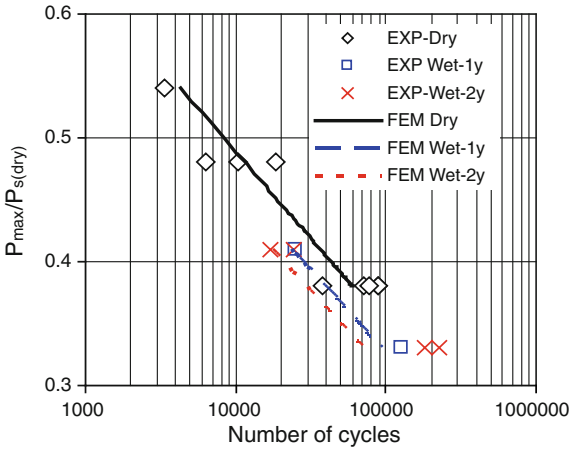

Fig. 20 Load-life plots of the LDB specimens

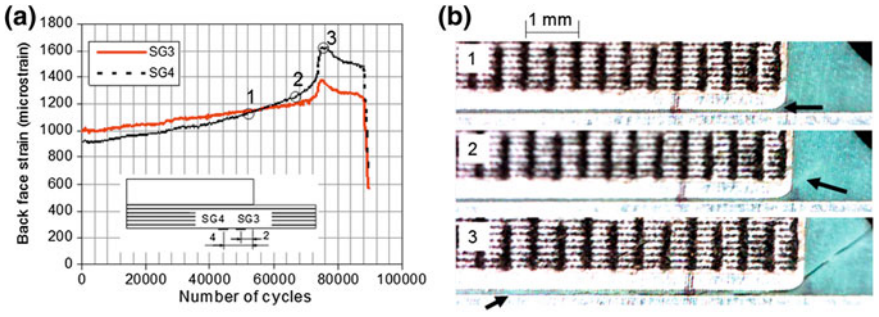

Fig. 21 Illustrating the link between the pronounced backface strain rise (*left*) and fillet cracking (*right*) in a LDB specimen

6 Predictive Modelling

This section provides an overview of the progressive damage fatigue modelling undertaken on moisture degraded adhesive joints. A more comprehensive account of this can be found in Sugiman et al. [30, 31]. The general approach taken is to determine material parameters wherever possible from independent tests then to use the MSLJ data to fine tune these parameters. Finally, these parameters are used, unchanged, in the damage modelling of the LDB for validation.

6.1 FE Models

3D FE modelling has been undertaken of the LDB as it is necessary to model the moisture diffusion from all four sides of the adhesive layer. However, as the MSLJ was fully saturated by 1 year, diffusion analysis was not required and hence a more conventional 2D FE model was constructed and used for these joints. Details of the FE models for both joints are shown in Figs. 22 and 23. As the fillet was small in the MSLJ it was not included in the model. However, as discussed above, the fillet played a more significant role in the LDB specimens and so was included in the model. In both cases the cohesive zone has been included as a thin layer running though the centre of the bondline. This location was chosen because all failures were at the centre of the bondline, with similar thickness of adhesive left on both substrates. Another advantage of using a thin cohesive zone element is that it is now possible to model the continuum response of the adhesive as well. This might be useful for modelling advanced plasticity or viscoplasticity, although in this modelling work this option has not be exercised and only a linear response of the surrounding adhesive continuum has been modelled. A convergence study was undertaken to assess the effect of Cohesive Zone mesh size on the FE results and the size of element used here was well within the convergence region. In the LDB, as only the main (doubler) bondline experienced any damage, cohesive zone elements were not used in the laminate bondlines.

6.2 Model Parameters

The adhesive continuum was assigned linear elastic material properties whilst the aluminium was modelled using a von Mises elasto-plastic model. Initial values for the CZM were based on bulk adhesive stress–strain data (stiffness and critical traction) and DCB fracture toughness tests (G_I^c). Values for shear stiffness and critical traction, and mode II parameters were estimated assuming a von Mises

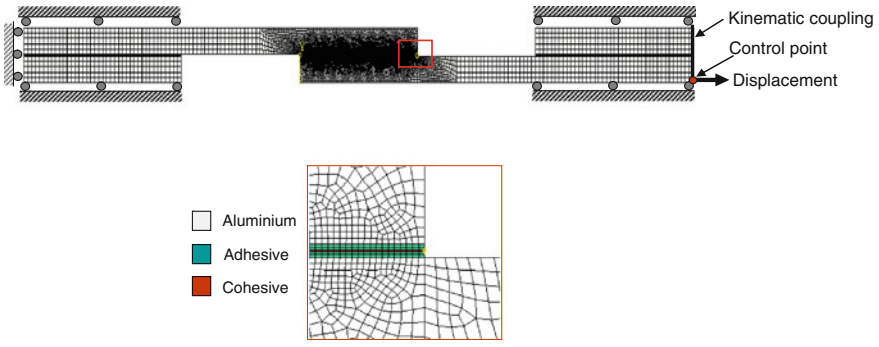

Fig. 22 Details of the FE mesh for the MSLJ analyses

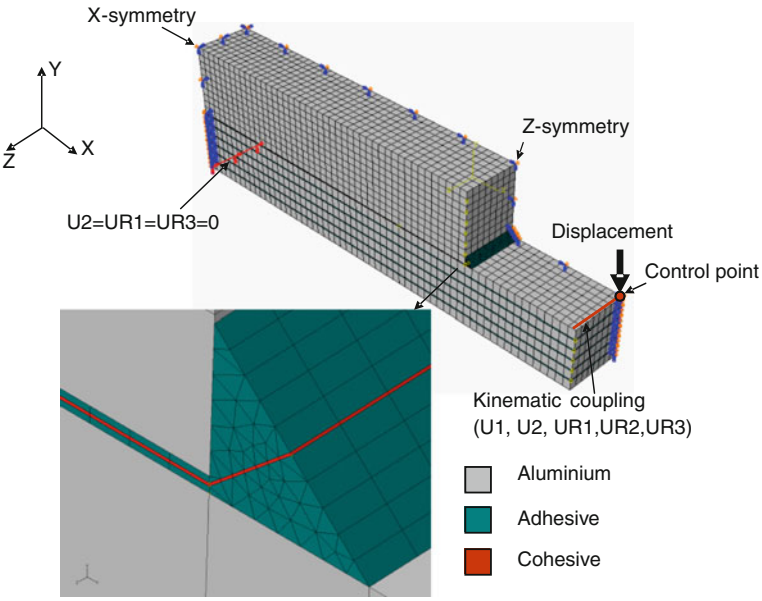

Fig. 23 Details of the FE mesh used for the LDB analyses

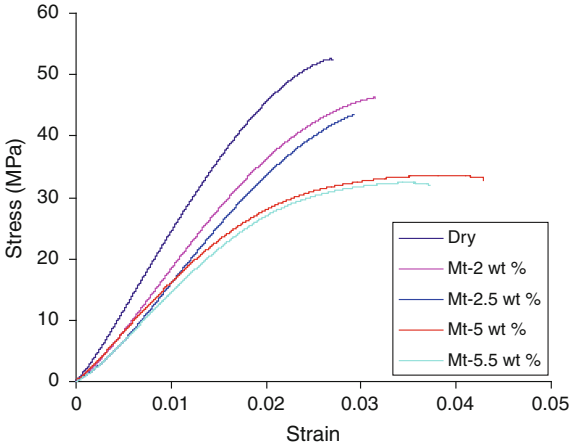

Fig. 24 Moisture dependent stress–strain response of the adhesive FM73M

equivalent stress principle. Moisture dependent material properties were degraded in line with the bulk adhesive moisture dependent material properties, see Fig. 24, and were then fine-tuned using MSLJ backface strain data. A summary of the key adhesive moisture dependent material properties found in this way are shown in Table 3. Additional data required for the adhesive FM73M for the static analyses include coefficients of moisture and thermal expansion (*CHE* and *CTE*

Table 3 A summary of the key moisture dependent adhesive material data

	E (MPa)	K_n (N/mm^3)	$K_s = K_t$ (N/mm^3)	T_n (MPa)	$T_s = T_t$ (MPa)	G_{IC} (kJ/m^2)	$G_{IIC} = G_{IIIC}$ (kJ/m^2)
Dry	2300	100,000	35,750	53	30.5	2.5	5
1 year	1960	80,000	28,550	39.1	23	2.1	4.2
2 year	1862	79,250	28,350	35.8	21	1.98	3.96

Table 4 A summary of other key adhesive material data (see text) required for the static analyses

CHE	CTE	D
0.0062/wt %	5.86×10^{-5}/°C	5.55×10^{-13} m^2/s

respectively) and the diffusion coefficient (D). These were all found from tests on bulk adhesive samples and are presented in Table 4.

The fatigue parameters (α, β, and ε_{th}) in the fatigue damage model outlined in Eq. 7 were found by calibrating against the MSLJ data and then used to predict the LDB data. As all fatigue cycling was undertaken at a fixed load ratio ($R = 0.1$) a correction for mean load effects was not required and thus the factor γ^n was removed from Eq. 7. Khoramishad et al. [13] conducted a parametric study on the effect of these parameters on the fatigue life. Increasing α accelerated fatigue damage evolution uniformly at all load levels while increasing β and ε_{th} decelerated fatigue damage evolution and this was more pronounced at lower load levels. Knowing the effect of the fatigue parameters on the fatigue life, an iterative method was used in conjunction with the MSLJ data to obtain appropriate values. These parameters were used in the fatigue damage model to degrade both the aged and unaged cohesive zone model parameters. The effect of cyclic increment size was assessed and convergence was obtained with increment sizes less than $N_f/100$. The fatigue parameters determined from the monolithic single lap joint (MSLJ) modelling can be seen in Table 5.

A final parameter to consider was the way in which the fatigue damage was applied to the material parameters. It was found that a linear degradation model was more appropriate for the LDB whilst a non-linear model (where parameters degraded more quickly initially) was more appropriate for the MSLJ specimens. This is discussed in more detail in Sugiman et al. [30, 31].

Table 5 A summary of the cyclic degradation parameters used in Eq. 7

Type of joint	α	β	ε_{th}
MSLJ (dry and wet)	0.0015	2.5	0.01

6.3 Modelling Results

The initial step of the modelling is to determine the moisture distribution. Figure 25 shows the predicted moisture distribution for the LDB (showing only a symmetric quarter of the overlap area) after 1 year of ageing. It can be seen that in the centre of the joint the moisture has only reached about 40 % of its saturation value. Even after 2 years exposure it had not reached full saturation.

The experimental and predicted residual static strengths for both configurations at all ageing conditions are shown in Fig. 26a and b. It can be seen that there is good correlation between the measured and predicted results.

Further confidence in the reliability of the static modelling results can be seen by considering the damage. A model that predicts the strengths but not the damage correctly is of limited use. One way of assessing the damage is to consider the backface strains. Figure 27a shows the predicted and measured backface strains at three positions along the overlap for the unaged MSLJ. The non-linearity that is seen in these plots between 1 and 1.5 kN is due to adhesive damage. Substrate yielding does occur but not until the loads exceed about 2.5 kN. There is good agreement between the predicted and the measured backface strain. The extent of

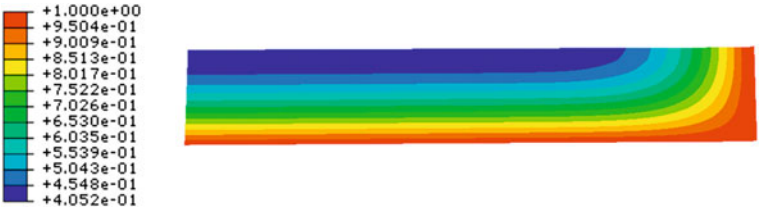

Fig. 25 Showing the normalised moisture distribution in the LDB after 1 year of ageing

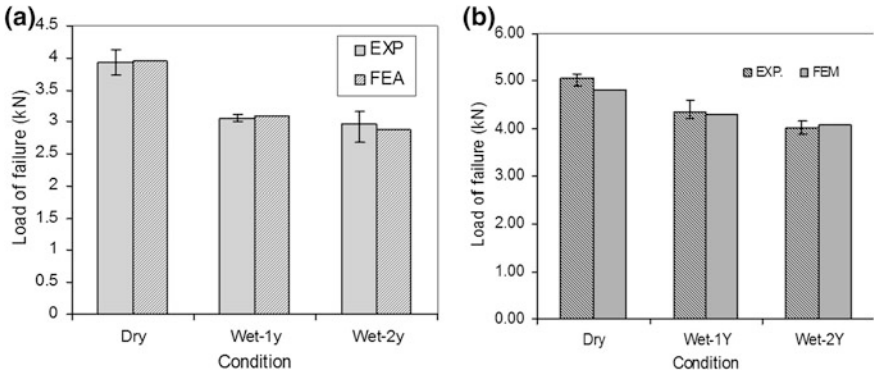

Fig. 26 Predicted and measured residual static strengths for **a** MSLJ and **b** LDB

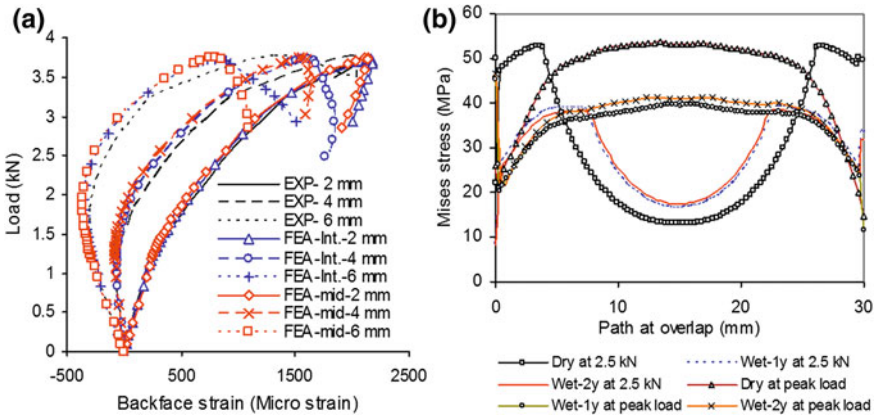

Fig. 27 **a** Measured and predicted backface strain *curves* at 3 separate locations on the unaged MSLJ as it is loaded to failure. **b** The adhesive von Mises stress distribution adjacent to the layer of CZM elements for aged and unaged MSLJ at 2 levels of loading

predicted damage can be seen in Fig. 27b for both unaged and aged MSLJ at 2.5 kN and close to the peak load. Consider first the curves at 2.5 kN. The dry joint has some damage extending over about 4 mm, as evidenced by the decreasing von Mises stress over this zone at the overlap ends. The aged curves at 2.5 kN show damage extending over a larger zone (about 8 mm). The von Mises stresses at the overlap ends are around 25 MPa and have been reduced both due to moisture degradation and to static damage. As the joint is saturated it can be deduced that the moisture reduces the stress to around 38 MPa (the value at around 8 mm inside the overlap where there is a transition in the stresses at the damaged/undamaged boundary). This is what would be expected from Table 3 in Sect. 6.2 and the static damage reduces it still further. Damage here relates to any point on the TSL that is beyond the critical traction. In this region, known as the process zone, the damage ranges between 0 and 1. Turning to the stress distributions near the failure load, the undamaged inner region has now disappeared in all 3 curves as the adhesive layer is damaged along the entire overlap. Separate plots, not shown here, allow the region to be determined where the adhesive is essentially entirely damaged (damage >0.97). This zone is just over 1 mm for the aged joints at 2.5 kN and about 4.5 mm for all joints loaded to almost peak load. These zones tie up well with fully damaged regions identified from in situ video-microscopy during the testing and reported in Sect. 5.2.

In some ways, one might expect to obtain a good correlation between the experimental and predicted results for the MSLJ because a subset of this data was used to calibrate the CZM parameters. So another assessment of the effectiveness of this model is to see how well it can predict the response of the LDB. Independent experimental and predicted backface strains are shown in Fig. 28a. The match between the data is really quite good, particularly when it is considered that the predicted data is batch averaged whilst the experimental data obvious will not

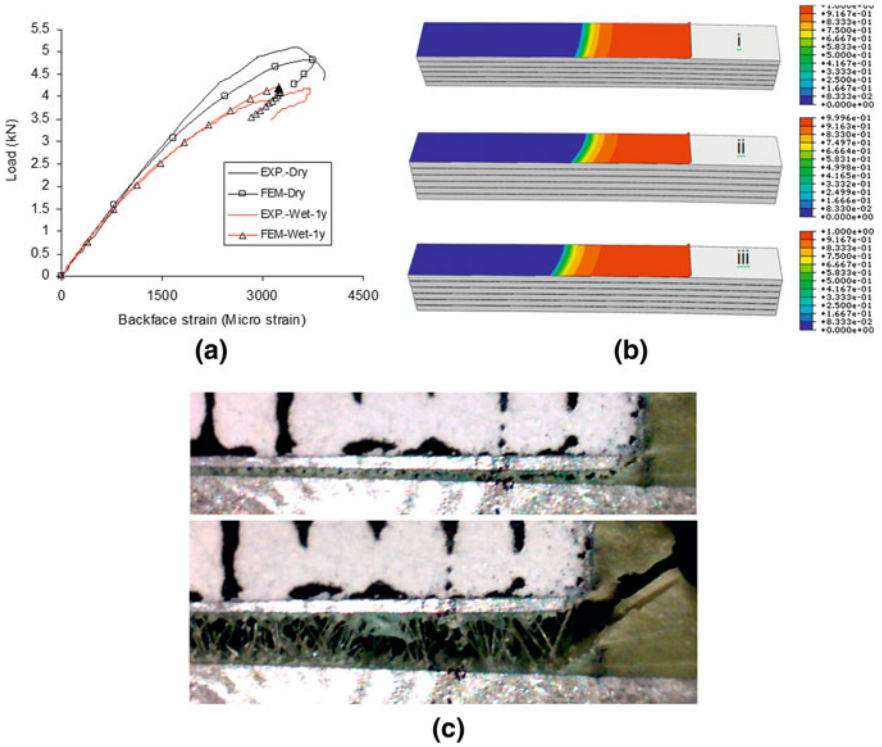

Fig. 28 **a** Predicted and measured load backface strain for LDB. **b** Predicted damage contour plots for LDB at peak load unaged (i), 1 year (ii) and 2 year (iii) exposure, **c** in situ plot of damage in dry LDB at peak load and just past peak load

be the same as the batch averaged data. Plots of predicted damage at the peak load are shown in Fig. 28b. It can be seen that the damage is slightly more advanced at the exposed edge than the drier interior, as might be expected as the material is degraded more on the exposed edge where it is fully saturated. Again, a measure of the damage can be extracted from these and similar plots to compare with measured damaged adhesive zones. At 3.9 kN, the length of zone that had damage >0.97 was 1, 3 and 5 mm for the unaged and 1 and 2 year aged specimens respectively. At the peak load the damage zone lengths are about 8 mm for all ageing conditions. These zone lengths are in good agreement with the measured damage zones. Figure 28c shows the data for the dry LDB at the peak load and it can be seen that the damage zone just extends off the left hand side of the image, a little over 6 mm from the end of the overlap. Also, the crack is about to run through the fillet, as seen in the lower image taken just post peak load.

We turn now to the degraded fatigue response of the MSLJ and the LDB. Fatigue results in a steady build up of damage leading to failure at levels of load significantly below those required for static failure. This implies that the use of reliable techniques to monitor and measure damage will be essential. Thus the use

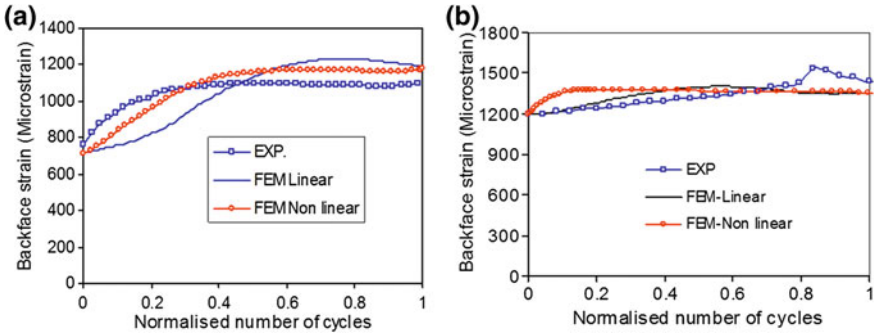

Fig. 29 Comparing measured backface strain with predictions assuming linear and non-linear degradation for unaged **a** MSLJ and **b** LDB

of backface strain as a means of monitoring damage forms a very important part of calibrating and validating the progressive damage models. Extensive measurement of backface strain were made on both the MSLJ and LDB specimens and it was noted that the shape of the evolving curves were quite different, as can be seen in Fig. 29. Other experimental data has already been presented in Figs. 19 and 21 for the MSL and the LDB respectively. Different axes have been used in Figs. 19 and 21 (log cycles for MSLJ and linear cycles for LDB) and this masks the trend somewhat. If one was to replot the LDB data on log axes the slope of the curve would be much flatter. Thus it appears that fatigue damage evolution appears much later in the LDB specimens. The reasons for this are not yet fully understood but may be due to differences in mode mixity in the two specimens. However, this remains a topic for future work. At this stage, as discussed in Sect. 6.2, a linear relationship was used linking parameter degradation with fatigue damage in the LDB and a non linear relationship was used with the MSLJ, promoting damage earlier. Figure 29 shows clearly the difference between using a linear and non-linear relationship on the backface strain and the better fit provided by the non-linear relationship for the MSLJ and by the linear relationship for the LDB.

The predicted load-life data for the MSLJ has already been presented with the experimental data in Fig. 19 in Sect. 5.3. The predictions are quite good, but one might expect that as a subset of the MSLJ data were used to calibrate the model parameters.

It was noted in Sect. 5.3 that sometimes the fatigue damage was asymmetric, propagating faster at one end than at the other in a joint. Whilst there may be a number of reasons for this, this is an aspect that can be explored through simulation. There are various ways of introducing asymmetry in the model and in the case discussed below this was achieved by varying the thickness of the adhesive and cohesive elements along the length of the joint. Stresses and hence damage will be more rapid at the end of the overlap that contains the thinnest adhesive layer. The measured and predicted backface strain and damage zone size is shown in Fig. 30 for an unaged MSLJ at the highest level of applied loading. It can be

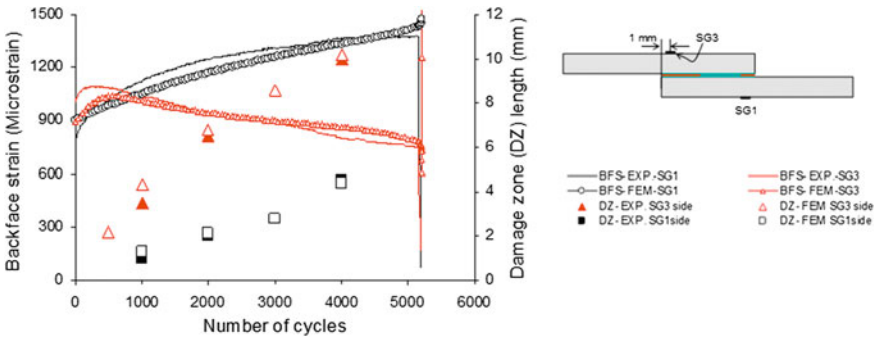

Fig. 30 Asymmetric measured and predicted damage growth in an unaged MSLJ fatigued at 60 % of the static strength

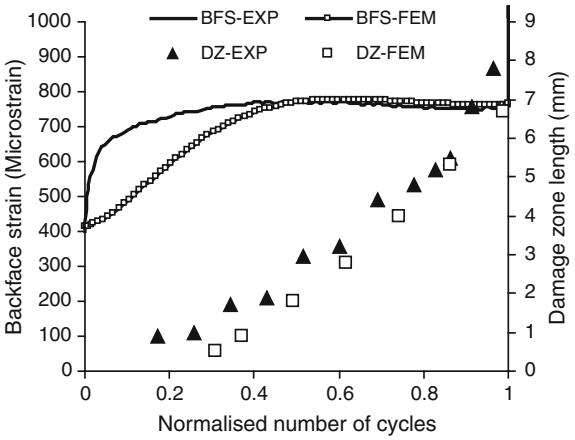

Fig. 31 Measured and predicted fatigue response of a MSLJ age for 1 year and tested at 50 % of the aged static strength

seen that the damage builds up preferentially at the left hand side of the overlap with the damage passing under the strain gauge SG3 fairly early on in the life of the joint. The experimental and predicted backface strains match well over the life of the joint.

A final comparison of measured and predicted data for MSLJs is shown in Fig. 31 for a specimen aged for 1 year and then fatigued at 50 % of the aged static strength. The damage growth was more symmetrical in this case and so only damage at one side is considered. It can be seen that experimentally the initial build up of damage was quicker than predicted and this caused the backface strain (measured at 2 mm inside the overlap in this case) to grow more rapidly initially. However, the final backface strain, damage zone and fatigue lives matched well.

When the fatigue damage model parameters summarised in Table 5 in Sect. 6.2 were used to predict the fatigue lives of the aged LDB, good agreement was achieved, see Fig. 20 in Sect. 5.3. However measured fatigue lives for the unaged LDB were shorter than the values predicted using the parameters given in Table 5.

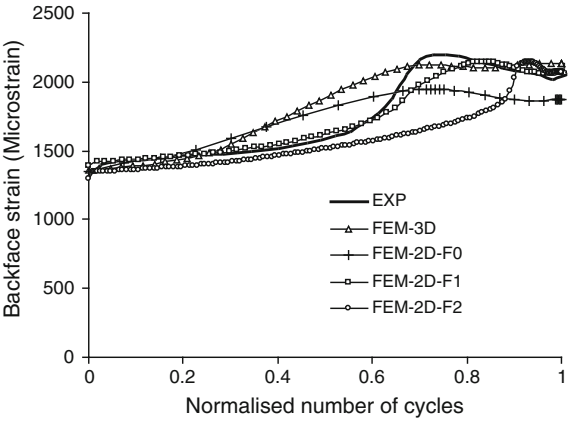

Fig. 32 Showing the effect of fillet size on the predicted backface strain response of an unaged LDB

It was found necessary to increase the parameter α from 0.0015 to 0.003. It is conjectured that this difference could be attributed to differences in the manufacturing technique and the age of the adhesive used for MSLJ and LDB. It would appear that these differences are alleviated by the ageing process as both aged LDB are modelled correctly using the MSLJ parameters.

It is also seen that the fillet size can have a more significant effect on fatigue life than on static strength. Figure 32 shows the measured backface strain for an unaged LDB and corresponding predictions for models with various fillet sizes. The 3D model (shown in Fig. 23) has a small fillet and it can be seen that the backface strain transition occurs fairly early on in the fatigue life (around 25 %). Various 2D models were then constructed with different fillet sizes (as the joint is unaged a 2D model is acceptable as there is no moisture distribution in the joint). It can be seen that the effect of increasing the fillet size shifts the backface strain transition to later in the fatigue life. For the data shown in Fig. 32 it would seem that the fillet size F1 (1.8 mm high and 1 mm long) best matches the experimental data.

To consider this further, the fatigue failure process for another unaged LDB specimen is considered in Fig. 33. Again, the 2D FE model has been used and the fillet size in the model and in the actual joint were both large (2.34 mm in the FE model). It can be seen that the predicted and measured backface strain match well but possibly more importantly the sequence of failure is illuminating. The labels on the damage contour plots match the corresponding point on the backface strain life curve. It can be seen that the early damage (point 2) is at the embedded substrate corner but that the damage grows more rapidly into the adhesive layer than into the fillet. The region from 2 to 3 is of stable crack growth, mainly along the overlap region. The sharp strain jump from 3 to 4 is associated with the crack running through the fillet. At this point the crack length was about 5.5 mm which was very close to the crack length measured experimentally for this specimen, see Fig. 21 in Sect. 5.3. This is then followed by further crack growth along the overlap (beyond point 4) before final failure. It should be noted that the difference noted in backface

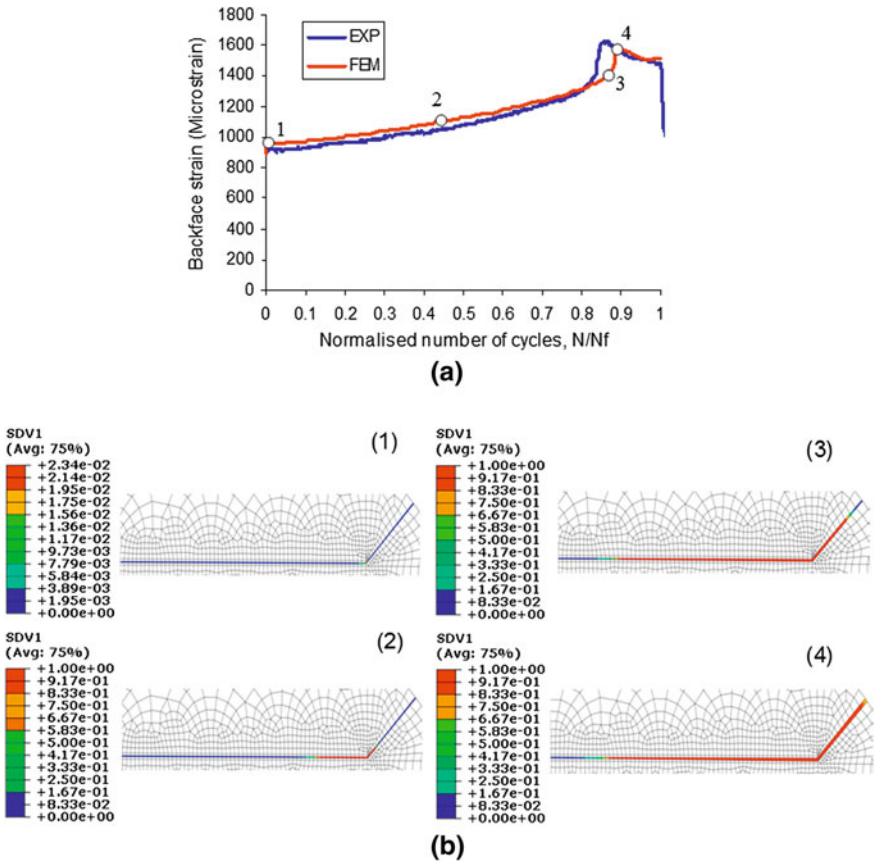

Fig. 33 Showing **a** The predicted backface strain evolution and **b** Predicted adhesive damage at selected points on the backface strain *curve*

strain evolution between MSLJ and LDB and shown in Figs. 31 and 32 could be attributed to different fillet responses rather than, or as well as, mode mixity as was suggested earlier.

A final plot, Fig. 34, shows the predicted and measured backface strain for a LDB that has been aged for 1 year and fatigued at 50 % of its aged static strength. There is a reasonable match between the predicted and measured data and important trends such as a cross over in the strains as the crack grows from the 2 mm to the 4 mm location gauge. It is not clear why the experimentally measured strains decreased towards the end of the fatigue life unless at these large crack lengths (and thus correspondingly high actuator movements) the servo-hydraulic fatigue machine was unable to apply the cyclic loads specified.

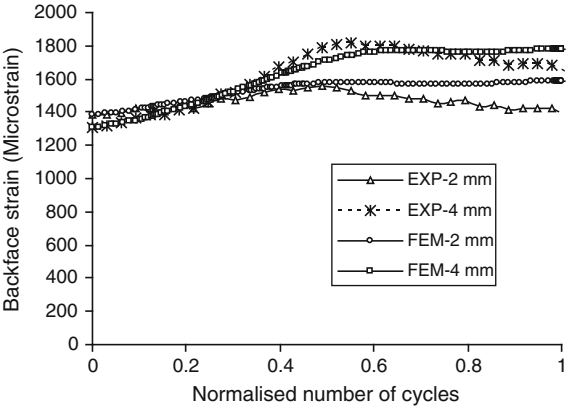

Fig. 34 Showing the measured and predicted backface strains in a LDB aged for 1 year

7 Conclusions

A number of approaches have been used to apply progressive damage FE modelling to adhesively bonded joints. The most commonly used approach is one based on cohesive zone modelling and, although this is very robust and relatively insensitive to mesh size, it does have the limitation of needing to know the failure path a priori. However in many cases in adhesively bonded joints this is not a major restriction, as failure is constrained to propagate along the adhesive layer. Other approaches include continuum damage and the use of XFEM (extended finite element method). These techniques do not require special elements to be seeded and so are particularly suitable for modelling damage in regions such as the adhesive fillet or the "noodle" in a composite T joint. Finally they can be combined with cohesive zone elements to model multisite failure.

Progressive damage modelling of fatigue in adhesively bonded joints is a relatively new area of research. A number of approaches have been adopted including a cycle-by-cycle approach and one that is based on the maximum fatigue load. This latter approach can include a parameter that accounts for varying load ratios and has been shown to be very effective in predicting the fatigue response of joints subjected to variable amplitude as well as constant amplitude loading.

The inclusion of moisture degradation in progressive damage modelling of bonded joints has a little more history than fatigue damage modelling. Essentially it involves a coupled diffusion-stress progressive damage analysis and the coupling can be parallel or sequential in nature. Both the interface and the bulk adhesive can be degraded by moisture and in the damage modelling this degradation can be achieved by making the material properties of both a function of moisture.

Moisture degraded fatigue damage modelling has been achieved by using fatigue damage to further degrade the material properties. Currently this fatigue damage has only been applied to the bulk adhesive properties (reflected in the TSL parameters). Whilst a reasonable amount of experimental characterisation of moisture degraded fatigue response of adhesive joints has been undertaken

progressive damage modelling in this area is in its infancy and testing and modelling has been undertaken on two configurations of joint, both using the same materials.

The damage models are both calibrated and validated using measurements of joint damage as well as fatigue life. Joint damage has been measured directly using in situ video microscopy and indirectly using backface strain measurements. It has been shown that a relatively simple fatigue damage model can be applied to relevant material parameters and give a reasonable estimate of joint damage and fatigue life. However, this is ongoing research and, at the time of writing, further work is required to refine the approach and this is discussed briefly in the next section.

Although this area will benefit from further work, in the authors' opinion, the concept of (a) using the maximum fatigue load with a correction for the mean load to characterise the fatigue loading (b) defining a cyclic fatigue damage law to degrade moisture dependent material parameters and (c) combining these in coupled moisture-stress progressive damage modelling has huge potential to enhance service life predictions of adhesively bonded structures.

8 Future Work

Perhaps the major area that will benefit from further work is the refinement of the fatigue damage model. Currently all parameters are degraded for fatigue damage in the same way and this is too simplistic. One might anticipate that parameters associated with different modes of loading may degrade differently and that parameters defining different material properties may degrade differently. From the work cited in this chapter it is clear that asymmetrical damage and variations in features such as the adhesive fillet can caused a considerable (and unwanted) increase in complexity. This could be considerably reduced by using a configuration with only a single site of fatigue failure and where considerable care is taken in controlling the consistency of the joint configuration, including controlling the adhesive fillet.

Another area for future work is the combined application of load and environment. There is evidence that the state of strain within the joint will affect the moisture transport as well as the underlying integrity of the adhesive and the interface. Loading during exposure also may lead to creep becoming an important damage mechanism.

As well as fluctuating loads during exposure it will also be important to consider the affect of a fluctuating environment. There is already evidence that diffusion is different on second and subsequent absorption cycles and that desorption is not simply the reverse of adsorption. To build in stress dependency to this complex moisture transport will be quite a challenge.

Finally, the approach taken so far has been unashamedly phenomenological in nature. It would be a significant benefit if the models developed could be more

mechanistic, being modified to reflect the underlying processes at whatever is the appropriate length scale.

Acknowledgments The authors are indebted to a large number of fellow researchers and PhD students and these include Dr Sugiman (on whose PhD much of Sects. 5 and 6 are based) and Dr Khorimshad (who played a key part in developing the fatigue damage model). We also gratefully acknowledge the financial support of the Technology Strategy Board and the technical input from Industrial collaborators Airbus and BAe Systems.

References

1. Ashcroft, I.A., Wahab, M.M.A., Crocombe, A.D.: Predicting degradation in bonded composite joints using a semi-coupled finite-element method. Mech. Adv. Mater. Struct. **10**, 227–248 (2003)
2. Ashcroft, I.A., Crocombe, A.D.: Modelling fatigue in adhesively bonded joints (Ch 7). In: da Silva, L.F.M., Ochsner, A. (eds.) Modelling of Adhesively Bonded Joints. Springer, Berlin (2008)
3. Crocombe, A.D.: Durability modelling concepts and tools for the cohesive environmental degradation of bonded structures. Int. J. Adhes. Adhes. **17**, 229–238 (1997)
4. Crocombe, A.D., Ong, C.Y., Chan, C.M., et al.: Investigating fatigue damage evolution in adhesively bonded structures using backface strain measurement. J. Adhes. **78**, 745–776 (2002)
5. Crocombe, A.D.: Incorporating environmental degradation in closed form adhesive joint stress analyses. J. Adhes. **84**, 212–230 (2008)
6. Crocombe, A.D., Ashcroft, I.A., Wahab, M.A.W.: Environmental degradation. In: Da Silva, L.F.M., Oschner, A. (eds.) Modelling of Adhesively Bonded Joints. Springer, Berlin (2008)
7. Curley, A.J., Hadavinia, H., Kinloch, A.J., et al.: Predicting the service-life of adhesively-bonded joints. Int. J. Fract. **103**, 41–69 (2000)
8. Erpolat, S., Ashcroft, I.A., Crocombe, A.D., et al.: A study of adhesively bonded joints subjected to constant and variable amplitude fatigue. Int. J. Fatigue **26**, 1189–1196 (2004)
9. Fernando, M., Harjoprayitno, W.W., Kinloch, A.J.: A fracture mechanics study of the influence of moisture on the fatigue behaviour of adhesively bonded aluminium-alloy joints. Int. J. Adhes. Adhes. **16**, 113–119 (1996)
10. Hua, Y., Crocombe, A.D., Wahab, M.A., et al.: Continuum damage modelling of environmental degradation in joints bonded with EA9321 epoxy adhesive. Int. J. Adhes. Adhes. **28**, 302–313 (2008)
11. Jethwa, J.K., Kinloch, A.J.: The fatigue and durability behaviour of automotive adhesives. Part I: Fracture mechanics tests. J. Adhes. **61**, 71–95 (1997)
12. Katnam, K.B., Sargent, J.P., Crocombe, A.D., et al.: Characterisation of moisture-dependent cohesive zone properties for adhesively bonded joints. Eng. Fract. Mech. **77**, 3105–3119 (2010)
13. Khoramishad, H., Crocombe, A.D., Katnam, K.B., et al.: Predicting fatigue damage in adhesively bonded joints using a cohesive zone model. Int. J. Fatigue **32**, 1146–1158 (2010)
14. Khoramishad, H., Crocombe, A.D., Katnam, K.B., et al.: A generalised damage model for constant amplitude fatigue loading of adhesively bonded joints. Int. J. Adhes. Adhes. **30**, 513–521 (2010)
15. Khoramishad, H., Crocombe, A.D., Katnam, K.B., et al.: Fatigue damage modelling of adhesively bonded joints under variable amplitude loading using a cohesive zone model. Eng. Fract. Mech. **78**, 3212–3225 (2011)

16. Liechti, K.M., Arzoumanidis, G.A., Park, S.J.: Fatigue fracture of fully saturated bonded joints. J. Adhes. **78**, 383–411 (2002)
17. Liljedahl, C.D.M., Crocombe, A.D., Wahab, M.A., et al.: Modelling the environmental degradation of the interface in adhesively bonded joints using a cohesive zone approach. J. Adhes. **82**, 1061–1089 (2006)
18. Mackie, R.I., Su, N.: The effect of aging and environment on the static and fatigue-strength of adhesive joints. J. Adhes. **42**, 191–207 (1993)
19. Maiti, S., Geubelle, P.H.: A cohesive model for fatigue failure of polymers. Eng. Fract. Mech. **72**, 691–708 (2005)
20. Nguyen, O., Repetto, E.A., Ortiz, M., et al.: A cohesive model of fatigue crack growth. Int. J. Fract. **110**, 351–369 (2001)
21. Crocombe, A.D., Richardson, G.: Assessing stress state and mean load effects on the fatigue response of adhesively bonded joints. Int. J. Adhes. Adhes. **19**, 19–27 (1999)
22. Robinson, P., Galvanetto, U., Tumino, D., et al.: Numerical simulation of fatigue-driven delamination using interface elements. Int. J. Numer. Meth. Eng. **63**, 1824–1848 (2005)
23. Roe, K.L., Siegmund, T.: An irreversible cohesive zone model for interface fatigue crack growth simulation. Eng. Fract. Mech. **70**, 209–232 (2003)
24. Rushforth, M.W., Bowen, P., McAlpine, E., et al.: The effect of surface pre-treatment and moisture on the fatigue performance of adhesively-bonded aluminium. J. Mater. Process. Technol. **153**, 359–365 (2004)
25. Shenoy, V., Ashcroft, I.A., Critchlow, G.W., Crocombe, A.D., Abdel Wahab, M.M.: Strength wearout of adhesively bonded joints under constant amplitude fatigue. Int. J. Fatigue **31**, 820–830 (2009)
26. Shenoy, V., Ashcroft, I.A., Critchlow, G.W., Crocombe, A.D., Abdel Wahab, M.M.: An evaluation of strength wearout models for the lifetime prediction of adhesive joints subjected to variable amplitude fatigue. Int. J. Adhes. Adhes. **29**, 639–649 (2009)
27. Shenoy, V., Ashcroft, I.A., Critchlow, G.W., et al.: Fracture mechanics and damage mechanics based fatigue lifetime prediction of adhesively bonded joints subjected to variable amplitude fatigue. Eng. Fract. Mech. **77**, 1073–1090 (2010)
28. Graner Solana, A., Crocombe, A.D., Ashcroft, I.A.: Fatigue life and backface strain predictions in adhesively bonded joints. Int. J. Adhes. Adhes. **30**, 36–42 (2010)
29. Su, N., Mackie, R.I., Harvey, W.J.: The effects of aging and environment on the fatigue life of adhesive joints. Int. J. Adhes. Adhes. **12**, 85–93 (1992)
30. Sugiman, S., Crocombe, A.D., Aschroft, I.A.: Experimental and numerical investigation of the static response of environmentally aged adhesively bonded joints. Int. J. Adhes. Adhes. **40**, 224–237 (2013)
31. Sugiman, S., Crocombe, A.D., Aschroft, I.A.: The fatigue response of environmentally degraded adhesively bonded aluminium structures. Int. J. Adhes. Adhes. **41**, 80–91 (2013)
32. Tumino, D., Cappello, F.: Simulation of fatigue delamination growth in composites with different mode mixtures. J. Compos. Mater. **41**, 2415–2441 (2007)
33. Turon, A., Costa, J., Camanho, P.P., et al.: Simulation of delamination in composites under high-cycle fatigue. Compos. Part A: Appl. Sci. Manuf. **38**, 2270–2282 (2007)
34. Wahab, M.M.A., Ashcroft, I.A., Crocombe, A.D., et al.: Finite element prediction of fatigue crack propagation lifetime in composite bonded joints. Compos. Part A: Appl. Sci. Manuf. **35**, 213–222 (2004)
35. Zhang, Y., Vassilopoulos, A.P., Keller, T.: Environmental effects on fatigue behavior of adhesively-bonded pultruded structural joints. Compos. Sci. Technol. **69**, 1022–1028 (2009)